csernak.gabor_124_23

HIDDEN CHAOTIC OSCILLATIONS IN APPLIED MECHANICAL PROBLEMS

Gábor Csernák

Department of Applied Mechanics
Budapest University of Technology and Economics

A thesis submitted for the degree of
Doctor of Hungarian Academy of Sciences (DSc)

Budapest, 2023

csernak.gabor_124_23

Acknowledgements

I am indepted to several people without whom I could not have prepared this dissertation.

I thank all my colleagues at the Department of Applied Mechanics at BME for providing a supportive and motivating atmosphere.

First and foremost, I would like to express my sincere gratitude to my former PhD supervisor, Professor Gábor Stépán, for giving me the opportunity to perform my studies under his guidance. His dynamics and motivation have deeply inspired me and the trust he placed in me opened the way to my academic career.

I am especially grateful to two of my roommates at the department: Dénes Takács, for his helpfulness, friendship and the enjoyable discussions about mechanics, and Tamás Insperger, who encouraged me to apply for the title of Doctor of the Hungarian Academy of Sciences.

I wish to express my gratitude to Professor Zoltán Pálmai (Department of Manufacturing Science and Technology, BME), for involving me in his research work. Our fruitful cooperation resulted in my most practice-oriented papers.

I would also like to thank two of my professors at the Janus Pannonius University: Kornél Szlachányi (KFKI Research Institute for Particle and Nuclear Physics) and Péter Hraskó (Department of Theoretical Physics, University of Pécs), for setting me up in scientific life. Both of them had a great impact on my outlook of nature.

Special thanks to my parents, my wife and my children for their emotional support.

The research work presented here was supported by the National Research, Development and Innovation Office, under grant numbers NKFIH 128422, NKFIH 83890 and OTKA F049242.

Contents

Chapter 1

Introduction

The present thesis is a summary of the scientific work I have done since receiving my PhD degree in 2003. Three different topics are discussed: Chapter 2 is devoted to the examination of a harmonically excited dry friction oscillator, Chapter 3 deals with the nonlinear analysis of chip formation, and finally, the effects of sampling and quantization on the dynamics of certain controlled mechanical systems are analysed in Chapter 4. These seemingly unrelated dynamical systems have an interesting feature in common: all of them can exhibit chaotic vibrations, but the irregular behaviour of the corresponding real systems is often attributed by scientists and engineers to random noise – i.e., chaos is *hidden* in some sense.

- In case of the dry friction oscillator (Chapter 2), chaotic behaviour was detected only if the static coefficient of friction was significantly larger than the kinetic one. Since special – periodic, but asymmetric – solutions emerge as the friction coefficients become different, the analysis of these orbits was the key to find the origin of chaos. Indeed, chaotic solutions were found to bifurcate from the asymmetric ones. So far rather few papers reported the existence of asymmetric oscillations, however, the traces of this kind of motion can be detected even experimentally. My main scientific contributions in this topic are the formulation of the conditions of having non-sticking symmetric solutions, the derivation and stability analysis of non-sticking asymmetric solutions, the extended bifurcation analysis of the system, and the detection of chaotic solutions that hide in rarely examined parameter domains.

- The formation of chips during cutting (Chapter 3) is a remarkably complex thermo-mechanical process. To understand this phenomenon, my colleague, Zoltán Pálmai put forward several models to describe the variation of shear stress and temperature in the so-called shear zone. During our cooperation, my task was the nonlinear analysis of the models. I pointed out that chaotic (aperiodic) chips are formed in certain parameter domains and that chaos is reached via period-doubling cascades, occuring according to Feigenbaum's ratio. Technological experts typically focus on stable periodic or equilibrium solutions. Taking into account the elasticity of the tool or the workpiece, the analysis showed that a small amplitude chaotic oscillation may be superposed on equilibrium solutions, i.e, aperiodic unevenness may occur on the profile of continuous chips. Thus, chaos is hidden in this case, too. The chip formation model was extended further, to incorporate the effects caused by a gradually increasing and suddenly detaching built-up edge. I determined the largest Lyapunov exponent of the system described by a set of piecewise smooth delay-differential equations, and showed that a finite-dimensional chaotic attractor hides in the infinite-dimensional phase-space.

- Micro-chaos (Chapter 4) is a phenomenon when the so-called digital effects turn the neighbourhood of the desired state of a controlled mechanical system into one or more small strange attractors or repellers. The corresponding small amplitude vibrations are usually considered as noise in the practice, however, as we will see, the source of these hidden chaotic vibrations is deterministic dynamics. Based on the concept of micro-chaos, I gave complete proofs of chaos in case of two different two-dimensional micro-chaos maps. In the presence of dry friction, the chaotic vibrations may disappear after a finite time interval. I developed a method for the estimation of the mean lifetime of transient chaos, based on the determination of the fractal dimension of the repeller. Finally, since the phase-space of micro-chaos maps is naturally partitioned due to the quantization, my PhD student Gergely Gyebrószki and I developed a new cell mapping algorithm for the exploration of the global dynamics.

Certainly, the methods applied for the analysis of these systems are also similar, but not entirely identical. For example, although the largest Lyapunov exponent is determined in all of the three cases, different methods are applied for this purpose. It is also common in the analysed problems that – besides exhibiting chaotic behaviour – there are parameter domains where one encounters transient chaos, i.e., the trajectories escape from the so-called repeller set and tend to an attractor or another repeller. This feature also contributes to the hidden nature of chaotic oscillations.

It is important to emphasize that the found strange sets are *not* „hidden attractors": in mathematical terms, an attractor is called a hidden attractor if its basin of attraction does not intersect with a certain open neighbourhood of equilibrium points. However, in the considered cases the adjective „hidden" refers to the relatively small amplitude of the chaotic vibrations that are difficult to distinguish from external noise.

Due to the differences between the three themes, the literature review of each topic is provided in the first section of the appropriate chapter. The other parts of the chapters discuss my own results, except for the last sections in each chapter, that present the joint work with my former PhD students: Gábor Licskó and Gergely Gyebrószki.

To separate my achievements from those of others, references to my publications are printed in boldface (e.g., **[27]**) and the last chapter (Chapter 5) of the thesis summarizes my principal results. In order to improve the readability of the thesis, some technical details are presented in appendices.

The main text is everywhere written in first person plural without distinction between my independent work and the joint work with others. Nevertheless, the principal results have been stated in singular or plural in accordance with the number of contributors.

Chapter 2

Harmonically Excited Dry Friction Oscillator

2.1 INTRODUCTION AND LITERATURE REVIEW

The effects of dry friction on the relative motion of contacting bodies are difficult to predict. On the one hand, the underlying physical mechanisms are very complex. On the other hand, various mathematical difficulties can appear during the analysis of frictional systems, that require special tools to solve [7]. Moreover, friction models applied to characterise the contact of rigid bodies can lead to indeterminate or self-inconsistent solutions [22, 164].

Several friction models have been introduced so far – typically as the generalization of the Coulomb model [11, 45, 46, 61, 86, 87, 92, 93, 123]. However, even the Coulomb model poses challanges to the dynamical systems' researcher. This model is inherently non-smooth, since the direction of the friction force $F(v)$ is opposite to the relative velocity v of the examined body, and sticking may occur at $v = 0$. The situation is even more complicated if the static μ_0 and kinetic μ coefficients of friction are different, as it is illustrated in Fig. 2.1.

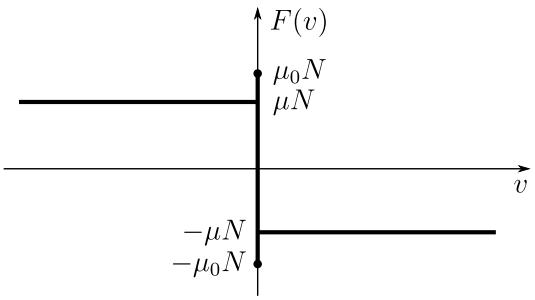

Figure 2.1: *The Coulomb friction characteristic. N denotes the (positive) normal force pressing the contacting bodies together.*

The nonlinear nature of friction implies that several different types of periodic solutions can appear in the phase space of these systems. Moreover, certain sophisticated models (e.g., [6, 62]) exhibit chaotic behaviour. Naturally arises the question: which is the simplest dry friction oscillator model where chaotic vibrations can occur and the friction characteristic is the only source of nonlinearity? While the „simplicity" of a model cannot be rigorously measured, a possible answer will be given to this question in the present chapter.

To understand the dynamics of frictional systems, two typical settings were often studied in the literature: oscillators on a moving belt [56, 68, 89, 96, 118, 134] and harmonically forced oscillators [51, 82, 83, 120, 136, 142]. Den Hartog [51], one of the pioneers in the

field of the theory of vibrations, obtained the exact, non-sticking solution of the steady state motion of a harmonically excited single degree of freedom oscillator (see Fig. 2.2), assuming that these solutions are symmetric. Hong and Liu [82, 83] and Pratt and Williams

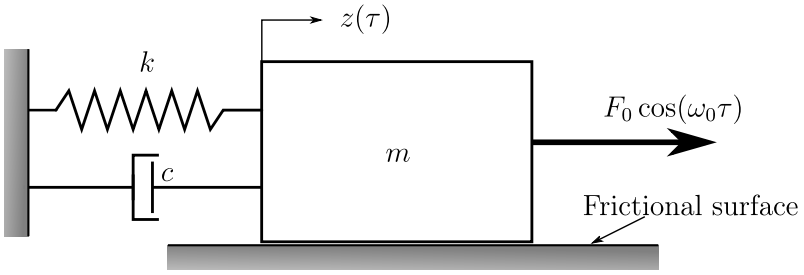

Figure 2.2: *Harmonically excited frictional oscillator*

[136] extended Den Hartog's work by the numerical examination of solutions which have multiple sticking segments during a period. Shaw [142] made a further big leap towards the understanding of frictional systems by considering different static and kinetic coefficients of friction and complementing the previous studies with a linear stability analysis. Similar results were published by Natsiavas [119] and Deimling [49] – the latter study is based on the theory of differential inclusions (set-valued differential equations). As the details of the so-called Filippov theory [7, 12, 65] had been elaborated and became widely known among the researchers, several other papers were devoted to the analysis of dry-friction systems, e.g., [101, 102]. Note, that the Filippov theory has several other areas of application, too, e.g., in power electronics and control theory [100, 163].

In the present chapter, special responses of the harmonically excited block-spring system shown in Fig. 2.2 are analysed. The equation of motion of this system assumes the form

$$mz'' + cz' + kz = F_0\cos(\omega_0\tau) - \mu mg\ f(z'), \tag{2.1}$$

where m is the mass of the block, k is the spring stiffness, c is the coefficient of viscous damping, F_0 is the force amplitude, and ω_0 is the angular frequency of excitation. $()'$ denotes the derivative $\mathrm{d}/\mathrm{d}\tau$ with respect to time τ. Coordinate z is measured from the untensioned state of the spring and the friction characteristic is described by the function

$$f(z') = \begin{cases} 1 & \text{if } z' > 0 \\ [-\mu_0/\mu, \mu_0/\mu] & \text{if } z' = 0 \\ -1 & \text{if } z' < 0 \end{cases}, \tag{2.2}$$

where μ and μ_0 denote the kinetic and static coefficient of friction, respectively. Mechanically, Eq. (2.2) is interpreted as follows: if the velocity is non-zero (i.e., the body slips), the kinetic friction force always opposes the velocity. Thus, different differential equations describe the motion at positive and negative velocities. This is why the zero-velocity subset of the phase space is called *switching manifold*.

To make the treatise simpler, one can rescale time and displacement as $t = \tau\sqrt{k/m}$, $x = zk/F_0$ [142] and introduce the parameter t_0 such that time t is measured from one of the turnaround instants – i.e., when the trajectory crosses the switching manifold **[27]**:

$$\ddot{x} + 2\ \alpha\ \dot{x} + x = \cos(\Omega(t + t_0)) - S\ f(\dot{x}), \tag{2.3}$$

where $\dot{()}$ denotes $\mathrm{d}/\mathrm{d}t$, $\alpha = c/(2\sqrt{km})$, $\Omega = \omega_0\sqrt{m/k}$, $S = \mu mg/F_0$, and $f(\dot{x}) \equiv f(z')$, with $S_0 = \mu_0 mg/F_0 > S$. Since (2.3) is non-autonomous, its phase space is 3-dimensional with state variables x, $v \equiv \dot{x}$ and t.

Function $f(\dot{x})$ is meant to take (mathematically) indetermined values at zero – this corresponds to the sticking phase, when the friction force adjusts itself to make equilibrium with other external forces acting on the body. The transition from stick to slip is allowed only if the magnitude of external forces reaches the maximal static friction force $\mu_0 N$, while the slip to stick transition can happen at any value of the friction force in the interval $[-\mu_0 N, \mu_0 N]$. The phase space domain where the oscillator sticks to the ground is referred to as *sliding manifold* in mathematical terms. In Fig. 2.3, the blue, dotted area shows this region. One can see in the lower subfigure that the green sticking segments of the numerically determined trajectory indeed seem to slide on the $v = 0$ plane. However, engineers prefer to focus on the physical properties of the motion. Consequently, we drop the mathematical term of sliding manifold and refer to this region as *sticking domain* or *sticking region*.

Using the introduced notations, the *condition of sticking* can be formulated as follows:

$$|x - \cos(\Omega(t + t_0))| < S_0 \quad \text{and} \quad \dot{x} = 0. \tag{2.4}$$

It can be seen from this inequality, that the width of the sticking region is $2S_0$ everywhere along the t axis, and the largest coordinate x, where sticking may occur equals $1 + S_0$. This property is illustrated in Fig. 2.3.

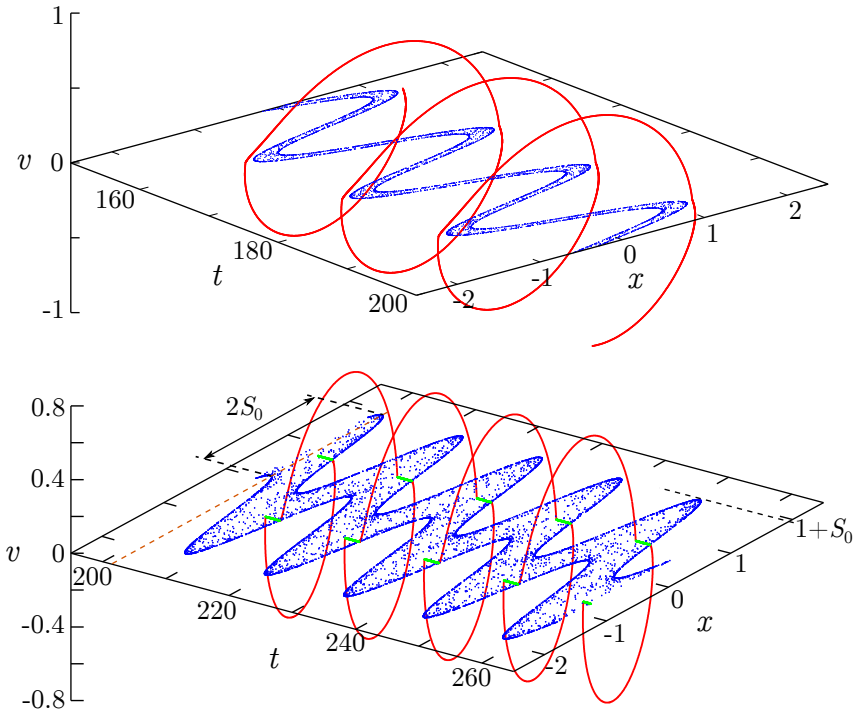

Figure 2.3: *Numerically obtained solutions (red and green) and the sticking region (blue). Upper panel:* $S = S_0 = 0.15$, $\Omega = 0.45$. *Lower panel:* $S = S_0 = 0.9$, $\Omega = 0.5$.

Filippov [65] assumed that different vector fields govern the dynamics on opposite sides of a switching manifold (the $v = 0$ plane in our case), and the convex combination of these vector fields describes the behaviour of the oscillator in the sticking domain (sliding manifold in mathematical terms). Unfortunately, the Filippov theory is difficult to apply in cases when the static and kinetic coefficients of friction are different. As it was shown in [109], this friction model cannot be treated as a differential inclusion, because this approach would lead to the non-uniqueness of solutions. Thus, although the Filippov theory provides an elegant framework for the analysis of non-smooth systems, we cannot rely on its results if the friction coefficients are different.

It was shown in [49] that an additional positive viscous damping would result in a single globally stable $2\pi/\Omega$-periodic solution, provided that the two friction coefficients are equal. As follows, we focus on the case when the viscous damping is negligible, i.e., $\alpha = 0$.

By exploiting the piecewise linear nature of Eq. (2.3), explicit solutions can be found between the successive stops **[27]**,[142]. If the velocity of the block is negative, the solution assumes the form

$$x^-(t) = A^- \cos(t) + B^- \sin(t) + L\cos(\Omega t) + K\sin(\Omega t) + S, \tag{2.5}$$

while in case of positive velocity

$$x^+(t) = A^+ \cos(t) + B^+ \sin(t) + L\cos(\Omega t) + K\sin(\Omega t) - S. \tag{2.6}$$

The constants K and L can be expressed as

$$K = \frac{\sin(\Omega t_0)}{\Omega^2 - 1} \quad \text{and} \quad L = -\frac{\cos(\Omega t_0)}{\Omega^2 - 1}. \tag{2.7}$$

If the initial conditions are given, A^- and B^-, or A^+ and B^+ can be determined. For example, if the initial phase t_0 is chosen such that $t = 0$ corresponds to a turnaround moment – when the initial displacement (and the amplitude) is x_0, the velocity is zero and the acceleration is negative – we obtain

$$x^-(0) = A^- \cos(0) + B^- \sin(0) + L\cos(\Omega \cdot 0) + K\sin(\Omega \cdot 0) + S = x_0, \tag{2.8}$$
$$\dot{x}^-(0) = -A^- \sin(0) + B^- \cos(0) - L\Omega\sin(\Omega \cdot 0) + K\Omega\cos(\Omega \cdot 0) = 0. \tag{2.9}$$

Thus,

$$A^- = x_0 - S - L = x_0 - S + \frac{\cos(\Omega t_0)}{\Omega^2 - 1}, \quad \text{and} \tag{2.10}$$
$$B^- = -K\Omega = -\frac{\Omega\sin(\Omega t_0)}{\Omega^2 - 1}. \tag{2.11}$$

Piecing together the solutions (2.5) and (2.6) provides a general solution. Unfortunately, this matching cannot be done analytically in the general case, since the next turnaround time $t = \theta_1$ can be determined using the following transcendental equation only:

$$\dot{x}^-(\theta_1) = -A^- \sin(\theta_1) + B^- \cos(\theta_1) - L\Omega\sin(\Omega\theta_1) + K\Omega\cos(\Omega\theta_1) = 0. \tag{2.12}$$

There is still a possibility to find solutions analytically: by searching for specific solutions, based on pre-defined requirements. In the aforementioned papers [51, 83, 142], the authors exploited the assumption that the periodic solutions are necessarily symmetric both in time and displacement. Our first goal is the *revision of this symmetry assumption.* As it will be demonstrated in the subsequent sections, it is possible to find asymmetric periodic solutions analytically.

In Section 2.2, we search for periodic, non-sticking solutions, using as few special assumptions about these solutions as possible **[28]**. The presented calculation leads to the same results as it was published in [51] and [142], but the derivation is different since it focuses on the conditions of symmetry. The validity of solutions is discussed in Section 2.2.2, that is an extension of the similar results from [142]. The stability analysis of linearly marginally stable solutions found in [142] is also extended by a third-order calculation, following **[29]**.

Based on the aforementioned results, Section 2.3 is devoted to the formulation and analysis of asymmetric solutions **[29]**. Although the found special cycles exist in measure zero

subsets of the parameter space, it is shown numerically in Section 2.4 that these special parameter domains open up if the static coefficient of friction is larger than the kinetic one.

The transitions between the symmetric and asymmetric solutions are examined in Sections 2.5.1 and 2.5.2 using a customized continuation algorithm **[31]**. Certain gaps were found in the determined one-parameter bifurcation diagrams where no stable periodic solutions were detected. It is pointed out in Section 2.5.3 that chaotic solutions occur in the corresponding parameter regions. Finally, Section 2.6 summarizes certain further results of our joint work with Gábor Licskó **[110]**.

2.2 $2\pi/\Omega$-PERIODIC, NON-STICKING SYMMETRIC SOLUTIONS

2.2.1 Analytical formulation of the solutions – non-resonant case

Suppose that the solutions are periodic with period $T = 2\pi/\Omega$ and one period of the motion consists of two non-sticking segments that take the times θ_1 and θ_2, respectively, i.e., $T = \theta_1 + \theta_2$. Without loss of generality, we assume that the velocity is negative in the first phase and positive in the second one. According to these assumptions, $\dot{x}^-(\theta_1) = 0$, and so we can obtain another expression for A^- besides (2.10):

$$A^- = \Omega \frac{\sin(\Omega(t_0+\theta_1)) - \sin(\Omega t_0)\cos(\theta_1)}{\sin(\theta_1)(\Omega^2-1)}. \tag{2.13}$$

This expression is divergent if $\Omega \to 1$ or $\sin(\theta_1) \to 0$. The first case would correspond to the resonance phenomenon in the frictionless system, but as it was proven by Den Hartog [51], a sufficiently large friction coefficient $S > \pi/4$ leads to sticking solutions and finite amplitude at $\Omega = 1$. In the latter case ($\sin(\theta_1) = 0$), an infinity of asymmetric solutions may appear, as it will be shown in Section 2.3. Now we restrict ourselves to $\sin(\theta_1) \neq 0$ and $\Omega \neq 1$ – this case will be referred to as *non-resonant case* **[28]**.

If we substitute expressions (2.7), (2.11), and (2.13) into (2.5) and consider the time instants $t = 0$ and $t = \theta_1$, we can formulate the initial position x_0 and the displacement x_1 at the next turnaround instant:

$$x_0 = \frac{\Omega(\sin(\Omega(t_0+\theta_1)) - \sin(\Omega t_0)\cos(\theta_1)) - \cos(\Omega t_0)\sin(\theta_1)}{\sin(\theta_1)(\Omega^2-1)} + S, \tag{2.14}$$

$$x_1 = \frac{\Omega\sin(\Omega(t_0+\theta_1))\cos(\theta_1) - \cos(\Omega(t_0+\theta_1))\sin(\theta_1) - \Omega\sin(\Omega t_0)}{\sin(\theta_1)(\Omega^2-1)} + S. \tag{2.15}$$

If the solution is symmetric, $x_1 = -x_0$. Thus, comparison of (2.14) and (2.15) leads to the following condition of symmetry:

$$\begin{aligned}&\sin(\theta_1)\ (2S(\Omega^2-1) - \cos(\Omega(t_0+\theta_1)) - \cos(\Omega t_0)) \\ &\quad + \Omega\ (1+\cos(\theta_1))\ (\sin(\Omega(t_0+\theta_1)) - \sin(\Omega t_0)) = 0.\end{aligned} \tag{2.16}$$

Since $x^+(\theta_1) = x_1$ and $\dot{x}^+(\theta_1) = 0$, the coefficients A^+ and B^+ in (2.6) can also be expressed:

$$A^+ = 2S\cos(\theta_1) + \Omega\ \frac{\sin(\Omega(t_0+\theta_1)) - \sin(\Omega t_0)\cos(\theta_1)}{\sin(\theta_1)(\Omega^2-1)}, \tag{2.17}$$

$$B^+ = 2S\sin(\theta_1) - \Omega\ \frac{\sin(\Omega t_0)}{(\Omega^2-1)}. \tag{2.18}$$

According to our assumptions, one cycle of the periodic motion finishes at $t = \theta_1 + \theta_2$. Consequently, $x^+(\theta_1 + \theta_2) = x_0$ and $\dot{x}^+(\theta_1 + \theta_2) = 0$. Exploiting that $\theta_1 + \theta_2 = 2\pi/\Omega$ and solving these equations for the friction parameter S, one obtains two expressions that are necessarily equal. The comparison of these expressions leads to the following equation:

$$\big(\sin(\Omega(t_0 + \theta_1)) + \sin(\Omega t_0)\big)\big(\sin(\theta_1) + \sin(\theta_2) - \sin(2\pi/\Omega)\big) = 0. \tag{2.19}$$

Thus, using that $\theta_1 + \theta_2 = 2\pi/\Omega$ and $\sin(\theta_1) \neq 0$, we obtain

$$\sin(\Omega(t_0 + \theta_1)) = -\sin(\Omega t_0), \tag{2.20}$$

which implies

$$\theta_1 = \frac{\pi}{\Omega}, \quad \text{and consequently} \quad \theta_2 = \frac{\pi}{\Omega}. \tag{2.21}$$

Solving $\dot{x}^+(\theta_1 + \theta_2) = 0$ for $\sin(\Omega t_0)$ leads to

$$\sin(\Omega t_0) = \frac{S(\Omega^2 - 1)\sin(\pi/\Omega)}{\Omega\,(\cos(\pi/\Omega) + 1)}. \tag{2.22}$$

Let us return to the examination of the condition of symmetry. Substituting $\theta_1 = \pi/\Omega$ into (2.16) and solving the equation for $\sin(\Omega t_0)$, the result is the same as (2.22). Thus, the quite trivial assumption about the period $T = 2\pi/\Omega$ implies that the non-sticking solutions are symmetric, i.e.,

$$x_1 = -x_0, \tag{2.23}$$

and the two phases of the cycles are of equal length – provided that $\Omega \neq 1$ and $\sin(\theta_1) \neq 0$. This symmetry of solutions was usually assumed to fulfil in the literature [51, 83, 142] but has not been proven until our proof was published in **[28]**.

A simple expression can be obtained for x_0 – the amplitude of the vibration– in the following way. Using (2.22) and $\dot{x}^-(\pi/\Omega) = 0$, one obtains

$$\cos(\Omega t_0) = x_0(1 - \Omega^2). \tag{2.24}$$

Exploiting that $\cos^2(\Omega t_0) + \sin^2(\Omega t_0) = 1$, the amplitude x_0 of the solution can be expressed as

$$x_0(\Omega, S) = \sqrt{\frac{1}{(\Omega^2 - 1)^2} - \frac{S^2 \sin^2(\pi/\Omega)}{\Omega^2\,(\cos(\pi/\Omega) + 1)^2}}, \tag{2.25}$$

that agrees with the corresponding formulas of Den Hartog [51] and Shaw [142]. This result, together with (2.10) and (2.24) implies $A^- = -S$.

The diagram described by formula (2.25) is similar to the frequency response diagrams of undamped systems – especially at high values of Ω –, as illustrated in Fig. 2.4. Here the amplitude values were calculated by numerical simulation, as well (see Section 2.4). However, as we will see later, interesting dynamic phenomena can be expected at low values of the dimensionless excitation frequency Ω (see Fig. 2.6).

2.2.2 Validity of results

We supposed that the periodic motion consists of two non-sticking phases and the sign of the velocity is constant during each phase. To obtain non-sticking motions,

$$|x_0 - \cos(\Omega t_0)| \geq S_0 \tag{2.26}$$

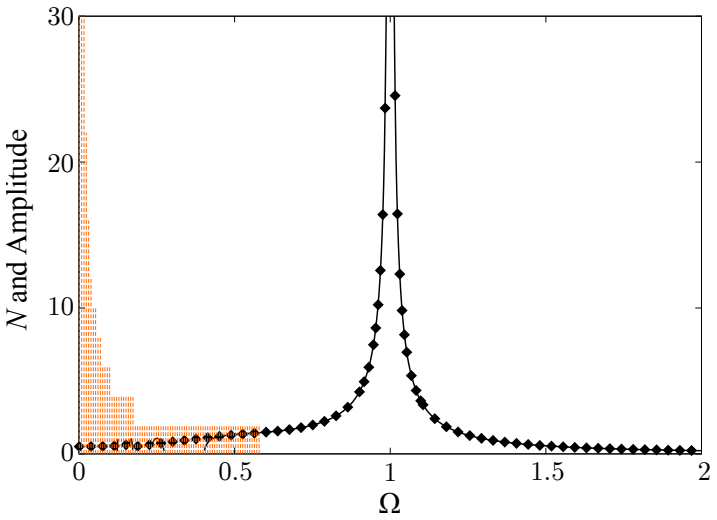

Figure 2.4: *Amplitude-frequency diagram for $S = S_0 = 0.5$. N (orange columns) denotes the number of sticking segments per period. Diamonds are the results of numerical simulation, while the solid line represents the analytical expression of x_0.*

must be fulfilled. Using (2.24), a remarkably simple *slipping* (or non-sticking) condition was given by Shaw [142]:

$$x_0(\Omega, S) \geq \frac{S_0}{\Omega^2}. \tag{2.27}$$

To check that the velocity changes sign twice during a period, we expressed the velocity in the following form:

$$\dot{x}^-(t) = S\sin(t) - x_0\Omega\sin(\Omega t) + \frac{S\sin(\pi/\Omega)(\cos(\Omega t) - \cos(t))}{1 + \cos(\pi/\Omega)} \leq 0, \quad t \in [0, \pi/\Omega]. \tag{2.28}$$

Thus, *the condition of two turnarounds per cycle* can be formulated as

$$x_0(\Omega, S) \geq S\,\frac{\sin(t) + \sin(\pi/\Omega)\cos(\Omega t) + \sin(t - \pi/\Omega)}{\Omega\sin(\Omega t)(1 + \cos(\pi/\Omega))} \equiv SH(t, \Omega), \quad t \in [0, \pi/\Omega]. \tag{2.29}$$

Note, that this condition was not examined in [142]. Although the check of two turnarounds can be found in Den Hartog's paper [51], the performed study was restricted to the case of equal static and dynamic coefficients of friction. It is straightforward to show the following properties of the function $H(t, \Omega)$ that is defined by (2.29):

$$\lim_{t\to 0} H(t, \Omega) = \frac{1}{\Omega^2}, \tag{2.30}$$

$$H(t, \Omega) = -H(\pi/\Omega - t, \Omega), \tag{2.31}$$

$$\lim_{t\to 0} \dot{H}(t, 1/(2n)) \equiv \lim_{t\to 0} \frac{\partial H(t, 1/(2n))}{\partial t} = 0, \quad \text{and} \tag{2.32}$$

$$\lim_{\Omega\to 1/(2n+1)^{\pm}} \left(\lim_{t\to 0} \dot{H}(t, \Omega)\right) = \pm\infty, \quad n = 1, 2, \ldots. \tag{2.33}$$

According to these equations and numerical evidence, we can conclude that

- If $\Omega \geq 1/2$, H takes its maximum at $t = 0$ (Fig. 2.5/a). Thus,

$$\max_t H(t, \Omega) \equiv H_{\max} = 1/\Omega^2 \quad \text{if} \quad \Omega \geq 1/2. \tag{2.34}$$

- As Ω is decreased below $1/2$, the slope of H increases at $t = 0$. Since $H(\pi/(2\Omega), \Omega) = 0$ (see (2.31)), a local maximum appears in $t \in [0, \pi/(2\Omega)]$ (Fig. 2.5/b). Consequently,

$$H_{\max} \geq 1/\Omega^2 \quad \text{if} \quad \Omega < 1/2. \tag{2.35}$$

- $\lim_{\Omega \to 1/3^+} H_{\max} = \infty$. The slope of H at $t = 0$ changes from ∞ to $-\infty$ at $\Omega = 1/3$. Thus, the point of maximum jumps from $[0, \pi/(2\Omega)]$ to $[\pi/(2\Omega), \pi/\Omega]$ (Fig. 2.5/c).

- The further decrease of Ω implies that the local maximum decreases as well, until Ω reaches $1/4$, where a new maximum $H_{\max} = 1/\Omega^2$ appears at $t = 0$ (Fig. 2.5/d).

As the excitation frequency Ω is decreased, further local maxima are born. A more detailed investigation of function $H(t, \Omega)$ shows that its temporal global maximum is either at $t = 0$ or at the first local maximum (i.e., where t is the smallest), independently on the value of Ω. Thus, a similar scenario describes the behaviour of $H(t, \Omega)$ between $\Omega = 1/4$ and $\Omega = 1/6$, and generally, between $\Omega = 1/(2n)$ and $\Omega = 1/(2n + 2)$, $(n = 1, 2, \dots)$, too. Since some maxima of $H(t, \Omega)$ are known to be at $t = 0$, $\Omega = 1/(2n)$, the other maxima, for $\Omega \neq 1/(2n)$ can be found quite easily using a continuation method. This is how Fig. 2.6 was generated.

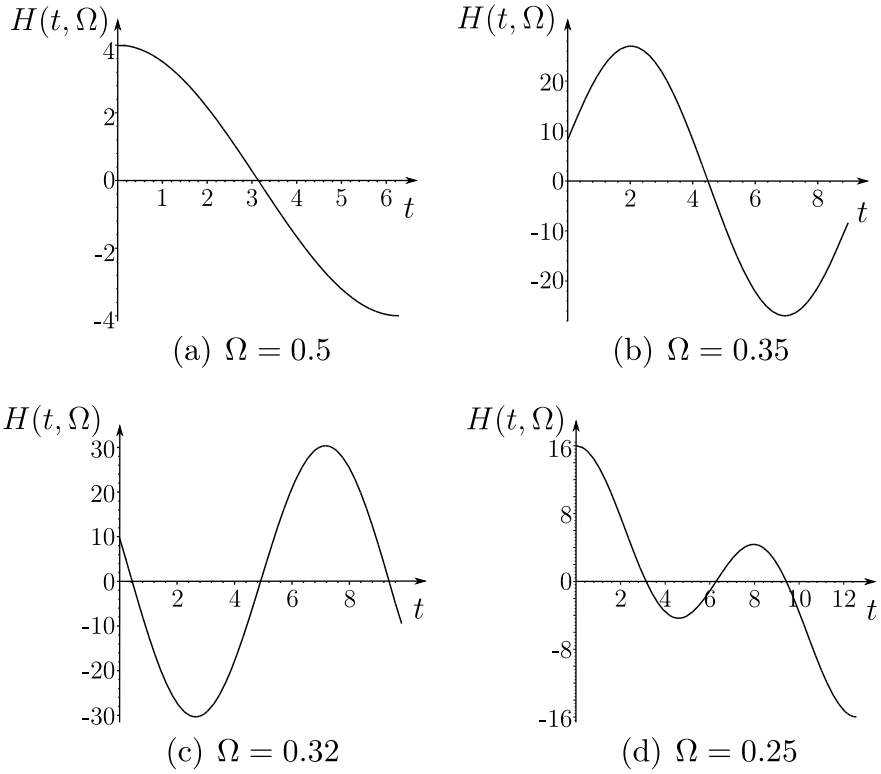

Figure 2.5: *Behaviour of function $H(t, \Omega)$*

It follows from the previous results **[28]** that

- if $\Omega \geq 1/2$, then $H(t, \Omega)$ takes its temporal maximum $H_{\max} = 1/\Omega^2$ at $t = 0$ (see Fig. 2.5/a). Thus, (2.29) – the condition of two turnarounds – implies $x_0 \geq S/\Omega^2$. Consequently, (2.29) is equivalent to (2.27) in this domain if $S_0 = S$. Otherwise – if $S_0 > S$ – the condition of two turnarounds has no importance: the slipping condition (2.27) fails first in this domain.

- Consider now the parameter domain $\Omega \in [0, 0.5]$. According to (2.35), $SH_{\max} \geq S/\Omega^2$ is fulfilled here. Thus, if $S = S_0$ the condition of two turnarounds (2.29) determines

whether the examined special solution exists or not. If $S_0 > S$, both conditions must be checked.

Table 2.1 summarizes the conditions of non-sticking solutions in different parameter domains. If one of the conditions was proved to be stronger, the other one is not shown.

Table 2.1: *Conditions of non-sticking solutions*

	$\Omega \geq 0.5$	$\Omega < 0.5$
$S = S_0$	$x_0 \geq \frac{S}{\Omega^2}$	$x_0 \geq SH_{\max}$
$S < S_0$	$x_0 \geq \frac{S_0}{\Omega^2}$	$x_0 \geq \frac{S_0}{\Omega^2}$ & $x_0 \geq SH_{\max}$

Besides the cases shown in the table, there is one more relation that is worth to consider. According to (2.25), x_0 is independent on S at the frequencies $\Omega = 1/(2n)$, $n = 1, 2, \ldots$, and assumes the value $x_0^n \equiv x_0(1/(2n), S) = (1 - 1/(4n^2))^{-1}$. Since at the intermediate frequencies x_0 is smaller than $1/(1 - \Omega^2)$, it assumes its maximal value in $\Omega \in [0, 0.5]$ at $\Omega = 0.5$, while S_0/Ω^2 has a minimum in this interval. Consequently, if $x_0(\Omega, S) < S_0/\Omega^2$ at $\Omega = 0.5$, the condition of sliding fails for the whole interval $\Omega \in [0, 0.5]$. Substituting $x_0(0.5, S) = 4/3$ into the condition of slipping (2.27) and solving for S_0, one obtains $S_0 = 1/3$. Thus, sticking occurs in $\Omega \in [0, 0.5]$ if $S_0 > 1/3$. Generalizing this result, we obtain the following necessary condition of having non-sticking symmetric solutions in $\Omega \in [0, 1/(2n)]$:

$$S_0 \leq \frac{1}{4n^2 - 1}. \tag{2.36}$$

Fig. 2.6 illustrates the amplitude-frequency diagram (2.25), the limit curve of slipping S_0/Ω^2 and the limit curve of two turnarounds per period $SH_{\max}$ at $S = S_0 = 0.02$ and $S = S_0 = 0.3$. As it can be seen, the conditions of validity can be approximated fairly well

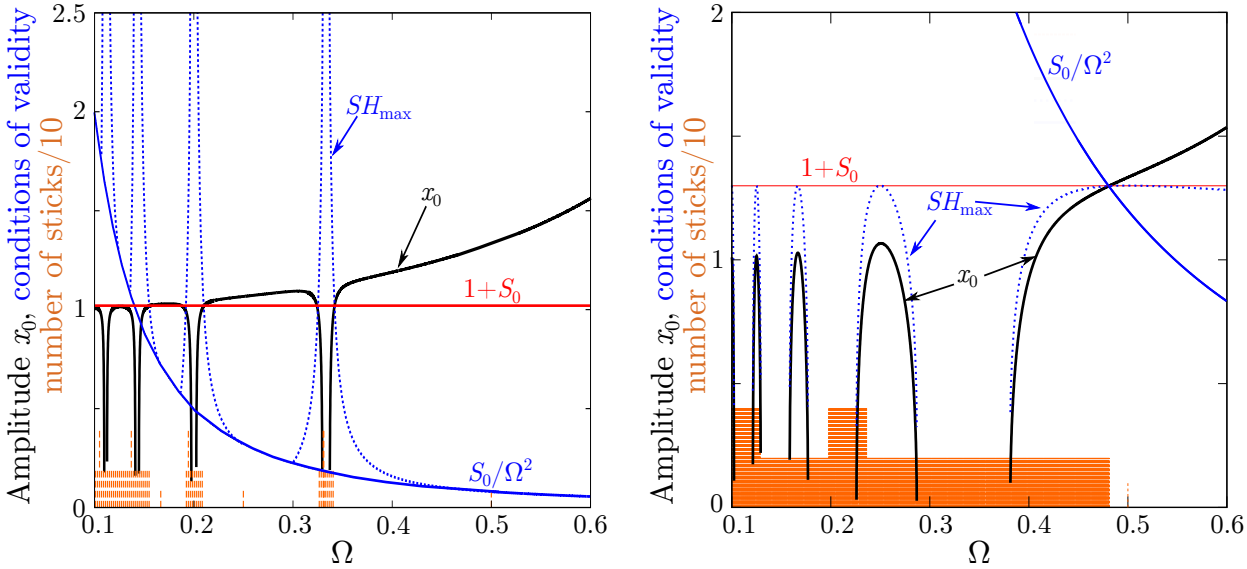

Figure 2.6: *Amplitude-frequency diagram at $S = S_0 = 0.02$ (left) and $S = S_0 = 0.3$ (right); x_0 was calculated according to (2.25). The orange-coloured columns show the number of sticking segments per excitation period/10.*

by $x_0 \geq 1 + S_0$ at these values of the friction coefficient. The analytically derived non-sticking solutions were accurately found by numerical integration of the equation of motion, as well.

The number of sticking segments per excitation period is also depicted in the figure, showing the parameter domains where (2.25) is not valid.

There are several possible methods in the literature that can be used to check the *stability* properties of the found periodic solutions. We applied two of them: an elegant, modern approach is based on the Filippov theory and the introduction of so-called saltation matrices [12, 65, 109]. (Appendix A.1), while the method developed by Shaw [142] (Appendix A.2) is more conventional and requires slightly longer calculations.

Fig. 2.7 illustrates the response amplitude and the leading eigenvalue $\max|\lambda_i|$, $i = 1, 2$ characterising the variational system of the non-sticking symmetric solution at $S = 0.05$.

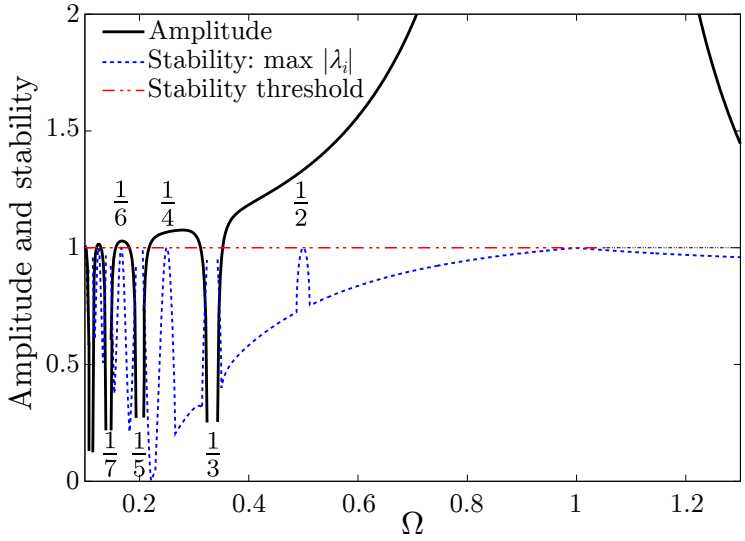

Figure 2.7: *Theoretical amplitude x_0 and stability of the symmetric non-sticking solution at $S = 0.05$.*

It can be seen in the figure that the periodic motion with amplitude (2.25) is linearly asymptotically stable i.e., $\max|\lambda_i| < 1$ in broad ranges of the excitation frequency. Moreover, expression (2.25) assumes imaginary values close to the frequencies $\Omega = 1/(2n+1)$, implying that the symmetric non-sticking solution does not exist in these parameter domains.

The results also show that the solution is only marginally stable (i.e., $\lambda_1 = 1$ and $0 < \lambda_2 < 1$) at $\Omega = 1, 1/2, 1/4, \ldots$. Thus, to clarify the stability properties of these special cycles, we extended Shaw's results in our paper **[29]** by a third-order nonlinear stability analysis, that is described in details in Appendix A.3. The following normal form map was obtained, assuming non-sticking solutions:

$$y_{i+1} = y_i, \tag{2.37}$$

$$\tau_{i+1} = \lambda_2 \tau_i + D y_i^2 \tau_i. \tag{2.38}$$

This map also indicates marginal stability at $\Omega = 1/(2n)$, provided that the perturbation does not lead to the appearance of sticking solutions.

2.3 ASYMMETRIC SOLUTIONS AT RESONANT FREQUENCIES

2.3.1 Formulation of solutions

The main results of Section 2.2 – Eqs. (2.22) and (2.25) – are valid only for $\sin(\theta_1) \neq 0$ and $\Omega \neq 1$, because (2.13) becomes divergent in the opposite case. In the present section, we

search for the possible $2\pi/\Omega$-periodic non-sticking solutions in case of $\sin(\theta_1) = 0$. Although this condition is fulfilled only in a measure zero subset of the parameter space, we showed in **[29]** that the frequency domain of the found special resonant solutions broadens if the static and kinetic coefficients of friction are different. Just as in Section 2.2, we assume that there are only two turnarounds per period, and the durations of the two phases of the motion are θ_1 and θ_2, respectively. Condition $\sin(\theta_1) = 0$ implies

$$\theta_1 = 2n\pi \quad \text{and} \quad \cos(\theta_1) = 1, \quad \text{where} \quad n = 1, 2, \dots, \quad \text{or} \tag{2.39}$$

$$\theta_1 = (2n+1)\pi \quad \text{and} \quad \cos(\theta_1) = -1, \quad n = 0, 1, 2, \dots \ . \tag{2.40}$$

The appearance of $\sin(\theta_1)$ in the denominator can be avoided if (2.7) and (2.10) are substituted into (2.12), and B^- is expressed instead of A^-:

$$B^- = \frac{\cos(\Omega t_0)\sin(\theta_1) - \Omega\sin(\Omega(t_0+\theta_1))}{\cos(\theta_1)(\Omega^2-1)} + (x_0 - S)\tan(\theta_1). \tag{2.41}$$

In the case of $\sin(\theta_1) = 0$, this expression reduces to

$$B^- = \frac{-\Omega\sin(\Omega(t_0+\theta_1))}{\cos(\theta_1)(\Omega^2-1)}, \tag{2.42}$$

which, clearly must be equal to (2.11). Comparing the two equations, one faces two cases:

- $\sin(\Omega t_0) = \sin(\Omega(t_0+\theta_1))$ if $\cos(\theta_1) = 1$ and consequently $\theta_1 = 2n\pi$, $n = 1, 2, \dots$. This case can be divided into two sub-cases:

  a) $\theta_1 = 2\pi/\Omega$ and $t_0 \neq 0$. This case will be disregarded since we assume that the time period is $\theta_1 + \theta_2 = 2\pi/\Omega$.

  b) $\theta_1 = \pi/\Omega$ and $t_0 = 0$. Since $\theta_1 = 2n\pi$,

  $$\Omega = 1/(2n). \tag{2.43}$$

- $\sin(\Omega t_0) = -\sin(\Omega(t_0+\theta_1))$ if $\cos(\theta_1) = -1$ (and $\theta_1 = (2n+1)\pi$). The solution of this equation is $\theta_1 = \pi/\Omega$. Consequently

  $$\Omega = 1/(2n+1), \quad n = 0, 1, 2, \dots. \tag{2.44}$$

Thus, we can conclude that $\sin(\theta_1) = 0$ implies $\Omega = 1/m$ and $\theta_1 = m\pi$, $m = 1, 2, \dots$. Note, that since the time period is $T = 2\pi/\Omega = 2m\pi$, the duration of the two segments of the motion is the same:

$$\theta_2 = T - \theta_1 = m\pi = \theta_1. \tag{2.45}$$

Substituting (2.7), (2.10), (2.42) and $t = \theta_1$ into (2.5) gives the displacement at the turnaround instant:

$$x_1 = \frac{\cos(\Omega t_0) - \Omega\sin(\theta_1)\sin(\Omega(t_0+\theta_1)) - \cos(\theta_1)\cos(\Omega(t_0+\theta_1))}{\cos(\theta_1)(\Omega^2-1)} + \frac{x_0 - S}{\cos(\theta_1)} + S. \tag{2.46}$$

Exploiting that $x^+(\theta_1) = x_1$ and $\dot{x}^+(\theta_1) = 0$, the coefficients A^+ and B^+ can be expressed as

$$A^+ = x_0 - S + 2S\cos(\theta_1) + \frac{\cos(\Omega t_0)}{\Omega^2 - 1}, \tag{2.47}$$

$$B^+ = \frac{\cos(\Omega t_0)\sin(\theta_1) - \Omega\sin(\Omega(t_0+\theta_1))}{\cos(\theta_1)(\Omega^2-1)} + \frac{(x_0 - S)\sin(\theta_1)}{\cos(\theta_1)} + 2S\sin(\theta_1). \tag{2.48}$$

Since one cycle of the periodic motion finishes at $t = \theta_1 + \theta_2 \equiv T$,

$$x^+(T) = x_0, \quad \text{and} \tag{2.49}$$
$$\dot{x}^+(T) = 0. \tag{2.50}$$

Substituting (2.47) and (2.48) into (2.49) and (2.50) and exploiting that $\theta_1 = \theta_2 = m\pi$ and $\Omega = 1/m$, we obtain the following equations:

$$x^+(T) - x_0 = 2S\left((-1)^{2m} - (-1)^m\right) = 0, \tag{2.51}$$
$$\dot{x}^+(T)\left(\frac{1}{m} - m\right) = \sin(t_0/m)\left((-1)^m + 1\right) = 0. \tag{2.52}$$

Eq. (2.51) can be satisfied only if m is even: $m = 2n$, $n \in \mathbb{Z}^+$. Thus, (2.52) implies that $\sin(t_0/m) = 0$. Consequently, there can be two different cases:

$$t_0 = 0 \quad \text{or} \quad t_0 = m\pi. \tag{2.53}$$

Coefficients B^-, B^+, and K disappear in both cases. Using (2.10), (2.47) and (2.7), one obtains

$$A^- = x_0 - S \pm \frac{1}{\Omega^2 - 1}, \tag{2.54}$$
$$A^+ = x_0 + S \pm \frac{1}{\Omega^2 - 1}, \tag{2.55}$$
$$L = \pm\frac{1}{1 - \Omega^2}, \tag{2.56}$$

where the $+$ and $-$ signs correspond to $t_0 = 0$ and $t_0 = m\pi$, respectively. As it will be shown in Section 2.3.2, $t_0 = m\pi$ leads to invalid solutions. Thus, here we present the displacements and velocities for the $t_0 = 0$ case, only:

$$x^-(t) = \left(x_0 - S + \frac{1}{\Omega^2 - 1}\right)\cos(t) - \frac{1}{\Omega^2 - 1}\cos(\Omega t) + S, \tag{2.57}$$
$$x^+(t) = \left(x_0 + S + \frac{1}{\Omega^2 - 1}\right)\cos(t) - \frac{1}{\Omega^2 - 1}\cos(\Omega t) - S, \tag{2.58}$$
$$\dot{x}^-(t) = -\left(x_0 - S + \frac{1}{\Omega^2 - 1}\right)\sin(t) + \frac{\Omega}{\Omega^2 - 1}\sin(\Omega t), \quad \text{and} \tag{2.59}$$
$$\dot{x}^+(t) = -\left(x_0 + S + \frac{1}{\Omega^2 - 1}\right)\sin(t) + \frac{\Omega}{\Omega^2 - 1}\sin(\Omega t). \tag{2.60}$$

Fig. 2.9 shows a solution of this kind. It can be checked easily that

$$\begin{aligned} x^-(0) &= x_0, \\ \dot{x}^-(0) &= 0, \\ x^-(2n\pi) = x^+(2n\pi) &= x_0 - \frac{8n^2}{4n^2 - 1} = x_1, \\ \dot{x}^-(2n\pi) = \dot{x}^+(2n\pi) &= \dot{x}^+(4n\pi) = 0, \quad \text{and} \\ x^+(4n\pi) &= x_0, \end{aligned} \tag{2.61}$$

where $n = 1, 2, 3, \ldots$. Note that these results are parametrized by the amplitude x_0, which means that a continuum of asymmetric solutions arise at these special frequencies.

2.3.2 Validity of results

According to (2.51), we found that $\Omega = 1/(2n)$, $n = 1, 2, \ldots$ is necessary for the validity of Eqs. (2.57)-(2.60). In addition to that, the condition of two turnarounds per cycle and the condition of no sticking will also be checked in the present section **[29]**.

The case $t_0 = 0$

The condition of two turnarounds can be formulated as $\dot{x}^-(t) \leq 0$, $t \in [0, 2n\pi]$ and $\dot{x}^+(t) \geq 0$, $t \in [2n\pi, 4n\pi]$. Using (2.59), one obtains that $\dot{x}^-(t) \leq 0$ can be expressed as

$$\left(1 + (S - x_0)(1 - \Omega^2)\right) \sin(t) \leq \Omega \sin(\Omega t), \quad t \in [0, \pi/\Omega]. \tag{2.62}$$

Taking into account that $\Omega = 1/(2n)$, this inequality can be transformed into

$$2n\left(1 + (S - x_0)(1 - 1/(4n^2))\right) \leq \frac{\sin(t/2n)}{\sin(t)}, \quad \text{if } \sin(t) \geq 0, \quad \text{or} \tag{2.63}$$

$$2n\left(1 + (S - x_0)(1 - 1/(4n^2))\right) \geq \frac{\sin(t/2n)}{\sin(t)}, \quad \text{if } \sin(t) \leq 0. \tag{2.64}$$

Consider inequality (2.63) first. $\sin(t) \geq 0$ is fulfilled if $t \in [0 + 2k\pi, (2k + 1)\pi]$, while $t \in [0, \pi/\Omega] \equiv [0, 2n\pi]$ implies that $\sin(t/2n)$ is non-negative. To obtain a condition for x_0, the minimum of $\sin(t/2n)/\sin(t)$ must be determined.

To make clear the ideas behind our calculation, we illustrate them via an example at $n = 3$. In Fig. 2.8, the graph of $\sin(t/6)/\sin(t)$ can be seen, with the graph of $\sin(t/6)$.

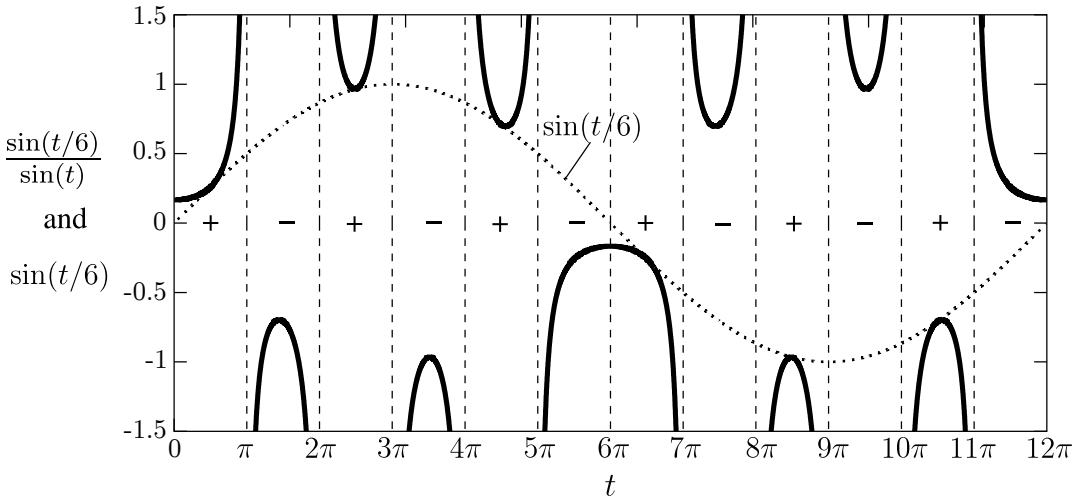

Figure 2.8: *Illustration for the calculation ($n = 3$).*

We divided the domain of definition into twelve intervals. The function $\sin(t)$ takes positive and negative values in these intervals, alternately – it is shown by $+$ or $-$ signs. As it can be seen in the figure, the function $\sin(t/6)/\sin(t)$ assumes positive values if $\sin(t) \geq 0$ and $t \in [0, 2n\pi]$, and its minimum is at $t = 0$. According to L'Hospital's rule,

$$\lim_{t \to 0} \frac{\sin(t/6)}{\sin(t)} = \frac{1}{6}. \tag{2.65}$$

Similarly, $\sin(t/(2n))/\sin(t)$ takes its positive minimum also at $t = 0$, and

$$\lim_{t \to 0} \frac{\sin(t/(2n))}{\sin(t)} = \frac{1}{2n}. \tag{2.66}$$

Thus, Eq. (2.63) is valid if

$$2n\left(1+(S-x_0)(1-1/(4n^2))\right)\leq\frac{1}{2n}, \tag{2.67}$$

which implies

$$x_0\geq 1+S. \tag{2.68}$$

Note, that $x_0\equiv x(0)=1+S$ is exactly on the boundary of the sticking region if $S=S_0$ and $t_0=0$ (see Fig. 2.3).

The analysis of formula (2.64) is similar, but now the maximum of $\sin(t/6)/\sin(t)$ must be found. As it can be seen in Fig. 2.8, $\sin(t)\leq 0$ implies that $\sin(t/6)/\sin(t)$ is negative, and its maximum is at $t=6\pi$, where the function takes the value $-1/6$. In the general case it leads to

$$2n\left(1+(S-x_0)(1-1/(4n^2))\right)\geq-\frac{1}{2n}, \tag{2.69}$$

which implies

$$x_0\leq\frac{4n^2+1}{4n^2-1}+S. \tag{2.70}$$

Using (2.60), the condition $\dot{x}^+\geq 0$ assumes the following form:

$$\left(1-(x_0+S)(1-\Omega^2)\right)\sin(t)\geq\Omega\sin(\Omega t),\quad t\in[\pi/\Omega,2\pi/\Omega]. \tag{2.71}$$

Taking into account that $\Omega=1/(2n)$, this inequality can be transformed into

$$2n\left(1-(x_0+S)(1-1/(4n^2))\right)\geq\frac{\sin(t/2n)}{\sin(t)},\quad\text{if }\sin(t)\geq 0, \tag{2.72}$$

or

$$2n\left(1-(x_0+S)(1-1/(4n^2))\right)\leq\frac{\sin(t/2n)}{\sin(t)},\quad\text{if }\sin(t)\leq 0, \tag{2.73}$$

where $t\in[2n\pi,4n\pi]$. Here $\sin(t/2n)\leq 0$, thus, $\sin(t)\geq 0$ implies that $\sin(t/2n)/\sin(t)$ is non-positive. In case of (2.72), the maximum of $\sin(t/2n)/\sin(t)$ must be found. As it is illustrated in Fig. 2.8, this extremum value is $-1/(2n)$. Thus, (2.72) implies

$$x_0\leq\frac{4n^2+1}{4n^2-1}-S. \tag{2.74}$$

Similarly, inequality (2.73) leads to the search for the positive minimum of $\sin(t/2n)/\sin(t)$ in $[2n\pi,4n\pi]$. This minimum value is $1/(2n)$, thus

$$x_0\geq 1-S. \tag{2.75}$$

Comparing (2.68), (2.70), (2.74), and (2.75), we obtain

$$1+S\leq x_0\leq\frac{4n^2+1}{4n^2-1}-S. \tag{2.76}$$

According to (2.61), $x_1=x_0-8n^2/(4n^2-1)$. Consequently,

$$\min x_1=\min x_0-\frac{8n^2}{4n^2-1}=1+S-\frac{8n^2}{4n^2-1}=\frac{1+4n^2}{1-4n^2}+S=-\max x_0, \tag{2.77}$$

$$\max x_1=\max x_0-\frac{8n^2}{4n^2-1}=\frac{4n^2+1}{4n^2-1}-S-\frac{8n^2}{4n^2-1}=-1-S=-\min x_0. \tag{2.78}$$

The condition of symmetric solutions is the following:

$$-x_0 = x_0 - \frac{8n^2}{4n^2-1} \quad \Rightarrow \quad x_0 = \frac{4n^2}{4n^2-1} = \frac{1}{1-\Omega^2}. \tag{2.79}$$

Of course, the same amplitude can be obtained using (2.25). Thus, the symmetric solution known from the literature (e.g., [51, 142]) is among the uncountable asymmetric solutions (2.57), (2.58).

Finally, let us determine the validity of (2.76):

$$1 + S \leq \frac{4n^2+1}{4n^2-1} - S \quad \Rightarrow \quad S \leq \frac{1}{4n^2-1}. \tag{2.80}$$

The condition of sticking was not examined yet. If $S = S_0$ and $t_0 = 0$, the extremal value of x_0 ($x_0 = 1 + S$) is at the stick-slip boundary (see Fig. 2.3), thus, the condition of slipping and the condition of having two turnarounds per period are equivalent. If $S_0 > S$,

$$S_0 \leq \frac{1}{4n^2-1} \tag{2.81}$$

must be fulfilled that agrees with (2.36) that was derived for the symmetric solutions. The possible values of x_0 are

$$1 + S_0 \leq x_0 \leq \frac{4n^2+1}{4n^2-1} - S. \tag{2.82}$$

Note, that only the lower bound changes with respect to (2.76), since this is influenced by the slipping condition.

Thus, we can conclude that a one-parameter family of solutions exists if $t_0 = 0$ with the range given by Eq. (2.82), provided that condition (2.81) is satisfied.

For example, $S_0 < 1/3$ must be fulfilled to have non-sticking (symmetric or asymmetric) solutions at $\Omega = 1/2$, and S_0 must be less than $1/15$ to find such solutions at $\Omega = 1/4$.

The case $t_0 = m\pi$

It is straightforward to show that $t_0 = m\pi$ (where $m > 0$ is an even integer number) implies that the less-than and greater-than signs flip in Eqs. (2.63), (2.64), (2.72) and (2.73). Thus, neither inequalities can be fulfilled in this case. Consequently, the resonant solutions (2.57)-(2.60) exist only at $t_0 = 0$.

2.3.3 Stability properties

The stability analysis discussed in Section 2.2.2 can be applied in the case of asymmetric solutions, too. As we have shown in **[29]** and in Appendix A.3, the two equations of the obtained normal form maps assume the form

$$y_{i+1} = y_i \tag{2.83}$$

and

$$\tau_{i+1} = \lambda_2 \tau_i + C y_i \tau_i \quad \text{or} \quad \tau_{i+1} = C y_i \tau_i + E \tau_i^3 \quad \text{or} \quad \tau_{i+1} = C y_i \tau_i + (E - AC)\tau_i^3, \tag{2.84}$$

depending on the type of solutions (see (A.60)-(A.63)). These results indicate marginal stability up to the third order terms if the perturbations are restricted to cases when no sticking solutions appear. Small perturbations can lead to sticking solutions in the extremal

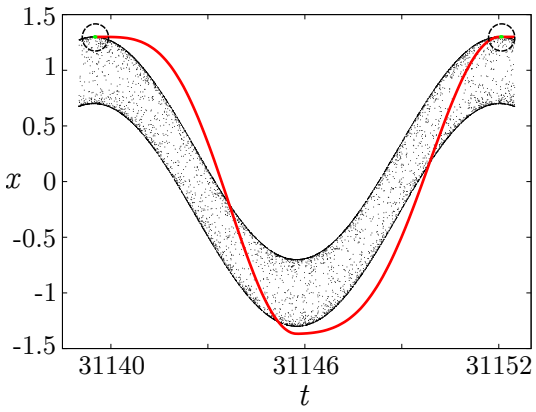

Figure 2.9: *An asymmetric solution with the sticking domain at $S = 0.3$ and $\Omega = 0.5$. The small sticking segments are encircled.*

case ($x_0 = 1 + S$) only. However, during the numerical simulations, the trajectories always converged to the extremal asymmetric solution, with a single short sticking segment per period. Fig. 2.9 shows such an asymmetric solution at $\Omega = 0.5$.

To gain information about the effect of perturbations that push the extremal solution into the sticking domain, we consider the case when the initial displacement is $\tilde{x}_0 = 1 + S - \varepsilon_0$, as shown in Fig. 2.10. The new perturbed solution (dashed lines in the figure) begins with a sticking segment and leaves the sticking domain with zero velocity at $\tilde{x}_0$ and $t = t_s$. Since

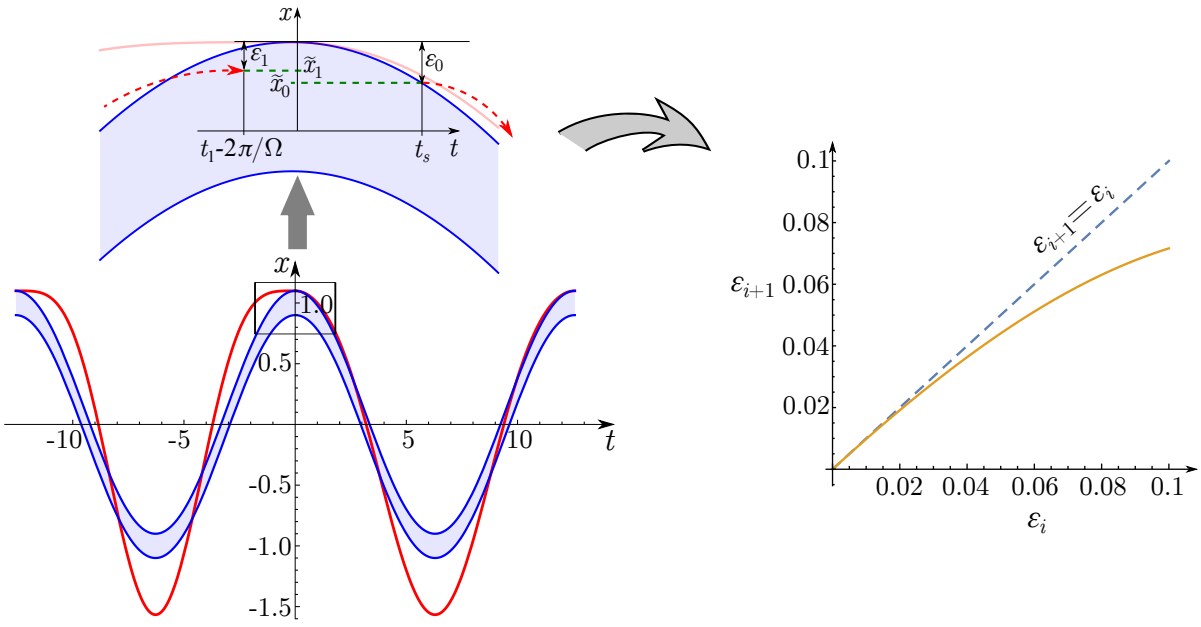

Figure 2.10: *An extremal asymmetric solution at $S = 0.1$, $\Omega = 0.5$, a possible perturbation, and the graph of the map describing the evolution of the perturbation.*

$t_0 = 0$ in the case of the non-perturbed asymmetric solutions, the boundary of the sticking region can be given approximately as

$$x_b(t) \equiv S + \cos(\Omega t) \approx 1 + S - \frac{\Omega^2 t^2}{2}. \tag{2.85}$$

Exploiting that $x_b(t_s) = \tilde{x}_0$, the time instant t_s can be expressed by ε_0. Now that the initial conditions are known, one can determine the solution of the equation of motion (2.3) for negative velocities, obtaining the expressions of $\tilde{x}^-(t)$ and $\dot{\tilde{x}}^-(t)$. By expanding $\dot{\tilde{x}}^-(t)$ into

Taylor series about $t = \pi/\Omega$, one can approximately determine the turnaround time t_t and turnaround displacement $\tilde{x}_t$ corresponding to $\dot{\tilde{x}}^-(t_t) = 0$. The solution of the equation of motion for positive velocities leads to the expressions of $\tilde{x}^+(t)$ and $\dot{\tilde{x}}^+(t)$. Just as before, the Taylor expansion of $\dot{\tilde{x}}^+(t)$ about $t = 2\pi/\Omega$ makes the determination of the next sticking instant t_1 and displacement $\tilde{x}_1$ possible[1]. The difference between $1 + S$ and $\tilde{x}_1$ defines the value of ε_1 as shown in Fig. 2.10, where the end of the obtained solution curve is depicted such that it is shifted back in time by $2\pi/\Omega$. Using the described procedure, a discrete map $P : \varepsilon_i \to \varepsilon_{i+1}$ can be defined. We used a second order approximation, i.e., the cubic and higher order terms of ε_i and t had been discarded in each step. The graph of the resulting map is also shown in Fig. 2.10. The results show that the map assumes the following form, independently on the value of the friction parameter: $P : \ \varepsilon_{i+1} = \varepsilon_i - 2\varepsilon_i^2$. Thus, we can conclude that the examined solution – that just touches the sticking region – is stable against the considered perturbation type, in accordance with the aforementioned numerical results.

2.4 NUMERICS AND STICKING SOLUTIONS

Although non-sticking solutions can be found and analysed analytically, this does not seem to be possible in case of sticking solutions, because of the appearance of transcendental equations. Thus, to explore the possible solutions, we implemented an algorithm in C++, which solves Eq. (2.3) numerically. The necessary duration of simulation can be estimated using the stability eigenvalues (characteristic multipliers) $\lambda_{1,2}$ (see Section 2.2.2) of the symmetric non-sticking solutions. As it is shown in Fig. 2.11, the decay of the relative error of the amplitude is not uniform, but the graph has an envelope curve, whose slope equals the logarithm of the modulus of the leading characteristic multiplier $\lambda_{\max}$. The characteristic

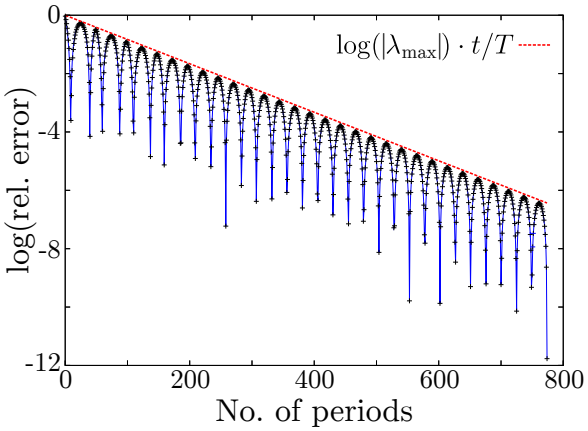

Figure 2.11: *Convergence to the symmetric solution at* $S = 0.1$ *and* $\Omega = 0.98$

multipliers are complex numbers in broad parameter domains. It means that – besides the primary angular frequency Ω – a secondary frequency appears in the transients that is related to the argument φ of the characteristic multipliers: $\Omega_2 = \mathrm{Im}(\log(\lambda_1))/T = \varphi/T$, where $T = 2\pi/\Omega$ is the excitation period. The observed secondary period T_2 of the transients is

$$T_2 = \frac{2\pi}{\Omega_2} = \frac{4\pi^2}{\Omega\varphi}. \tag{2.86}$$

[1] $\tilde{x}_1$ is not to be confused with x_1 in (2.61). The latter is the maximal displacement of the periodic cycle in the negative direction, while $\tilde{x}_i$, $i = 1, 2, \ldots$ denotes the subsequent positive displacements during the transients of the perturbed solution.

Note that – due to this phenomenon – the appropriate simulation time cannot be determined by measuring the difference between successive amplitudes.

In Fig. 2.12, the numerically determined frequency-amplitude curves and the number N of sticking segments per period can be seen at four different values of the friction parameter $S = S_0$. At low values of S, sticking solutions appear only in the domain $\Omega \in [0, 1)$, and

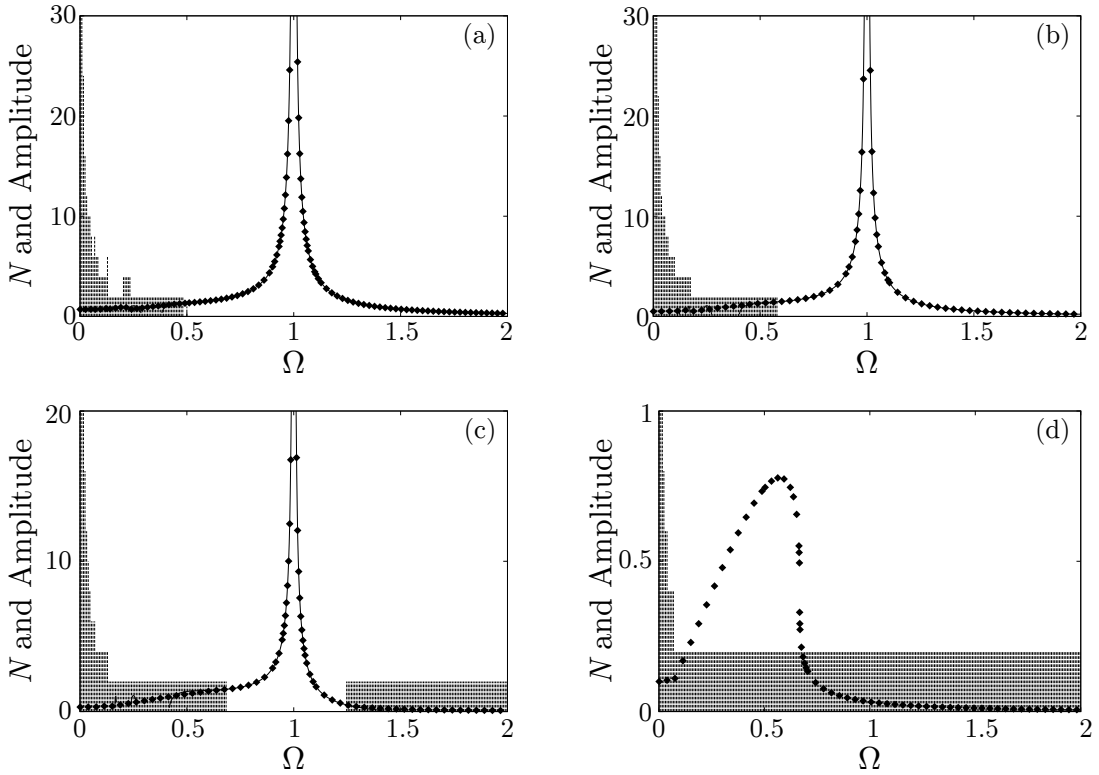

Figure 2.12: *Frequency-response curves at some values of the friction parameter. (a) $S = 0.3$, (b) $S = 0.5$, (c) $S = 0.7$, (d) $S = 0.9$. ◆ Numerically determined amplitude, —— analytical result (Eq. (2.25)), ▒ number of sticking segments per period (divided by 10 in case (d)).*

the $N(\Omega)$ diagram is not monotone decreasing at very low values of the friction parameter (see Fig. 2.12/a). As S is increased, the local maxima of the $N(\Omega)$ diagram disappear (Fig. 2.12/b). The further increase of S leads to the appearance of another sticking domain in $\Omega \in (1, \infty)$ (Fig. 2.12/c). Finally, these two domains of sticking solutions merge and the amplitude assumes finite values at all values of Ω (Fig. 2.12/d).

The critical friction coefficient, where sticking solutions appear in $\Omega \in (1, \infty)$, can be estimated as follows **[28]**. At large values of Ω, we approximate $\sin(\pi/\Omega)$ by π/Ω and $\cos(\pi/\Omega)$ by 1 in (2.25). Thus, (2.27) assumes the form

$$\lim_{\Omega\to\infty} x_0(\Omega) = \lim_{\Omega\to\infty} \sqrt{\frac{1}{(\Omega^2-1)^2} - \frac{S^2\pi^2}{4\Omega^2}} < \frac{S_0}{\Omega^2}, \quad \text{that implies} \tag{2.87}$$

$$S > \left(\frac{S_0}{S} + \frac{\pi^2}{4}\right)^{-1/2}. \tag{2.88}$$

This result agrees with the calculations of Kowalczyk and Piiroinen [101] that were performed by a continuation method for the case $S_0 = S$.

To check the validity of (2.25), (2.27), and (2.29), we examined the frequency-amplitude diagram at low values of the friction parameter. In Fig. 2.13, the amplitude of the symmetric

solution (2.25), the stick-slip boundary (2.27), and the numerically estimated $SH_{\max}$ curves are shown at $S = S_0 = 0.02$, together with the numerically determined amplitude and the number of sticking segments per excitation period.

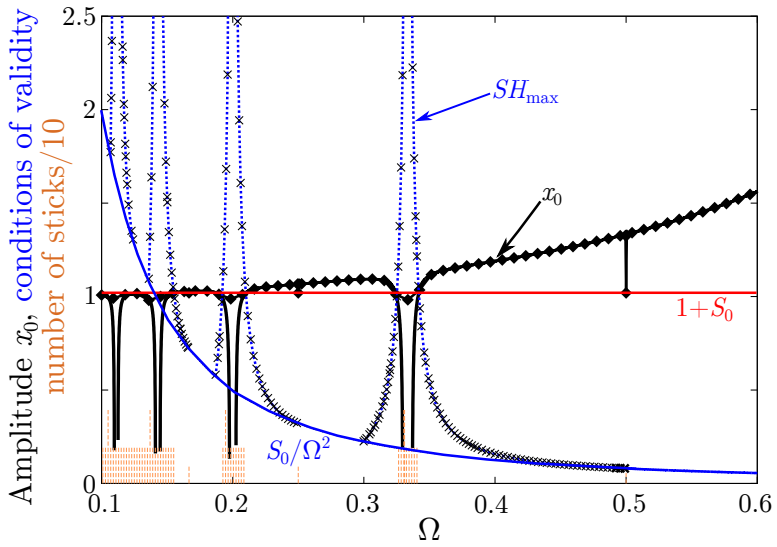

Figure 2.13: *Amplitude-frequency diagram at $S = S_0 = 0.02$; —◆— numerically determined amplitude; ——— analytically determined amplitude (Eq. (2.25)). The number of sticking segments is shown by orange columns.*

As it can be seen in the figure, the numerically and analytically determined amplitude curves exactly coincide in case of slipping motion, and the separation of these curves occurs according to (2.27) and (2.29). The significance of (2.29) is clearly seen close to the values $\Omega = 1/3$, $\Omega = 1/5$, etc., where the analytically calculated amplitude curves tend to zero, while $SH_{\max}$ tends to infinity.

Note that there are two points that apparently do not fit into the series of the results at $\Omega = 0.5$ and $\Omega = 0.25$. Only one sticking segment occurs at these parameters per period, which means that the steady-state solutions are asymmetric, as it was predicted in Section 2.3. As Fig. 2.14 shows, the parameter domain of asymmetric solutions opens up if $S_0 > S$. This result indicates the possibility that asymmetric solutions can occur in real mechanical systems of this kind. Indeed, the experimental investigation of a corresponding oscillator (Marino and Cicirello, [112]) demonstrated the existence of asymmetric periodic cycles.

2.5 BIFURCATIONS AND CHAOS

2.5.1 Reformulation of the problem for the continuation method

In order to reveal the bifurcations leading to the emergence of asymmetric solutions among the symmetric ones, the continuation method [2] was applied. The continuation method is capable of the quick, reliable calculation of bifurcation diagrams. One of the most widely used continuation software is AUTO [53]. Unfortunately, AUTO is not able to deal with non-smooth systems. However, a recently implemented Matlab toolbox COCO (COntinuation COre, [48]) provides the possibility for the analysis of these kinds of systems, too.

To be able to analyse a piecewise smooth system with COCO, one must have an initial guess about the solution's structure. It means that the temporal order of the subsequent smooth segments in the periodic solution must be known, together with the switching conditions – formulated as zeros of smooth functions. Physically, the oscillator can be in one

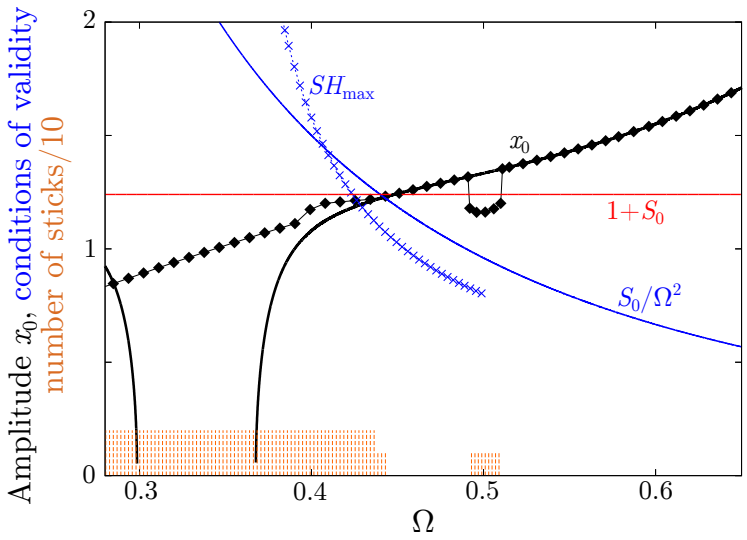

Figure 2.14: *Amplitude-frequency diagram at $S = 0.2$ and $S_0 = 0.24$; —◆— numerically determined amplitude; —— analytically determined amplitude (Eq. (2.25)). The number of sticking segments is shown by orange columns.*

of the following three states: sliding with positive speed, sliding with negative speed, or sticking, as it is formulated by Eqs. (2.2) and (2.3).

As we saw in Section 2.1, the switching conditions between the sticking and sliding cases are given by an equation and a non-smooth inequality:

$$\dot{x} \equiv v = 0 \quad \text{and} \quad |x - \cos(\Omega t)| < S_0. \tag{2.89}$$

Note that here we dropped parameter t_0 since although it had been useful for the analytical calculations, it is irrelevant if the solutions are sought numerically (cf. Eq. (2.4)). The reformulation of these conditions as zeros of smooth functions is not a trivial task.

To solve this problem, we partitioned the three-dimensional (x, v, t) phase space into domains in such a way that the sign change of a smooth event function (indicating that a solution segment crosses a boundary) uniquely determines the type of the solution in the next segment **[31]**. Taking this requirement into account the phase space was divided into 7 domains – 6 different sliding states and a sticking state – according to the values of v and x. The corresponding domains are given in Table 2.2 and illustrated in Fig. 2.15. The

Table 2.2: *The introduced phase space domains*

Notation	Condition 1	Condition 2
x^+v^+	$x > \cos(\Omega t) + S_0$	
x^0v^+	$\cos(\Omega t) - S_0 < x < \cos(\Omega t) + S_0$	$v > 0$
x^-v^+	$x < \cos(\Omega t) - S_0$	
x^+v^-	$x > \cos(\Omega t) + S_0$	
x^0v^-	$\cos(\Omega t) - S_0 < x < \cos(\Omega t) + S_0$	$v < 0$
x^-v^-	$x < \cos(\Omega t) - S_0$	
x^0v^0	$\cos(\Omega t) - S_0 < x < \cos(\Omega t) + S_0$	$v = 0$

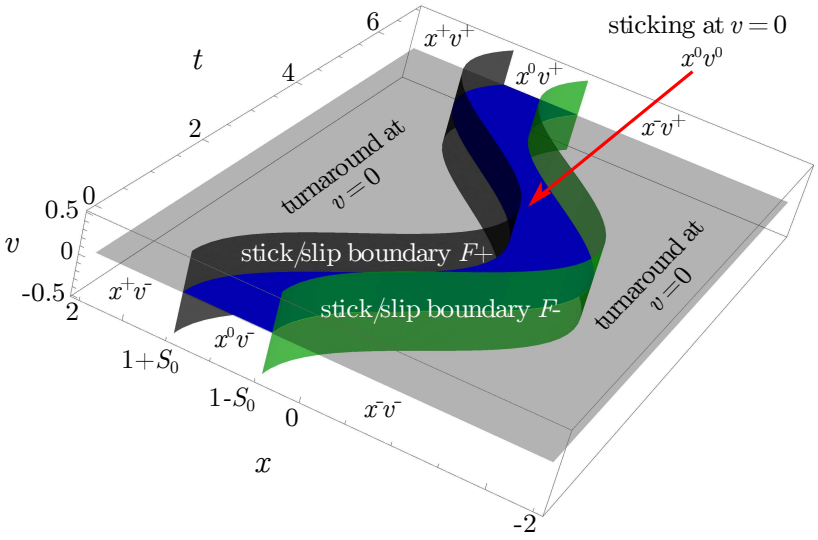

Figure 2.15: *Illustration of 6 sliding states and the sticking state, according to the values of x, v and t (cf. Fig. 2.3).*

domains are separated by three switching surfaces that are also depicted in Fig. 2.15. Two of them separate the states with respect to the displacement x – these are the boundaries $F+$ and $F-$ of the sticking region, respectively. The third switching surface is the $v = 0$ plane. Thus, the corresponding event functions can be formulated as

- $F+: \quad \cos(\Omega t) + S_0 - x = 0,$
- $F-: \quad \cos(\Omega t) - S_0 - x = 0,$
- $v = 0.$

If the actual state of the system is known, the triggering of an event function unambigously indicates the next state that the system enters. For example, if the oscillator's state is x^+v^+ (see Table 2.2), two possible events are possible:

- $F+ \Longrightarrow x^0v^+,$
- $v = 0 \Longrightarrow x^+v^-.$

There are three possible switches from the state x^0v^+:

- $F+ \Longrightarrow x^+v^+,$
- $v = 0 \Longrightarrow x^0v^0$ (sticking),
- $F- \Longrightarrow x^-v^+.$

The remaining four sliding cases (x^-v^+, x^+v^-, x^0v^-, x^-v^-) can be analysed similarly. If the oscillator is in the sticking state x^0v^0, the collision with the boundary $F-$ means that the resultant of forces acting on the block becomes positive. Thus, the next state will be x^-v^+. Similarly, crossing $F+$ leads to x^+v^-:

- $F+ \Longrightarrow x^+v^-,$
- $F- \Longrightarrow x^-v^+.$

These two switches can happen only if the static coefficient of friction S_0 is greater than the kinetic one. In the opposite case, sliding in the opposite direction occurs. This possibility will be excluded from the analysis due to its non-physical nature.

Once the states and event functions are properly defined, the bifurcations of the oscillator can be explored by COCO. However, this process is not straightforward, since besides the conventional bifurcations (e.g., period-doubling), several discontinuity-induced or non-smooth bifurcations (e.g., grazing-sliding, crossing-sliding, switching-sliding or adding-sliding) can occur. These bifurcations are accompanied by the change of the type and order of segments – the so-called *signature* of the solution – during a period. Thus, one has to make an educated guess about the possible order of states after each non-smooth bifurcation. Besides the bifurcations, other events can also take place that are related to the order of switches among the possible states shown in Table 2.2, but do not correspond to physically meaningful changes in the periodic solutions. For example, segments can appear or disappear when a sliding solution curve touches one of the stick-slip boundary surfaces $F+$ or $F-$. This event is denoted by T in Fig. 2.17. The disappearance of segments could be predicted by monitoring the durations of solution segments. To detect the appearance of new segments inside an existing one, the validity of solutions had to be checked during each run. Our experiences show that bifurcations often lead to a completely different solution signature. While the local qualitative change of the trajectory can be known in these cases as well, the signature of the whole periodic orbit is required for the continuation, that is often difficult or practically impossible to predict.

For the initiation of the calculation, the analysis by COCO was accompanied by the solution of the initial value problem, i.e., numerical simulation. Clearly, only stable solutions can be found with this approach, but once a solution type is found by COCO, it can be continued even after the loss of stability. Besides the calculation of the numerical solution, several files must be initialized for COCO – these are also done automatically by the Matlab code.[2] In addition to the initialization, we also implemented utility functions for the proper continuation from a previously obtained solution point, with the possibility to change the signature of the solution.

As it will be shown, four different periodic solution types can be detected in large domains of the examined parameter space. Each of these typical periods consists of 6 segments, thus, the number of segments will be denoted only if it is different from 6. The four typical solutions will be denoted by 2s, 0s, 2a and 1a, where 2, 1 or 0 shows the number of sticking segments in a period, while 's' or 'a' tells whether the solution is symmetric or asymmetric.

The bifurcation points or curves will be denoted accordingly. For instance, SN_{1a} and PD_{1a} denote the saddle-node and period-doubling bifurcation of a 1-stick asymmetric solution, respectively. Sliding bifurcations lead to the change of the number of sticking segments. In these cases only the symmetry property will be shown as CS_s, SS_a or AS_a.

Since the symmetry plays an important role in the classification of solutions, the measure of asymmetry was introduced as follows:

$$\Psi = \left| \frac{\max x + \min x}{\max x - \min x} \right|. \tag{2.90}$$

This quantity was also monitored during each continuation run.

[2]The first version of the initialization code was written by Gábor Licskó, whose help is acknowledged.

2.5.2 One-parameter bifurcation analysis

Bifurcation parameter: S

It was shown by Kunze [103] that the examined system does not exhibit chaotic solutions if the static and kinetic coefficients of friction are equal. Thus, to explore the possible chaotic solutions, the dimensionless kinetic coefficient of friction S was chosen to be the bifurcation parameter at a fixed static coefficient S_0. Since the symmetric non-sticking solutions are stable at the non-resonant excitation frequencies, it seemed to be reasonable to search for chaotic solutions at the sub-harmonic resonant frequencies of the asymmetric solutions (Section 2.3). Thus, the excitation frequency was chosen to be $\Omega = 0.5$, while the static coefficient of friction was fixed at $S_0 = 0.4$, just as we did in **[110]**. An initial solution guess was generated by numerical simulation at these parameters in Matlab – see Fig. 2.16.

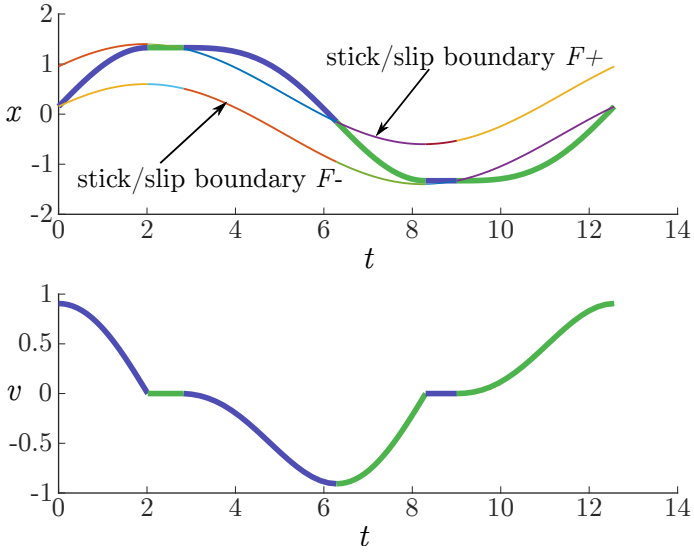

Figure 2.16: *The initial solution (thick line) generated numerically at* $S = S_0 = 0.4$ *and* $\Omega = 0.5$. *Subsequent segments are printed in different colours.*

The following solution types were detected **[31]**:

- The initial guess is symmetric and has the following structure at $S = 0.4$:

$$x^0v^+ \to x^0v^0 \text{ (stick)} \to x^+v^- \to x^0v^- \to x^0v^0 \text{ (stick)} \to x^-v^+$$

  This solution (denoted by 2s in Fig. 2.17) loses stability via a saddle-node (SN_{2s}) bifurcation at $S \approx 0.33358$.

- Below this parameter, the initialization process found only a pair of stable solutions (denoted by 1a). These solutions are asymmetric with one sticking segment per period. One of them has the following structure:

$$x^+v^+ \to x^+v^- \to x^0v^- \to x^0v^0 \text{ (stick)} \to x^-v^+ \to x^0v^+$$

  Certainly, the mirror image of this solution also exists at the same parameters. Both solutions lose stability via a period doubling (PD_{1a}) bifurcation at $S \approx 0.068$.

- The emerging pair of double-periodic asymmetric solutions (denoted by 2a,14seg) consist of 14 segments. One of these cycles has the following structure (the other is its mirror image):

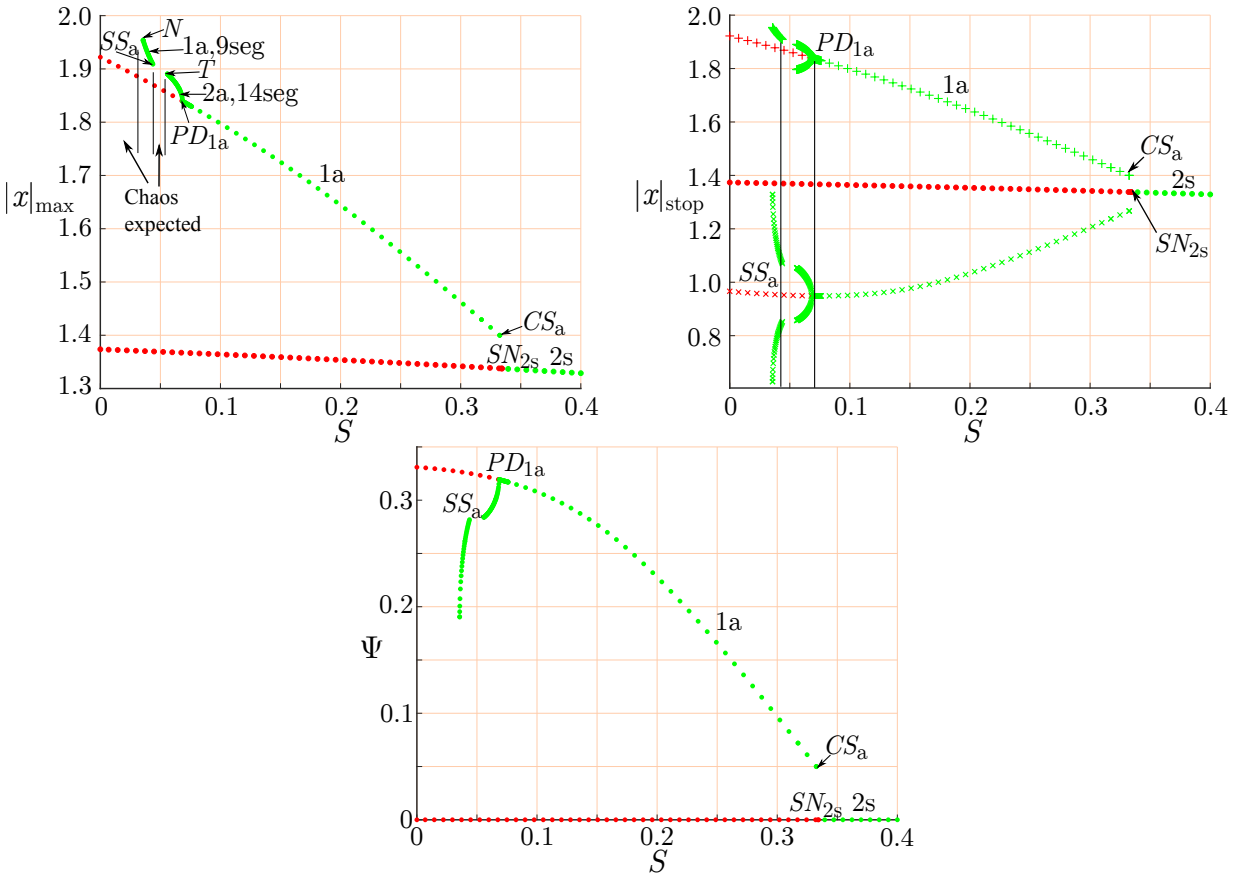

Figure 2.17: *Bifurcation diagrams I. $\Omega = 0.5$, $S_0 = 0.4$. Maximal displacement (top left), positions of stops (top right) and asymmetry Ψ (bottom) versus parameter S. Green symbols denote stable, red symbols denote unstable solution branches.*

$$x^+v^+ \to x^+v^- \to x^0v^- \to x^-v^- \to x^0v^- \to x^0v^0 \text{ (stick)} \to x^-v^+ \to x^0v^+ \to x^+v^+ \to x^+v^- \to x^0v^- \to x^0v^0 \text{ (stick)} \to x^-v^+ \to x^0v^+.$$

The solution's structure breaks down at $S \approx 0.05578$, where the 11^{th} solution segment (x^0v^-) just touches the stick-slip boundary F^-. This event – denoted by T in the figures – is related to the change of the order and number of segments.

No stable periodic solution was found in the range $S = [0.043479, 0.055787]$. The numerical initial problem solver detected a seemingly periodic solution, but it turned out to be unstable according to COCO. This experience indicates that the found solution is only slightly unstable, such that the stabilizing effect of the numerical algorithm could overcome its instability. Since no attracting periodic solution was found, the existence of multi-periodic solutions or chaos is expected in this parameter domain.

- In the range $S = [0.035620, 0.043479]$, an asymmetric solution (1a,9seg) with one stick per period was detected. This solution emerges at $S = 0.043479$ via a switching sliding (SS_a) bifurcation. It can be divided into 9 segments:

$$x^+v^+ \to x^+v^- \to x^0v^- \to x^-v^- \to x^-v^+ \to x^0v^+ \to x^0v^0 \text{ (stick)} \to x^-v^+ \to x^0v^+.$$

This solution could not be continued past the value $S = 0.035620$ due to the divergence of the numerical method (point N in Fig. 2.17). No stable periodic solution was found at even smaller values of S, where the occurrence of a chaotic domain is expected.

Bifurcation parameter: Ω

As the previous calculation showed, asymmetric solutions (denoted by 1a in the figures) appeared at $S \approx 0.33358$ at the discontinuity of the bifurcation diagrams. In the present section, we search for the origin of these asymmetric solutions. For this purpose, continuation was initiated in the vicinity of their appearance, at $S = 0.32$ and $S_0 = 0.4$, varying the excitation frequency Ω near 0.5. The results are depicted in Fig. 2.18.

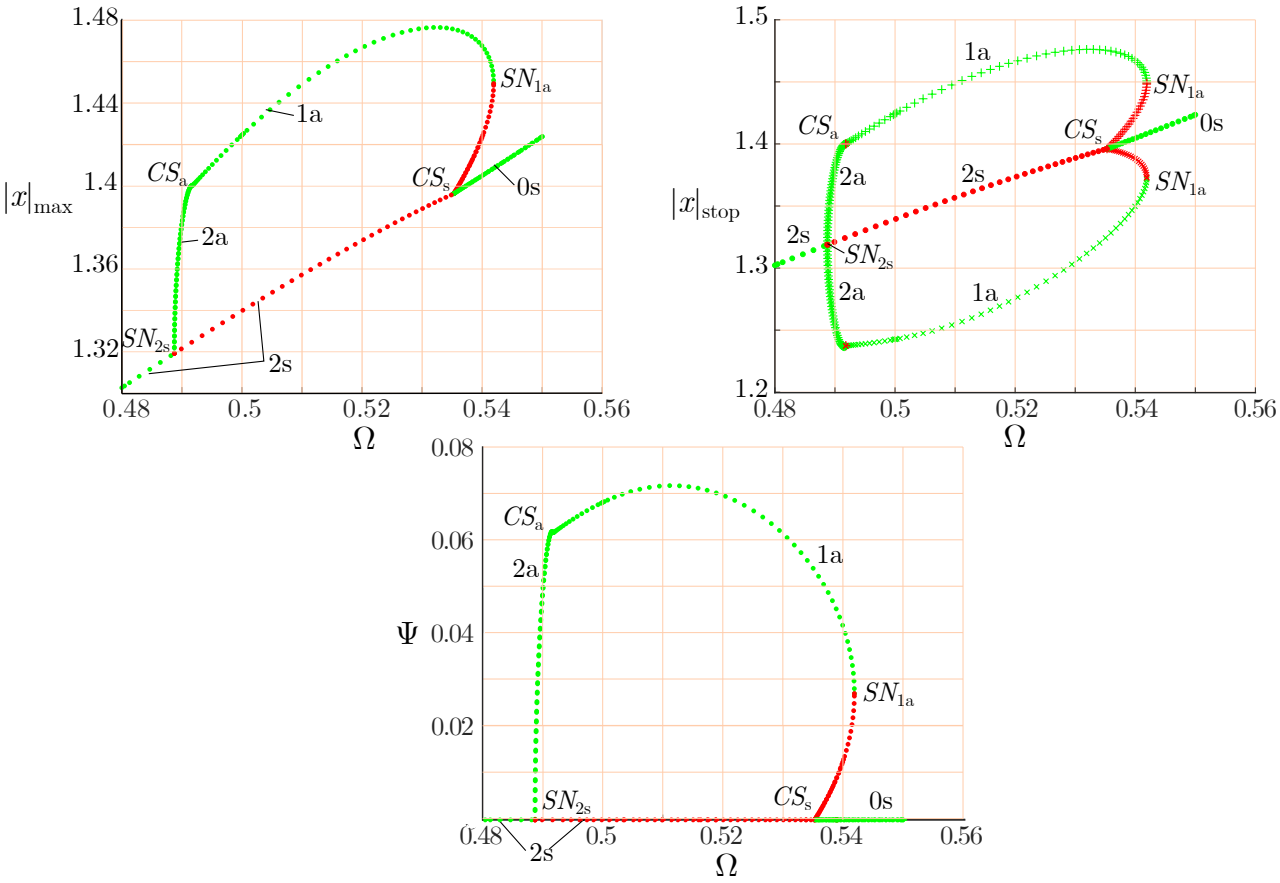

Figure 2.18: *Bifurcation diagrams II. $S = 0.32$, $S_0 = 0.4$. Maximal displacement (top left), positions of stops (top right) and asymmetry of solutions (bottom).*

- The continuation is initiated at $\Omega = 0.5$ with the numerically detected solution type

$$x^0v^+ \to x^+v^+ \to x^+v^- \to x^0v^- \to x^0v^0 \text{ (stick)} \to x^-v^+.$$

  This asymmetric solution (1a) is stable in the range $\Omega \in [0.49182, 0.54191]$. At the lower end, a new solution (2a) with two sticking segments appears via a degenerate crossing-sliding (CS_a) bifurcation, when the second segment (x^+v^+) disappears as the trajectory touches the $v = 0$ plane and the $F+$ boundary simultaneously. This bifurcation is asymmetric since no such event occurs at $F-$.

  The stability of solution 1a is lost via a saddle-node (SN_{1a}) bifurcation at $\Omega = 0.54191$. Finally, another crossing-sliding bifurcation (CS_s) takes place at $\Omega = 0.53529$, where the solution becomes symmetric and both sticking segments touch the $v = 0$ plane and the $F+$ or $F-$ boundary simultaneously.

- The signature of solution 2a, that is born at $\Omega = 0.49182$ via crossing-sliding, is

$$x^0v^+ \to x^0v^0 \text{ (stick)} \to x^+v^- \to x^0v^- \to x^0v^0 \text{ (stick)} \to x^-v^+.$$

This solution branch undergoes a saddle-node (SN_{2s}) bifurcation at $\Omega = 0.48874$. Here the solution is just symmetric, thus, this bifurcation is the crossing point between two coexisting asymmetric solutions that are each other's mirror images.

- A symmetric solution (2s) also appears at the frequency $\Omega = 0.48874$ with the same segment structure as the asymmetric solution 2a. Solution 2s is stable below $\Omega = 0.48874$, but unstable in the domain $\Omega \in [0.48874, 0.53529]$.

- At $\Omega = 0.53529$, both sticking segments become sliding ones via crossing-sliding (CS_s) and the symmetric, non-sticking stable solution 0s appears with the signature

$$x^0v^+ \to x^+v^+ \to x^+v^- \to x^0v^- \to x^-v^- \to x^-v^+.$$

This is the same parameter where the the asymmetric solution 1a branches out.

According to these results, the abrupt appearance of asymmetric solutions is related to the fold bifurcation (SN_{1a}) of solution 1a that emerges from the symmetric solution via a crossing-sliding bifurcation CS_s. At the critical parameter, where the symmetric non-sticking solution disappears, the trajectory just touches the stick-slip boundaries on both the positive and the negative side. However, the appearing symmetric sticking solution is unstable, while a pair of asymmetric sticking solutions appears.

The bifurcation structure depicted in Fig. 2.18 remains qualitatively unchanged at larger values of the kinetic friction parameter S, but the domain of asymmetric solutions shrinks and disappears at $S \approx 0.38$. However, significant changes occur if S is decreased: the connection between the solutions 1a and 2a breaks, giving rise to multi-periodic and chaotic solutions (see Fig. 2.19).

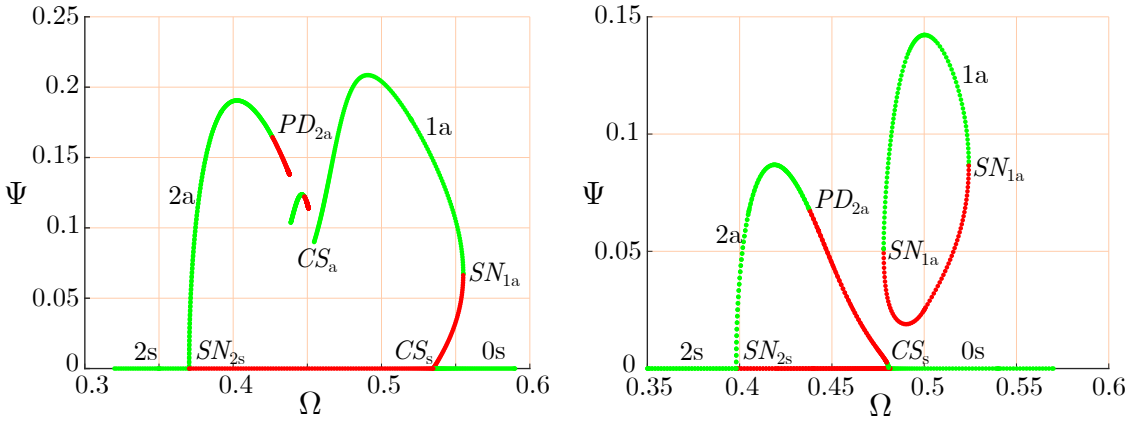

Figure 2.19: *Asymmetry of solutions versus parameter Ω at $S = 0.22$. Left: $S_0 = 0.4$. Multi-periodic and chaotic solutions exist between CS_a and PD_{2a}. Right: $S_0 = 0.3$. The domains of asymmetry are separated.*

Similar bifurcation structures can be observed at higher values ($S_0 = 0.5, \ldots, 0.9$) of the static coefficient of friction as well, but the frequency domain of asymmetric solutions extends towards higher values of Ω. However, the reduction of parameter S_0 leads to the separation of the domains of the asymmetric solutions 1a and 2a, as it is shown in Fig. 2.19. If S becomes larger, the two loops shrink and disappear at $S = S_0 = 0.3$. If the static coefficient of friction is reduced further ($S_0 = 0.2$) , the loop in the diagram corresponding to solution 1a persists at $\Omega = 0.5$, but solution 2a disappears. Still, multi-periodic or chaotic responses can be detected in the interval $\Omega \in (0.18, 0.38)$.

2.5.3 Two-parameter bifurcation analysis and search for chaos

As it was mentioned earlier, the occurrence of multi-periodic or chaotic solutions is expected in certain parameter domains. To localize these domains, two-parameter bifurcation analysis was performed on the $S-\Omega$ plane at various values of the static friction parameter S_0. The obtained diagrams are shown in Figs. 2.20 - 2.21.

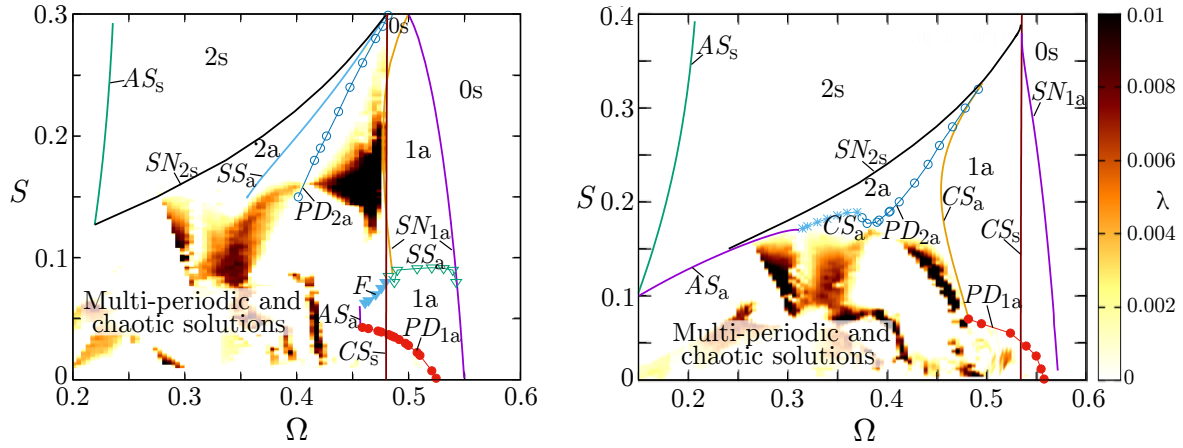

Figure 2.20: *Two-parameter bifurcation diagrams at $S_0 = 0.3$ (left) and $S_0 = 0.4$ (right)*

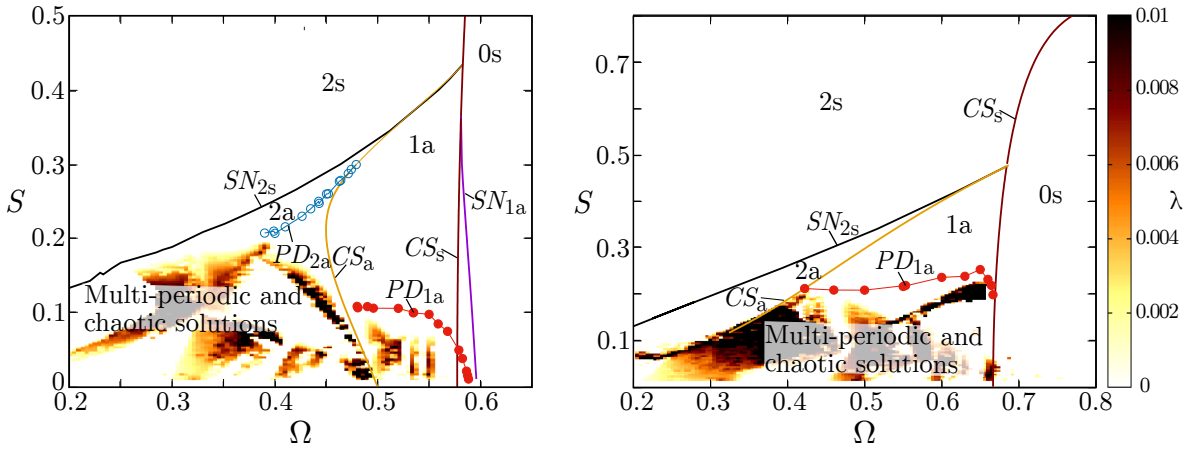

Figure 2.21: *Two-parameter bifurcation diagrams at $S_0 = 0.5$ (left) and $S_0 = 0.8$ (right)*

Perhaps the most important result of this analysis is that the switch from solution type 0s to 1a via bifurcation SN_{1a} happens during the reduction of the kinetic coefficient of friction (see Fig. 2.20). Thus – quite counterintuitively – a *smaller* friction coefficient leads to the appearance of *sticking solutions* in these cases.

Note, that we examined the same mechanical model with non-harmonic but periodic excitation signals, too. The bifurcation structure remained qualitatively similar **[31]**.

In addition to the bifurcation analysis with COCO, we wanted to check whether there are chaotic solutions. An important feature of chaotic systems is the sensitivity to initial conditions. It means that nearby trajectories of a chaotic system diverge at an exponential rate as time passes, until the separation attains the characteristic size of the attractor.

To characterise the rate of separation, we estimated the largest Lyapunov exponent (LLE) of solutions on grids of size 100×100 or 150×150 on the depicted $\Omega - S$ parameter planes. During each run, the evolution of two nearby orbits was traced and the variation of their phase space distance $d_i \to d_{i+1}$ was monitored in time steps Δt. In the simplest case, the

LLE can be estimated as

$$\lambda \approx \frac{1}{N}\sum_{i=1}^{N}\frac{1}{\Delta t}\log\frac{|d_{i+1}|}{|d_i|}, \tag{2.91}$$

where N denotes the number of steps. Note, that it may happen that one or the other solution is just in a sticking phase at $t = (i+1)\Delta t$ for some index i. In this case, a later time instant $t = (i+j)\Delta t$ was chosen such that both solutions slide, and the distance d_{i+j} was taken into account considering $\frac{1}{j\Delta t}\log(|d_{i+j}|/|d_i|)$ in the sum. This approach provides adequate results, as it was pointed out in [8]. Moreover, a similar procedure was already tested on the same system in **[110]** (see Section 2.6.1) and the results agreed well with the Lyapunov exponents calculated by the robust method of Stefanski and Kapitaniak [147].

The initial conditions (x_0, v_0, t_0) for the two solutions were $(1 + 0.9S_0, 0, 0)$ and $(1 + 0.9S_0 + 10^{-12}, 0, 0)$, respectively. The value of LLE was estimated at each parameter set at most until 600 exitation periods. The simulation finished earlier if the distance d reduced below 10^{-18} or the relative error between subsequently calculated estimates dropped below 10^{-3}. Since we are interested in chaotic responses, only parameter domains with positive Lyapunov exponents are coloured in Figs. 2.20 - 2.21.

The results show that chaotic solutions are typically enclosed by the bifurcation curves SN_{2s} (where the 2-stick symmetric solution loses stability) and CS_s (where the solution curve just touches the border of the sticking domain on both sides, giving rise to asymmetric solutions). Thus, the chaotic responses are bifurcating from asymmetric solutions, as we expected earlier **[110]**. Since asymmetric solutions had been detected at $\Omega = 0.5$ for the case $S = S_0$, this frequency was chosen in **[110]** to search for chaotic solutions. However, our results clearly show that the choice $\Omega = 0.5$ was rather unlucky and more pronounced chaotic regimes can be found at lower values of the frequency Ω.

According to the results, quite simple connections can be found between the friction coefficients and the location of the chaotic domain:

- Irrespectively of the exact value of the static coefficient (provided $S_0 > S$), the frequency domain of asymmetric solutions stemming from $\Omega = 0.5$ – and the enclosed domain of possible chaotic solutions – expands if the kinetic coefficient of friction S is decreased. The same trend was observed near $\Omega = 0.25$ at $S_0 < 1/15$ (see Eq. (2.82)).

- The increase of the rescaled static coefficient of friction in the interval $S_0 \in [0.3, 0.8]$ implies that the domain of multi-periodic or chaotic solutions is extended towards larger frequencies.

It can also be seen in the figures that $S < 0.2$ is needed for chaotic responses at almost all values of the static friction parameter S_0. However, a narrow parameter regime was found at $S_0 = 0.3$ where the Lyapunov exponent is positive even at $S \approx 0.265$. The corresponding ratio $S_0/S \approx 1.13$ is quite realistic, thus, the occurrence of chaotic responses cannot be excluded in similar models of real mechanical systems. Note, that the case $S_0 = 0.3$ seems to be an exception, since the further reduction of S_0 does not lead to the increase of the chaotic domain: only small islands of positive Lyapunov exponents were detected at $S_0 = 0.2$.

According to our experiences, the introduction of a non-zero viscous damping leads to the reduction of the LLE in the order of magnitude of the damping ratio. Thus, although the considered Coulomb friction model is rather simple, certain theoretically derived solution types could be observed even experimentally by Marino and Cicirello [112]. Since quite simple qualitative rules could be established between the frequency domain of irregular solutions and the coefficients of friction, these rules may be applicable to real mechanical systems, too.

2.6 FURTHER NUMERICAL RESULTS

In the present section, some results of the joint work with Gábor Licskó **[110]** are summarized.

2.6.1 Monte Carlo bifurcation diagram

The continuation method-based bifurcation analysis presented in Section 2.5.2 was preceded by the construction of the Monte Carlo bifurcation diagram, shown in Fig. 2.22.

The points on the diagram were determined by long numerical simulations. The simulation code was built up of functions written in MATLAB. No ODE solvers were needed since the analytical solution between two consecutive stops of the oscillating block of mass is known, according to Eqs. (2.5) and (2.6). Numerical approximation therefore is only needed at points where the block's velocity changes sign (turning points) or when the stuck block starts moving again due to the excitation force (starting point). Between these points, the solution can be calculated exactly. The switching point was determined by a relative tolerance of $\epsilon = 10^{-15}$. In order to find all the co-existing stable solutions, 10 simulations were started with random initial conditions (from the ranges of $x\,(0) \in [-1, 1]$, $\dot{x}\,(0) \in [-1, 1]$, $t_0 \in [-2\pi/\Omega, 2\pi/\Omega]$) for each value of parameter S.

During simulation several quantities were recorded, for example, crossings of the Poincaré surface defined by $t = 2k\pi/\Omega, k = 1, 2, ...$, and the last ten displacements where the block stuck. Also vectors containing all time instants of sticking and turning were stored. On top of Fig. 2.22, the recorded sticking displacements are shown versus the bifurcation parameter S. The lower panel of the figure shows a corresponding diagram that was obtained by the continuation method – a properly scaled part of Fig. 2.17 is depicted here. Comparing this diagram with the Monte-Carlo diagram in the upper subfigure, one can see that the non-sticking stops of the asymmetric solutions are not shown there.

To characterise the asymmetry of solutions, its measure Ψ was redefined since definition (2.90) assumes that the stationary periodic solution is already known. For the evaluation of numerical simulations, another formula is needed:

$$\Psi = \left| \sum_{i=1}^{n} \sum_{(i_j)} x(\hat{t}_{i_j}) \right|,$$

where $\hat{t}_{i_j}$ is the j^{th} time instant during the i^{th} excitation period when the velocity becomes zero, i.e. $\dot{x}(\hat{t}_{i_j}) = 0$ for $\hat{t}_{i_j} \in \left(T_0 + (i-1)\frac{2\pi}{\Omega}, T_0 + i\frac{2\pi}{\Omega}\right]$, $i = 1, \ldots n$. Here T_0 is chosen to be beyond the initial transients. Summing up all these displacements in n subsequent periods would result zero in case of symmetric solutions.

To characterise the chaotic solutions, two different numerical methods were applied to obtain the maximal Lyapunov exponent. One of them is based on the divergence of nearby trajectories – a similar method was used in Section 2.5.3. This direct method was easy to apply, however, we used a more refined procedure, too, in order to validate the results.

This latter method was developed by Stefanski and Kapitaniak specifically for piecewise-smooth problems [147]. It is based on the synchronisation of two chaotic systems, by implementing a uni-directional coupling between the original system of equations and a secondary

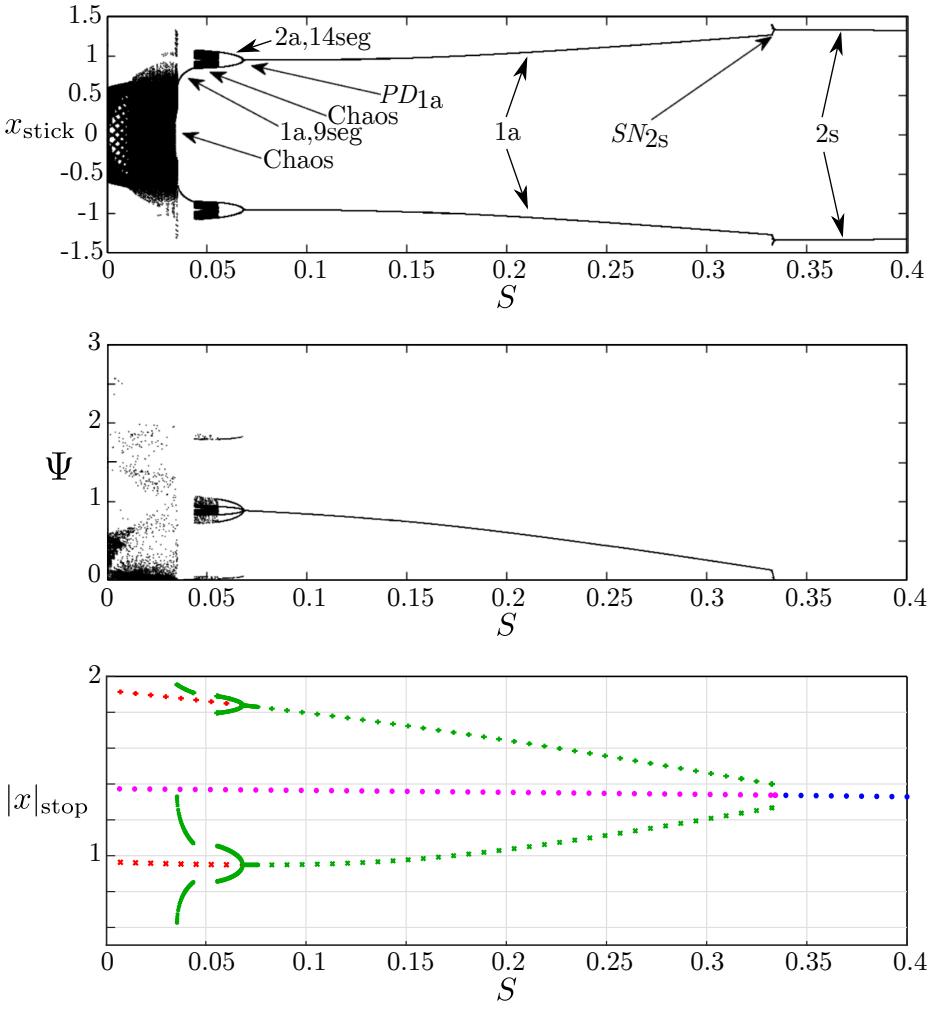

Figure 2.22: *Monte Carlo bifurcation diagram at parameters $S_0 = 0.4$ and $\Omega = 0.5$, depicting the sticking displacement (top) and asymmetry of solutions (middle). The bottom panel (generated by continuation method) shows all the displacements where stops occured.*

system. For our problem, the resulting set of first order equations is the following:

$$\begin{aligned}
\dot{x_1} &= x_2, \\
\dot{x_2} &= -x_1 + \cos\left(\Omega\left(t + t_0\right)\right) - Sf\left(\dot{x_1}\right), \\
\dot{x_3} &= x_4 + q\left(x_1 - x_3\right), \\
\dot{x_4} &= -x_3 + \cos\left(\Omega\left(t + t_0\right)\right) - Sf\left(\dot{x_3}\right) + q\left(x_2 - x_4\right),
\end{aligned}$$

where q is the coupling coefficient. The minimal value of q for which we obtain full synchronisation is an upper estimate of the largest Lyapunov exponent. To determine its value, we had to carry out a brute-force bifurcation calculation taking q as a bifurcation parameter. We had to watch when $x_1 - x_3$ vanished and recorded the corresponding value of q that provided an estimate of the LLE. Fig. 2.23 presents a sample run with parameters $S_0 = 0.4$, $S = 0.05$ and $\Omega = 0.5$ for which the system behaves chaotically. Above $q = 0.0073$ the two coupled systems are fully synchronised and thus the estimated maximal Lyapunov exponent is $\lambda \approx 0.0073$. The application of this procedure is rather time-consuming because one has to construct a second bifurcation diagram with respect to q. For this reason, we used the synchronisation method only at certain points. We also have to note that the minimum value for the coupling coefficient q cannot be less than zero. This is why we obtained $\lambda = 0$ for periodic solutions using this method.

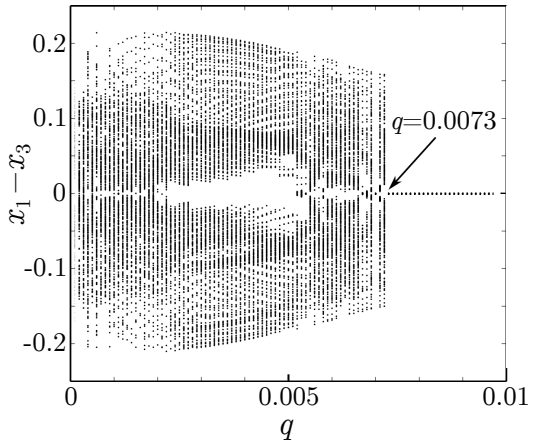

Figure 2.23: *Monte Carlo diagram for the coupling parameter q as bifurcation parameter. Synchronisation occurs at $q = 0.0073$, thus $\lambda \approx 0.0073$. ($S_0 = 0.4$, $S = 0.05$, $\Omega = 0.5$)*

In Fig. 2.24, we plotted the left part of the bifurcation diagram of Fig. 2.22 together with the Lyapunov exponents. It is clearly visible that between $S = 0.0436$ and $S = 0.0556$, and below $S = 0.0356$ the estimated maximal Lyapunov exponents are positive. The results of the two methods correlate, however, there is a small deviation between the calculated values since parameter q must be larger than the actual LLE for the synchronization of the two subsystems.

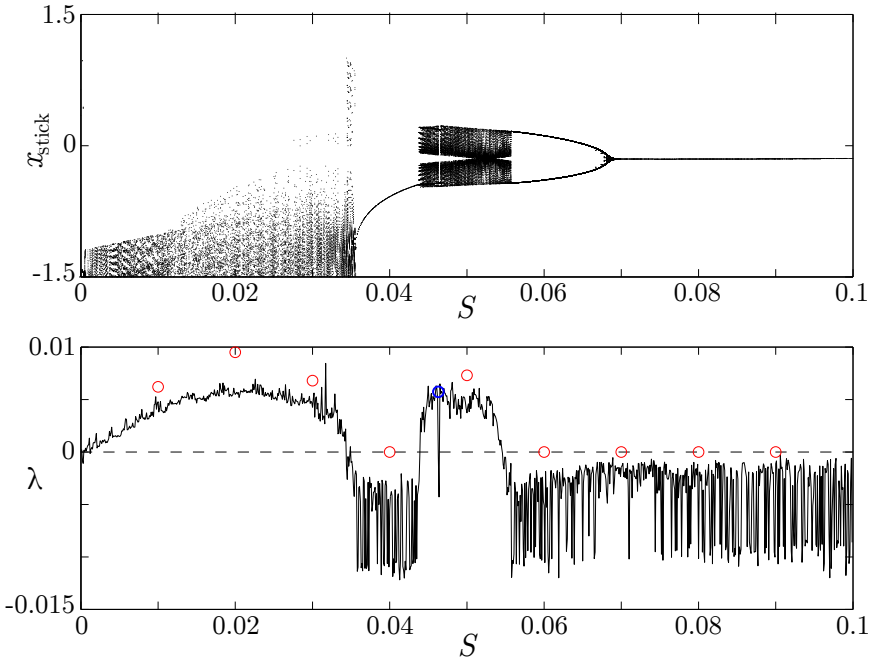

Figure 2.24: *Bifurcation diagram and largest Lyapunov exponents for parameters $S_0 = 0.4$ and $\Omega = 0.5$. (Solid lines – direct numerical simulation of nearby trajectories, red circles – method of Stefanski and Kapitaniak [147], blue circle – estimate based on a 1D map.)*

2.6.2 Transient chaos

We can observe in Fig. 2.24 that there is a negative spike at $S \approx 0.0465$ in the Lyapunov exponent plot and the chaotic band clears up here in the bifurcation diagram, opening a

very narrow gap of periodic motion. Numerical simulation showed that the chaotic transient at the beginning of the simulation suddenly turns into a period-three orbit (see Fig. 2.25).

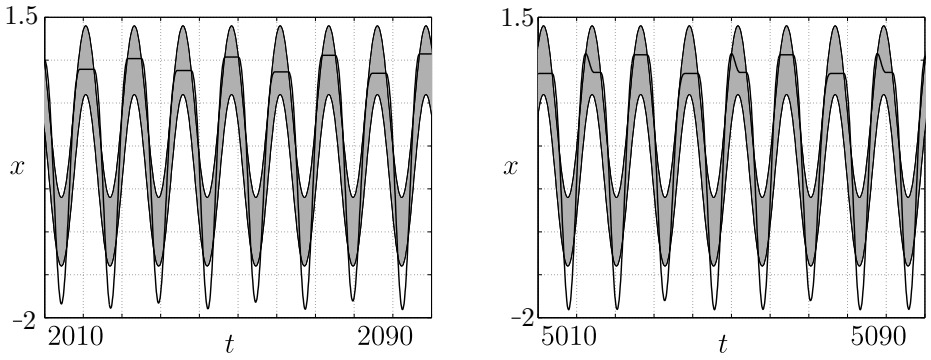

Figure 2.25: *Chaotic behaviour (left), that turns into a period-three motion (right).* ($S = 0.0465$, $S_0 = 0.4$, $\Omega = 0.5$)

To analyse this transient chaotic solution, we started simulations from several initial states and detected every *third* sticking. We obtained a one-dimensional map (Fig. 2.26) with three stable and an unstable fixed point. The chaotic trajectories can escape from the repeller at the stable points, where the graph of the map has three very small segments. One of these segments is shown in Fig. 2.26/b. We approximated the map by seven straight line segments and used it to estimate the finite time Lyapunov exponent that is valid in the transient phase. The trajectory of the piecewise-linear map started near the unstable fixed

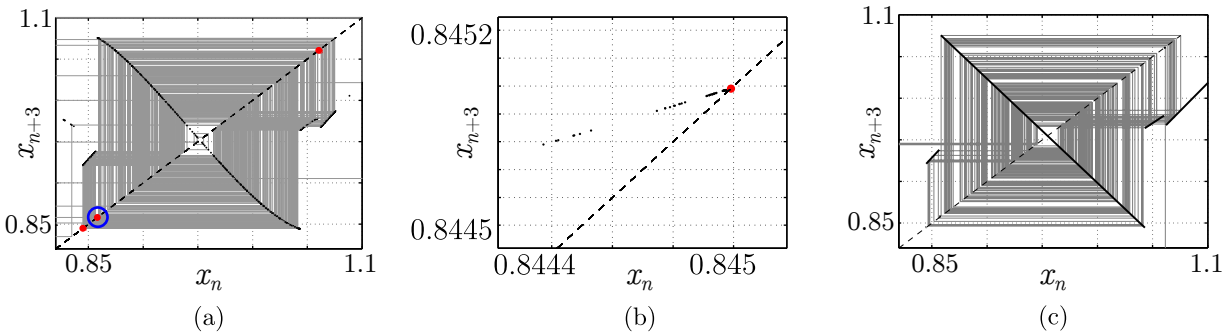

Figure 2.26: *Cobweb diagram for $S = 0.0465$ with three fixed points ((a), red dots) and the neighbourhood of the marked one (b). Piecewise-linear approximation of the map (c).*

point (at $x = 0.945$). We calculated the probability that the solution hits the i^{th} line segment in an iteration step using the formula $P(i) = n(i)/N_{tot}$, where $n(i)$ is the hit count of the i^{th} line segment and N_{tot} is the total number of iterations until escape. Having a constant slope along each segment we could approximate the LLE, that is $\lambda_{map} = \sum_{i=1}^{7} P_i \ln |a_i| = 0.2167$ in this case, where a_i is the slope of the i^{th} line segment. After scaling we obtained $\lambda_{flow} = \lambda_{map}/\bar{\tau} = 0.005748$, where $\bar{\tau}$ is the mean time between two steps of the iteration. This value fits in the series of calculated exponents – see the blue circle in Fig. 2.24. It is worth to note that the experimental detection of irregular vibrations of a similar oscillator was reported by Marino and Cicirello in [112]. Among the possible explanations, the authors mention the occurrence of transient chaotic motions, too.

Chapter 3

Nonlinear Analysis of Chip Formation

3.1 INTRODUCTION AND LITERATURE REVIEW

3.1.1 Sources of self-excited oscillations during cutting

The oscillations of the cutting machine-tool-workpiece system engages the attention of the theoreticians and technological experts for more than 80 years [54]. The topic of self-excited oscillations is especially important in the research efforts related to cutting technologies [5, 158, 159]. These oscillations can be traced back to three primary sources:

a) During *chip segmentation*, the surface of the chip becomes rugged, as shown in Fig. 3.1. The chip's pattern indicates that the cutting force and other characteristics of the material formation oscillate. The phenomenon was described first by Piispanen

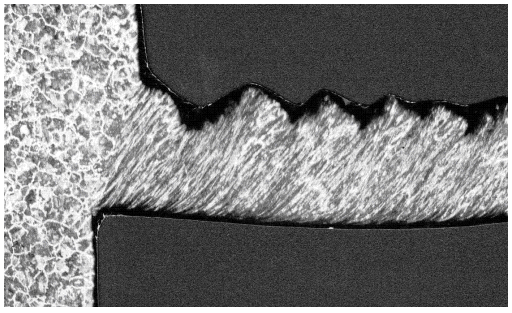

Figure 3.1: *A lamellar (periodic) chip.*

[132, 133]. Landberg [107] examined the phenomenon experimentally, but the detailed analysis is due to Albrecht [1]. A limiting case of chip segmentation is the *aperiodic chip formation* that was analysed in details by Field and Merchant [64]. In these cases, the dynamics of chip formation is influenced by various thermo-mechanical effects that can be coupled with the oscillations of the tool or the workpiece.

b) *Built-up-edge* (BUE) is the accumulation of the cut material on the rake face of the tool, near its tip. BUE was first examined in details by Ernst and Martellotti [59], who pointed out that the BUE continuously builds up and tears off, generating periodic variations in the cutting force.

c) In the case of *regenerative chatter*, the thickness of the chip cut at time t is influenced by the chip thickness during the previous cut, i.e., at $t - T$, where T is the characteristic period of the machining process. Since the tool and the workpiece are not ideally

rigid, this effect may lead to the loss of stability of the stationary cutting. This model can be traced back to the important contributions of Tlusty [158] and Tobias [159]. A comprehensive review of the modeling of nonlinear regenerative effects in metal cutting was given by Stépán in [149]. Kalmár-Nagy and Moon [90] incorporated in their model the displacements of the tool holder and the torsion of the tool, as well.

The analysis of machine tool vibrations has a vast literature: from experimental papers and books to contributions proposing refined mathematical models. However, as it can be seen from the literature review in **[129]**, thermal effects are typically not taken into account in the cutting models, although these effects have a great influence on the characteristics of the material of the workpiece, and consequently, on the cutting process itself. An exception in this respect is the continuum mechanical cutting model, introduced by Burns and Davies [20]. Their calculations were verified both experimentally and numerically by the finite element method, but the induced vibrations were not examined.

Following Burns and Davies, new, thermo-mechanical models of chip formation were put forward by Zoltán Pálmai (see e.g., [127]). The present chapter deals with the analysis of Pálmai's three different models. Section 3.1.2 introduces Pálmai's 4D chip formation model. An extended model – see Section 3.1.3 – was also proposed by Pálmai that takes into account the effect of the cutting speed variation induced by the vibrating tool or workpiece. Section 3.1.4 describes Pálmai's third model that deals with the influence of a periodically varying built-up edge on the dynamics of chip formation.

Our contributions are detailed in the subsequent sections of this chapter. The bifurcation analysis of the 4D model is presented in Section 3.2, based on **[32]**. The results show that the occurrence of chaotic behaviour is expected at the chosen parameter set. The analysis of the case when the cutting speed can vary was published in **[129]** and is presented in Section 3.3, while Section 3.4 deals with the characterisation of the chaotic vibrations that occur as a consequence of BUE **[131]**. Finally, a new model, incorporating both the thermo-mechanical processes and the regenerative effect **[74]** is briefly described in Section 3.5.

3.1.2 Pálmai's 4D chip formation model

The properties of the cutting phenomenon can be characterised by the chips formed during the process. For the sake of simplicity, only three types of chips will be distinguished here: continuous (Fig. 3.2/a), aperiodic (Fig. 3.2/b), and periodic (segmented or lamellar) chips (Fig. 3.2/c).

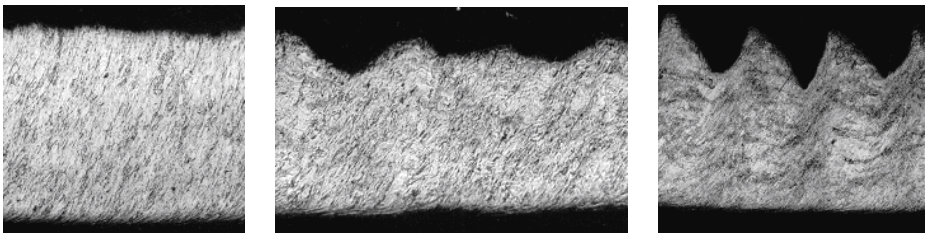

(a) (b) (c)

Figure 3.2: *Austenitic (stainless) steel chips formed at different cutting speeds. a) Continuous chip, $v = 0.3$ m/s; b) Aperiodic (chaotic) chip, $v = 0.58$ m/s; c) Periodic (segmented or lamellar) chip, $v = 3.6$ m/s. The experiments were conducted by Zoltán Pálmai.*

Xie, Bayoumi and Zbib [168] found that the occurence of segmented (periodic) chips is related to the phenomenon of thermoplastic instability, while Szalai, Stépán and Hogan [151]

examined the process as a dynamical system of the tool and the workpiece. They explored various types of bifurcations and demonstrated the existence of chaotic motion. Pálmai's model deals with the phenomena that can be derived from the characteristics of the material of the workpiece.

The first version of the model consisted of five non-linear differential equations and a constitutive equation [127], but later it was exchanged by a 4D model **[32]**. It is based on Piispanen's [133] result: in case of technologies that cause fast plastic deformation, the deformation is concentrated into one or a few nearly adiabatic shear zones. According to the observation of Luttervelt [111], two deformation bands can be identified in the shear zone. The developed model of chip formation adopts this idea, as it is shown in Fig. 3.3. The details of the derivation of the governing equations can be found in Appendix B.1.

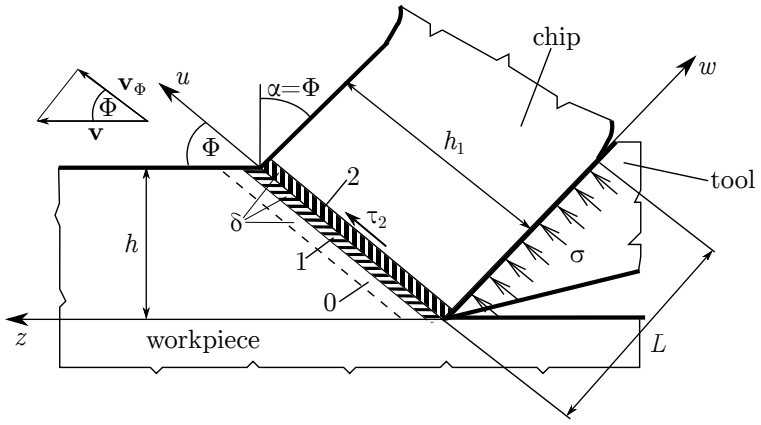

Figure 3.3: *The model of chip formation.*

The shear process is examined in two dimensions, assuming a so-called free cutting state, which occurs in the so-called primary strain zone or shear zone. Two deformation bands of thickness δ are introduced that are denoted by 1 and 2 in Fig. 3.3. Besides the bands 1 and 2, a "quasi" layer (denoted by 0) is also introduced, where no plastic deformation occurs, but this layer plays an important role in the thermal processes. The length of the shear zone is h_1 – this size characterises the bands, too.

The material of the workpiece first enters layer 0, where no plastic deformation occurs yet, however, layer 1 is deformed and heated up, as a result of which heat flows from layer 1 to layer 0. A similar process occurs between layers 1 and 2, too. For the sake of simplicity, it is assumed that the temperatures T_0, T_1 and T_2 in layers 0, 1 and 2 are identical everywhere within layers at a given moment, but – naturally – they are not necessarily equal, and all vary in time. It is also assumed that the inclination angle Φ of the shear zone and rake angle α of the tool are equal and constant. The material properties are taken into account by the following constitutive equation [128]:

$$F_i(\tau_i, T_i) \equiv \frac{\dot{\gamma}_i(t)}{\dot{\varepsilon}_\Phi} = \frac{T_i + 1}{T_\Phi + 1} \exp \frac{\tau_i - 1 + a(T_i - T_\Phi)}{b(T_i + 1)}, \quad (i = 1, 2). \tag{3.1}$$

Here $\dot{\gamma}_i(t)$ denotes the deformation velocity in the i^{th} shear zone at time t, $\dot{\varepsilon}_\Phi$ is the mean deformation velocity in the case of continuous chips, while τ_i denotes the plastic shear stresses in the layers $i = 1, 2$. a and b are constant terms characteristic of the material, and T_Φ denotes the temperature of the shear zone during the formation of continuous chips.

It is assumed that the plastic shear stress τ_i $(i = 1, 2)$ occurring in the shear zone of size h_1 is in mechanical balance with the normal stress σ acting along the chip on length

L, causing an elastic deformation Δu (see Fig. 3.3), i.e., the inertial forces are neglected. Pálmai introduced the characteristic time

$$K = \frac{\tau_\Phi h^2}{ELv\ \sin^2(\Phi)\ \cos(\Phi)}, \tag{3.2}$$

with which a dimensionless time could be introduced. Here h is the thickness of the cut layer, E is Young's modulus and v is the cutting speed, while τ_Φ denotes the mean shear stress [132] in the shear zone during the formation of continuous chips. According to the generally accepted approximation of the cutting theory, τ_Φ can be considered as a material constant. Exploiting the mechanical balance, the shear stresses along the deformation bands can be expressed in the following dimensionless forms:

$$\dot{\tau}_1 = p\left(1 - (F_1 + F_2)\right), \tag{3.3}$$
$$\dot{\tau}_2 = 1 - (F_1 + F_2), \tag{3.4}$$

where

$$p = 1 + \frac{\sqrt{3}\delta}{h}\sin(\Phi). \tag{3.5}$$

Eqs. (3.3) and (3.4) imply $\dot{\tau}_1 = p\dot{\tau}_2$, thus

$$\tau_1 = p\tau_2 + s, \tag{3.6}$$

where parameter s depends on the initial conditions.

The variation of the material's heat content ($c\rho\dot{T}$, where c means heat capacity and ρ is density) during chip formation is composed of three elements: mechanical power, thermal conduction and heat transfered by the moving material. Taking into account these effects (see [127]), the energy balance equations for the three layers assume the following dimensionless forms:

$$\dot{T}_0 = \zeta(T_1 - 2T_0) - \xi T_0, \tag{3.7}$$
$$\dot{T}_1 = \eta\tau_1 F_1(\tau_1, T_1) - \zeta(2T_1 - T_2 - T_0) - \xi(T_1 - T_0), \tag{3.8}$$
$$\dot{T}_2 = \eta\tau_2 F_2(\tau_2, T_2) - (\xi + \zeta)(T_2 - T_1), \tag{3.9}$$

with the system parameters

$$\eta = \frac{rK\tau_\Phi v\cos(\Phi)}{c\rho\delta T_w}, \quad \xi = \frac{Kv\sin(\Phi)}{\delta}, \quad \zeta = \frac{4K\lambda}{c\rho\delta^2}, \tag{3.10}$$

where λ denotes the thermal conductivity, T_w is the absolute temperature of the workpiece, and r is the energy ratio ($r \approx 0.95$).

Thus, the mathematical model of chip formation consists of the autonomous differential equations (3.4) and (3.7)-(3.9), together with (3.6) and the constitutive equations (3.1).

Equilibrium solutions of the governing equations correspond to the formation of continuous chips, the emergence of periodic solutions means that segmented or lamellar chips are formed, while chaotic solutions characterise the formation of aperiodic chips.

The parameters given by Eqs. (3.2), (3.5) and (3.10) can be interpreted as follows. The characteristic time scale K is related to both the elastic and plastic material characteristics and the technological parameters, and is inversely proportional to the most important technological parameter, the cutting speed. Parameter ξ is the dimensionless velocity of the chip, i.e., the reciprocal of the dimensionless time $\delta\hat{t}$ during which the material of the workpiece passes through the shear zone. Thus, $\xi = 1/\delta\hat{t}$ and it does not depend on the

cutting speed due to the scaling of the time by K. Parameter η – which can be rewritten as $\eta = \xi(r\tau_\Phi/c\rho T_w)$ cotan Φ – describes the amount of energy input. This parameter is related to the mechanical and thermal properties of the material and it is also independent of the cutting speed. Only parameter ζ depends on the cutting speed, while parameter p is determined by technological characteristics.

The dynamical system defined by Eqs. (3.4)-(3.9) can be characterised by 6 independent parameters: a, b, T_Φ, ξ η and ζ. Practically speaking, this six-dimensional parameter-space cannot be fully explored. However, there are three parameters that are especially important from the technological point of view: ξ, η, and ζ. To illustrate the rich dynamics of the examined system, Pálmai focused on the case $a = 0.3$, $b = 0.012$, $T_\Phi = 1$ (see [111]), $\xi = 4.8$ and $\eta = 4.4$ since these parameter values correspond to the chips of austenitic steel shown in Fig. 3.2. The system parameter ζ assumes the values a) $\zeta = 40$, b) $\zeta = 21$ and c) $\zeta = 3.4$ in the cases of the depicted continuous, aperiodic, and lamellar chips, respectively. The dimensionless system parameters were determined according to the following physical parameters of the austenitic steel: $\rho = 7900$ kg/m^3, $c = 500$ J/(kg K), $\lambda = 16$ N/(msK) The thickness of the cut layer is $h = 0.35$ mm, while the inclination angle of the shear zone is $\Phi = 30^o$. Based on the results in [14], $\delta = 12.5$ μm is a realistic approximation of the thickness of the deformation bands, that implies $p = 1.03$, according to (3.5). The value of K that corresponds to the formation of the periodic chips in Fig. 3.2 is $K = 1.64 \cdot 10^{-4}$ s.

Considering the formation of continuous chips as the initial condition, $\tau_{1,2}(0) = 1$ and $T_i(0) = 0$, (i =0, 1 and 2) was chosen, which leads to $s = 1 - p$, i.e., $s = -0.03$ and $\tau_1 = p\tau_2 + 1 - p$.

3.1.3 Extension of the model to the case of a vibrating workpiece

In the basic model, described in Section 3.1.2, it is assumed that the cutting speed v is constant. However, the cutting speed may vary during machining. The most obvious example for such processes is the flat turning, but the taper-turning, the so-called back turning and the special polygon-turning also lead to the variation of the cutting speed. Moreover, according to the cutting examples described in [1, 98], the vibrations of the elastic machining system have a considerable influence on the cutting speed and on the whole process. To take the vibrations of the tool and/or the workpiece into account, Pálmai extended the 4D model of chip formation to the case when the workpiece vibrates parallel with the cutting velocity. The displacement of the workpiece is characterised by the dimensionless coordinate z that is measured with respect to the reference distance

$$\tilde{L} = \frac{2\tau_\Phi}{m_r} K_0^2. \tag{3.11}$$

$\dot{z}$ is the velocity of the vibration of the workpiece such that $\dot{z} > 0$ leads to the reduction of the effective cutting speed (see Fig. B.1). According to the derivation in Appendices B.2 and B.3, the following set of dimensionless equations was obtained:

$$\dot{\tau}_2 = f\left(1 - \frac{\dot{z}}{V_0 f}\right)\left(1 - (F_1 + F_2)\right), \tag{3.12}$$

$$\dot{T}_0 = \zeta(T_1 - 2T_0) - f\left(1 - \frac{\dot{z}}{V_0 f}\right)\xi T_0, \tag{3.13}$$

$$\dot{T}_1 = f\left(1 - \frac{\dot{z}}{V_0 f}\right)\Big(\eta(\tau_2 p + 1 - p)F_1(\tau_1, T_1) - \xi(T_1 - T_0)\Big) - \zeta(2T_1 - T_2 - T_0), \tag{3.14}$$

$$\dot{T}_2 = \eta f \left(1 - \frac{\dot{z}}{V_0 f}\right) \tau_2 F_2(\tau_2, T_2) - \left(f \left(1 - \frac{\dot{z}}{V_0 f}\right) \xi + \zeta\right) (T_2 - T_1), \tag{3.15}$$

$$\ddot{z} = \tau_2 - Az. \tag{3.16}$$

Parameter f denotes the ratio of the cutting speed v to a reference speed $v_0 = 3.6$ m/s – the latter is used to define the reference time scale as $K_0 = K(v = v_0)$, while $A = kK_0^2/m_r$ is the dimensionless stiffness of the elastic workpiece having stiffness k and equivalent mass m_r. The dimensionless velocity V_0 is defined as

$$V_0 = \frac{K_0 v_0}{\tilde{L}} = \frac{m_r v_0}{2\tau_\Phi K_0}. \tag{3.17}$$

If the deformation of the tool was modeled instead of the deformation of the workpiece, the same equations could be used, with the z axis reversed.

3.1.4 Effects of built-up edge induced oscillations

The models, analysed in the previous subsections, considered a constant cutting depth, but this latter condition is not fulfilled if some parts of the cut material stick to the tool, forming the so-called built-up edge (BUE). Built-up edge is typically formed during processes with

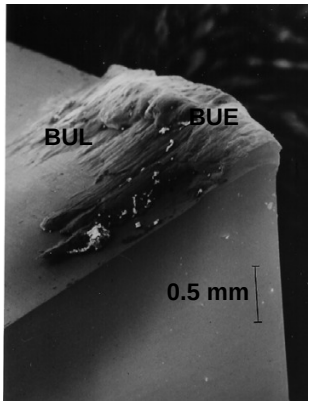

Figure 3.4: *Scanning electron microscope picture of BUE and BUL (built-up layer) on a high speed steel tool.*

small cutting speeds, like drilling or turning [66]. BUE can be encountered even on the most up-to-date tool materials (see Fig. 3.4). In principle, there is no BUE on tools with PVD or CVD coating, but if the coating abrases, BUE can develop. This is why this phenomenon is still subject to intensive research. The occurrence of BUE was first mentioned by Haussner in 1882 [79]. Later, Rosenhain and Sturney [140] realised that the built-up edge is often integral with the chip. Rapatz [138] showed that not the cutting speed but the temperature on the surface of the tool plays the primary role in the process. The formation of BUE was first examined in details by Ernst and Martellotti [59]. They pointed out that the built-up edge periodically increases and tears off, leading to harmful fluctuations of the cutting force and thickness of cut layer, which provide an excitation for the workpiece-machine-tool system. The frequency of this oscillation is 77-200 Hz, according to the measurements performed by Shteinberg [143]. A detailed literature review about the built-up-edge is found in **[131]**.

Pálmai put forward a time-delayed chip formation model (see Appendix B.4) that is able to describe the cutting process in the case of varying thickness of the cut layer. This new model can be used for the study of the effects of the formation of BUE on the type of the

produced chips. As it will be shown in Section 3.4, the occurrence of BUE turns fixed point solutions – that correspond to the formation of continuous chips – to chaotic vibrations, leading to the deterioration of the surface quality.

The differences between the original 4D model and the new model can be summarized as follows. In the previous model Pálmai neglected friction and assumed that the inclination angle Φ of the shear zone and rake angle α of the tool were equal. In the new model, these simplifying assumptions are disregarded: the shear stress is expressed such that it depends both on the coeffcient of friction μ and the difference $\Phi - \alpha$ (B.39). Instead of two deformation layers, only a single shear band (active layer) is introduced that is characterised by temperature T, shear stress τ and shear strain γ. There is also an inactive layer (characterised by temperature T_0), that plays a role in the thermal processes, only (see Fig. B.2). The temperature, shear stress, deformation angle and time are transformed to dimensionless form: $\hat{T} = (T - T_w)/T_w$, $\hat{\tau} = \tau/\tau_\Phi$,$\hat{\gamma} = \gamma/\varepsilon_\Phi$, $\hat{t} = t/K$, where T_w denotes the temperature of the workpiece, and the time-scale is

$$K = \frac{(\lambda' + 1)h_0^2 \tau_\Phi \cos(\Phi - \alpha)}{ELv \sin^2(\Phi)\cos(\alpha)} \frac{1}{1 - \mu \tan(\Phi - \alpha)}. \tag{3.18}$$

Here λ' characterises the stress distribution along the surface of the tool (see (B.39)).

As it was shown in **[129]**, the energy balance equation of the inactive layer assumes the following dimensionless form:

$$\frac{d\hat{T}_0(\hat{t})}{d\hat{t}} = \zeta(\hat{T}(\hat{t}) - 2\hat{T}_0(\hat{t})) - \frac{1}{\delta\hat{t}}\hat{T}_0(\hat{t}). \tag{3.19}$$

During the motion of the material, heat flows from the inactive layer to the active layer. In the new model [130] it is taken into account that time is necessary to cover the distance δ, which corresponds to the thickness of the layer. Consequently, a delayed value of the temperature $\hat{T}_0(\hat{t} - \delta\hat{t})$ must be used in the calculations. Therefore,

$$\frac{d\hat{T}(t)}{d\hat{t}} = \eta\hat{\tau}(\hat{t})F(\hat{t}) - \zeta(\hat{T}(\hat{t}) - \hat{T}_0(\hat{t})) - \frac{1}{\delta\hat{t}}(\hat{T}(\hat{t}) - \hat{T}_0(\hat{t} - \delta\hat{t})), \tag{3.20}$$

where the following dimensionless system parameters are introduced:

$$\zeta = \frac{4K\lambda}{c\rho\delta^2}, \quad \frac{1}{\delta\hat{t}} = \frac{Kv\sin(\Phi)}{\delta}, \quad \text{and} \quad \eta = \frac{rK\tau_\Phi v\cos(\Phi)}{c\rho\delta T_w \cos(\Phi - \alpha)}. \tag{3.21}$$

$F(\hat{t})$ denotes the deformation speed expressed with the help of the constitutive equation, characteristic of the material of the workpiece [126]:

$$F(\hat{t}) \equiv \frac{\dot{\gamma}}{\dot{\varepsilon}_\Phi} = \frac{\hat{T} + 1}{\hat{T}_\Phi + 1} \exp\frac{\hat{\tau} - \frac{1+\varepsilon_\Phi^n \hat{\gamma}^n}{1+\varepsilon_\Phi^n} + a(\hat{T} - \hat{T}_\Phi)}{b(\hat{T} + 1)}, \tag{3.22}$$

where a, b, and n are constant values, characteristic of the thermal softening, the sensitivity to velocity of deformation, and the strain-hardening, respectively. The deformation is described by the following equation [126]:

$$\frac{d\hat{\gamma}(\hat{t})}{d\hat{t}} = \left[F(\hat{t}) - F(\hat{t} - \delta\hat{t})\right] \frac{1}{\delta\hat{t}}. \tag{3.23}$$

As the BUE periodically develops and tears off, the thickness of the cut layer varies approximately according to a saw-tooth profile (see Section B.4.2), in the form

$$h(\hat{t}) = h_0[1 + Hf_1(\hat{t})], \tag{3.24}$$

where $H = \Delta h/h_0$, and – by introducing parameter Ω that characterises the frequency of BUE formation –

$$f_1(\hat{t}) = \frac{\Omega}{2\pi}\left(\hat{t} \bmod \frac{2\pi}{\Omega}\right) \equiv \frac{\Omega}{2\pi}\hat{t}_m. \tag{3.25}$$

Thus, the equation of mechanical balance (cf. (3.4)) turns into the following non-dimensional formula:

$$\frac{d\hat{\tau}}{d\hat{t}} = \frac{1 - F(\hat{t})}{\left[1 + H\frac{\Omega}{2\pi}\hat{t}_m\right]^2} - 2\hat{\tau}\frac{H\frac{\Omega}{2\pi}}{1 + H\frac{\Omega}{2\pi}\hat{t}_m}. \tag{3.26}$$

In summary, the new mathematical model of chip formation comprises the autonomous differential equations (3.19), (3.20), (3.23) and (3.26), along with the expression of the deformation speed (3.22).

3.2 ANALYSIS OF PÁLMAI'S 4D MODEL

The governing equations of the chip formation model of Section 3.1.2 can be summarized as follows:

$$\begin{aligned}
\dot{\tau}_2 &= 1 - (F_1 + F_2), && (3.27)\\
\dot{T}_0 &= \zeta(T_1 - 2T_0) - \xi T_0, && (3.28)\\
\dot{T}_1 &= \eta(p\tau_2 + 1 - p)F_1(\tau_2, T_1) - \zeta(2T_1 - T_2 - T_0) - \xi(T_1 - T_0), && (3.29)\\
\dot{T}_2 &= \eta\tau_2 F_2(\tau_2, T_2) - (\xi + \zeta)(T_2 - T_1), && (3.30)
\end{aligned}$$

where

$$\begin{aligned}
F_1(\tau_2, T_1) &\equiv \frac{\dot{\gamma}_1(t)}{\dot{\varepsilon}_\Phi} = \frac{T_1 + 1}{T_\Phi + 1}\exp\frac{p\tau_2 - p + a(T_1 - T_\Phi)}{b(T_1 + 1)},\\
F_2(\tau_2, T_2) &\equiv \frac{\dot{\gamma}_2(t)}{\dot{\varepsilon}_\Phi} = \frac{T_2 + 1}{T_\Phi + 1}\exp\frac{\tau_2 - 1 + a(T_2 - T_\Phi)}{b(T_2 + 1)}.
\end{aligned} \tag{3.31}$$

To find the possible solutions, we used the continuation and bifurcation software AUTO [53]. For the application of this software, a stable equilibrium-type solution must be found first by numerical simulation. The variation of the location of equilibrium states can be followed by AUTO as one of the parameters is varied. Moreover, the bifurcation points are also detected during this process, making the search for periodic solutions also possible. To explore the bifurcations that lead to the switches among the three chip types of austenitic steel (Fig. 3.2), parameter ζ would be the most practical bifurcation parameter, since this parameter depends on the cutting speed. Unfortunately, the software AUTO was unable to find the fine details of the corresponding bifurcation diagram, thus, we chose another approach. We determined bifurcation diagrams with respect to the bifurcation parameter ξ, and then performed a two-parameter (ξ-ζ) analysis. A typical bifurcation diagram is shown in Fig. 3.5 at $\zeta = 21$. As it can be seen in the figure, the stable equilibrium loses stability via a supercritical Hopf bifurcation at $\xi = 4.42808$, and becomes stable again at $\xi = 11.8039$. These Hopf bifurcation points are denoted by H in the figure. The unstable periodic solutions emerging at these points undergo fold bifurcations (denoted by F) at $\xi = -1.85529$ and $\xi = 13.5244$ and become stable. Note, that negative values of parameter ξ are physically unfeasible, but we had to extend our studies to this domain during the continuation process.

Stability changes again at $\xi = 3.11285$ and $\xi = 10.6639$, where double periodic solutions appear (see Fig. 3.5/a). At these points cascades of period doubling bifurcations (denoted by PD1 and PD2 in Fig. 3.5) begin, leading to chaotic behaviour. In Table 3.1, the detected

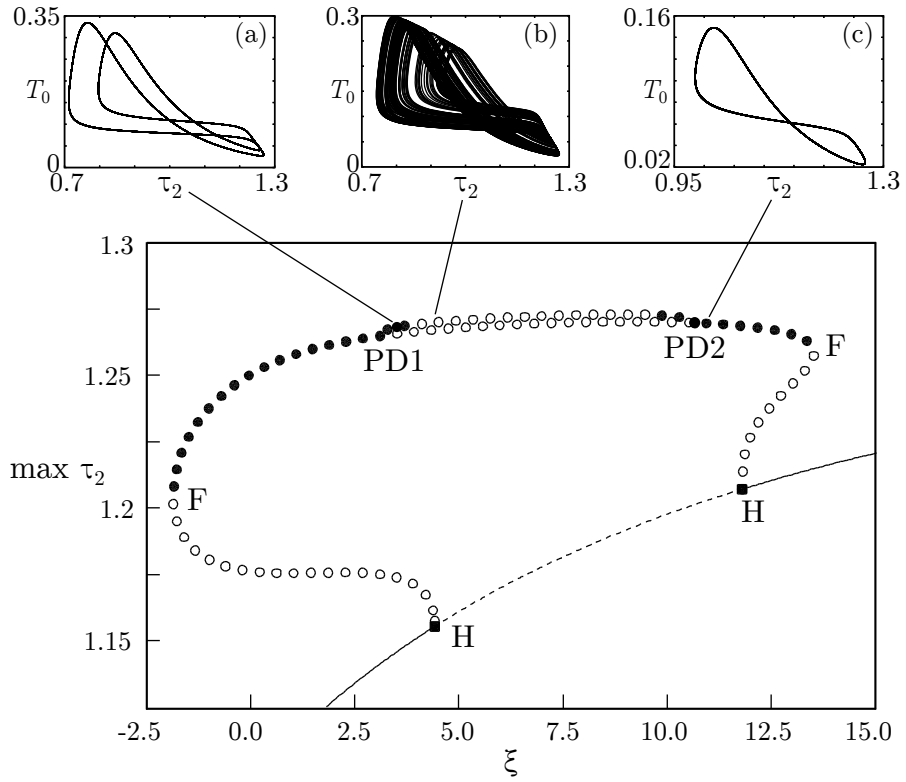

Figure 3.5: *Bifurcation diagram at $\zeta = 21$. Solid lines and full circles denote stable equilibria and periodic solutions, respectively. Dashed lines and open circles denote unstable solutions. (a) double periodic solution at $\xi = 3.5$, (b) chaotic solution at $\xi = 4.8$, corresponding to the case shown in Fig. 3.2/b, (c) periodic solution at $\xi = 11$.*

period doubling bifurcation points are listed, together with the ratio of the differences between the successive bifurcation parameter values. The results indicate that the bifurcation points tend to follow each other according to the so-called Feigenbaum ratio [63]

$$\delta_F = \lim_{i\to\infty} \frac{\xi_i - \xi_{i-1}}{\xi_{i+1} - \xi_i} \approx 4.6692. \tag{3.32}$$

To check this possibility, we determined several points of the trajectory of the solution shown in Fig. 3.5/b. Since map-like data can be analysed more precisely than flow-like data, we performed a Poincaré-transformation: the values of τ_2 were detected at the intersection points of the trajectory and the $T_0 = 0.1$ plane. The average time period between two crossings was $\Delta t \approx 0.558$. The successive values of τ_2 define a one-dimensional Poincaré

Table 3.1: *Detected period doubling bifurcations*

Bifurcations at PD1			Bifurcations at PD2		
i	$\xi_i^{(1)}$	$\frac{\xi_i^{(1)}-\xi_{i-1}^{(1)}}{\xi_{i+1}^{(1)}-\xi_i^{(1)}}$	i	$\xi_i^{(2)}$	$\frac{\xi_i^{(2)}-\xi_{i-1}^{(2)}}{\xi_{i+1}^{(2)}-\xi_i^{(2)}}$
1	3.11285	-	1	10.6639	-
2	4.03007	3.84514	2	9.52126	3.57611
3	4.26861	4.21225	3	9.20174	4.34485
4	4.32524	4.57062	4	9.1282	4.58193
5	4.33763	-	5	9.11215	-

map, as depicted in Fig. 3.6. The numerically obtained points clearly trace out an unimodal map, thus, the corresponding period doubling sequence indeed must obey Feigenbaum's law.

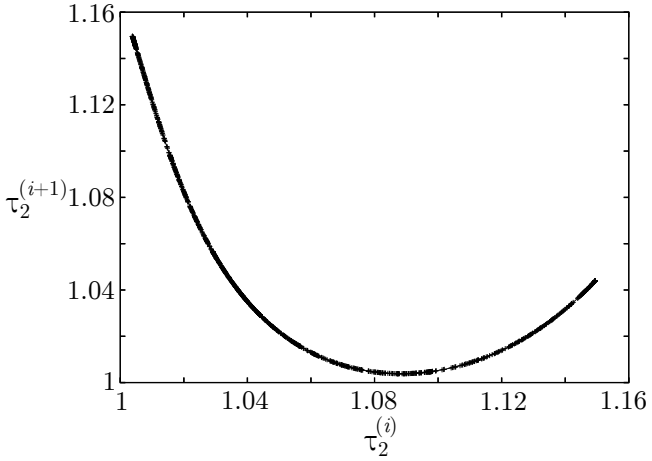

Figure 3.6: *One-dimensional Poincaré-map.*

Consequently, the parameters corresponding to the onset of chaos – the limits of the Feigenbaum sequences – can be estimated quite easily:

$$\xi_{crit}^{(1)} \approx \xi_5^{(1)} + \sum_{j=1}^{\infty} \frac{\xi_5^{(1)} - \xi_4^{(1)}}{\delta_F^j} = 4.34074 \tag{3.33}$$

gives the critical parameter belonging to the period-doubling cascade PD1, while the upper boundary of the chaotic regime is expected to be near PD2, at

$$\xi_{crit}^{(2)} \approx \xi_5^{(2)} - \sum_{j=1}^{\infty} \frac{\xi_5^{(2)} - \xi_4^{(2)}}{\delta_F^j} = 9.10808. \tag{3.34}$$

In this way we found that chaotic solutions may occur in the parameter domain $\xi \in (4.341, 9.108)$. This result implies that chaotic and stable equilibrium solutions coexist between $\xi = 4.341$ and $\xi = 4.42808$ (where the Hopf bifurcation occurs).

Note that the results provided by AUTO only indicate that chaotic solutions may exist. To characterise the numerically obtained solutions, we applied the TISEAN nonlinear time series analysis software package [80] on the time series $\tau_2^{(i)}$ of the Poincaré map, and determined the largest Lyapunov exponent λ. The algorithm, implemented in TISEAN, reproduces the topology of the whole phase-space using only a single scalar time series, then measures how the distance of selected pairs of points changes over time [91]. By plotting the logarithm of the distance S versus the number of iteration steps Δn for five different initial distances, we obtained the graph shown in Fig. 3.7. Since the curves have quite long linear sections, we can state that the divergence of trajectories is exponential, indeed. Consequently, the analysed solution – corresponding to the chip shown in Fig. 3.2/b – is chaotic. The slope of the curves at the linear part is a good approximation of the Lyapunov exponent: $\lambda_{\mathrm{Lyap,map}} \approx 0.361$. This value characterises the Poincaré map. To find the maximal Lyapunov exponent of the flow, we must take into account the dimensionless average time period Δt of the crossings of the Poincaré surface. Using this value, $\lambda_{\mathrm{Lyap,flow}} = \lambda_{\mathrm{Lyap,map}}/\Delta t \approx 0.647$. Dividing this number by the value of the characteristic time, one obtains the Lyapunov exponent expressed with respect to the real, physical time as $\lambda = 0.647/K \approx 3945$ 1/s. This result indicates that the chaotic dynamics of thermo-mechanical processes is typically much

faster than other typical dynamical mechanisms during cutting, e.g., the vibrations related to the regenerative effect.

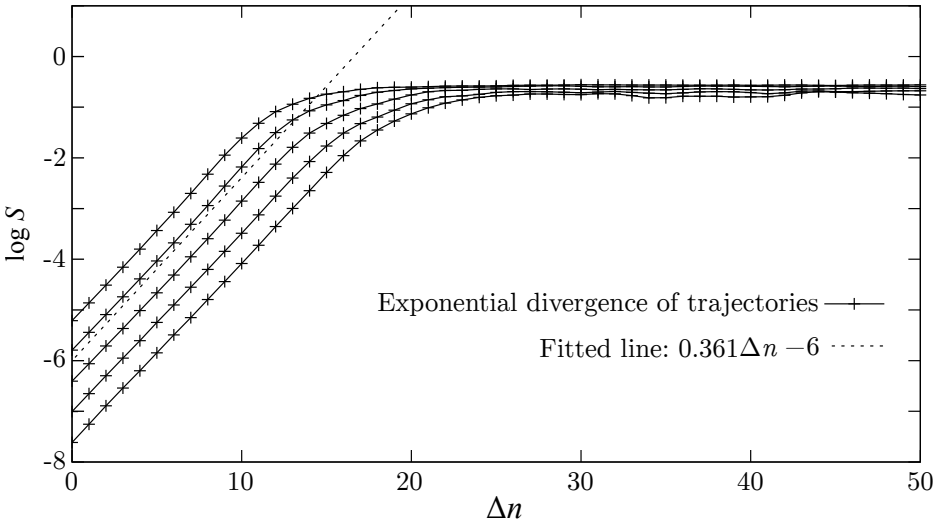

Figure 3.7: *Estimation of the Lyapunov exponent using TISEAN.*

The bifurcation software AUTO is capable of the continuation of bifurcation points in two parameters, as well. The bifurcations detected during the one-parameter bifurcation calculations – like the ones shown in Fig. 3.5 – provide starting points for this two-parameter analysis. The resulting bifurcation curves separate the domains of qualitatively different solutions. In Fig. 3.8, the $\xi - \zeta$ parameter plane is shown.

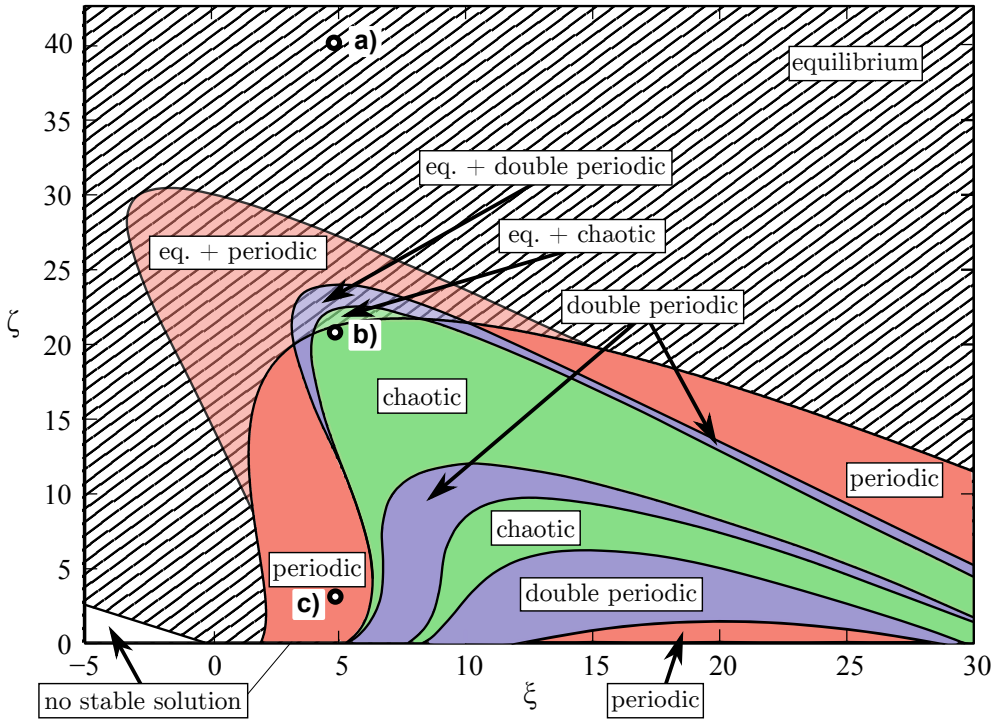

Figure 3.8: *Possible solutions in the $\xi - \zeta$ parameter plane. The parameter values at points a), b) and c) correspond to Figs. 3.2/a-c.*

As it can be seen, there are domains where different types of solutions coexist, and strips of double periodic orbits separate the found chaotic regimes. The boundaries of these latter domains were approximated by the period doubling bifurcation curves where four-periodic

solutions are born. It is worth mentioning that although the solutions have no physical meaning at negative values of the parameters, the structure of the parameter plane can be looked over more easily by extending the figure to include hypothetical parameter domains. Point a) in the equilibrium domain, point b) in the chaotic domain and point c) in the periodic domain correspond to the continuous, aperiodic, and lamellar chips shown in Figs. 3.2/a, 3.2/b and 3.2/c, respectively.

As the bifurcation diagram shows, there are parameter domains where a small change of a parameter or initial condition may lead to an abrupt change in the dynamics of chip formation, influencing the cutting process. This fact can be the explanation of certain unexpected phenomena, which are well-known by technology experts, when the type of chip formation suddenly changes, apparently without any external influence.

3.3 EFFECTS OF THE VIBRATIONS OF THE WORKPIECE

In the present section, the model described in Section 3.1.3 will be analysed, i.e., we consider the case of turning and take into account that the workpiece is elastic. As a consequence, it can perform vibrations that influence the cutting process according to Eqs. (3.12)-(3.16).

Three realistic technological examples are considered that correspond to the cases examined in Section 3.2. The system parameters of the model are $a = 0.3$, $b = 0.012$, $T_\Phi = 1$, $p = 1.03$. The cutting speed is $v_1 \equiv v_0 = 3.6$ m/s ($f_1 = 1$), leading to periodic solutions by the 4D model, and $\xi = 4.8$, $\eta = 4.4$, and $\zeta = 3.4$. The time scale is $K_0 = 1.64 \cdot 10^{-4}$ s. We examined the system at two additional cutting speeds, too. At $v_2 = 0.58$ m/s ($f_2 = 0.58/3.6 \approx 0.16$), we obtained chaotic, while at $v_3 = 0.3$ m/s ($f_3 = 0.3/3.6 \approx 0.083$) fixed point solutions.

Let the turned workpiece be a steel beam of size $\varnothing 40 \times 200$ mm, with $\tau_\Phi = 900$ MPa. The equivalent mass of this beam is approximately $m_r \approx 0,662$ kg, with stiffness $k \approx 9.42 \cdot 10^6$ N/m, and eigenfrequency $\nu \approx 600$ Hz. Using these values, the reference length is $\tilde{L} = 0.0732$ mm according to (3.11), while the dimensionless stiffness A and velocity V_0 in Eq. (3.16) are $A = 0.383$, and $V_0 = 8.07$ (see (B.25) and (3.17)). The initial conditions were chosen to be $\tau_2(0) = 1$, $T_0(0) = T_1(0) = T_2(0) = 0$, $z(0) = \dot{z}(0) = 0$, like in the case of the 4D model.

3.3.1 Change of the stable periodic solution of the 4D model

The solution of the oscillator model, described in Section 3.1.3, can be seen in Figs. 3.9 and 3.10 at the cutting speed $v_1 = 3.6$ m/s. The so-called principal cutting force – which is parallel with the cutting speed – can be obtained using (B.21): $F_v = 2\tau_\Phi = 1800$ N. The static deflection of the beam is $\tilde{L} z_{stat} = F_v k \approx 1.9 \cdot 10^{-4}$ m $= 0.19$ mm under this force. As it can be seen in Fig. 3.9/a, the initial amplitude of the evolving oscillations is $z \approx 2.2$, corresponding to $\tilde{L} z \approx 0.16$ mm. This value is a bit less than the static deflection. As it is clearly visible, the amplitude increases initially, but the dynamics becomes stationary at about $t = 2000$ (Figs. 3.9/b and 3.10/a). According to Fig. 3.10/a, the amplitude is approximately $z \approx 18.25$ in this state, that corresponds to very large deflections of 1.36 mm. Thus, the originally periodic process of chip formation may lead to harmful oscillations in the case of certain workpieces with critical geometry. This fact is well known in the engineering practice, so this result provides an evidence for the applicability of our model. The eigenfrequency $\nu = 600$ Hz of the workpiece and its harmonics are clearly visible in the

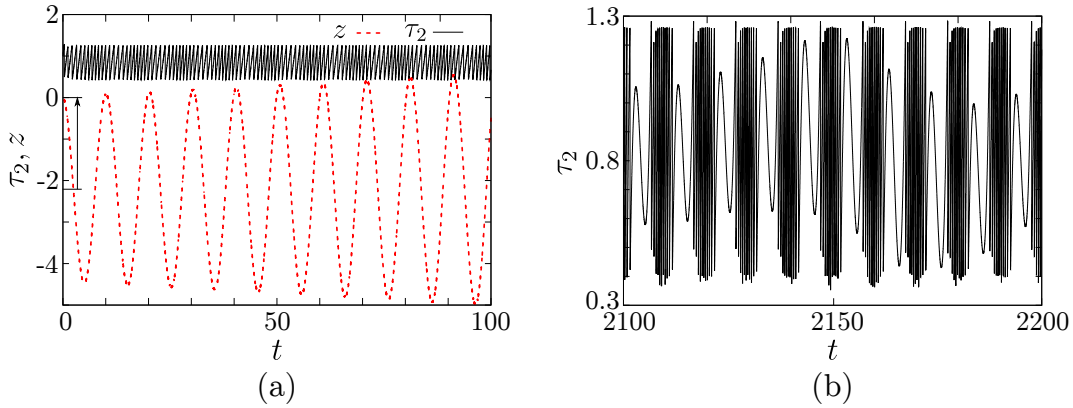

Figure 3.9: *Simulation results at $v_1 = 3.6$ m/s: (a) Increasing amplitudes, (b) Stationary oscillation of τ_2*

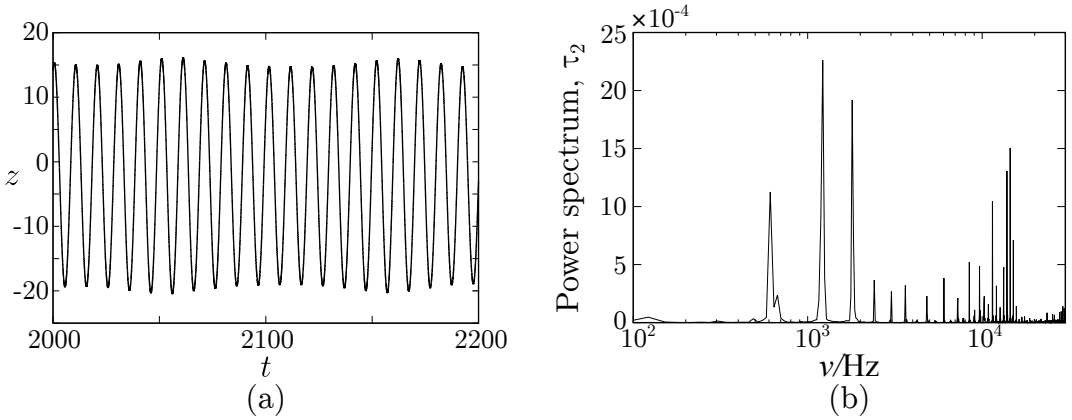

Figure 3.10: *Quasiperiodic oscillations (a) and the power spectrum (b) at $v_1 = 3.6$ m/s*

power spectrum of the oscillations (Fig. 3.10/b), together with other large peaks at about 12000 Hz. Thus, we conclude that the motion became quasiperiodic as the oscillations of the workpiece and the chip forming process superimposed. Note that the spectra of the other variables are similar, but the spectrum of τ_2 provided the most pronounced peaks. Although the horizontal axis was transformed to show the frequency in Hz, the vertical axis was kept dimensionless.

3.3.2 Change of the aperiodic (chaotic) solution of the 4D model

As it was shown in Section 3.2, the solution of the original 4D model is chaotic at the cutting speed $v_2 = 0.58$ m/s. We experienced chaotic behaviour during the initial part of the numerical simulation in the extended system, too, at $f_2 = 0.16$ (Fig. 3.11/a). There is still a peak in the spectrum at $\nu \approx 600$ Hz, but this is not dominant, and there are much more frequencies in the vibration than in the previous case (Fig. 3.11/b). To analyse the chaotic behaviour, we generated time series by numerical simulation and used the TISEAN software package [80, 91] to characterise the divergence of nearby trajectories. In the examined case, the phase-space is 6-dimensional with the variables τ_2, T_0, T_1, T_2, z, and $\dot{z}$. However, according to Takens' embedding theorem [152] if the delayed values of a single variable of a time series are considered – for example, the subsequent maxima of τ_2 – we can reconstruct the chaotic attractor in the phase-space of delayed coordinates so that it will be topologically similar to its original image in the real 6D phase space. To illustrate the phase-space reconstruction, we plotted a 2D projection of the reconstructed chaotic attractor in Fig. 3.12/a. The appropriate number

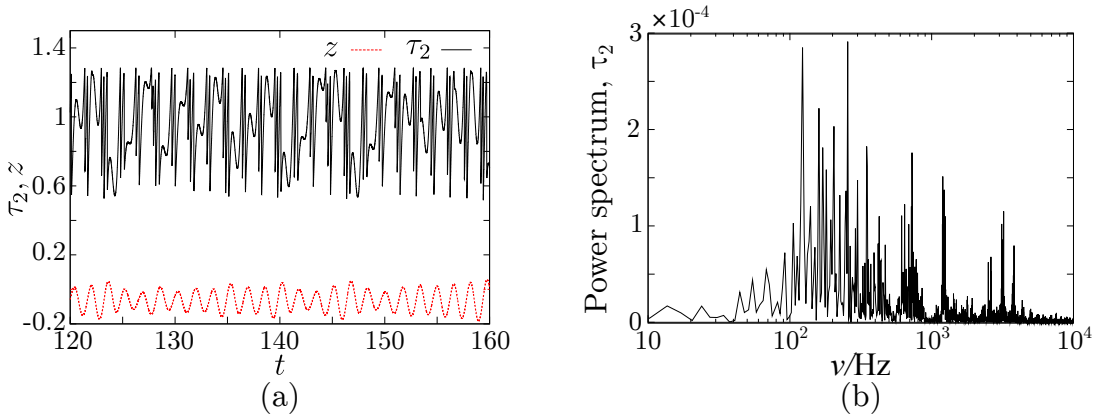

Figure 3.11: *Chaotic oscillations at $v_2 = 0.58$ m/s: (a) Time series, (b) Power spectrum*

of delayed coordinates – i.e., the embedding dimension m of the reconstructed phase-space – can be estimated by the so-called false nearest neighbours method [91]. In the considered case, we obtained $m \approx 10 \ldots 12$. These embedding dimensions were used to reconstruct the phase-space from the time series of τ_2, and to determine the maximal Lyapunov exponent. Plotting the logarithm of the average distance (separation, S) for several initial distances and embedding dimensions $m = 10, 11, 12$ against the number of iteration steps, the Lyapunov exponent can be estimated as the slope of the linear parts of the curves (Fig. 3.12/b). Since

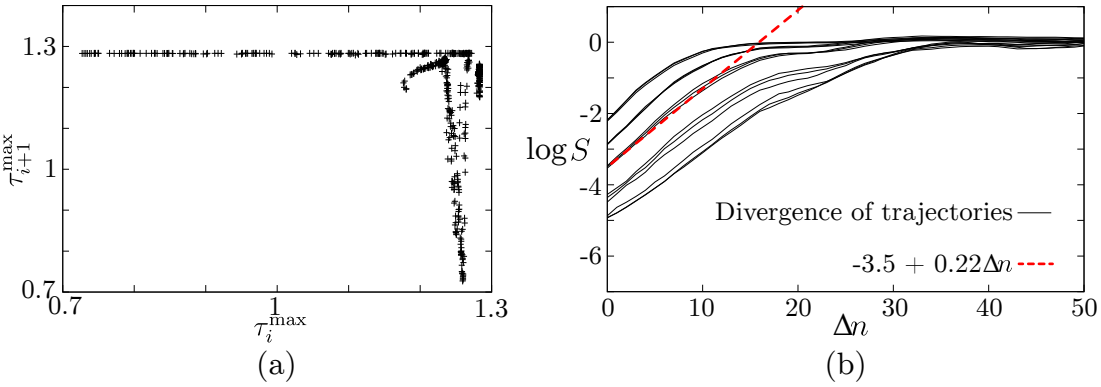

Figure 3.12: *Time series analysis of the chaotic part of the signal at $v_2 = 0.58$ m/s: (a) A projection of the attractor, (b) Estimation of the Lyapunov exponent*

the distance of two trajectories cannot be larger than the size of the attractor, this is why a saturation can be observed in the figure. Averaging the estimated slopes of the linear parts of the curves, we obtained 0.22. The time step was 0.0005 during the simulation, there were on average 930 steps between two maxima of τ_2, and the time scale was $K_0/f_2 = 1.025 \cdot 10^{-3}$ s. Thus, the Lyapunov exponent is $\lambda \approx 0.22/(0.0005 \cdot 930 \cdot K_0/f_2) = 462$ 1/s. Since both the linear parts of the curves and the saturation are clearly visible in Fig. 3.12/b, we can claim that the examined solution is chaotic during the first part of the simulation. However, later this chaotic state comes to an end as Fig. 3.13/a shows. The eigenfrequency $\nu \approx 600$ Hz becomes dominant after $t \approx 1000$ in the spectum (see Fig. 3.13/b), and there is another high peak, too. Consequently, the chaotic motion switches to quasiperiodic vibration, i.e., we found transient chaotic behaviour. Note that since the stiffness parameter A usually increases during the cutting process, we examined the behaviour of the system at larger values of A, too. According to our experiences, the mean lifetime of transient chaos decreases as parameter A is increased. Moreover, at sufficiently large stiffnesses the final solution becomes an equilibrium, instead of a quasiperiodic vibration.

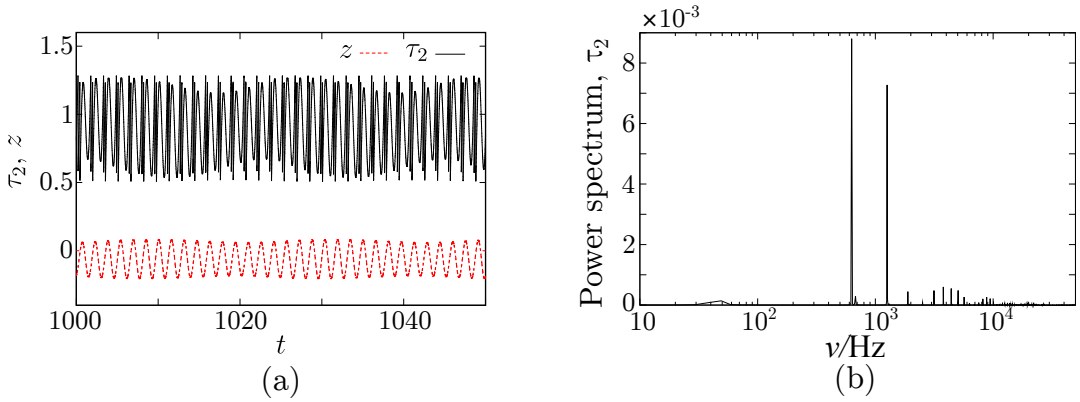

Figure 3.13: *Quasiperiodic vibrations after the chaotic part of the motion, at $v_2 = 0.58$ m/s: (a) Time series of τ_2 and z, (b) Power spectrum*

3.3.3 Change of the equilibrium solution of the 4D model

At the cutting speed $v_3 = 0.3$ m/s, the steady-state solution of the 4D model was an equilibrium. However, we observed aperiodic vibrations in the extended model with $f_3 = 0.083$. The deflection-time diagram can be seen in Fig. 3.14, showing that the real vibration amplitudes $\tilde{L}z$ are in the order of microns. To characterise these vibrations, we applied

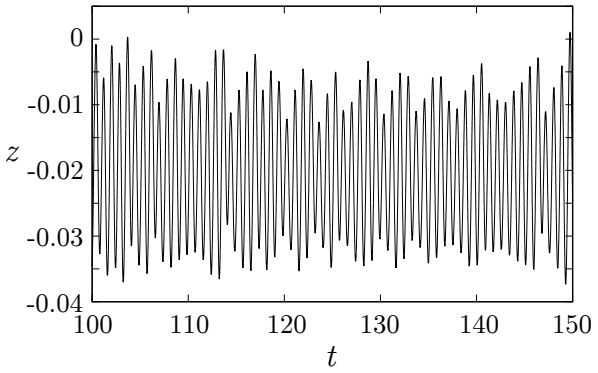

Figure 3.14: *Deflection-time diagram at $v_3 = 0.3$ m/s*

nonlinear time series analysis. We determined the minima of τ_2 and plotted its subsequent values in Fig. 3.15/a. The embedding dimension is $m \approx 8 \ldots 9$, according to the false nearest neighbours method. The divergence of trajectories is shown in Fig. 3.15/b. The slope of the linear part of the curves is approximately 0.17. The time step was 0.0005 during the simulation and the average number of steps between two minima was 507.4 at the time scale $K_0/f_3 = 1.97 \cdot 10^{-3}$ s. Thus, the real value of the Lyapunov exponent is $\lambda \approx 0.17/(0.0005 \cdot 507 \cdot K_0/f_3) = 340$ 1/s. It means that *a chaotic, but small amplitude unevenness occurs on the profile of continuous chips*, as it often found in the practice.

Note that it may also happen that the effective cutting speed $v_{\text{eff}} = fv_0 - \dot{z}$ drops to zero or – hypothetically – to negative values due to the high frequency vibration of the workpiece. In these cases the cutting process becomes interrupted and the tool leaves the workpiece. This process may lead to impacts and other undesired effects that are not discussed here.

We found that the detachments of the tool and the workpiece are typically short, but lead to very large variations in the stresses. Fig. 3.16 depicts the pattern on the (A, f) parameter plane where the aforementioned phenomenon was detected by numerical simulation within 6000 dimensionless time steps. In the cases analysed in this section, the effective cutting speed was always positive.

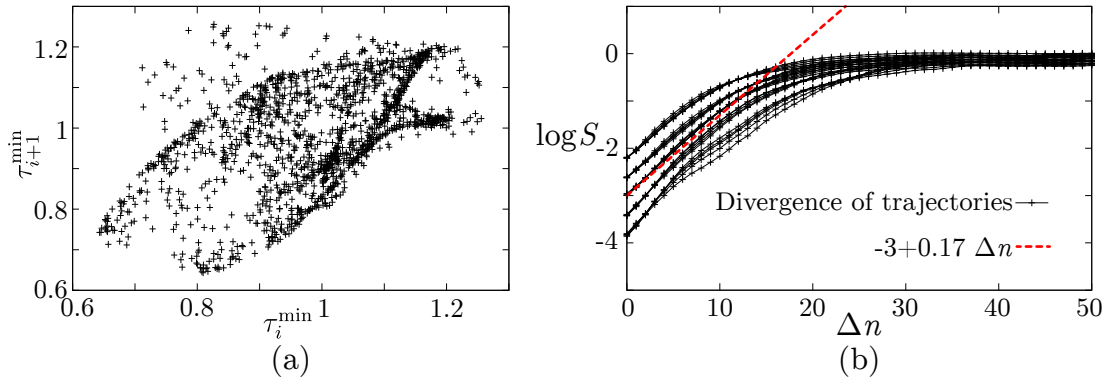

Figure 3.15: *Time series analysis of the chaotic part of the signal at $v_3 = 0.3$ m/s: (a) A projection of the attractor, (b) Estimation of the Lyapunov exponent.*

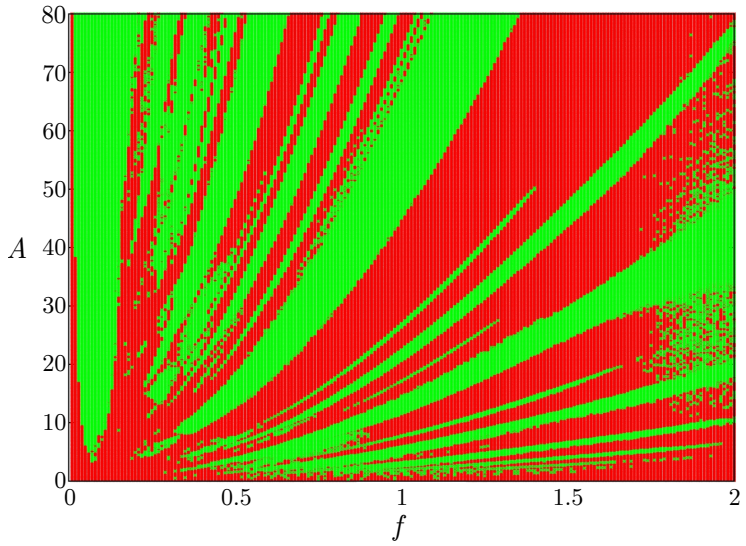

Figure 3.16: *The effective velocity was always positive in the green parameter domains, while interrupted cutting was detected in the red regions.*

3.4 ANALYSIS OF THE EFFECT OF BUE ON CHIP FORMATION

This section is devoted to the analysis of the delayed chip formation model – described in Section 3.1.4 –, that takes the effect of the periodic formation and breaking of the built-up edge into account during turning.

3.4.1 Numerical simulation

We performed numerical simulation of the model defined by Eqs. (3.19), (3.20), (3.23), (3.26) and (3.22). These equations were applied as follows: only the shear stress could change in the initial interval $\hat{t} = 0 \dots \delta\hat{t}$, according to (3.26), with initial condition $\hat{\tau}(0) = 0$. This part of the solution corresponds to the formation of the deformation band. The other three variables remain zero in this period: $\hat{T}_0(\hat{t}) = 0$, $\hat{T}(\hat{t}) = 0$, $\hat{\gamma}(\hat{t}) = 0$. For times $\hat{t} > \delta\hat{t}$, the solution previously obtained for the shear stress provides the time history for the delayed differential equations.

The used parameters correspond to Pálmai's experiments, described in Appendix B.4.2. The experimental material was soft steel – its chemical composition is given in Table B.1.

The physical and mechanical properties of the chips can be characterised by the following set of dimensionless parameters: $a = 0.3$; $b = 0.012$; $n = 0.2$; $T_\Phi = 1.2$; $\varepsilon_\Phi = 2.44$. The cutting speed, feed rate, rake angle, approach angle, shear angle and speed of the chip assumed the values $v = 0.5$ m/s, $f_{\text{feed}} = 0.3$ mm/rev, $\alpha = 6^o$, $\kappa_r = 0^o$, $\phi = 25.7^o$ and $v_{\text{chip}} = 0.23$ m/s, respectively. Consequently, the dimensionless technological parameters are $\delta\hat{t} = 0.4$, $\eta = 4$, and $\zeta = 30$. The parameters describing the formation of BUE were chosen to be $H = 0.1$ and $\Omega = 0.18$. We found that the solution of the set of differential equations quickly tends to

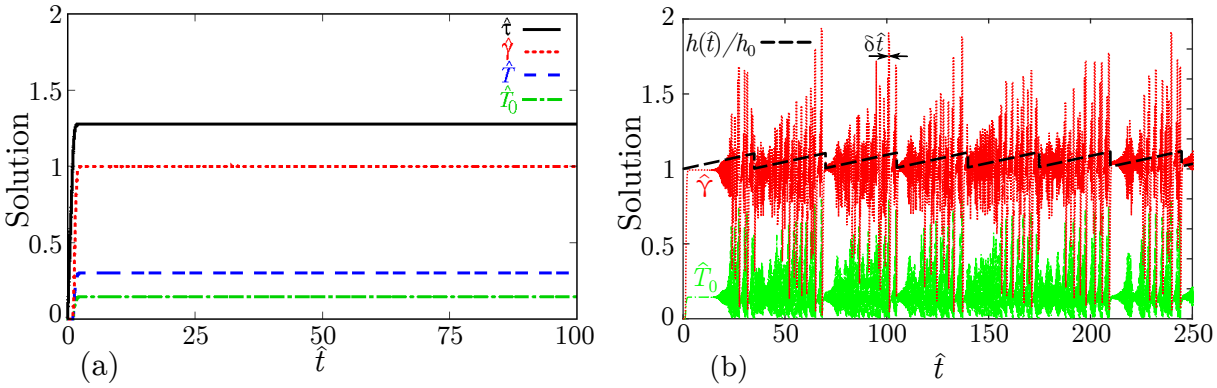

Figure 3.17: *Solution curves without (a) and with (b) built-up edge.*

an equilibrium point (Fig. 3.17/a) if the formation of BUE is not taken into account, i.e., if $H = 0$. However, the response becomes chaotic in the opposite case. Fig. 3.17/b shows the first few periods of the formation of the BUE, where $h(\hat{t})/h_0 = \left[1 + Hf_1(\hat{t})\right]$ (see (3.24)).

As depicted in Fig. 3.17/b, the effect of the excitation with period $2\pi/\Omega \approx 34.9$ is clearly visible on the solution curves. There is an irregular oscillation with increasing amplitude at the beginning of each period that finally leads to extremely large deformations. According to numerical evidence, the duration of the extremal deformations is just equal to the delay time $\delta\hat{t}$ – this is the time period that is spent by the material of the workpiece in the shear zone. The variables return near to their equilibrium value at the end of each cycle.

3.4.2 Nonlinear analysis of the solutions

To show that the solutions are indeed chaotic, we applied two different numerical procedures for the determination of the largest Lyapunov exponent. The main difficulties with delay-differential equations (DDE) are originated from the fact that the phase-space of these equations is infinite dimensional. We used a special procedure that was developed by Farmer [60] in order to determine a finite dimensional approximation of the Lyapunov spectrum. For the application of the method, we rewrote the set of differential equations to a high-dimensional map, according to the Euler integration scheme. The time step was chosen to be $\Delta\hat{t} = \delta\hat{t}/N$ (where $\delta\hat{t}$ is the delay), and the state of the system was approximated by N samples from the interval $[\hat{t}, \hat{t} - \delta\hat{t}]$:

$$\begin{aligned}\mathbf{x} = [x_1, x_2, \ldots, x_{4(N+1)}] = &[\hat{\tau}(\hat{t}), \hat{\tau}(\hat{t} - \Delta\hat{t}), \ldots, \hat{\tau}(\hat{t} - N\Delta\hat{t}),\\ &\hat{T}_0(\hat{t}), \hat{T}_0(\hat{t} - \Delta\hat{t}), \ldots, \hat{T}_0(\hat{t} - N\Delta\hat{t}),\\ &\hat{T}(\hat{t}), \hat{T}(\hat{t} - \Delta\hat{t}), \ldots, \hat{T}(\hat{t} - N\Delta\hat{t}),\\ &\hat{\gamma}(\hat{t}), \hat{\gamma}(\hat{t} - \Delta\hat{t}), \ldots, \hat{\gamma}(\hat{t} - N\Delta\hat{t})].\end{aligned} \tag{3.35}$$

To partially determine the Lyapunov spectrum, the evolution of the so-called orthogonal initial separation vectors $\mathbf{\Delta x}_i$, $i = 1, \ldots, 4(N + 1)$ was also followed by the algorithm,

according to the variational equation

$$\frac{d}{d\hat{t}}\mathbf{\Delta x}_i = \mathbf{J}\mathbf{\Delta x}_i, \quad i = 1, ..., 4(N+1), \tag{3.36}$$

where $\mathbf{J}$ denotes the Jacobian matrix of the discretized differential equations. By rewriting Eq. (3.36) according to the Euler scheme, one obtains another high-dimensional map. To apply the method, the $4(N+1)$-dimensional map describing the evolution of the system and the $4^2(N+1)^2$-dimensional map describing the evolution of the elements of the separation vectors are iterated simultaneously. These latter vectors must be renormalized after a couple of iteration steps using the Gram-Schmidt orthogonalization procedure. The individual Lyapunov exponents can be determined as the rate of stretching of the separation vectors.

The practical application of the method is rather difficult since the time step is $\Delta\hat{t} = \delta\hat{t}/N$; thus, the shorter the stepsize, the larger the dimension of the problem. Moreover, Eqs. (3.19), (3.20), (3.23) and (3.26) form a stiff and piecewise smooth set of differential equations. We implemented the algorithm in Matlab and divided the time intervals of length $\Delta\hat{t}$ into even smaller intervals using a 3$^{\text{rd}}$ order variable stepsize Runge-Kutta integration scheme for the evaluation of the system's state. Several different values of parameter N were applied. The Gram-Schmidt procedure was performed after $GS = 10 \dots 60$ iteration steps. We found that this latter parameter did not have significant influence on the results. Since the algorithm provided an approximation of the Lyapunov spectrum λ_i, the so-called Kaplan-Yorke dimension could also be determined [60]:

$$D_{KY} = j + \frac{\sum_{i=1}^{j}\lambda_i}{|\lambda_{j+1}|}, \tag{3.37}$$

where j is the largest integer for which $\lambda_1 + \dots \lambda_j \geq 0$, if the exponents are arranged in a decreasing order.

The results of the calculations are listed in Table 3.2. As Fig. 3.18 shows, the value of the largest Lyapunov exponent tends to $\lambda_1 \approx 2.8$ if $N = 120$. Moreover, the system is hyper-chaotic, since even the second Lyapunov exponent is positive: $\lambda_2 \approx 0.9$. The examination of the case $N = 120$ required the simultaneous solution of 484 differential equations for each of the 484 separation vectors. Consequently, the computation took weeks. Since our goal was merely to show that the system was chaotic, we did not run further simulations for the more exact determination of the maximal Lyapunov exponent.

N	GS	λ_1	λ_2	D_{KY}	time
10	11	4.76	1.93	3.65	1000
20	10	4.49	1.60	3.64	1000
40	20	3.72	1.48	3.60	690
60	30	3.43	1.32	3.51	315
100	40	2.96	1.04	9.03*	555
120	60	2.81	0.9	5.15*	132

Table 3.2: *The two largest Lyapunov exponents, the Kaplan-Yorke dimension and the duration of simulation in dimensionless time. (*: Slow convergence, unreliable result.)*

The calculation of the Kaplan-Yorke dimension provided less precise results due to the rather slow convergence of the smaller Lyapunov exponents. The convergence was especially slow in the case $N = 100$. We partially overcame this problem by tuning the initial stepsize

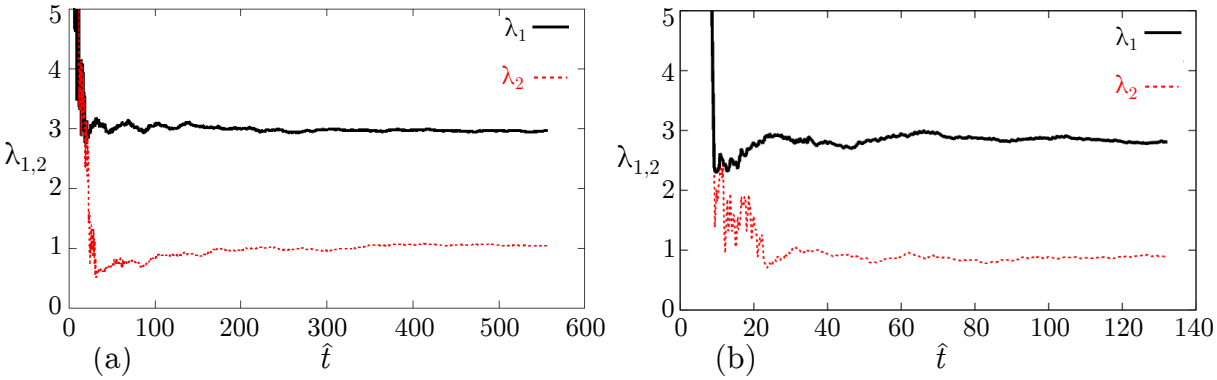

Figure 3.18: *The convergence of the two largest Lyapunov exponents. (a) $N = 100$, (b) $N = 120$.*

of the Runge-Kutta integration in the case $N = 120$. In summary, we can claim that the dimension of the attractor is finite, since $D_{KY} < 6$.

Although Farmer's method seemed to be applicable for the examined set of stiff, piecewise smooth differential equations, we checked our results with another procedure, too. Stefanski, Kapitaniak and Dabrowski [147, 148] developed an algorithm that is capable of the determination of the largest Lyapunov exponent of piecewise smooth delayed systems. This method is based on the synchronization of the identical systems $\dot{\mathbf{x}} = \mathbf{f}(\mathbf{x}(t), \mathbf{x}(t-\tau))$ and $\dot{\mathbf{y}} = \mathbf{f}(\mathbf{y}(t), \mathbf{x}(t-\tau))$, by a feedback mechanism:

$$\dot{\mathbf{x}} = \mathbf{f}(\mathbf{x}(t), \mathbf{x}(t-\tau)) + \mathbf{Q}(\mathbf{y}(t) - \mathbf{x}(t)), \tag{3.38}$$

$$\dot{\mathbf{y}} = \mathbf{f}(\mathbf{y}(t), \mathbf{x}(t-\tau)). \tag{3.39}$$

where $\mathbf{Q} = \mathrm{diag}[q, q, \ldots, q] \in \mathbb{R}^k$ and $\mathbf{x} \in \mathbb{R}^k$, $\mathbf{y} \in \mathbb{R}^k$, if the set of equations comprises k equations. The synchronization occurs when q is greater than the greatest Lyapunov exponent. In order to apply the method, we numerically integrated the set of Eqs. (3.19), (3.20), (3.23) and (3.26), coupled to an identical system and varied the value of q according to the bisection method. If the systems synchronized (i.e., the difference between the variables became negligible) in the interval $0 < \hat{t} < 300$, the value of q was reduced. Otherwise, it was increased. The threshold value of the coupling coefficient provided an estimate for the largest Lyapunov exponent: $\lambda_1 \approx 2.78$. The obtained value is quite close to the Lyapunov exponent calculated by Farmer's method.

3.5 CHIP FORMATION WITH SURFACE REGENERATION EFFECT

Pálmai's 4D chip formation model (Eqs. (3.19), (3.20), (3.23), (3.26), and (3.22)) was combined with the traditional linear orthogonal turning model in the framework of a joint work **[74]**. This latter model takes the surface regeneration effect into account: besides the feed per revolution h_0, the actual chip thickness $h(t)$ depends also on the difference of the actual and one period earlier position of the tool: $h(t) = h_0 - x(t) + x(t-\tau)$. Here τ denotes the time delay, i.e., the period of spindle rotation.

Expressing the cutting coefficient by the shear stress τ_2 at the root of the chip, one obtains the following delay-differential equation in dimensionless form, with the time scaled by the angular natural frequency ω_n of the tool:

$$\ddot{x}(t) + 2\kappa\dot{x}(t) + x(t) = \tau_2(t)(h_0 - x(t) + x(t-\tau)), \tag{3.40}$$

where κ is the damping ratio. According to (3.2), the timescale K used in the chip formation model depends on the actual chip thickness $h(t)$, providing a coupling between the two models. To match the temporal scaling of these models, the right-hand side of each differential equation in Pálmai's model was divided by $K(h(t))\omega_n$.

As Fig. 3.19/a shows, the shear stress is constant at low feed rates, corresponding to the formation of continuous chips without meaningful dynamical phenomena. However,

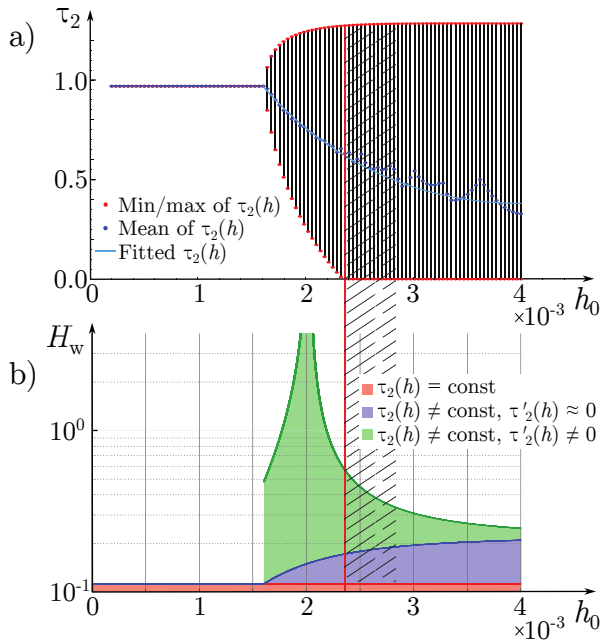

Figure 3.19: *(a) Minimum, maximum and average values of τ_2 (b) Domains of stability*

segmented chips are formed at higher feed rates. In this case, the oscillation of the shear stress is several orders of magnitudes faster than the motion of the tool. Thus, it was sufficient to use the average value of τ_2 to reveal the effects of the periodic chip formation dynamics on the stability of the turning process.

The results of the stability calculation are depicted in Fig. 3.19/b on the parameter plane of feed h_0 and dimensionless chip width H_w. The red domain of stability corresponds to $\tau_2(h) = \text{const}$, i.e., when the chip formation dynamics is neglected. The blue domain was obtained using the coupled system of equations, but the term $\partial\tau_2(h)/\partial h_0$ was neglected in the characteristic equation of (3.40). The consideration of this term led to a further increase of the domain of stability, shown in green colour. It is important that these results are valid only if the shear stress is positive – see the red boundary line in the figure.

In summary, it was found that in case of chip segmentation the increase in chip thickness may lead to the reduction of both the average shear stress in the shear layer and the cutting force. Moreover, the segmentation radically improves the stability properties of the turning process according to this simple model.

Chapter 4

Micro-Chaos in Digitally Controlled Systems

4.1 INTRODUCTION AND LITERATURE REVIEW

Parallel with the fast development of computer technology, more and more commercial products are operated using digital control loops. For the design of these devices, engineers must take into account that the stability properties of digital and analog control systems are different due to the so-called digital effects (see e.g., [81]). The main digital effects are sampling, processing delay and quantization. *Sampling* means that the control system receives data about the measured state variables periodically, according to a certain sampling period. Since some time is necessary to compute the control feedback, the *processing delay* between signal measurement and control effort output is unavoidable. The signals measured by sensors are often represented in a finite amount of bits, just like the numbers in digital processors. The corresponding limited precision leads to *rounding (or quantization)* in calculations.

The consideration of sampling and delay during the design of control systems is a routine tasks among electrical engineers. Still, digital control systems often exhibit strange, irregular behaviour [24, 50, 104]. The occuring small amplitude vibrations are usually considered as stochastic noise in practice [166], however, as we will see, their source may be deterministic chaotic dynamics, due to the quantization.

The stochastic approach to quantization can be traced back to the seminal work of Widrow [165], who described the phenomenon in the frequency domain. Bertram [13] focused on the upper bound – the so-called Bertram bound – of the quantization error. It is calculated as the sum of the responses to unit impulses at the inputs of the system, multiplied by the maximum error in one quantizing operation. Bertram's calculation was improved later by several researchers, e.g., [4, 144, 146]. The chaotic nature of the quantization-induced vibrations was unclear to the researchers until the end of the 1980s, when Ushio and Hsu [162] showed that output quantization may lead to chaos.

In the present chapter, we will supplement the literature results in three areas:

1. analysis of transient chaotic solutions of digitally controlled systems,
2. exploration of their phase-space structure, and
3. development of advanced numerical methods for the analysis of the global dynamics.

On the following pages, simple models of digitally controlled mechanical systems will be analysed, where both the mechanical model and the control scheme are linear, and the desired state of the uncontrolled system is unstable. We consider full-state feedback systems

with sampling period τ. It is assumed that the control force $\mathbf{u}$ is kept constant between two successive sampling instants $t_j \equiv j\tau$ and $t_{j+1} \equiv (j+1)\tau$, according to the so-called zero-order hold scheme (Fig. 4.1).

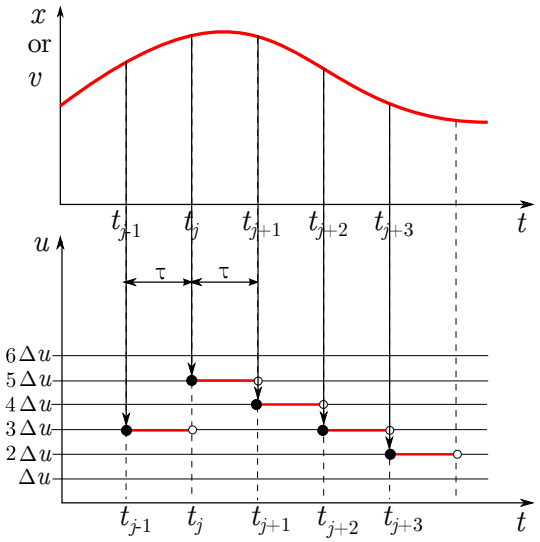

Figure 4.1: *Sample and hold (or zero-order hold) control scheme with negligible processing delay and quantized, scalar-valued control force u.*

The control effort may depend also on earlier values of the state variables. For example, the speed is often expressed by the actual and delayed values of the displacement, using a difference scheme. The corresponding processing delay is an integer multiple of the sampling period in the general formulas of Section 4.2, but the multiplier will be 0 (neglected processing delay) or 1 in the examples discussed in this chapter.

The notion of micro-chaos was introduced by George Haller and Gábor Stépán [78]. They found that digital control leads to small amplitude chaotic vibrations during the sliding motion of a block if the contact is characterised by Stribeck friction. The velocity x_j of the block was described by a one-dimensional map – a so-called *micro-chaos map*:

$$x_{j+1} = a\, x_j - b\, \mathrm{Int}(x_j), \qquad j = 1, 2, \ldots, \tag{4.1}$$

where the Int() function rounds towards the origin, representing the effect of quantization. The fixed points $x^*_m = x_j = x_{j-1}$ of the map can be determined by the following formula:

$$x^*_m = \frac{bm}{a-1}, \quad \text{if} \quad 0 \le m \le x^*_m < m+1 \quad \text{or} \quad 0 \ge m \ge x^*_m > m-1, \tag{4.2}$$

where m stands for the integer part of x^*_m. If $0 \le m \le x^*_m < m+1$ or $0 \ge m \ge x^*_m > m-1$ do not fulfil, the corresponding point x^*_m is a *virtual* fixed point, i.e., its calculated value does not correspond to a valid equilibrium position.

Fig. 4.2 illustrates the graph of the map with the cobweb diagram of a trajectory. The graph consists of an infinity of small line sections in the intervals defined by the integer numbers. If $a > 1$, the fixed points are unstable. However, on large scales, we see that the trajectories tend to the neighbourhood of the origin, provided that $|a - b| < 1$. This locally unstable, but globally stable behaviour is the source of chaos. The concepts behind this simple model can be extended to other areas of science, too. For example, similar models were introduced in population dynamics [114] and neurology [21].

It follows from the proof in [78] that the 1D micro-chaos map (4.1) is chaotic in Devaney's sense [52]: there exists an attracting set that is topologically transitive under the application

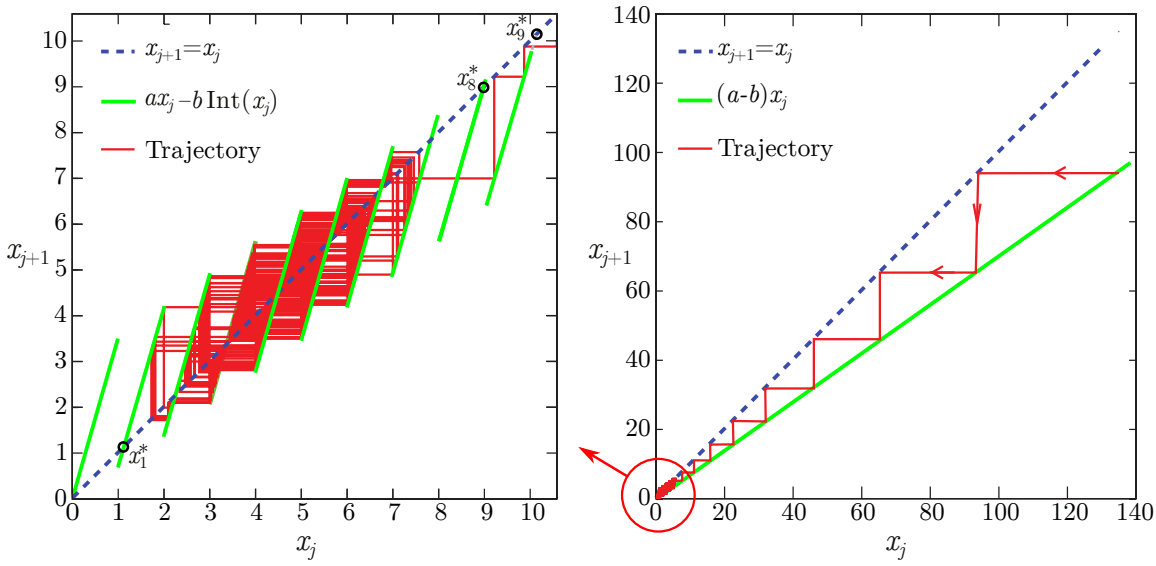

Figure 4.2: *Graph of the micro-chaos map (4.1) at $a = 3.5$ and $b = 2.8$. All the regular fixed points are shown for positive x values. $x_8^* = 8.96$ (regular fixed point), but $x_9^* = 10.08 > 10$ (virtual fixed point).*

of the map, there exists an infinity of periodic orbits that are dense in the set, and the system's behaviour sensitively depends on the initial conditions.

As it will be shown in Section 4.2, it is straightforward to prove in the general, finite-dimensional case that there exists a finite size absorbing sphere – global attractor – in the phase-space of the micro-chaos maps. Moreover, if an unstable equilibrium is to be stabilized by the control, the largest Lyapunov exponent is positive, corresponding to the sensitive dependence on initial conditions. However, the proof of topological transitivity and the existence of an infinity of unstable periodic orbits is usually rather difficult. There are a few examples for proof of chaos in similar, higher dimensional systems [9, 70, 116, 161, 171, 172], but these proofs were typically performed by computers, using interval-arithmetic.

Stépán's PhD student, Enikov attempted to give an analytical proof of chaos in the case of a 3D micro-chaos map [58]. Although the proof is incomplete, the introduced formalism and certain results proved to be useful during the further analysis of micro-chaos maps.

Certain micro-chaos maps exhibit transient chaos: an escaping route opens on the chaotic attractor that turns to a repeller set. The chaotic oscillations disappear suddenly [44, 155] when the trajectory leaves the repeller, provided that it does not tend to another strange set. The probability that a trajectory has not yet escaped from the repeller decays exponentially in time, and the exponent κ is called *escape rate*. The mean number of iteration steps before the trajectories escape from the repeller – the escape number $\bar{N}_{esc}$ that characterises the settling time of the control system – is approximately the reciprocal of the escape rate: $\bar{N}_{esc} \approx 1/\kappa$. However, it was shown in **[35]** that the accurate relation can be formulated as

$$\bar{N}_{esc} = \frac{\sum_{n=1}^{\infty} n e^{-\kappa n}}{\sum_{n=1}^{\infty} e^{-\kappa n}} = \frac{1}{1 - e^{-\kappa}}. \tag{4.3}$$

We developed a recursive method for the exact calculation of $\bar{N}_{esc}$ in the case of a 1D piecewise linear micro-chaos map **[34]**, and this lifetime estimation method was extended to a 2D case, too **[36]**. Although these methods provide exact results, their application is very complicated and requires the detailed analysis of the dynamical system.

To facilitate the discussion of the micro-chaos phenomenon, two general forms of the micro-chaos maps are introduced in Section 4.2, and certain general properties of these

maps are pointed out. After that, specific micro-chaos maps are analysed.

Section 4.3 deals with a 1D transient chaotic micro-chaos map. A lifetime estimation method is introduced that is based on the fractal dimension of the repeller **[33, 35]**. If one takes into account a processing delay that is just equal to the sampling period, the micro-chaos map becomes two-dimensional, but the attractors can be covered by one-dimensional sets. The proof of chaos is presented for this map in Section 4.4, following **[38]**. Note, that a similar 2D map was introduced in [69] as a model of hysteresis. In Section 4.5, a detailed proof of chaos is given for another 2D micro-chaos map – a model of a PD controlled linear oscillator **[42]**. The examined map is a *multi-baker map*, i.e., its phase-space structure is composed of neighbouring baker's maps. As a consequence of this property, several small disconnected strange attractors may coexist far from the desired state of the system, showing that the digital effects can have a significant influence on the control error **[43]**.

The discovery of disconnected attractors revealed that the thorough exploration of the phase-space requires a numerical method which is capable of extending its domain of examination. This is why we developed the so-called Clustered Simple Cell Mapping method in the framework of a joint work with Gergely Gyebrószki **[72]** – see Section 4.6.

Finally, certain further results related to the micro-chaos phenomenon are summarized in Section 4.7, based also on the cooperation with Gergely Gyebrószki **[75, 76, 77]**.

4.2 PROPERTIES OF MICRO-CHAOS MAPS

4.2.1 Generalization of the micro-chaos concept

The behaviour of periodically sampled systems can be described by discrete maps. If there is *no quantization and no delay*, and both the model of the mechanical system and the control scheme are linear, the general form of these maps is

$$\left.\begin{aligned}\mathbf{x}_{j+1} &= \mathbf{A}\mathbf{x}_j + \mathbf{B}\mathbf{u}_j \\ \mathbf{u}_j &= \mathbf{K}\mathbf{x}_j\end{aligned}\right\} \quad \Rightarrow \quad \mathbf{x}_{j+1} = (\mathbf{A}+\mathbf{B}\mathbf{K})\,\mathbf{x}_j \equiv \mathbf{S}\mathbf{x}_j, \tag{4.4}$$

where $\mathbf{x}_j \in \mathbb{R}^n$ denotes the state vector at the jth sampling instant, $\mathbf{A} \in \mathbb{R}^{n\times n}$ and $\mathbf{B} \in \mathbb{R}^{n\times l}$ are the coefficient matrices, $\mathbf{u} \in \mathbb{R}^l$ is the vector of control signals and $\mathbf{K} \in \mathbb{R}^{l\times n}$ is the matrix of feedback gains. We consider systems whose $\mathbf{y} = \mathbf{0}$ state is unstable without control, thus, at least one of the eigenvalues of matrix $\mathbf{A}$ is outside the unit circle on the complex plane. If the *delayed values* of the state are also used by the control system, we distinguish between the physical state vector $\mathbf{x}_j$ of coordinates and velocities, and the extended state vector $\mathbf{y}_j$ that is built up of the actual and earlier values of $\mathbf{x}_j$. As it is shown in Appendix C.1, the map assumes the same form in this case, too:

$$\mathbf{y}_{j+1} = \mathbf{S}\mathbf{y}_j, \tag{4.5}$$

where we kept the same notation for the coefficient matrix $\mathbf{S}$, to highlight that it assures the *stabilization* of the state $\mathbf{y} = \mathbf{0}$, i.e., the moduli of its eigenvalues are less than one.

Linear systems cannot exhibit complicated behaviour, so we examine cases where the *quantization* is the source of nonlinearity. There are basically two analog-digital transformations during the operation of a control system: on the one hand, the state of the system is measured – this will be considered as the input of the control system – and the measured values are quantized. On the other hand, the calculated control signal – the output – can assume also only a finite number of values. While certain results about the input quantization and the so-called twofold quantization are discussed in Sections 4.3, 4.7 and Appendix

C.2, this thesis focuses on the effects of *output quantization*. Thus, the rounding during the measurement of state variables is neglected compared to the rounding of the control effort signal. For example, this assumption is valid in case of an Arduino Mega microcontroller that has 8-bit Pulse Width Modulation (PWM) resolution, while 12-bit analog-to-digital resolution is achievable by oversampling.

The elements of the calculated control vector $\mathbf{u}_j = [u_{1j} \quad u_{2j} \quad \dots \quad u_{lj}]^T$ can be quantized with different resolution values. In this case, the diagonal matrix

$$\mathbf{R}_O = \mathrm{diag}[r_{O1} \quad r_{O2} \quad \dots \quad r_{Ol}] \tag{4.6}$$

contains the values of the resolutions for the l control effort signals. Each signal must be an integer multiple of the corresponding resolution value. It is shown in Appendix C.2.1 that if d delayed values of the state are taken into account in the control effort as

$$\mathbf{u}_j = \mathbf{K}_0\mathbf{x}_j + \mathbf{K}_1\mathbf{x}_{j-1} + \cdots + \mathbf{K}_d\mathbf{x}_{j-d}, \tag{4.7}$$

the evolution of the extended state vector $\mathbf{y}_j = [\mathbf{x}_j \ \mathbf{x}_{j-1} \ \dots \ \mathbf{x}_{j-d}]^T$ can be formulated as

$$\mathbf{y}_{j+1} = \mathbf{A}^+\mathbf{y}_j + \mathbf{b}_j^+. \tag{4.8}$$

However, this formula can be rewritten as

$$\mathbf{x}_{j+1} = \mathbf{A}\mathbf{x}_j + \mathbf{B}\mathbf{R}_O\mathbf{Int}\left(\mathbf{R}_O^{-1}\sum_{i=0}^{d}\mathbf{K}_i\mathbf{x}_{j-i}\right) \equiv \mathbf{A}\mathbf{x}_j + \mathbf{B}\mathbf{R}_O\begin{bmatrix} m_{j1} \\ m_{j2} \\ \vdots \\ m_{jn} \end{bmatrix} \equiv \mathbf{A}\mathbf{x}_j + \mathbf{b}_j, \tag{4.9}$$

where the function $\mathbf{Int}\colon \mathbb{R}^l \to \mathbb{Z}^l$ is an element-wise integer part function, rounding the elements of the output towards zero. This function corresponds to the so-called mid-tread quantizer with double deadzones. Thus, the behaviour of the analysed systems can be described by piecewise affine maps (4.9) that will be referred to as *micro-chaos maps*.

If there is only one control signal, i.e., vector $\mathbf{u}_j$ is one-dimensional with resolution r_O, a single integer number m_j characterises the quantization at each sampling instant:

$$\mathbf{x}_{j+1} = \mathbf{A}\mathbf{x}_j + \mathbf{B}r_O\mathrm{Int}\left(r_O^{-1}\sum_{i=0}^{d}\mathbf{K}_i\mathbf{x}_{j-i}\right) \equiv \mathbf{A}\mathbf{x}_j + \mathbf{b}m_j, \tag{4.10}$$

where $\mathbf{b} = \mathbf{B}r_O$. According to Eq. (4.9), if the elements of the state vector are small (e.g., each element of $\mathbf{R}_O^{-1}\sum_{i=0}^{d}\mathbf{K}_j\mathbf{x}_{j-i}$ is less than one), the quantization can radically reduce the value of the intended control effort, while vector $\mathbf{b}_j$ becomes small compared to $\mathbf{A}\mathbf{x}_j$. Thus, the dynamics will be dominated by matrix $\mathbf{A}$, reflecting that the origin is locally unstable.

On the other hand, if the system's state is far from the origin, the effect of quantization is negligible. In these cases one may consider the quantization as a small perturbation to the non-quantized system. Thus, instead of adding the integer parts of the control terms to the state-space model of the uncontrolled system, it is possible to consider the controlled, non-quantized system and subtract the fractional parts of the control effort:

$$\mathbf{x}_{j+1} = (\mathbf{A} + \mathbf{B}\mathbf{K}_0)\,\mathbf{x}_j + \mathbf{B}\sum_{i=1}^{d}(\mathbf{K}_i\mathbf{x}_{j-i}) - \mathbf{B}\mathbf{R}_O\ \mathbf{F}_j, \tag{4.11}$$

where the vector of fractional parts $\mathbf{F}_j \in \mathbb{R}^l$ can be expressed as

$$\mathbf{F}_j = \mathbf{R}_O^{-1} \sum_{i=0}^{d} (\mathbf{K}_i \mathbf{x}_{j-i}) - \mathbf{Int}\left(\mathbf{R}_O^{-1} \sum_{i=0}^{d} (\mathbf{K}_i \mathbf{x}_{j-i}) \right). \tag{4.12}$$

These fractional parts do not influence considerably the behaviour of the system if the arguments of the **Int** function (i.e., the elements of $\mathbf{x}_{j-i}$) are large. Thus, the trajectories tend towards the origin in these cases. Reformulating the micro-chaos map as

$$\underbrace{\begin{bmatrix} \mathbf{x}_{j-(d-1)} \\ \vdots \\ \mathbf{x}_{j-1} \\ \mathbf{x}_j \\ \mathbf{x}_{j+1} \end{bmatrix}}_{\mathbf{y}_{j+1}} = \underbrace{\begin{bmatrix} \mathbf{0} & \mathbf{I} & \mathbf{0} & \dots & \mathbf{0} \\ \mathbf{0} & \mathbf{0} & \mathbf{I} & \dots & \mathbf{0} \\ \vdots & \vdots & \vdots & \ddots & \vdots \\ \mathbf{0} & \mathbf{0} & \mathbf{0} & \dots & \mathbf{I} \\ \mathbf{BK}_d & \mathbf{BK}_{d-1} & \dots & \mathbf{BK}_1 & \mathbf{A}+\mathbf{BK}_0 \end{bmatrix}}_{\mathbf{S}} \underbrace{\begin{bmatrix} \mathbf{x}_{j-d} \\ \vdots \\ \mathbf{x}_{j-2} \\ \mathbf{x}_{j-1} \\ \mathbf{x}_j \end{bmatrix}}_{\mathbf{y}_j} - \underbrace{\begin{bmatrix} \mathbf{0} \\ \mathbf{0} \\ \vdots \\ \mathbf{0} \\ \mathbf{BR}_O\mathbf{F}_j \end{bmatrix}}_{\mathbf{c}_j} \tag{4.13}$$

we see that the neighbourhood of the locally unstable origin behaves like an attractor on large scales, since the „stable" matrix $\mathbf{S}$ (cf. (4.4) and (4.5)) governs its large-scale behaviour. Certainly, if the control vector $\mathbf{u}_j$ is only one-dimensional, i.e., $l = 1$, vector $\mathbf{F}_j$ is reduced to a scalar value χ_j. Consequently, there is only one non-zero value in vector $\mathbf{c}_j$, and the micro-chaos map can be expressed as

$$\mathbf{y}_{j+1} = \mathbf{S}\mathbf{y}_j - \mathbf{c}\chi_j. \tag{4.14}$$

Note that since the eigenvalues of matrix $\mathbf{S}$ are inside the unit circle, map (4.13) is a contraction. Consequently, it defines an iterated function system, like Barnsley's tree [10].

It is shown in Appendix C.2 that the micro-chaos maps assume the forms (4.9) and (4.13) in case of input quantization and twofold quantization, as well.

4.2.2 Fixed points

Since unstable fixed points and periodic orbits form the skeletons of strange attractors, their location influences the phase-space structure. Moreover, as it was illustrated in Fig. 4.2, the regular fixed points are often accompanied by virtual fixed points. In the examined low-dimensional cases the virtual fixed points' unstable manifolds often form the natural borders of the attractor, leading the trajectories back towards the origin.

The fixed points' positions of the map (4.10) with scalar control effort can be expressed as follows. Let us denote the fixed point corresponding to $m = \mathrm{Int}\left(r_O^{-1} \sum_{i=0}^{d} \mathbf{K}_i \mathbf{x}_{j-i}\right)$ by $\mathbf{x}_m^*$. Substituting $\mathbf{x}_{j+1} = \mathbf{x}_j = \cdots = \mathbf{x}_{j-i} = \mathbf{x}_m^*$ into (4.10) one obtains

$$\mathbf{x}_m^* = \mathbf{A}\mathbf{x}_m^* + \mathbf{B}r_O \mathrm{Int}\left(r_O^{-1} \sum_{i=0}^{d} \mathbf{K}_i \mathbf{x}_m^* \right) \equiv \mathbf{A}\mathbf{x}_m^* + \mathbf{b}m, \tag{4.15}$$

where $\sum_{i=0}^{d} \mathbf{K}_i \mathbf{x}_m^* \equiv \tilde{\mathbf{K}}\mathbf{x}_m^*$. Thus,

$$\mathbf{x}_m^* = (\mathbf{I} - \mathbf{A})^{-1}\mathbf{b}m. \tag{4.16}$$

For the validity of this expression, it is required that

$$m \le r_O^{-1}\tilde{\mathbf{K}}\mathbf{x}_m^* < m+1 \qquad \text{if} \quad m > 0,$$

$$\begin{aligned} -1 < r_O^{-1}\tilde{\mathbf{K}}\mathbf{x}_m^* < 1 \qquad & \text{if} \quad m = 0, \\ m-1 < r_O^{-1}\tilde{\mathbf{K}}\mathbf{x}_m^* \leq m \qquad & \text{if} \quad m < 0. \end{aligned} \tag{4.17}$$

The maximal index m with which a regular fixed point can be found is

$$m_{\text{fix,max}} = \text{Int}\left(\frac{1}{\tilde{\mathbf{K}}(\mathbf{I}-\mathbf{A})^{-1}\mathbf{b}r_O^{-1}-1}\right) = \text{Int}\left(\frac{1}{\tilde{\mathbf{K}}(\mathbf{I}-\mathbf{A})^{-1}\mathbf{B}-1}\right). \tag{4.18}$$

The neighbouring virtual fixed point is at the index $m_{\text{fix,max}}+1$. Regular *p-periodic orbits* can be found in a similar manner:

$$\mathbf{x}_{m_p} \equiv \mathbf{x}_{m_0} = (\mathbf{I}-\mathbf{A}^p)^{-1}\left(m_0\mathbf{A}^{p-1} + m_1\mathbf{A}^{p-2} + \cdots + m_{p-1}\mathbf{A}^0\right)\mathbf{b}, \tag{4.19}$$

where $\mathbf{x}_{m_j}$, $j = 0, 1, \ldots, p-1$ must be in the band characterised by m_j, as in (4.17).

4.2.3 Sensitive dependence on initial conditions

The linear term of the micro-chaos maps (4.9) or (4.10) is of the form $\mathbf{Ax}$, everywhere in the domain of definition. Thus, $\mathbf{A}$ is the Jacobian matrix of the system, consequently, the Lyapunov exponents are the logarithms of the singular values of $\mathbf{A}$:

$$\lambda_i = \log\sigma_i(\mathbf{A}), \quad i = 1, 2, \ldots, n. \tag{4.20}$$

We assumed that at least one of the eigenvalues of $\mathbf{A}$ is larger than one in modulus. This is true for the delayed micro-chaos map (see (4.8) and (C.10)), as well, since the eigenvalues of $\mathbf{A}$ appear among the eigenvalues of the extended matrix $\mathbf{A}^+$, according to the Leibniz formula for determinants. Since $\mathbf{A}$ is not a normal matrix in general, its eigenvalues and singular values are not equal. However, the greatest singular value is not less than the spectral radius, i.e., $\sigma_{\max} \geq |\lambda_{\max}|$. Thus, the micro-chaos maps have at least one Lyapunov exponent that is greater than zero, indicating sensitive dependence on initial conditions.

4.2.4 Existence and size of an absorbing sphere

From the practical point of view, the most important characteristics of micro-chaotic behaviour are the expected amplitude of the oscillations (size of the attractor) and the maximal possible control error. The quantization-related vibration amplitude is typically small, hence the name micro-chaos. However, it was found **[38, 40]** (see Section 4.5), that several disconnected strange attractors may coexist in certain cases, even rather far from the origin. Nevertheless, all the attractors can be found inside a finite domain, in a so-called *absorbing sphere*. To estimate the size of this sphere, we rewrite the map $\mathbf{y}_{j+1} = \mathbf{S}\mathbf{y}_j - \mathbf{c}_j$ (4.13) as

$$\mathbf{y}_{j+1} = \mathbf{S}^j\mathbf{y}_0 - \sum_{k=0}^{j-1}\mathbf{S}^k\mathbf{c}_k. \tag{4.21}$$

The maximal possible norm $|\mathbf{y}_\infty|$ of the vectors $\mathbf{y}_j$ in the limit $j \to \infty$ provides an estimate for the size of the attracting domain at the origin [58].

Unfortunately, matrix $\mathbf{S}$ is typically not a normal matrix, i.e., its norm (the greatest singular value) can be larger than 1. Still – since $\mathbf{S}$ is chosen such that its largest eigenvalue μ_{max} is less than one in modulus –, $\lim_{j\to\infty}||\mathbf{S}^j|| = \lim_{j\to\infty}\mu_{max}^j = 0$ is fulfilled **[38]**. Thus,

$$|\mathbf{y}_\infty| = \max\left|\sum_{k=0}^{\infty}\mathbf{S}^k\mathbf{c}_k\right|. \tag{4.22}$$

$|\mathbf{y}_\infty|$ is necessarily finite, since $|\mu_{max}|$ is less than one. Thus, there exists a finite attracting domain for each version of the micro-chaos map in the neighbourhood of the origin. Its size can be approximated by the methods from the literature [4, 13], or by the approaches that we developed in **[43]**. We found only slight differences between the results.

A positive Lyapunov exponent and the existence of an attractor are only necessary conditions of chaotic behaviour: it is also required that the micro-chaos map must be topologically transitive and the periodic points must be dense on the attractor. Still, the two proven properties of the micro-chaos maps are quite strong indicators of chaos. In the subsequent sections, simple versions of the micro-chaos map will be analysed.

4.3 ESCAPE RATE OF THE 1D TRANSIENT MICRO-CHAOS MAP

4.3.1 Mechanical model

The mechanical model of a polishing machine can be seen in Fig. 4.3. It consists of a revolving cylinder sliding on the surface of a fixed block. The velocity v of the shaft (feed) can be controlled, while the circumferential velocity of the polishing tool $v_0 = R\omega_0$ is constant.

Besides the dry friction force C acting on the shaft, a mixed dry-viscous friction force $N\mu(v_{\rm rel})$ also acts on the polishing tool of mass M, where N denotes the normal force between the revolving tool and the workpiece. This Stribeck-like friction force depends on the relative velocity $v_{\rm rel} = v_0 + v$. At low relative speeds, the effective friction coefficient μ is

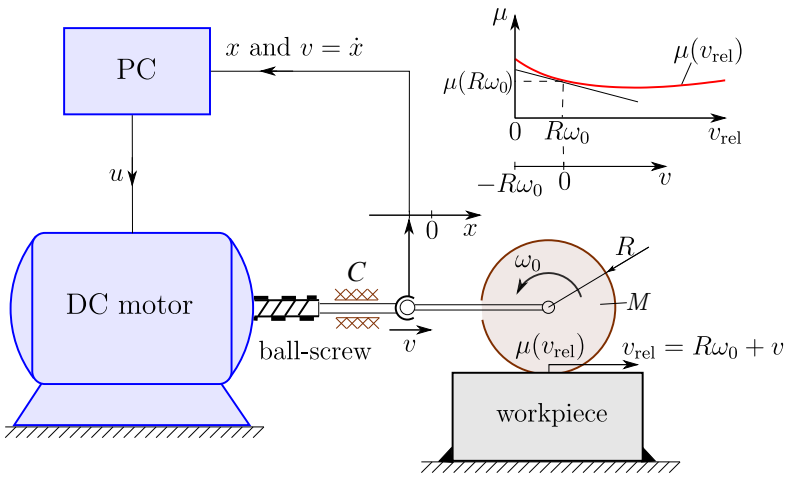

Figure 4.3: *The mechanical model of the computer-controlled polishing machine*

locally decreasing as the relative velocity $v_0 + v$ increases (see Fig. 4.3). As a consequence, the state with zero feed ($v = 0$) becomes unstable. As it was derived in the PhD thesis **[30]**, applying digital control with differential gain D, sampling period τ, and a finite resolution h in the velocity measurement, the dynamics of this system can be expressed by the following piecewise linear map:

$$x_{j+1} \equiv f(x_j) = \begin{cases} ax_j - b\ \mathrm{Int}(x_j) - c & \text{if } \ c/a < x_j, \\ 0 & \text{if } \ -c/a \le x_j \le c/a, \quad \text{and} \\ ax_j - b\ \mathrm{Int}(x_j) + c & \text{if } x_j < -c/a, \end{cases} \tag{4.23}$$

where $x_j = v(j)/h$, $v(j)$ denotes the velocity at the j^{th} sampling instant, and

$$a = e^{\frac{gN\tau}{M}} > 1, \qquad b = \frac{D}{gN}\left(e^{\frac{gN\tau}{M}} - 1\right) > 0, \tag{4.24}$$

$$c = \left(e^{\frac{gN\tau}{M}} - 1\right)\frac{C}{gNh} > 0, \qquad g = |\mu'(v_0)| = -\left.\frac{\mathrm{d}\mu(v_{\text{rel}})}{\mathrm{d}v_{\text{rel}}}\right|_{v_0} > 0. \tag{4.25}$$

Map (4.23) is a transient chaotic version of the micro-chaos map (4.1): while the error is not detected at small velocities, the Coulomb friction stops the shaft before the next sampling instant. Comparing this map with the general formulas of Section 4.2, one obtains that $\mathbf{A} = a$, $\mathbf{b} = -b$ and $\mathbf{K} = 1$. Note that there is practically no difference between input and output quantization in the 1D case because the state variable (input) is proportional with the control force (output). The fixed points of the map can be determined similarly to (4.2):

$$\begin{aligned} x^*_m &= \frac{bm + c}{a - 1}, \quad \text{if} \quad 0 \le m \le x^*_m < m + 1, \quad \text{or} \\ x^*_m &= \frac{bm - c}{a - 1}, \quad \text{if} \quad 0 \ge m \ge x^*_m > m - 1. \end{aligned} \tag{4.26}$$

The assumption $a > 1$ implies that all the fixed points are unstable. However, since the points on the interval $[-c/a, c/a]$ are mapped to the zero value, the occurrence of transient chaos is expected. Fig. 4.4 illustrates the graph of the map, together with the cobweb diagram of a transient chaotic trajectory that escapes from the repeller set.

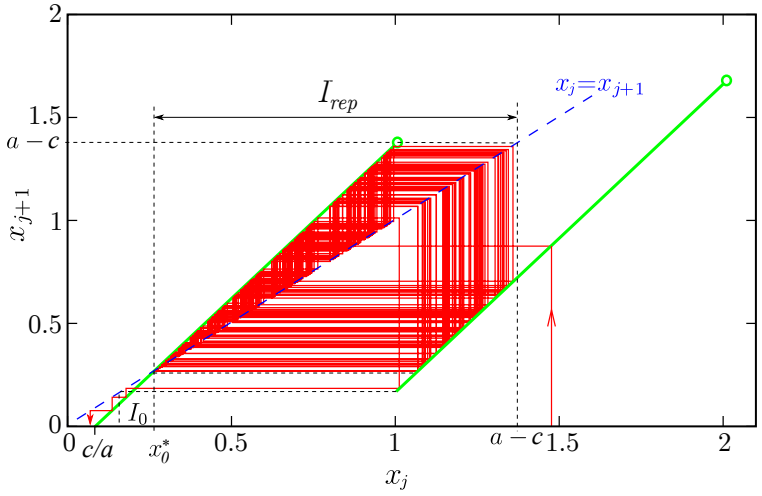

Figure 4.4: *A long trajectory at* $a = 1.5$, $b = 1.2$, *and* $c = 0.13\dot{3}$ ($|I_0| = 0.1$).

We consider the special case when the map has only one fixed point in the domain $x \ge 0$. In such cases, the chaotic repeller of the map is confined in the interval $I_{rep} \equiv [x^*_0, a - c)$, where x^*_0 is the fixed point: $x^*_0 = c/(a-1)$, while $a - c = \lim_{x_j \to 1^-} f(x_j)$ (see Fig. 4.4).

It can be seen in Fig. 4.4 that there is a sub-interval I_0 just left of the fixed point which is directly reachable from the right by a trajectory. If a solution arrives at I_0, the transient chaotic behaviour is over. The size of I_0 can be given as

$$|I_0| = a\,\frac{c}{a-1} - (a - b). \tag{4.27}$$

We introduce $|I_0|$ to be a new parameter instead of c, because it characterises the system better than the rescaled friction parameter c, and it is uniquely related to that.

In the thesis **[30]**, we determined the mean lifetime of chaotic transients in limited parameter domains. Later, the developed procedure was reformulated and generalized as a recursive method in **[34]**. In the present work, we use another approach published in **[35]** that is based on the approximation of the fractal dimension of the repeller. To find a good approximation, the structure of the repeller must be explored.

4.3.2 Structure of the repeller

Fig. 4.5 presents the structure of a part of the domain of definition of map (4.23). The number of steps needed to escape – i.e., to reach the interval I_0 – is naturally known in case of the pre-images of I_0. Some of these numbers are shown in the figure. Certain pre-images of the fixed point x_0^* are also depicted, to guide the eye. These points divide the depicted part of the domain of definition into the intervals A, B and C. Points in interval C are mapped into A or B in one step, so we focus on the interval $A \cup B$.

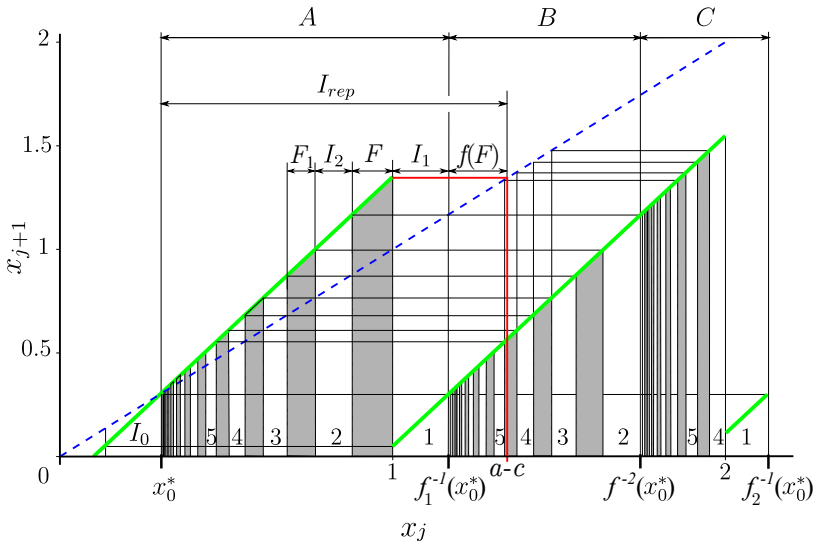

Figure 4.5: *The structure of the domain of definition at $a = 1.5$, $b = 1.3$, and $|I_0| = 0.25$. The numbers show how many steps are needed to reach I_0.*

I_0 has one first pre-image in A, which is denoted by I_1 in Fig. 4.5. I_1 has two pre-images in $A \cup B$, one in the interval A – it is denoted by I_2 – and another one in the interval B. As it is shown in the figure, two steps are needed to escape from these intervals. Similarly, I_2 has a pre-image in A and another one in B. Each interval A, B, and C contain an infinity of sub-intervals of size $|I_0|/a^j$, from where j steps are necessary to escape. These intervals and numbers will be referred to as *fundamental escape intervals* and *escape numbers*, respectively. The intervals between the fundamental escape intervals are denoted by shaded coloumns in the figure and will be referred to as *fundamental fractal intervals* F_j because a part of interval C is mapped on them, leading to self-similar structures. Intervals F_j are the jth pre-images of interval F, that is found between I_1 and I_2. The size of $F \equiv F_0$ is

$$|F| = \frac{a\ |I_{rep}| - b}{a^2}, \tag{4.28}$$

while the size of the jth pre-images of F can be given as $|F_j| = |F|/a^j$.

The right border of the repeller practically never coincides with the right border of a fractal interval: usually a truncated sub-interval appears at the right border of the repeller – see Fig. 4.5, where the border of the repeller (red line) cuts a fractal interval in two parts.

Since $f(F)$, the image of F, appears at the right border of the repeller, a truncated sub-interval can be found at the right border of F, too. Thus, the fractal intervals are not exactly self-similar. There are two possibilities to achieve exact self-similarity: the truncated sub-interval can be completed or deleted – see Fig. 4.6. As a consequence, the structure of the new interval becomes similar to that of A or $A \setminus I_1$.

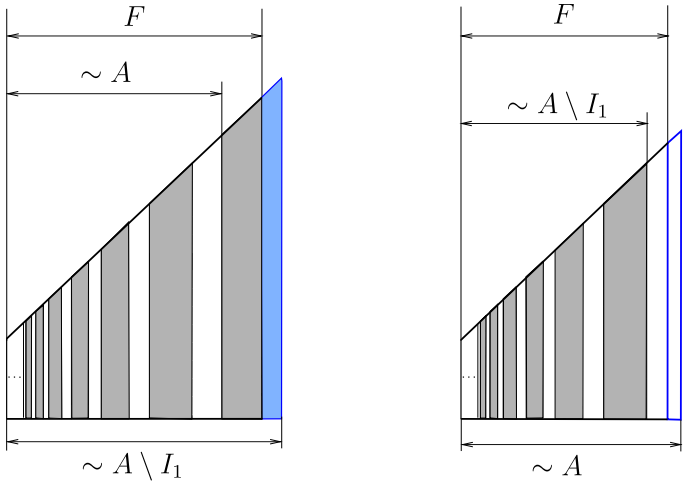

Figure 4.6: *Completion or deletion of the truncated intervals. a) truncated fractal interval, b) truncated escape interval at the right border of F.*

The fractal dimension of the repeller can be estimated as follows. Set A, set F, and an infinity of smaller copies of F has a similar structure. The scaling factor of F is between

$$C_1 = \frac{|F|}{|A| - |I_1|} = 1 + \frac{b}{a(|I_0| - b)} \quad \text{and} \quad C_2 = \frac{|F|}{|A|} = 1 - \frac{a|I_0| + b}{ab}, \tag{4.29}$$

while the scaling factors of the other intervals are between

$$r_{j1} = C_1 \; a^{-j} \quad \text{and} \quad r_{j2} = C_2 \; a^{-j}. \tag{4.30}$$

Thus, the repeller is a *multi-scale fractal*, with an infinity of scaling factors $r_j = Ca^{-j}$. The fractal dimension D_0 of multi-scale fractals can be calculated by solving the equation

$$\sum_{j=1}^{N} r_j^{D_0} = 1, \tag{4.31}$$

where N denotes the number of different scales and the r_j's are the scaling factors [154]. In the present case, Eq. (4.31) can be rewritten as

$$\sum_{j=0}^{\infty} a^{-jD_0} = C_i^{-D_0} \; , \quad i = 1, 2. \tag{4.32}$$

Solutions of Eqs. (4.32) provide lower and upper limits for the fractal dimension D_0.

4.3.3 Escape rate and mean escape number

For the calculation of the escape rate, Pesin's identity [155] can be applied:

$$\kappa = (1 - D_1)\lambda, \tag{4.33}$$

where λ is the Lyapunov exponent and D_1 denotes the information dimension of the repeller.

Using (4.20), the Lyapunov exponent can be calculated as the logarithm of the slope of the map: $\lambda = \log(a)$. Since it is constant, dimension D_1 is equal to the fractal dimension D_0 [154, 155]. Thus, after solving Eqs. (4.32) numerically, upper and lower limits can be calculated for the escape rate, using (4.33).

The mean escape number $\bar{N}_{esc}$ can be obtained by Eq. (4.3). The results of this calculation $\bar{N}_{esc}(a)$ are shown in Fig. 4.7 at $b = 1.3$ and $|I_0| = 0.25$. According to (4.28), the fractal intervals shrink to discrete points and the fractal dimension tends to zero at

$$a_{crit} = \frac{b}{|I_{rep}|} \approx 1.238. \tag{4.34}$$

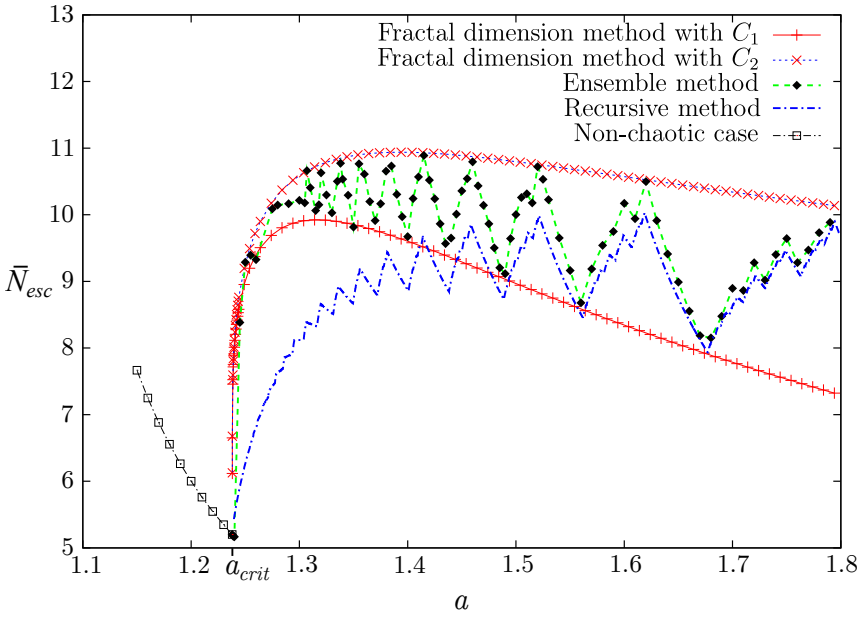

Figure 4.7: *Estimation of the mean escape number at $b = 1.3$ and $|I_0| = 0.25$.*

To check the fractal dimension-based results, we measured the escape rate using the so-called ensemble method [155], and determined the mean escape number by our recursive method **[34]**, too (Fig. 4.7). This latter procedure provides the exact value of the mean number of steps necessary to escape, by exploiting the self-similarity of the repeller.

As it can be seen in Fig. 4.7, the results of the recursive method differ from the other results, and this difference decreases as parameter a is increased. The reason of this phenomenon is that the rate of escape is not exactly exponential at low values of parameter a, since many trajectories visit only fundamental escape intervals. It means that relation (4.3) does not provide exact result for the mean *escape number* in such cases, not even if the *escape rate* is precisely estimated. However, we do not need to assume exponential escape for the application of the recursive method to obtain the value of the mean escape number.

We found that the fractal dimension increases with parameter a and decreases with parameter $|I_0|$ in the considered parameter range, this is why the difference between the results of the lifetime estimation methods disappears as a is increased or $|I_0|$ is decreased.

Our considerations can be extended to the so-called border state of transient chaos [155], too, i.e., when the fundamental fractal intervals shrink to discrete points **[33]**. In this case, $f_1^{-1}(x_0^*) > a - c$ (cf. Fig. 4.5), thus, $f(F)$ also shrinks to zero size. Consequently, interval I_1 will be at the right border of the non-strange "repeller" with size $|I_1| = a - c - 1$. The mean

escape number can be obtained by calculating the corresponding weighted sum:

$$\bar{N}_{esc} = |I_1| \frac{\sum_{i=1}^{\infty} i a^{1-i}}{|I_{rep}|} = \frac{a}{a-1}, \tag{4.35}$$

thus, the result does not depend on $|I_0|$ or b. Note, that the fractal dimension is zero in this case, leading to $\kappa = (1 - D_0)\log(a) = \log(a)$. Substituting this expression into (4.3), one obtains $\bar{N}_{esc} = a/(a-1)$ that agrees with the previous result.

Interestingly, the quickest escape is obtained at the critical parameter a_{crit}, i.e., when the fractal intervals shrink to discrete points.

4.4 2D MICRO-CHAOS MAP WITH DELAY

In the present section, we neglect the dry friction in the physical model of the 1D micro-chaos map (4.23), but take a processing delay (equal with the sampling period) into consideration. It means that not the actual state x_j, but a one step earlier state x_{j-1} of the system is used for the calculation of the control effort **[38]**:

$$x_{j+1} = a\ x_j - b\ \mathrm{Int}(x_{j-1}). \tag{4.36}$$

The underlying physical system can be the same machine that is depicted in Fig. 4.3.

4.4.1 Fundamental properties of the 2D delayed micro-chaos map

Eq. (4.36) can be formally rewritten as a 2D map $\mathbf{f}\colon \mathbb{R}^2 \to \mathbb{R}^2$ by introducing the state vector $\mathbf{y}_j \equiv [x_{j-1}\ x_j]^T$:

$$\mathbf{y}_{j+1} \equiv \begin{bmatrix} x_j \\ x_{j+1} \end{bmatrix} = \mathbf{f}(\mathbf{y}_j) \equiv \begin{bmatrix} 0 & 1 \\ 0 & a \end{bmatrix} \begin{bmatrix} x_{j-1} \\ x_j \end{bmatrix} + \begin{bmatrix} 0 \\ -b \end{bmatrix} \mathrm{Int}(x_{j-1}) \equiv \mathbf{A}^{+}\mathbf{y}_j + \mathbf{b}^{+}m. \tag{4.37}$$

where m denotes $\mathrm{Int}(x_{j-1})$. This map can be rewritten to the form of (4.10) with the coefficients $r_O = 1$, $\mathbf{B} = \mathbf{b} = -b$, $\mathbf{A} = a$, $\mathbf{K}_0 = 0$, and $\mathbf{K}_1 = 1$. Our goal is to prove that this version of the micro-chaos map is chaotic in large (non-zero measure) sets of the parameters.

For this purpose, we determine the parameter domain where the origin can be stabilized if the *quantization is disregarded*. The corresponding map assumes the following scalar form:

$$x_{j+1} = a\ x_j - b\ x_{j-1}. \tag{4.38}$$

In this case the origin is the single fixed point, which – according to Jury's criterion [104], i.e., the Moebius-transformed Routh-Hurwitz criterion – is stable if

$$(a, b) \in G = \left\{(\alpha, \beta) \in \mathbb{R}^2 |\ \alpha > 1, \beta < 1, \beta > \alpha - 1\right\}, \tag{4.39}$$

where we exploited that $a > 1$, according to (4.25).

During the analysis of (4.37), we will restrict ourselves to the domain of stability G (see Fig. 4.8), and will focus on cases when the variables are positive ($x_{j-1} > 0$, $x_j > 0$).

Now we return to the analysis of the quantized map (4.37), that is equivalent to a multi-valued version of the 1D micro-chaos map – see Fig. 4.9. The successive iteration steps can be followed on a modified cobweb diagram: starting from an initial point, the next point is found by projecting the point "horizontally" to the diagonal, then "vertically" to the line

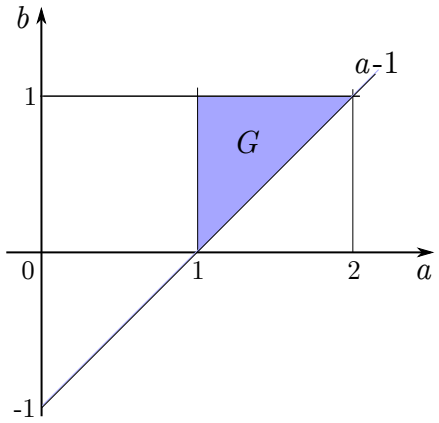

Figure 4.8: *The stable parameter domain G if the quantization is neglected.*

section of the attractor. In the multi-valued domains the appropriate branch is selected according to the previous value of the coordinate x_{j-1}.

To examine the properties of (4.37), we divided the plane (x_{j-1}, x_j) into parallel bands, according to the integer part of x_{j-1}, as shown in Fig. 4.9. The fixed points can be given as $\mathbf{y}^*_m = [x^*_m \; x^*_m]^T$, where the index m is the integer number $m = \mathrm{Int}(x^*_m)$. According to (4.16),

$$x^*_m = \frac{mb}{a-1}. \tag{4.40}$$

$\mathbf{y}^*_m$ is a regular fixed point if $0 \le m \le x^*_m < m+1$ or $m-1 < x^*_m \le m \le 0$. Otherwise, the fixed point is virtual. Since $b > a-1$ in the domain of stability, virtual fixed points appear farther from the origin than the band their belong to.

There can be at most one regular fixed point in each band and all of them are hyperbolic according to the eigenvalues of $\mathbf{A}^+$: $\lambda_1 = 0$ and $\lambda_2 = a > 1$. The unstable manifold of the fixed point $\mathbf{y}^*_m$ can be formulated as $U_m\colon x_j = ax_{j-1} - bm$. A direct consequence of the definition of map (4.37) is that any point $\mathbf{y}_j = [x_{j-1} \; x_j]^T$ in band $m = \mathrm{Int}(x_{j-1})$ is mapped to $\mathbf{y}_{j+1} = [x_j \quad ax_j - bm]^T$, i.e., to the manifold U_m of the fixed point $\mathbf{y}^*_m$. Since the trajectories immediately reach these manifolds, a possible strange attractor must consist of segments of certain unstable manifolds, as shown in Fig. 4.9.

The intersection point of the manifold U_m and the line $x_{j-1} = n$ $(n \ge 0)$ is denoted by

$$\mathbf{p}^m_n \equiv \begin{bmatrix} x^m_n \\ y^m_n \end{bmatrix} \equiv \begin{bmatrix} n \\ an - bm \end{bmatrix}, \tag{4.41}$$

where the upper index refers to the serial number of the unstable manifold, while the lower index shows the first coordinate of the point. Since points in the mth band are mapped onto the unstable manifold of $\mathbf{y}^*_m$, the leftmost point that can be reached from U_m is

$$\mathbf{f}(\mathbf{p}^m_m) \equiv \mathbf{p}^m_{\mathrm{inf}} \equiv \begin{bmatrix} x^m_{\mathrm{inf}} \\ y^m_{\mathrm{inf}} \end{bmatrix} = \begin{bmatrix} (a-b)m \\ (a^2 - ab - b)m \end{bmatrix} \tag{4.42}$$

(see $\mathbf{p}^2_2$ and $\mathbf{p}^2_{\mathrm{inf}}$ in Fig. 4.9). Moreover, since $\mathbf{p}^m_{m+1}$ belongs to the band where $\mathrm{Int}(x_{j-1}) = m+1$, its "upper" image

$$\mathbf{f}(\mathbf{p}^m_{m+1}) \equiv \mathbf{p}^m_{\mathrm{sup}} \equiv \begin{bmatrix} x^m_{\mathrm{sup}} \\ y^m_{\mathrm{sup}} \end{bmatrix} = \begin{bmatrix} (a-b)m + a \\ (a^2 - ab - b)m + a^2 \end{bmatrix} \tag{4.43}$$

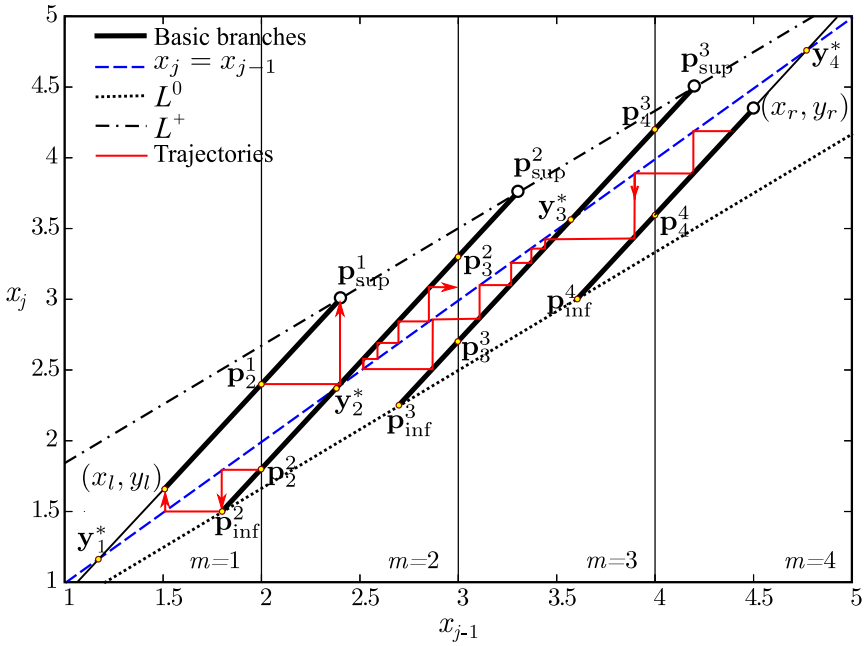

Figure 4.9: *Attractor of the 2D micro-chaos map, $a = 1.5$, $b = 0.6$. Black solid line segments are the basic branches of the unstable manifolds U_m of the fixed points $\mathbf{y}^*_m$, $m = 1, 2, 3, 4$. Their thick parts belong to the attractor.*

is the rightmost accumulation point of the points that can be reached from U_m (see $\mathbf{p}^1_2$ and $\mathbf{p}^1_{\rm sup}$ in Fig. 4.9). The points $\mathbf{p}^m_{\rm sup}$ fit to a line L^+, while points $\mathbf{p}^m_{\rm inf}$ are on another line L^0 that passes through the origin. According to these results, the *basic branch* [156] of the fixed point $\mathbf{y}^*_m$, i.e., the continuous piece of its unstable manifold is the line section between $\mathbf{p}^m_{\rm inf}$ and $\mathbf{p}^m_{\rm sup}$. We found that there are finite domains in the parameter plane (a, b), where parts of the basic branches of certain fixed points form the attractor of the system.

4.4.2 Proof of chaos

In this section we will prove that map (4.37) has chaotic solutions in finite parameter domains. Since the sensitive dependence on initial conditions and the existence of an attracting set have already been shown in Section 4.2, now we examine the topological transitivity.

Topological transitivity

We focus on the parameter domains shown in Fig. 4.10, where the structure of the attractor is particularly simple. We require that $(a, b) \in G$, variable x_j cannot assume negative values, and points of the mth basic branch cannot be mapped on the unstable manifolds U_{m+1} and U_{m-1} outside the interval bounded by the lines L^+ and L^0. We also require that there are no finite sections inside the basic branches that are unreachable, and maximum two basic branches can overlap. It is shown in Appendix C.3.1, that there exist integer numbers $m_{\rm min}$ and $m_{\rm max}$ in this case, such that the attractor consists of $m_{\rm max} - m_{\rm min} + 3$ parallel line segments and its rightmost accumulation point is

$$\mathbf{f}(\mathbf{p}^{m_{\rm max}}_{\rm sup}) \equiv \begin{bmatrix} x_r \\ y_r \end{bmatrix} = \begin{bmatrix} (a(a-b)-b)m_{\rm max} + a^2 \\ ax_r - b(m_{\rm max}+1) \end{bmatrix}, \tag{4.44}$$

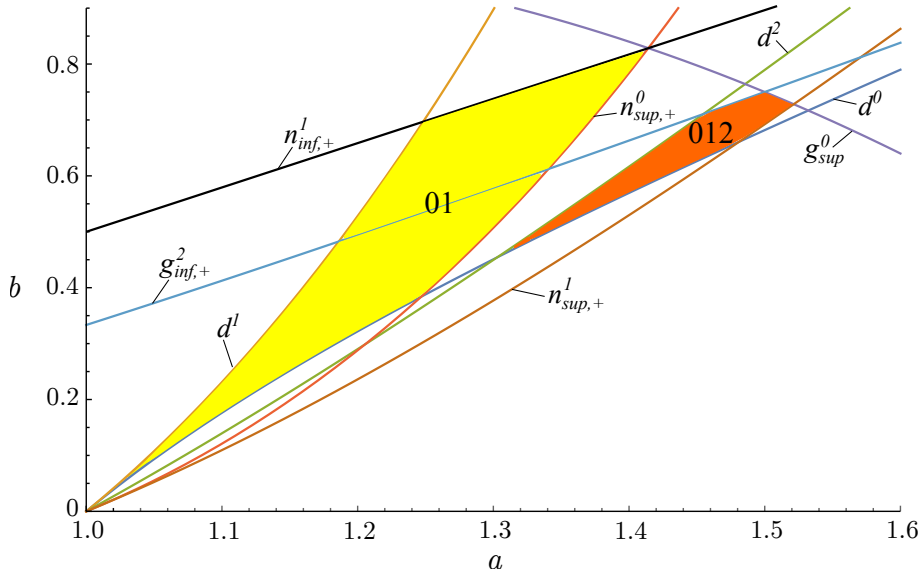

Figure 4.10: *Considered parameter domains and their boundary curves (Appendix C.3.1).*

while the leftmost point of the attractor can be obtained as

$$\mathbf{f}(\mathbf{p}_{\text{inf}}^{m_{\min}}) \equiv \begin{bmatrix} x_l \\ y_l \end{bmatrix} = \begin{bmatrix} (a(a-b)-b)m_{\min} \\ ax_l - b(m_{\min}-1) \end{bmatrix}, \tag{4.45}$$

where

$$m_{\min} = \text{Int}\frac{b}{a^2(b+1-a)}, \quad \text{and} \quad m_{\max} = \text{Int}\frac{b(a^2-1)}{a^2(b+1-a)}. \tag{4.46}$$

"Full" basic branches exist on U_m (from $\mathbf{p}_{\text{inf}}^m$ to $\mathbf{p}_{\text{sup}}^m$) that belong to the attractor if $m_{\min} \le m \le m_{\max}$. The images of the extremal endpoints of these basic branches ($\mathbf{f}(\mathbf{p}_{\text{inf}}^{m_{\min}})$ and $\mathbf{f}(\mathbf{p}_{\text{sup}}^{m_{\max}})$) form the borders of the attracting set $\mathcal{A}$, like in Figure 4.9, where $m_{\min} = 2$ and $m_{\max} = 3$.

It can also happen that $m_{\min} = m_{\max} + 1$ (see Figure 4.11). In this case the attractor consists of two truncated basic branches that are shorter than the segment from $\mathbf{p}_{\text{inf}}^m$ to $\mathbf{p}_{\text{sup}}^m$.

In both cases, the attractor consists of segments of the lines $x_j = ax_{j-1} - bk$, where

$$x_{j-1} \in (x_l, x_{\text{sup}}^{m_{\min}-1}), \quad k = m_{\min} - 1 \tag{4.47}$$

$$x_{j-1} \in (x_{\text{inf}}^{m_{\min}}, x_{\text{sup}}^{m_{\min}}), \quad k = m_{\min} \tag{4.48}$$

$$\vdots$$

$$x_{j-1} \in (x_{\text{inf}}^{m_{\max}}, x_{\text{sup}}^{m_{\max}}), \quad k = m_{\max} \tag{4.49}$$

$$x_{j-1} \in (x_{\text{inf}}^{m_{\max}+1}, x_r), \quad k = m_{\max} + 1. \tag{4.50}$$

We restrict ourselves to the case when there are only two basic branches, on the manifolds U_0 and U_1. The corresponding parameter domain is denoted by '01' in Figs. 4.10 and C.3. Our goal is to show that there are certain subdomains in '01' where the attractor $\mathcal{A}$ can be partitioned in such a way that the partition is irreducible and primitive [139]. In such a partition, every region can be reached from any other region and there is at least one region whose image fully covers at least two other regions. As an example, consider the attractor of map (4.37) at parameters $a = 1.3$ and $b = 0.66$ (see Fig. 4.11).

The partition of the attractor is constructed as follows: the open intervals on the basic branches between the line $x_{j-1} = 1$ and the lines L^0 or L^+ are the *basic regions*, denoted

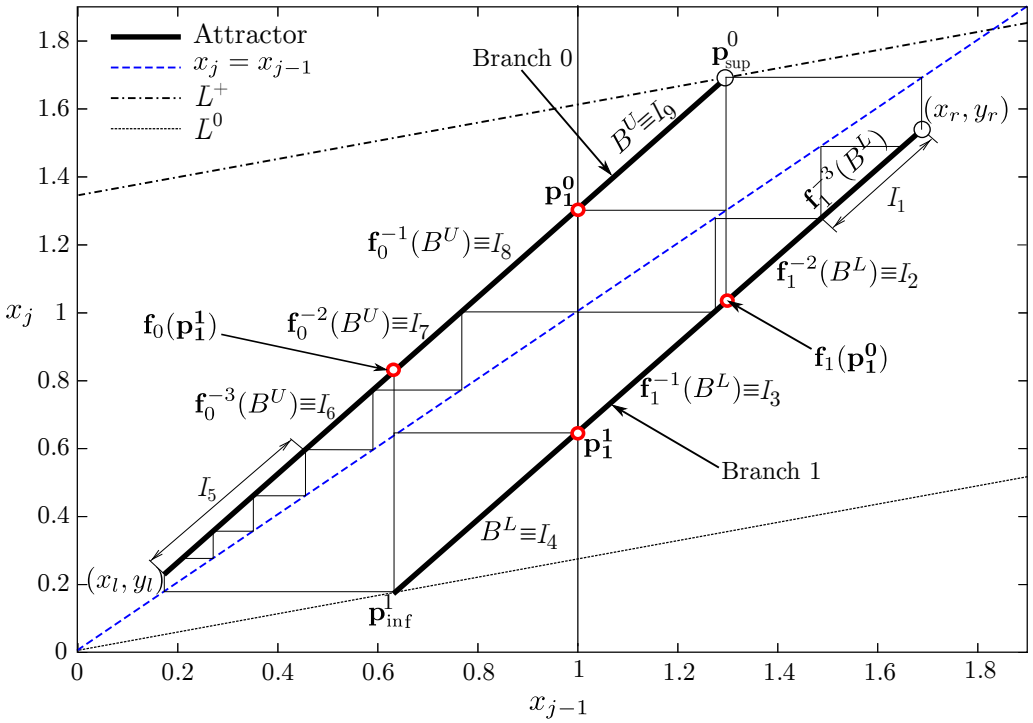

Figure 4.11: *Partition of the attractor ($a = 1.3$, $b = 0.66$)*

by $B^L \equiv I_4$ and $B^U \equiv I_9$ on the lower and upper branches, respectively, in Fig. 4.11. The subscripts 4 and 9 are the serial numbers of these regions. The outermost endpoints of the regions coincide with the endpoints of the corresponding basic branches, according to our requirements. Thus, these basic regions are well defined. The pre-images of these segments form the remaining regions. The inverse of $\mathbf{f}$ is not unique, thus, we define the inverse function $\mathbf{f}_m^{-1}$ such that it maps to the mth basic branch (here $m = 0$ or 1):

$$\mathbf{f}_m^{-1}\left(\begin{bmatrix} z_1 \\ z_2 \end{bmatrix}\right) = \begin{bmatrix} \frac{z_2+bm}{a^2} + \frac{bm}{a} \\ \frac{z_2+bm}{a} \end{bmatrix}. \tag{4.51}$$

As it can be seen in Fig. 4.11, the fourth pre-image of region B^L on the lower branch would stretch over (x_r, y_r), this is why the rightmost region – region I_1 – consists of region $\mathbf{f}_1^{-3}(B^L)$ and the remaining part of the branch. This construction ensures that the closure of the image of region I_1 fully covers region $\mathbf{f}_1^{-2}(B^L)$, whose image also fully covers region $\mathbf{f}_1^{-1}(B^L)$, etc. It is also important that the image of region B^U fully covers region I_1 – this is not a consequence of the introduced construction, thus, must be checked.

The upper branch – Branch 0 – can be partitioned in a similar way: certain pre-images of section B^U are marked in the figure: $\mathbf{f}_0^{-1}(B^U)$, $\mathbf{f}_0^{-2}(B^U)$, and $\mathbf{f}_0^{-3}(B^U)$. As it can be observed, the image of region B^L, i.e., $\mathbf{f}(B^L)$, fully covers region $\mathbf{f}_0^{-3}(B^U)$ and the remaining part of the upper basic branch. The condition of this situation must also be checked. To construct a primitive partition, it is enough to form only a single additional region I_5 on the left hand side of Branch 0. According to this partitioning, every region can be reached from any other region and the image of region I_4 fully covers two other regions. The conditions for the construction of similar irreducible and primitive partitions are derived in Appendix C.3.2. It is shown there that there is a finite parameter domain (see Fig. C.3), where the necessary conditions are fulfilled.

Denoting the ith region in the partition by I_i, $i = 1, \ldots, r$, we can introduce the transition

matrix $\mathbf{P} \in \mathbb{R}^{r\times r}$ of the partition as

$$P_{ij} = \begin{cases} 1 & \text{if } \overline{\mathbf{f}(I_i)} \supset I_j \\ 0 & \text{otherwise} \end{cases} . \tag{4.52}$$

In the example shown in Fig. 4.11, there are $r = 9$ regions, and the transition matrix can be written as

$$\mathbf{P} = \begin{bmatrix} 0 & 1 & 0 & 0 & 0 & 0 & 0 & 0 & 0 \\ 0 & 0 & 1 & 0 & 0 & 0 & 0 & 0 & 0 \\ 0 & 0 & 0 & 1 & 0 & 0 & 0 & 0 & 0 \\ 0 & 0 & 0 & 0 & 1 & 1 & 0 & 0 & 0 \\ 0 & 0 & 0 & 0 & 0 & 1 & 0 & 0 & 0 \\ 0 & 0 & 0 & 0 & 0 & 0 & 1 & 0 & 0 \\ 0 & 0 & 0 & 0 & 0 & 0 & 0 & 1 & 0 \\ 0 & 0 & 0 & 0 & 0 & 0 & 0 & 0 & 1 \\ 1 & 0 & 0 & 0 & 0 & 0 & 0 & 0 & 0 \end{bmatrix} . \tag{4.53}$$

In the examined parameter domain, the structure of the partition and the transition matrix is similar to the example, i.e., there is one non-zero element in every row and column, not in the main diagonal, and there is an additional non-zero element P_{kj}:

$$\begin{aligned} P_{i(i+1)} &= 1, \quad i = 1, \dots, r-1 \\ P_{r1} &= 1, \\ P_{kj} &= 1, \quad \text{where } k \neq j,\ k+1 \neq j. \end{aligned} \tag{4.54}$$

These matrices are irreducible and primitive, as well, i.e., there exists an integer number $N > 0$, such that every element of $\mathbf{P}^N$ is positive. This property can be proved as follows: in the case shown above, $P^2_{(k-1)j} > 0$ (i.e., the $(k-1, j)$ element of $\mathbf{P}^2$ is positive) if $k > 1$, or $P^2_{rj} > 0$ if $k = 1$, and $P^2_{k(j+1)} > 0$ if $j < r$, or $P^2_{k1} > 0$ if $j = r$. Thus, the existence of the additional non-zero element P_{kj} implies the appearance of two additional non-zero elements. Moreover, $P^2_{i(i+2)} > 0$ if $i < r-1$, or $P^2_{i1} > 0$ if $i = r-1$, or $P^2_{i2} > 0$ if $i = r$. Thus, the diagonal non-zero elements are simply shifted to the right. It can be proved by induction, that the number of non-zero elements increases at least by one during the multiplication by $\mathbf{P}$. Thus, $\mathbf{P}^N$ contains only positive elements, where $N \leq r^2 - r$. In the example, $N = 65 < 9^2 - 9 = 72$.

The time evolution can be given by semi-infinite symbol sequences that describe which regions of the attractor are visited. It is obvious, that to every such symbol sequence corresponds at least one point on the attractor. However, there may exist points (e.g., those that are mapped from I_4 to I_7), whose itinerary cannot be described by the symbolic dynamics on the introduced partition. Let us introduce the subset $\mathcal{L}$ of the attractor that correspond to a symbol sequence. The proved property of the transition matrix $\mathbf{P}$ implies that the micro-chaos map is topologically transitive on $\mathcal{L}$ and there exists a countable infinity of periodic orbits, an uncountable infinity of nonperiodic orbits and a dense orbit (see [78]). Thus, according to e.g. [139, 167], the 2D micro-chaos map is chaotic on the set $\mathcal{L}$.

4.5 2D MICRO-CHAOS MAP WITHOUT DELAY

Since micro-chaos phenomenon can occur if an unstable state is stabilized by a digital control system, the present section is devoted to the analysis of the simplest 1DoF mechanical system with unstable equilibrium: the linearized inverted pendulum.

4.5.1 Mathematical model

Consider an oscillator with negative stiffness, whose equation of motion is linearized about the unstable equilibrium. Taking into account a control force $u(\tilde{x}, \dot{\tilde{x}})$, the equation of motion assumes the following form:

$$M\ddot{\tilde{x}}(t) + d\dot{\tilde{x}}(t) - k\tilde{x}(t) = u(\tilde{x}, \dot{\tilde{x}}), \tag{4.55}$$

where $\tilde{x}$ is the general coordinate, M denotes (generalized) mass, $d \geq 0$ is the damping coefficient, and $k > 0$ characterises the (generalized) stiffness. Digital PD control is applied in order to stabilize the position $\tilde{x} = 0$, $\dot{\tilde{x}} = 0$.

Effect of sampling

If quantization is not considered, the equation of motion of the digitally controlled system becomes piecewise linear on the intervals $t \in [j\tau, (j+1)\tau)$ between the sampling instants:

$$\ddot{\tilde{x}}(t) + \frac{d}{M}\dot{\tilde{x}}(t) - \frac{k}{M}\tilde{x}(t) = -\frac{\tilde{P}\tilde{x}_j + \tilde{D}\dot{\tilde{x}}_j}{M}, \tag{4.56}$$

where $\dot{\tilde{x}}_j = \dot{\tilde{x}}(j\tau)$, $j \in \mathbb{N}$, while $\tilde{P}$ and $\tilde{D}$ denote the proportional and differential gains, respectively. Thus, the control force can be given as $u_j = -(\tilde{P}\tilde{x}_j + \tilde{D}\dot{\tilde{x}}_j)$, $t \in [j\tau, (j+1)\tau)$.

Let us introduce a dimensionless displacement coordinate $x = \tilde{x}/\tilde{h}$, where $\tilde{h}$ is a reference distance – to be defined later –, and a non-dimensional time $T = t/\tau$, where τ is the sampling period and t is the physical time. With this new time variable, $\dot{\square} \equiv \frac{d}{dt}\square = \frac{1}{\tau}\frac{d}{dT}\square \equiv \frac{1}{\tau}\square'$, thus, denoting the differentiation with respect to T by prime, one obtains the equation of motion for $T \in [j, (j+1))$:

$$\frac{1}{\tau^2}\tilde{h}x''(T) + \frac{d\tilde{h}}{M\tau}x'(T) - \frac{k\tilde{h}}{M}x(T) = -\frac{\tilde{P}\tilde{h}\tau x_j + \tilde{D}\tilde{h}x'_j}{M\tau}. \tag{4.57}$$

After rearranging terms, the equation assumes the following dimensionless form:

$$x'' + 2\beta x' - \alpha^2 x = -\left(Px_j + Dx'_j\right), \tag{4.58}$$

where

$$\beta = \frac{d\tau}{2M}, \quad \alpha = \tau\sqrt{\frac{k}{M}}, \quad P = \frac{\tilde{P}\tau^2}{M}, \quad D = \frac{\tilde{D}\tau}{M}. \tag{4.59}$$

As it can be seen, the reference distance $\tilde{h}$ does not influence the form of the equation of motion and the dimensionless variables. It is worth noting that parameter α is the ratio of the sampling period and the characteristic time constant of the oscillator. Its value is usually kept very small in practical applications (in the order of $10^{-2} \dots 10^{-5}$) by increasing the sampling frequency. Introducing the notation $\gamma = \sqrt{\alpha^2 + \beta^2}$, the general solution of Eq. (4.58) assumes the following form in $T \in [j, (j+1))$:

$$x(T) = C_1 e^{(\gamma-\beta)T} + C_2 e^{(-\gamma-\beta)T} + \frac{Px_j + Dx'_j}{\alpha^2}. \tag{4.60}$$

Using the matching conditions $x(j) = x_j$ and $x'(j) = x'_j$, the coefficients – and consequently, x_{j+1} and x'_{j+1} – can be expressed by x_j and x'_j. Thus, one can construct the map

$$\mathbf{x}_{j+1} = \mathbf{S}\mathbf{x}_j, \tag{4.61}$$

where

$$\mathbf{S} = \frac{1}{e\gamma}\begin{bmatrix} \frac{(\alpha^2-P)(\beta s+\gamma c)+Pe\gamma}{\alpha^2} & \frac{\alpha^2 s-(\beta s+\gamma c-e\gamma)D}{\alpha^2} \\ (\alpha^2-P)\,s & \gamma c-(\beta+D)s \end{bmatrix}, \tag{4.62}$$

while $\mathbf{x}_j \equiv [x_j \quad x_j']^T$, $s \equiv \sinh(\gamma)$, $c \equiv \cosh(\gamma)$, and $e \equiv \exp(\beta)$.

According to our assumption, the eigenvalues of $\mathbf{S}$ are less than one in modulus, i.e., the origin of the sampled system is asymptotically stable if the round-off is not taken into account. It is shown in Appendix C.4.1 and in **[42]** that the borders of the domain of stability are $P = \alpha^2$, $D = D_{b0}$, and $D = D_{b1}$, where the expressions of D_{b0} and D_{b1} are given by Eq. (C.47). The maximal value of P in the domain of stability (see Fig. 4.12) can be determined as the intersection point of these boundary curves:

$$P_{\max} = \frac{\alpha^2\,(1-2ce-3e^2)}{1-2ce+e^2}. \tag{4.63}$$

It can also be shown that the equilibrium can be asymptotically stabilized at every positive value of the sampling time τ with properly chosen gains P and D.

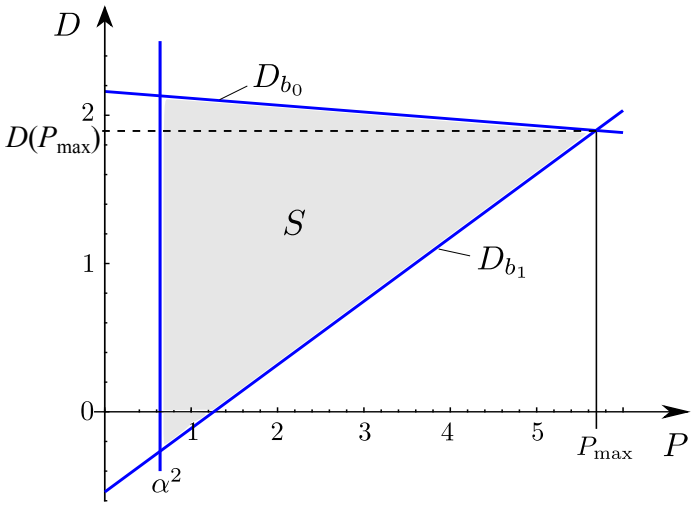

Figure 4.12: *The domain of asymptotic stability of the desired state* $\mathbf{x} = \mathbf{0}$ *without processing delay and quantization at* $\alpha = 0.8$ *and* $\beta = 0.3$.

Quantization – round-off at the output

If the output of the control system is quantized, the rounded control force must be an integer multiple of a certain resolution $r_O \equiv \Delta F$ (cf. Fig. 4.1):

$$\ddot{\tilde{x}}(t) + \frac{d}{M}\dot{\tilde{x}}(t) - \frac{k}{M}\tilde{x}(t) = -\frac{\Delta F}{M}\mathrm{Int}\left(\frac{\tilde{P}\tilde{x}_j + \tilde{D}\dot{\tilde{x}}_j}{\Delta F}\right),\ t \in [j\tau, (j+1)\tau). \tag{4.64}$$

The odd function Int() rounds towards the origin. Introducing the new dimensionless variables $T = t/\tau$ and $x = M\tilde{x}/(\Delta F\tau^2)$ (i.e., the appropriate choice of the reference distance is $\tilde{h} = \Delta F\tau^2/M$, cf. Eq. (4.57)), one arrives at the equation

$$x''(T) + 2\beta x'(T) - \alpha^2 x(T) = -\mathrm{Int}\left(Px_j + Dx_j'\right), \tag{4.65}$$

where $T \in [j, (j+1))$, and the parameters are the same as in (4.59). The dynamics of the quantized system can be described by the following mapping:

$$f(\mathbf{x}_j) \equiv \mathbf{x}_{j+1} = \mathbf{A}\mathbf{x}_j + \mathbf{b}\ \mathrm{Int}\left(Px_j + Dx_j'\right) \equiv \mathbf{A}\mathbf{x}_j + \mathbf{b}m, \tag{4.66}$$

where $m = \mathrm{Int}\left(Px_j + Dx'_j\right)$, $\mathbf{x}_j = [x_j\ x'_j]^T$,

$$\mathbf{A} = \frac{1}{e\gamma}\begin{bmatrix} \gamma c + \beta s & s \\ \alpha^2 s & \gamma c - \beta s \end{bmatrix}, \quad \mathbf{b} = \begin{bmatrix} \frac{e-c}{e\alpha^2} - \frac{\beta s}{e\gamma\alpha^2} \\ -\frac{s}{e\gamma} \end{bmatrix} \quad \text{and} \quad \mathbf{K} = [P\ D], \tag{4.67}$$

according to the notations of Section 4.2. Since the resolution became unity due to the scaling of the variables, $\mathbf{B} = \mathbf{b}$ is fulfilled, thus, $\mathbf{S} = \mathbf{A} + \mathbf{bK}$.

The local stability properties of the mapping are determined by the matrix $\mathbf{A}$ with eigenvalues $\lambda_{1,2} = \exp(-\beta \pm \gamma)$. Since $\gamma > \beta$, the origin is locally unstable and all the existing fixed points are saddle points. The eigenvectors – showing the directions of the stable and unstable manifolds of fixed points, respectively – are

$$\mathbf{e}_\mathrm{s} = \begin{bmatrix} 1 \\ -\gamma - \beta \end{bmatrix} \quad \text{and} \quad \mathbf{e}_\mathrm{u} = \begin{bmatrix} 1 \\ \gamma - \beta \end{bmatrix}. \tag{4.68}$$

The evolution of the state of the system can be described by another map, as well:

$$\mathbf{y_{j+1}} = \mathbf{Sy_j} - \mathbf{b}\chi_j, \tag{4.69}$$

where $\mathbf{S}$ is given by (4.62) and $-1 < \chi_j < 1$ is the fractional part of the control force. Thus, the fractional part of the control force is subtracted in this case, instead of the addition of its integer part.

4.5.2 Bands, fixed points and strange sets

The domain of definition of (4.66) can be divided into discrete bands, according to the value of the number m. The computer sends out the same output signal within such a band, due to the round-off. The bands are separated by the lines

$$SW_m\colon \qquad x' = \frac{m - Px}{D}, \quad |m| = 1, 2, 3, \ldots, \tag{4.70}$$

thus, these switching lines cross the line $x' = 0$ at $x = m/P$. The direction field of the mapping, the switching lines, fixed points and example trajectories are shown in Fig. 4.13.

The fixed points of map (4.66) can be given according to (4.16):

$$\mathbf{x}^*_m \equiv (\mathbf{I} - \mathbf{A})^{-1}\,\mathbf{b}m = \left[\frac{m}{\alpha^2}\ 0\right]^T. \tag{4.71}$$

If the fixed point $\mathbf{x}^*_m$ crosses the switching line SW_{m+1}, i.e.,

$$P = \alpha^2\frac{|m|+1}{|m|}, \tag{4.72}$$

a *border collision bifurcation* occurs (see Fig. 4.14) and the fixed point becomes virtual. The maximal index where a regular fixed point can exist can be determined using (4.18). Since the phase-space is symmetric to the origin and the origin is always a regular fixed point, the number of regular fixed points is

$$N_\mathrm{fixed} = 2\ \mathrm{Int}\left(\frac{\alpha^2}{P - \alpha^2}\right) + 1. \tag{4.73}$$

The notions of regular and virtual fixed points are also illustrated in Fig. 4.13, where the outmost regular fixed point $\mathbf{x}^*_2$ is in band $m = 2$ and the virtual fixed point $\mathbf{x}^*_3$ is in band

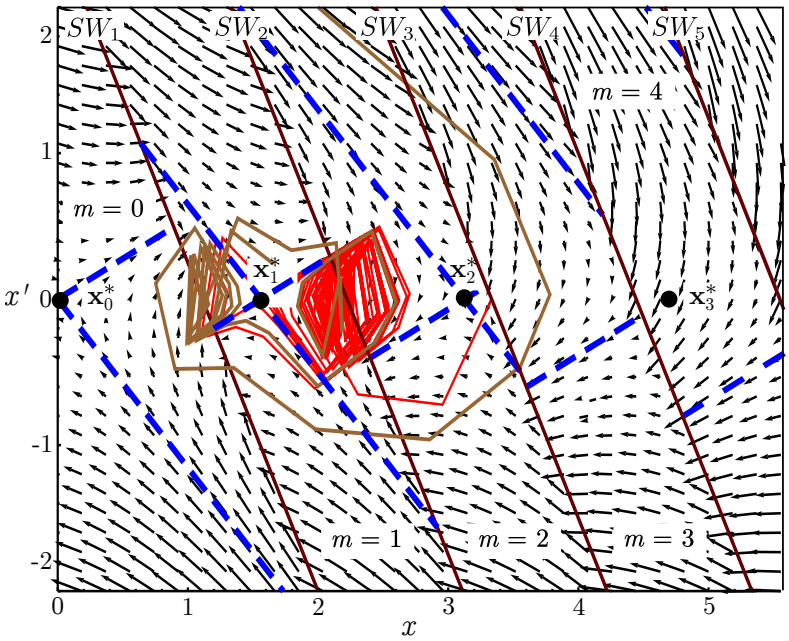

Figure 4.13: *The direction field of the mapping with switching lines (SW_1 ... SW_5) and fixed points ($\mathbf{x}_0^*$ ... $\mathbf{x}_3^*$) with stable and unstable manifolds (dashed lines) at $\alpha = 0.8$, $\beta = 0.3$, $P = 0.9$, and $D = 0.4$. Three regular fixed points and one virtual fixed point ($\mathbf{x}_3^*$) are depicted. Two trajectories are also shown, leading to the same attractor. The points of the trajectories are connected with continuous line segments for better visualization.*

$m = 4$. Even two communicating chaotic repellers are depicted that together form a chaotic attractor. As it will be shown, the distribution of disconnected attractors and repellers is closely related to the structure of fixed points **[43]**. This is why the parameter dependence of the number of regular fixed points is important to understand the dynamics of the system.

According to (4.73), the number of fixed points tends to infinity as $P \to \alpha^2$, while the origin is the single regular fixed point if $P > 2\alpha^2$. Even "supervirtual" fixed points can born by further border collisions of the virtual fixed point at values $P = n\alpha^2$, $n = 2,3,\ldots$.

The minimal possible number of fixed points at a given α, β pair – if P is chosen from the domain of stability – can be found by substituting $P = P_{\max}$ (see (4.63)) into (4.73). The results are depicted in Fig. 4.14. In practical applications, the damping parameter β is usually small. Thus, at relatively large values of α ($\alpha \gtrsim 2$), the phase-space structure becomes rather complicated with several fixed points. On the other hand, if α is sufficiently small, e.g., $3\alpha^2 < P$, the supervirtual fixed points – situated several bands away from the regular fixed points – can influence the dynamics in the neighbourhood of the origin.

The control force is in equilibrium with other forces at the fixed points. Thus, if a phase-space point is farther away from the origin than the fixed point (i.e., larger control force would be necessary), but in the same band (i.e., the control force is the same), the dynamics will push the trajectory even farther, to the next band. Since the control force is one unit larger there, the dynamics will lead back to the band that is closer to the origin. Because switches occur at the sampling instants, trajectories can cross the switching lines and the actual switching may happen well inside the bands, resulting in the mixing of trajectories.

According to the reasoning above, the appearance of strange sets is expected between the neighbouring fixed points $\mathbf{x}_{m-1}^*$ and $\mathbf{x}_m^*$, at the crossings of the switching lines (4.70) and the $x' = 0$ line (see Fig. 4.13), i.e., at

$$x_m = \frac{m}{P}. \tag{4.74}$$

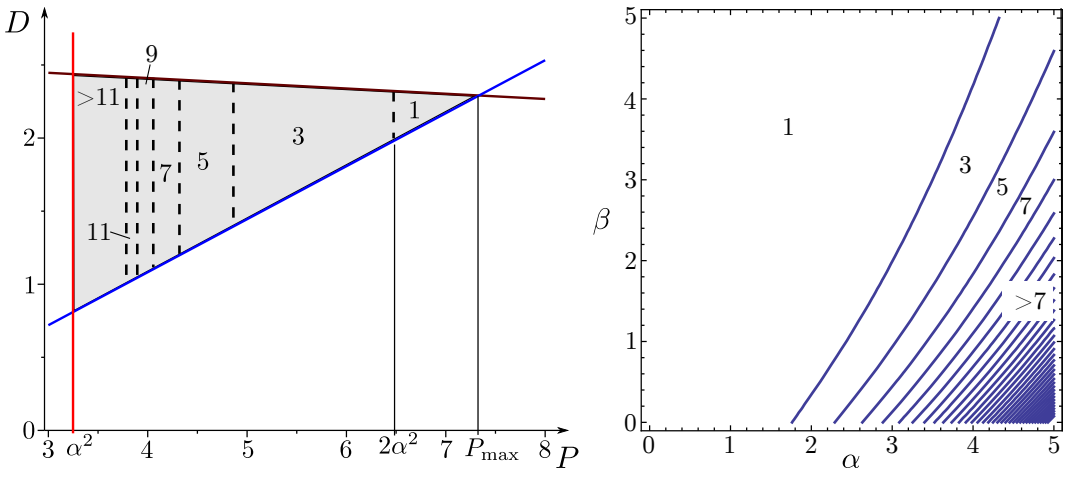

Figure 4.14: *Left: the number of fixed points at $\alpha = 1.8$ and $\beta = 0.3$ and the border collision bifurcation curves (vertical dashed lines). Right: the minimal number of fixed points if the gains P and D are chosen from the domain of stability. The maximal possible number of fixed points is unbounded.*

Thus, the strange sets can be indexed by the corresponding integer indices m of switching lines. Since there is a possible attractor or repeller between the "last" regular fixed point with

$$m = m_{\text{fix,max}} \equiv \text{Int}\left(\frac{\alpha^2}{P-\alpha^2}\right) \tag{4.75}$$

(see (4.18) and (4.73)) and the "first" virtual fixed point at $m = m_{\text{fix,max}} + 1$, the index $m_{\max}$ of the strange structure that is farthest from the origin is

$$m_{\max} = m_{\text{fix,max}} + 1 = \text{Int}\left(\frac{\alpha^2}{P-\alpha^2}\right) + \frac{P-\alpha^2}{P-\alpha^2} = \text{Int}\left(\frac{P}{P-\alpha^2}\right). \tag{4.76}$$

Depending on the parameters, the evolving structures may be chaotic attractors or repellers with transient chaotic dynamics.

4.5.3 Smale horseshoes

The sensitive dependence on initial conditions and the existence of an attractor follows from the general proofs in Sections 4.2.3 and 4.2.4. To complement the proof of chaos, we searched for Smale horseshoe structures. As initial domains, we chose the parallelograms $Q_r = L \cup R$, $r \in \mathbb{N} \setminus \{0\}$ defined by the stable and unstable manifolds W_L^S, W_L^U, W_R^S and W_R^U of neighbouring fixed points $\mathbf{x}_l^*$ and $\mathbf{x}_r^*$ (see Fig. 4.15).

Here r denotes the index of the switching line SW_r between the two fixed points. l and r are the integer numbers corresponding to the integer part of the control force in the bands next to the switching line SW_r. Each parallelogram is divided into two trapezoids (denoted by R on the right and L on the left, see the crosshatched regions in Fig. 4.15) by a switching line. The vertices of the trapezoid L are the fixed point $\mathbf{x}_l^*$, the intersection point P^{RULS} of the manifolds W_R^U and W_L^S, the intersection point P^{RUSW} of W_R^U and the switching line, and the crossing point P^{LUSW} of manifold W_L^U and the switching line, as shown in Fig. 4.15. The vertices of the right trapezoid are P^{LUSW}, P^{RUSW}, $\mathbf{x}_r^*$, and P^{LURS}. The coordinates of the aforementioned points can be obtained by straightforward analytical calculation:

$$P^{RULS} = \left(\frac{-\beta + (2m-1)\gamma}{2\alpha^2\gamma}, -\frac{1}{2\gamma}\right),$$

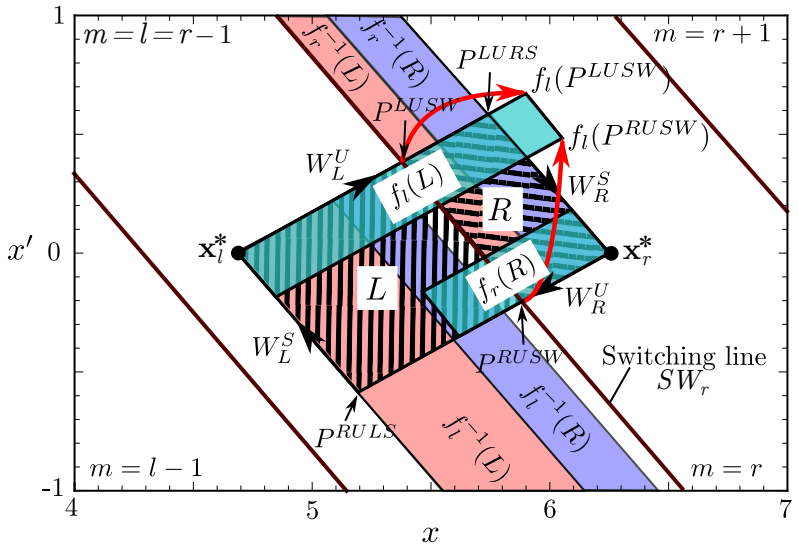

Figure 4.15: *Schematic picture of the horseshoe-structure in the parallelogram $Q_r = L \cup R$. The figure was generated at $r = 4$, $\alpha = 0.8$, $\beta = 0.3$, $P = 0.7$ and $D = 0.6$. The switching lines and stable manifolds are parallel in this case. This property is not exploited in the derivations, but helps the visualization of the Smale horseshoe structure.*

$$
\begin{aligned}
P^{RUSW} &= \left(\frac{(\alpha^2 + D(-\beta+\gamma))\, m}{\alpha^2(-\beta D + D\gamma + P)}, -\frac{(\beta-\gamma)m\,(\alpha^2 - P)}{\alpha^2(-\beta D + D\gamma + P)} \right), \\
P^{LUSW} &= \left(\frac{D(\beta-\gamma)(-1+m) - \alpha^2 m}{\alpha^2(\beta D - D\gamma - P)}, \frac{(\beta-\gamma)\,(\alpha^2 m + P - mP)}{\alpha^2(\beta D - D\gamma - P)} \right), \\
P^{LURS} &= \left(\frac{\beta + (2m-1)\gamma}{2\alpha^2\gamma}, \frac{1}{2\gamma} \right).
\end{aligned}
$$

The images of trapezoids L and R can be calculated by restricting the dynamics to the corresponding band, i.e., to the case $m = l$ or $m = r$. Thus, we can introduce the restricted versions of the micro-chaos map (4.66): $f_l = f|_{m=l}$ and $f_r = f|_{m=r}$. The images of the quadrangles $f_r(R)$ and $f_l(L)$ are stretched along the unstable manifolds, while the pre-images $f_r^{-1}(R)$, $f_l^{-1}(L)$, $f_l^{-1}(R)$ and $f_r^{-1}(L)$ are stretched along the stable manifolds. One must be careful during the determination of pre-images, since e.g. $f_r^{-1}(L) = \tilde{f}_r^{-1}(L) \cap R$, where

$$\tilde{f}_r^{-1}(L) = \left\{ \tilde{\mathbf{x}} \mid \tilde{\mathbf{x}} = \mathbf{A}^{-1}(\mathbf{x} - \mathbf{b}r), \mathbf{x} \in L \right\}. \tag{4.77}$$

Thus, it may happen that some parts of the calculated pre-image set $\tilde{f}_r^{-1}(L)$ are cut away by the switching line SW_r.

The crossing images and pre-images of the sets R and L in Fig. 4.15 indicate the existence of a Smale horseshoe structure. Moreover, since $f_l(L) \setminus Q_r \neq \emptyset$, i.e., $f_l(L)$ is stretched out from the initial parallelogram, the correspondig set is a transient chaotic repeller. Several different attractors and repellers may coexist at certain parameters. For instance, Fig. 4.16 shows four strange objects next to each other. Two of them (at SW_4 and SW_7) are repellers, while the images of the parallelograms do not stretch out from the initial domain at $m = 5, 6$, thus, two separated attractors exist here. Thus, the phase-space structure of the map can be described as a series of baker's maps that reside between fixed points.

To get a better insight into the complexity of the examined system, we determined the topological entropy h_0 at various values of parameter P by the algorithm given in [23]. The initial regions were chosen to be the parallelograms Q_m, defined previously, at several values of the index m. If the invariant set (or conditionally invariant set in case of transient chaos)

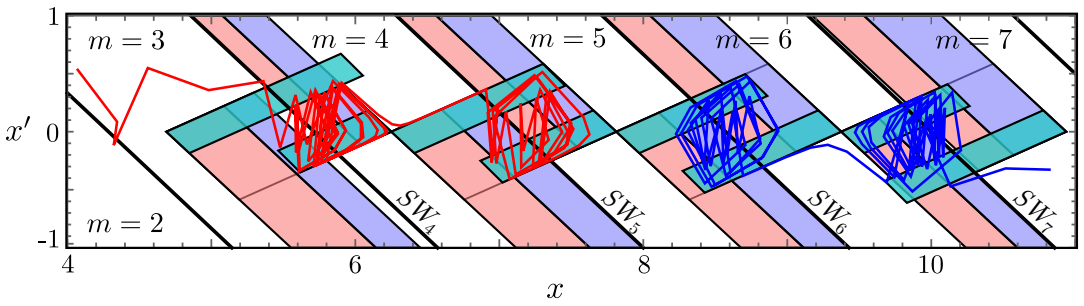

Figure 4.16: *Horseshoe-structures at the switching lines $SW_{4,5,6,7}$ at $\alpha = 0.8$, $\beta = 0.3$, $P = 0.7$, $D = 0.6$. Two trajectories are also shown, leading to disconnected attractors. The points of the trajectories are connected by lines to guide the eye.*

is larger than Q_m, the results provide a lower estimate for the topological entropy. Fig. 4.17 shows the results obtained in the neighbourhood of the switching line SW_3.

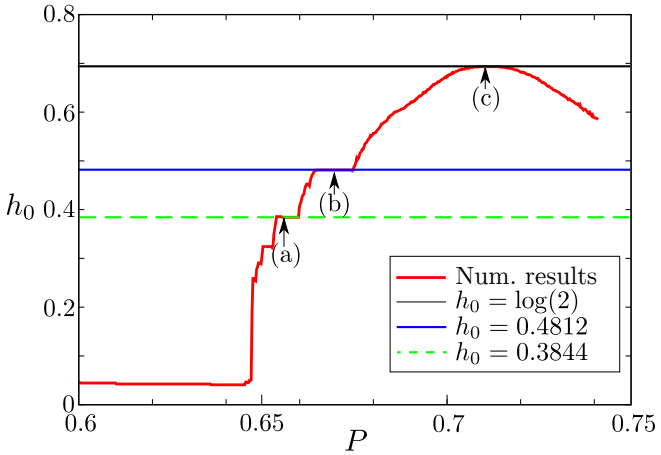

Figure 4.17: *Topological entropy (h_0) versus parameter P at $m = 3$, $\alpha = 0.77$, $\beta = 0.02$ and $D = 0.83$.*

The images and pre-images of the parallelogram Q_m can be calculated analytically. We determined the second pre-images and the third images of the trapezoids on either side of SW_3 at the parameters given in the caption of Fig. 4.17. Parameter P was chosen at three different plateaus of the topological entropy curve. The results are depicted in Fig. 4.18.

In Fig. 4.18(c) the images and pre-images fully intersect, forming a Smale horseshoe structure. The numerically obtained topological entropy is very close to $h_0 = \log(2)$ at this parameter. Indeed, a binary symbolic dynamics can be introduced with symbols denoting the bands on the left and on the right of the switching line. Thus, the examined dynamical system is conjugate to a full binary shift [139]. This property implies that the trajectories are sensitive to initial conditions, the map is topologically transitive and there exists a countable infinity of periodic orbits, an uncountable infinity of nonperiodic orbits and a dense orbit. Thus, map (4.66) is indeed chaotic in a finite parameter domain.

To have a subsystem in the neighbourhood of a certain switching line that is conjugate to a binary shift, the images of the trapezoids L and R (see Fig. 4.15) must stretch out from the initial parallelogram. That is, $f_l(P^{LUSW})$ and $f_l(P^{RUSW})$ must be to the right of the manifold W_R^S (see Fig. 4.15), while $f_r(P^{LUSW})$ and $f_r(P^{RUSW})$ must be to the left of the manifold W_L^S. The fulfilment of these four escape conditions also ensures that the calculated pre-images are in the appropriate bands, i.e., $\tilde{f}_l^{-1}(R) \cap R = \emptyset$ and $\tilde{f}_r^{-1}(L) \cap L = \emptyset$ (cf. Eq. (4.77)). The parameter domains where the aforementioned conditions fulfil, are shown in

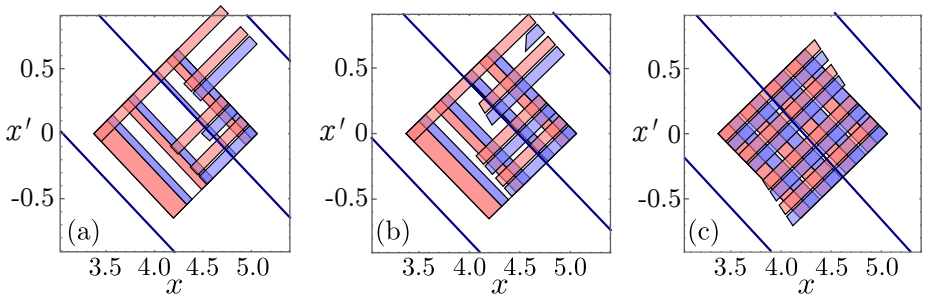

Figure 4.18: *Second pre-images and third images of the trapezoids left (red) and right (blue) of the switching line SW_3. $\alpha = 0.77$, $\beta = 0.02$ and $D = 0.83$. (a) $P = 0.655$, (b) $P = 0.67$, (c) $P = 0.71$, corresponding to Fig. 4.17.*

Fig. 4.19, according to Eqs. (C.48)-(C.51).

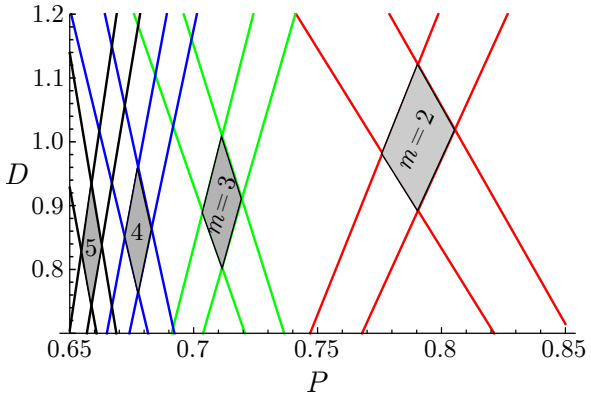

Figure 4.19: *Parameter domains where the dynamics can be described by a full binary shift at parameters $\alpha = 0.77$ and $\beta = 0.02$ at the switching lines $SW_{2,3,4,5}$. Lines with the same colour correspond to the four escape conditions evaluated at the same value of m.*

If $f_l(P^{LUSW})$ or $f_l(P^{RUSW})$ cross the stable manifold W_R^S of $\mathbf{x}_r^*$, a boundary crisis bifurcation occurs and trajectories escape from the quadrangle $L \cup R$ away from the origin. This situation is shown in Fig. 4.15. However, if $f_r(P^{LUSW})$ or $f_r(P^{RUSW})$ cross the stable manifold W_L^S of $\mathbf{x}_l^*$, trajectories escape towards the origin. Consequently, the attracting and repelling properties of the phase-space objects between the fixed points can be determined by evaluating the positions of the aforementioned image points. Note, however, that as parameters are changed, points P^{LURS} and P^{RULS} can be shifted to a neighbouring band, distorting the results. This phenomenon is also a special bifurcation whose conditions can be checked easily – typically, the corner points tend to be in a "wrong" band if parameter P is large.

Fig. 4.20 shows how the attracting/repelling properties of structures at the switching lines vary as the proportional gain is changed. The continuous curves show the attractor/repeller positions at several values of index m, according to (4.74). Possible attractors disappear via border collision bifurcations at $P = m\alpha^2/(m-1)$, this is why curves with higher index m are shorter. Arrows above the curves indicate the attracting or repelling property of the corresponding structure in the direction away from the origin, while arrows below the curves show these properties in the direction towards the origin. Based on these properties, various types of attractors can be defined. A single attractor that is confined to the neighbourhood of the switching line SW_m – i.e., no escape is possible in either direction – is denoted by S_m. If two or more adjacent repellers merge, e.g., that reside in the neighbourhoods of switching lines $m-1$, m and $m+1$, the corresponding large attractor is denoted by $M_{m-1,m,m+1}$.

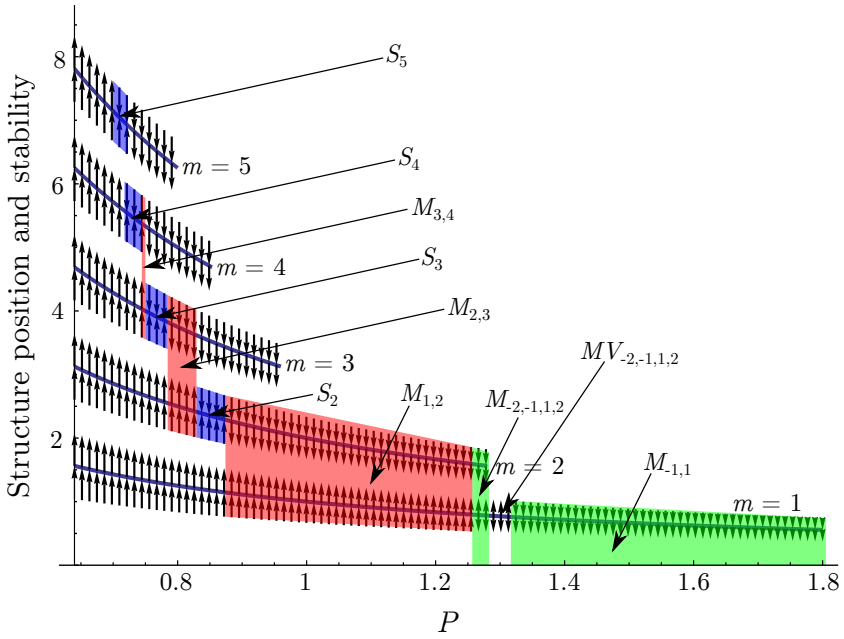

Figure 4.20: *The attracting/repelling properties of phase-space structures at $\alpha = 0.8$, $\beta = 0.3$ and $D = 0.6$, by the crisis-based prediction. Shading indicates various attractors.*

The aforementioned attractors are designated by shaded areas in Fig. 4.20. Note, that a special attractor exists at $P \approx 1.3$, denoted by $MV_{-2,-1,1,2}$. At these parameters, the first virtual fixed point is $\mathbf{x}_1^*$, thus, no strange set is expected in the position indexed by $m = 2$. Although there is a repeller at the switching line SW_1, numerical results indicate that the global dynamics leads back towards the origin, resulting in a larger attractor.

It can be shown that if the parameters are chosen from the domain of stability, the increase of parameter P increases the attractivity of the origin. This trivial result implies that as P is increased, the arrows can flip downwards, only (cf. Fig. 4.20). Consequently, there are only two different scenarios possible at a certain value of m: both arrows are directed upwards at small P. As P is increased, either the lower or the upper arrow flips downward. If the upper arrow flips first, a single attractor is born. However, if the lower arrow flips, the structure will repel in both directions. Finally, at even larger values of the proportional gain, the other arrow flips, too, giving rise to a repeller directing the trajectories towards the origin. We could also show analytically that no escape away from the origin is possible close to the border collision bifurcation points, i.e., at the right endpoints of the lines the upper arrows always point downwards.

It must be emphasized that the classification of the strange sets based on their attracting or repelling properties is not always accurate, especially near the borders of the domain of stability. As we pointed out in **[43]**, there are two major sources of the inaccuracies: either not all the parts of the theoretically predicted attractor are visited by the trajectories, or the trajectories "jump over" whole bands instead of arriving in a neighbouring band. It can be shown that the damping strongly influences this kind of behaviour: the length of jumps is approximately proportional to $e^{\gamma-\beta}$.

In a real control system the sampling period is significantly shorter than the shortest characteristic time of the mechanical system. Consequently, the realistic values of α, β, P and D – and the sizes of the attractors – are rather small and the effect of one iteration step of map (4.66) on the trapezoids L and R is hard to visualize. However, the topology of the phase-space is similar to the one shown in Fig. 4.16. The results of a simple cell mapping technique [85], **[42]** are depicted in Fig. 4.21 at parameters of a real experimental device [58]

– an inverted pendulum with mass moment of inertia $M = 0.042\,\mathrm{kg\,m^2}$ and length $l = 0.5\,\mathrm{m}$. The parameters of digital control are $\tau = 0.001\,\mathrm{s}$ and $\Delta F = 0.024\,\mathrm{Nm}$. The maximal control error is about $0.08\,\mathrm{rad} \approx 4°$. The colours in the figure characterise the number of steps necessary to reach an attractor. The triangular red regions in the upper right and lower left corners correspond to points that leave the computational domain in a couple of steps.

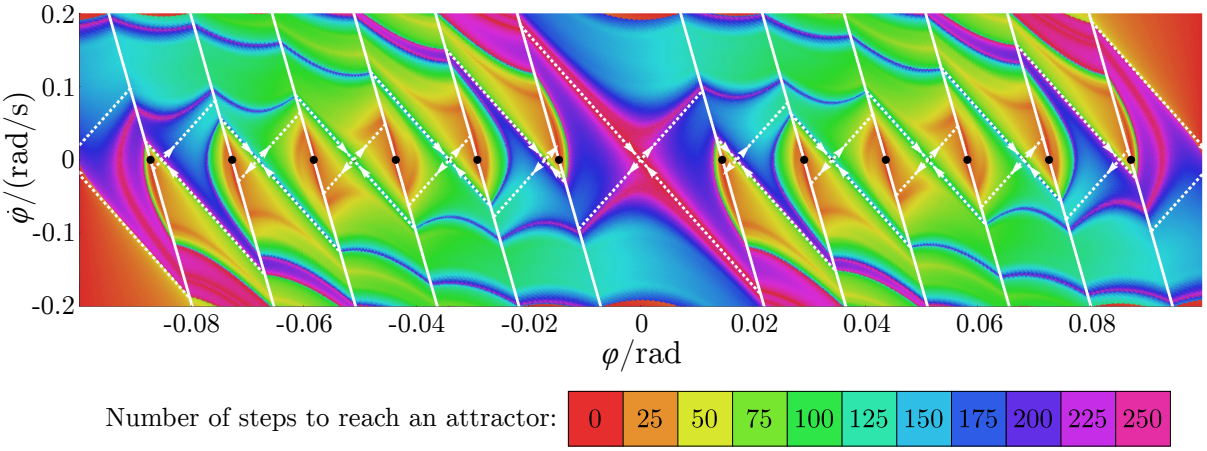

Figure 4.21: *Cell mapping results showing the domains of attraction (coloured domains) of 12 tiny disconnected attractors (covered by the black points) at parameters* $\alpha = 6.8511 \cdot 10^{-3}$, $\beta = 0$, $P = 5.4997 \cdot 10^{-5}$, *and* $D = 2.5665 \cdot 10^{-3}$. *The switching lines (solid, white) and the stable and unstable manifolds (dashed, white) are also shown.*

As this figure illustrates, there are parameter domains where several disconnected chaotic attractors coexist in the phase space. Although the diameter of these sets is usually negligibly small in practice, they can reside very far from the origin, leading to remarkable deviance from the desired state. This is why the size of the absorbing sphere can be important for applications: it provides an upper limit of the control error.

It is worth to mention that a secondary digital effect occured at small values of α ($\alpha < 0.01$): during the simulation of the micro-chaos map certain trajectories could escape from attractors far from the origin. This phenomenon is clearly related to the finite number of digits used during the simulation [55].

4.5.4 Control error estimation

The simplest estimation of the size of the absorbing sphere is based on the topological considerations, described in Section 4.5.2. According to the results presented there, the attractor that is farthest from the origin can be located at the $m_{\max}$th switching line (see (4.76)), at position $x^{SW}_{\max}$:

$$m_{\max} = \mathrm{Int}\left(\frac{P}{P-\alpha^2}\right), \quad x^{SW}_{\max} = \frac{m_{\max}}{P}. \tag{4.78}$$

These results are valid if the diameters of the attractors are small compared to the distance of switching lines, i.e., no jumps or other escaping mechanisms occur. In this case

$$x^{SW}_{\max} \approx \frac{1}{P-\alpha^2} \tag{4.79}$$

provides a conservative estimate for the maximal control error. Note, that we developed an estimation method in **[43]** that leads to a similar result

$$\mathbf{x}_{\max} = \begin{bmatrix} \frac{1}{P-\alpha^2} \\ 0 \end{bmatrix}, \tag{4.80}$$

provided that the leading eigenvalue of $\mathbf{S}$ is positive. In case of complex eigenvalues, only rather crude error estimates can be obtained analytically. Typically truncated series are evaluated to obtain an upper bound [4], **[43]**. The micro-chaos map was also derived in the case of an inverted double pendulum **[75]**. The results support the applicability of the general formulae of Section 4.2.

4.6 CLUSTERED CELL MAPPING METHOD

4.6.1 Introduction

Cell Mapping methods (or shortly CM methods) were introduced by C.S. Hsu [84, 85], to make the quick and thorough global analysis of nonlinear mechanical systems possible. He applied the mathematical background of cell mapping even in case of digitally controlled systems [162].

Cell mapping methods discretize a region of the state space, thus creating the so called cell state space. For each cell one or more image cells are assigned (to where the dynamics lead from that cell), and by analysing the resulting graph or Markov-chain, periodic orbits, fixed points and their domains of attraction can be found. Consequently, as we demonstrated in Section 4.5.3, CM methods can provide valuable information about the global dynamics of systems with complicated phase-space structure.

The simplest CM method is the Simple Cell Mapping (SCM) and in the simplest case the cell state space is an n-dimensional grid of cells of the same size. The basic idea of the SCM method is that each cell has a single image, which is usually determined using the Centre Point Method [85], namely, a single trajectory from the centre of the *cell domain* is examined. In other words, all states within a cell are mapped to a single cell. Due to this property, the method is able to classify cells either as *periodic* cells (belonging to a periodic group) or *transient* cells (leading to a periodic group). The successful classification of all cells forms the *solution of the SCM*.

There are many variations of the CM methods, usually a relatively fast CM method (for example SCM) is applied to the initial state space region, then further analysis is carried out at certain locations, using more advanced methods (Generalized Cell Mapping, for instance), typically with a refined cell state space [169], [173]. These methods are excellent if the *interesting region* of the state space is known, but if that is not the case, a method capable of automatically extending the analysed state space region could be more suitable. As a result of a joint work with Gergely Gyebrószki, we extended the Simple Cell Mapping with such capability in **[72]**.

To emphasize the relevance of adaptive state space extension, one can recall the following situations:

- The dynamical system has an expectedly complex state space and the enclosing region of state space objects is not known.
- The dynamical system has more than one attractors, and not all of them are found in the initial state space region. Escaping trajectories indicate the possible direction of other attracting structures.

- A lower dimensional state space object, e.g., a basin boundary is being followed.
- Examination of global bifurcations or crises in dynamical systems in cases when the structure and/or the size of state space objects change abruptly during the variation of certain parameters.
- Analysing diffusion-like processes, for example intermittent maps [97].

Our approach to solve the problem of state space extension is to find an adjacent region to the initial state space, to where most of the trajectories escape. Afterwards, a separate CM solution is calculated on that region and the two solutions are joined. Upon the joining procedure, new state space objects residing on the boundary of the two cell state spaces are also discovered. The developed method of joining separate SCM solutions to a cluster of SCM solutions is referred to as Clustered SCM method **[72]**.

As an example of application, we show the analysis of the 2D micro-chaos map without delay that was introduced in Section 4.5. The behaviour of this piecewise smooth system fits into most of the aforementioned situations, as it exhibits a pattern of chaotic attractors and crisis phenomena with the appearance or disappearance of chaotic attractors/repellers.

Definitions and abbreviations

This section describes the basics terms, definitions and properties related to the Simple Cell Mapping (see Figure 4.22).

- *Cell state space* (CSS): the bounded and discretized state space region, which is continuously covered by arbitrary *cell domains*. In the simplest case n-dimensional rectangular cuboids of the same size can be used to discretize an n-dimensional state space.
- *Cell domain*: bounded domain of the state space, part of the *cell state space*. In the simplest case it can be represented by a centre point in the state space and lengths along each dimension.
- *Cell*: object having its unique *index* referencing to a *cell domain* and various properties (e.g. *image*, *pre-image*).
- *Cell index* (or shortly *index*): cell property; a unique identifier.
- *Image*: property of a cell, one or more references to other cells. The dynamics from the *cell domain* corresponding to the cell lead to the *cell domain(s)* indexed by the *image(s)*.
- *Pre-image*: property of a cell, one or more references to other cells. The dynamics from the *cell domain(s)* indexed by the *pre-image(s)* lead to the *cell domain* corresponding to the cell.
- *Sink cell* (SC): a special *cell* indexing the unbounded region of the state space outside the CSS. Once a trajectory enters the sink, its evolution is no longer followed. To express this property, the *image* of the sink is itself by definition.
- State-to-index (or shortly *index()*) function: is a surjective function returning the *index* corresponding to the *cell domain* covering the given point in the state space.
- Index-to-domain (or shortly *domain()*) function: is a bijective function returning the *cell domain* representation for the given *index*.

- *Cell sequence*: A set of cells formed by tracking the *image* of cells subsequently. (See cells $\{7, 2, 4, 11, 18, 24, 16\}$ in Figure 4.22.)

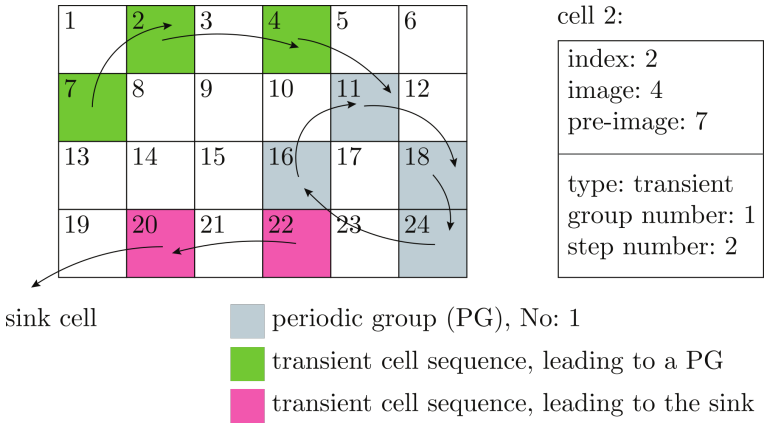

Figure 4.22: *Explanation of the definitions*

- *Periodic group* (PG): A part of a cell sequence, that might constitute a periodic motion. A periodic cycle of n cells forms a periodic group, with periodicity n (or shortly an n-P group). Each cell within the PG is a *periodic cell* with period n, or shortly n-P cell [85]. (For example, the sink cell is a 1-P cell and forms a 1-P group.)

- *Transient cell*: Cell sequences leading to an n-P cell contain an n-P group at the end of the sequence. All other cells within the sequence are *transient* cells leading to that periodic group, forming a *transient cell sequence*.

- *Transient cell sequence*: cell sequences with their destination n-P cells removed form a *transient cell sequence*, see Figure 4.22.

- *Group number* (g): For each periodic group a unique group number is assigned. All periodic cells within a PG and all transient cells leading to that PG have the same specific group number assigned.

- *Step number* (s): property of a cell, the number of steps required to reach a PG. *Periodic cells'* step number is $s = 0$, while *transient cells'* step number is $s > 0$.

- *Domain of Attraction* (DoA): the DoA of a PG with group number g is the set of (transient) cells with the same group number g and step number $s > 0$. The Domain of Attraction is a discretization of the *Basin of Attraction* [122].

- *SCM solution*: After the successful execution of the SCM method, besides the initial cell properties, the *group number* and *step number* properties are assigned to each cell. At this stage all periodic groups and their domains of attraction are found, and we call the cell state space and its properties the *SCM solution*.

4.6.2 Joining two SCM solutions

This section describes the procedure of joining two SCM solutions with non-overlapping cell state spaces. No other restrictions apply to the cell state spaces, even non-adjacent regions can be joined. First, the possible relationships between cells of the SCMs are examined, then the algorithm of joining is explained. We adopt the following conventions to aid the joining procedure:

- Group number $g = 0$ is assigned to the sink cell. Also the sink cell's index is 0.
- A new property, called *cell mapping index* (shortly: *cmid*) is assigned to each cell as an extension to its *group number* indicating which SCM contains the group referenced by the *group number*. Initially all SCM solutions have a unique *cmid*, and all cells within an SCM solution have the same *cmid*.
- Cells have an auxiliary *state* property, which can take any of the following three values: UNTOUCHED, UNDER_PROCESSING, PROCESSED. This property is used to keep track of the solution procedure.

Relationship of two SCM solutions

Upon joining two SCM solutions, transient cell sequences leading to the sink cell are examined, because these cell sequences might enter the other SCM's cell state space and lead to an object within the *united cell state space* – the union of the two cell state spaces. The state space region outside the *united cell state space* is called *reduced sink*. While examining an SCM solution's transient cell sequences that lead to its original sink, the following cases can occur (Figure 4.23):

1. The *transient cell sequence* leads to a known destination:
   (a) the *reduced sink* or
   (b) a *periodic* or *transient* cell with group number $g > 0$ of the other SCM.
2. The *transient cell sequence* leads to a cell of the other SCM, which belongs to the domain of attraction of its original sink (so the cell's group number is $g = 0$). This means that the final destination of the sequence is not known yet.

Considering the above cases, only Case 2 requires further analysis. Otherwise, transient cell sequences can be updated with a new group and step number (along with a new cell mapping id), corresponding to their new destination.

The procedure of joining two SCM solutions is therefore divided into two stages. Stage 1 enumerates all *transient cell sequences* and also updates those corresponding to Case 1. Stage 2 analyses the remaining sequences of Case 2.

Cell tree mapping

It is clear, that cell sequences leading to the other SCM's sink cell's domain of attraction (Case 2) will arrive eventually at one of the already existing periodic groups (including the *reduced sink*), or they might form a new periodic group – possibly with some extra transient cells leading to that PG.

This calls for the idea of mapping these remaining transient cell sequences onto each other (or onto some already determined cell). Transient cell sequences form trees called *cell trees* that lead to a single cell (which belongs to the other SCM), therefore these trees can be handled just like cells in SCM. The *image* of a *cell tree* is either a cell which was updated in the first stage of the joining procedure (Case 1), or a member cell of another *cell tree* of the other SCM. Tracking the images of *cell trees* creates *tree sequences*. A *tree sequence* either leads to an already existing periodic group or forms a new periodic group and some transient cells leading to that group. Figure 4.24 illustrates the procedure of cell trees mapping.

Shortly, the SCM method can be applied to the *cell trees*. If a *tree sequence* leads to a previously processed cell, all of its member cells can be tagged with the appropriate *cmid*,

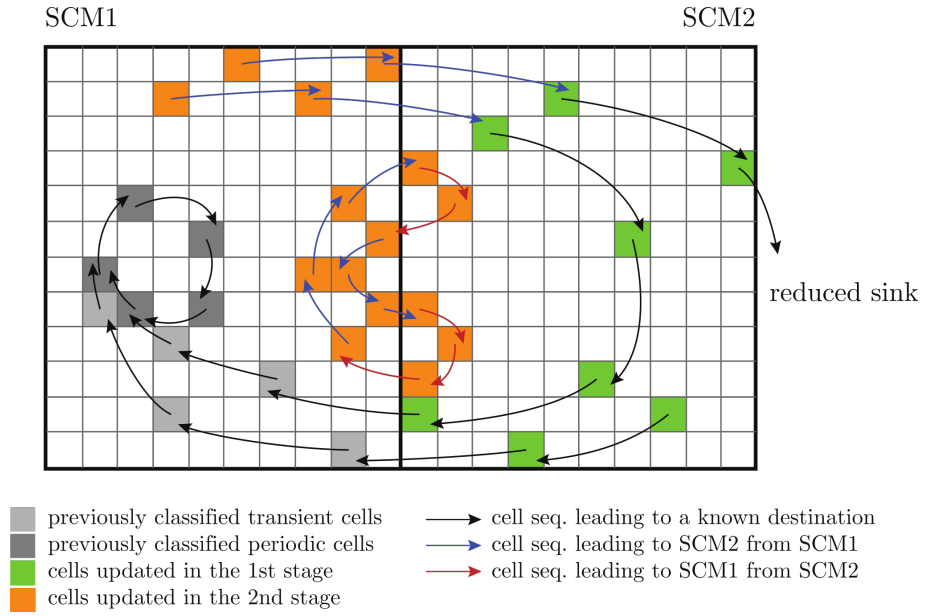

Figure 4.23: *Joining of previously calculated SCM solutions. Cell sequences leading to a known destination can be updated in Stage 1 (green cells), while sequences leading to another unclassified sequence or transient cell need further analysis in Stage 2 (orange cells). As a result, new periodic groups can be found near the boundary of SCM1 and SCM2.*

group and *step* numbers. Otherwise the trees form a graph containing a single cycle – the new periodic group – and branches which are transient cells belonging to that group, hence the *cmid*, *group* and *step* numbers can be updated. (The new periodic groups obtained this way must be added to one of the SCM solutions to have a valid *cell mapping index*.)

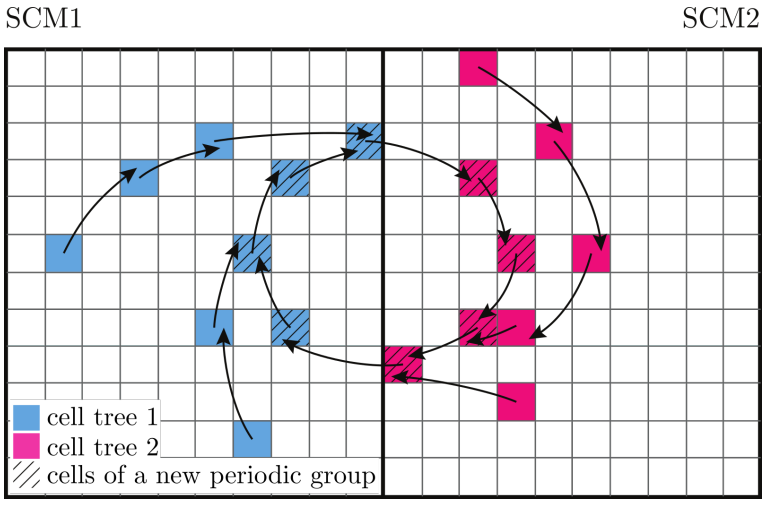

Figure 4.24: *Illustration of the notion of cell tree mapping. Cell trees 1 and 2 are mapped to each other. The graph formed by them contains a cycle (new periodic group), and all other branches are transient cells leading to that group.*

The algorithm of joining

The algorithm of joining two SCM solutions consists of three steps: preprocessing, and two stages of classifying cell sequences which previously led to the sink cell. The details of these steps are described in Appendix C.4.4 with pseudo codes.

During preprocessing, the cells corresponding to the domain of attraction of the sink cell for both SCM solutions are identified. This can be done by selecting cells with group number 0. Checking the step number is not necessary, since all cells with group number 0 must be transient cells. For the pseudo code of the preprocessing see Algorithms C.3 and C.4.

Once the domain of attraction of the sink cell is identified for each SCM solution, the first stage of joining examines *transient cell sequences* and updates cells that belong to Case 1, according to Algorithm C.5.

In the second stage, cell sequences belonging to Case 2 are analysed and a *cell tree mapping* is carried out (Algorithm C.6). In the end of Stage 2, all cell trees are processed and new periodic groups (if any) with their domain of attraction (transient cells) are found. The complete procedure of joining is summarized in Algorithm C.7.

Complexity of joining

The complexity of calculating an SCM solution is $O(n)$ where n is the number of cells in its cell state space. This comes from the fact that every cell needs constant amount of operations for initialization, and their state changes twice: first to UNDER_PROCESSING then to PROCESSED (Algorithm C.8).

The complexity of preprocessing (Algorithm C.3) is also linear, since a constant amount of operations must be performed for each cell. For SCM solutions with n and m cells, the complexity of preprocessing is $O(n + m)$.

During the first and second stages of the joining procedure (Algorithms C.5 and C.5), every cell is tagged with a new state maximum twice. Thus, these are also linear in terms of the number of cells to be processed. The linear nature of the joining procedure can also be seen in the computation times presented in Table 4.1.

4.6.3 Application and Results

The Clustered SCM method was applied to the micro-chaos map (4.66) at $\alpha = 0.078$, $\beta = 0$, $P = 0.007$, $D = 0.02$. The phase-space (or state-space) of the map is illustrated in Figure 4.25, showing two regions that are joined by the developed method. The resulting cluster

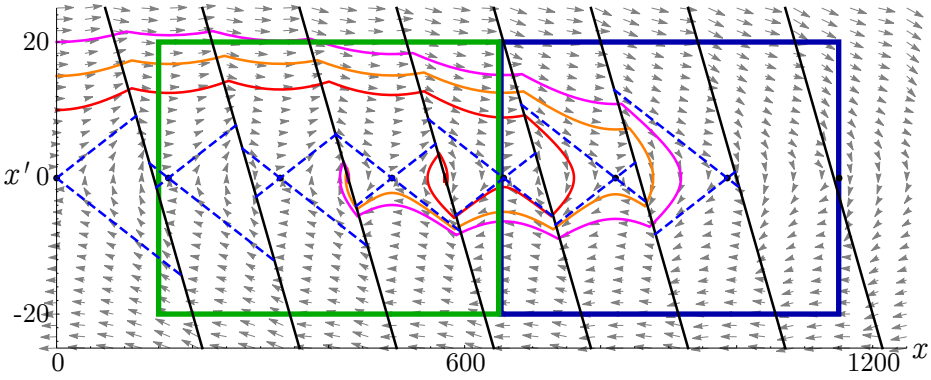

Figure 4.25: *The state space of micro chaos map. Dashed blue lines: stable and unstable manifolds of saddle points. Three example trajectories leading to chaotic attractors are shown; their subsequent points are connected with line sections for better visibility. The green and blue rectangles show the initial and the adaptively chosen state space regions, respectively (see Figure 4.26).*

of two SCM solutions is illustrated by coloured images in Figures 4.26-4.28. Red colour indicates transient cells leading to the sink, other coloured regions illustrate the domain of

attraction of other periodic groups. The periodic groups residing at the intersections of the x-axis and the switching lines are denoted by black dots. These PGs correspond to very small chaotic attractors of the micro-chaos map. White lines indicate the switching lines and dashed white lines denote the stable and unstable manifolds of the saddle points of the map. The initial state space region is placed on the left and the new subregion is on the right side, since the right adjacent state space region contains the most escaping trajectories.

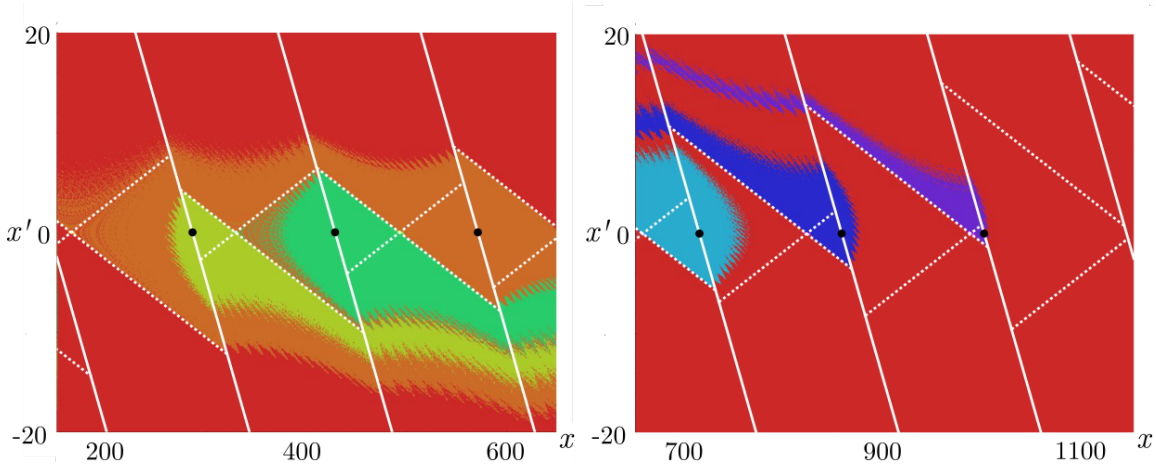

Figure 4.26: *Initial SCM solutions before the joining procedure. The image on the left shows the initial state space region, the one on the right is the adaptively selected region. Both regions contain 3 chaotic attractors, denoted by black points.*

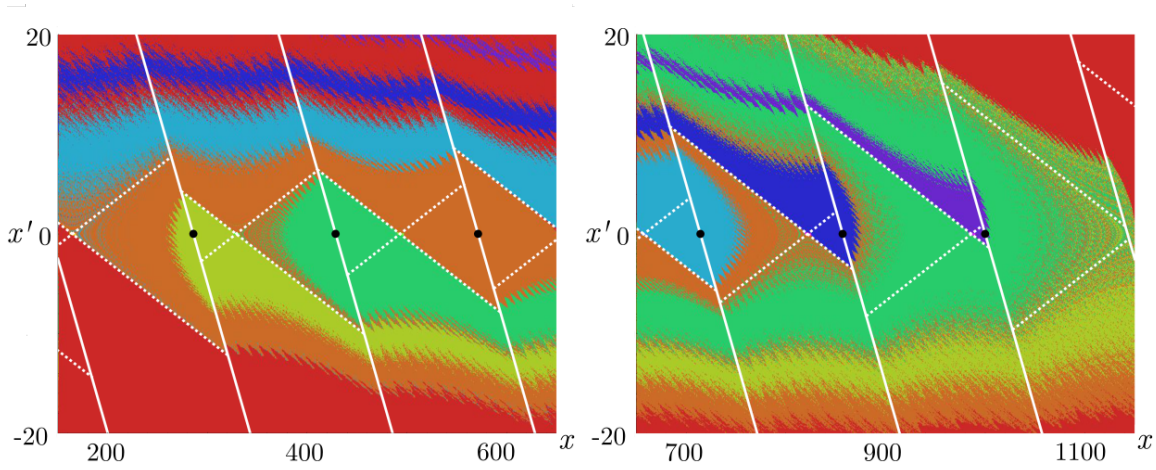

Figure 4.27: *SCM solutions after Stage 1 of the joining procedure. Cell sequences leading to a PG of the other SCM are updated (recoloured with the colour of the corresponding periodic group). The initial region contains some transient cell sequences which are stored for further processing in Stage 2. (See red bands at the top of the left image.)*

Comparison of real computational efforts

To support the statements in Section 4.6.2, computation times for Example are provided using the Clustered SCM and an SCM solution over the full region is calculated for comparison (see Table 4.1 and Figure 4.29). Since the calculation of SCM1 and SCM2 can be done in parallel, the total processing time is calculated as $t_{\text{total}} = \max(t_{\text{SCM1}}, t_{\text{SCM2}}) + t_{\text{joining}}$. (Computations were carried out using 2 cores of an Intel Core™ i7-4700MQ CPU.) The

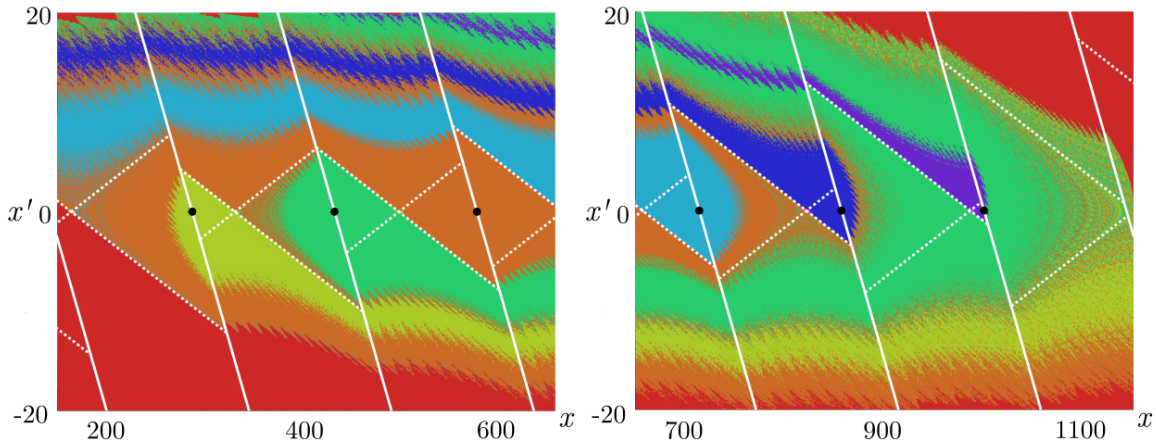

Figure 4.28: *SCM solutions after Stage 2 of the joining procedure. Examined cell trees are mapped to already processed cells (corresponding to the PGs with green and orange domain of attraction).*

joining time only depends on the number of cells and the state space topology, while the computation time of SCM solutions also depends on the effort needed to calculate the image cells. For systems, where greater effort is necessary for the calculation of images (e.g. flows), the computation time of joining is relatively smaller compared to the complete procedure.

Number of cells	CPU time [ms]				
	t_{SCM1}	t_{SCM2}	t_{joining}	t_{total}	SCM on full region
500000	395	386	89	484	844
1000000	780	791	190	981	1573
2000000	1550	1551	418	1969	3316
4000000	3234	3225	897	4131	6752
8000000	6638	6720	1935	8655	13389

Table 4.1: *Computation times in the example. (See Figures 4.26-4.28.)*

4.6.4 Advantages of the proposed method

Clustering has the following remarkable advantages.

- The method allows the adaptive extension of the SCM solution towards new state space regions. Solving an SCM for a new region and incorporating it into the cluster is cheaper than solving an SCM over the whole extended state space (see Table 4.1).

- Parallelization is trivial as separate SCM solutions can be generated independently before the joining procedure. Also Stage 1 of the joining procedure (for each previously calculated SCM solution) can be done in parallel.

- The method is useful in real-time situations, where the region of interest is changing as a parameter is varied. Clustered cell mapping handles screen panning well, as a separate SCM solution at the (narrow) state space region entering into the computer's screen can be calculated quickly and joined to the already existing cluster.

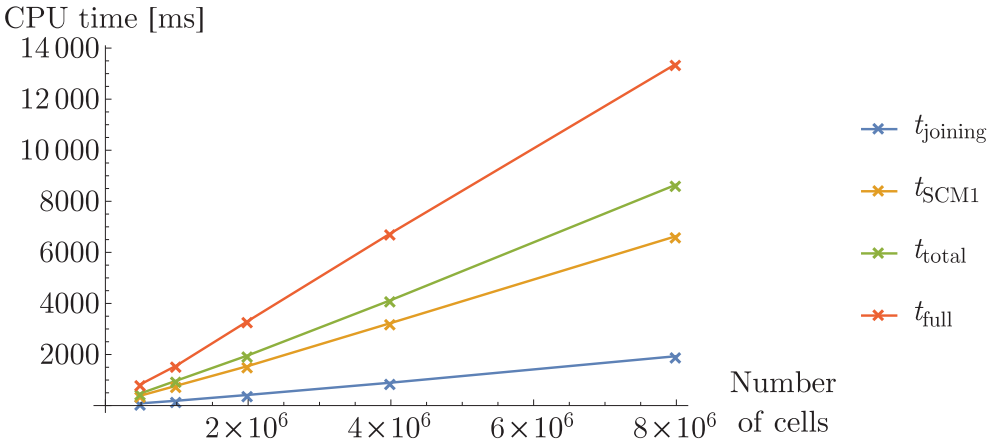

Figure 4.29: *Comparison of computation times listed in Table 4.1.*

- The proposed approach helps to overcome memory limitations by dividing large problems into smaller ones. During the generation of a clustered SCM solution, if all adjacent regions of a cluster are already examined, the SCM solution corresponding to the inner (fully surrounded) cluster can be written to disk and freed from memory.

4.7 EXTENSIONS AND EXPERIMENTAL RESULTS

This section discusses further results related to the micro-chaos phenomenon, which we obtained in the framework of our joint work with Gergely Gyebrószki **[72, 75, 76, 77]**.

4.7.1 The effect of dry friction

Real-world systems are all subject to various types of dissipating mechanisms. While viscous damping was taken into account in Section 4.5, it is natural to ask whether does micro-chaos persist if dry friction is present?

In order to answer this question, the equation of motion of the inverted pendulum (4.65) was supplemented by a dry friction term. After algebraic transformations, we obtained that if the sign of the dry friction term does not change between the jth and $j+1$st sampling instants, the following map describes the dynamics **[77]**:

$$\mathbf{x}_{j+1} = \mathbf{A}\,\mathbf{x}_j + \mathbf{b}\left(\underbrace{\mathrm{Int}(\hat{P}\,x_j + \hat{D}\,x'_j)}_{m_i} + \underbrace{\mathrm{sgn}(x'_j)\,\hat{\mu}}_{\mu_j}\right). \tag{4.81}$$

Here m_i is the control effort, μ_i is the friction force and $\mathrm{Int}(\cdot)$ denotes the integer part function representing the quantization of the control effort. This quantization is a *map-like switching* in the system: the controller updates the control effort at sampling instants, only. At $\hat{\mu} = 0$ (i.e., no friction), there is no other discontinuity in the system, so (4.81) fully describes the evolution of the solutions. However, the signum function corresponding to friction is a *flow-like switching*, because the sign of the friction force changes at every time instant when the velocity changes sign – regardless of the sampling. The combined effects of these two kinds of switching phenomena were also analysed by Budai et. al. [16, 17, 18], focusing on the stability and special (but non-chaotic) vibrations of mechatronic systems.

To handle the case when the velocity changes sign within the j^{th} sampling interval, the micro-chaos map was divided into three steps: 1) time evolution until the velocity becomes

zero at time instant $T_{0,j}$ (to be determined), 2) change of the sign of friction force (or sticking), and 3) time evolution until the next sampling interval. As a result, we obtained the so-called hybrid micro-chaos map **[77]**. The phase-space structure of this map was analysed by the Clustered Simple Cell Mapping (C-SCM) **[72]** introduced in Section 4.6. The results depicted in Fig. 4.30 show that certain chaotic attractors may persist if dry friction is present, while others are absorbed by sticking zones.

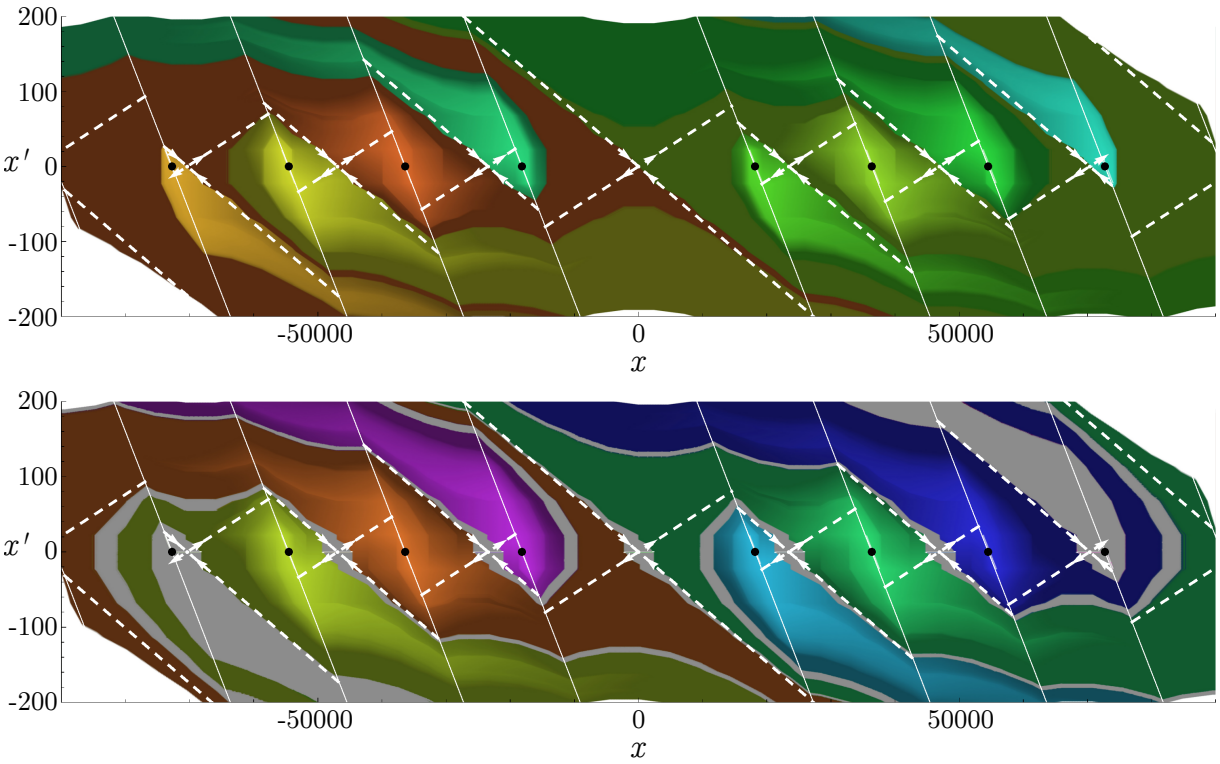

Figure 4.30: *C-SCM results for* $\alpha = 6.53 \times 10^{-3}$, $\beta = 0$, $P = 5.5 \times 10^{-5}$, $D = 2.5 \times 10^{-3}$, Top: $\hat{\mu} = 0$, Bottom: $\hat{\mu} = 0.095$. *Chaotic attractors are indicated by black dots, their basins of attraction are coloured regions. The fixed points' manifolds are shown as white dashed lines. The basins of attraction of sticking zones are grey; the bottom subfigure shows the case, when the outermost chaotic attractors are absorbed by sticking zones.*

4.7.2 Twofold quantization

In the micro-chaos models analysed in the previous sections, only the quantization of the control effort was considered. However, in real systems, both the input (e.g., measured displacement and velocity) and the output are quantized. Fig. 4.31 illustrates the case when the input – coordinate $\tilde{x}$ – is measured with resolution r_{I}, while the output – the control effort u – is sent out according to the resolution r_{O}, and the sampling period is τ.

It was shown in **[75]** for the case of an inverted pendulum that the effects of input quantization are similar to those that can be experienced if the output is quantized. However, chaotic vibrations are typically superimposed on a larger-scale periodic solution (see Fig. 4.32). The effects of twofold quantization were analysed in **[76]** via the extension of the model (4.57). Introducing the dimensionless time $T = t/\tau$, the equation of motion can be given as

$$\tilde{x}''(T) + 2\beta\tilde{x}'(T) - \alpha^2\tilde{x}(T) = -r_{\mathrm{O}}\,\tau^2\,\mathrm{Int}\left(\frac{P\,r_{\mathrm{I}}}{r_{\mathrm{O}}}\mathrm{Int}\left(\frac{\tilde{x}_j}{r_{\mathrm{I}}}\right) + \frac{D\,r_{\mathrm{I}}}{\tau\,r_{\mathrm{O}}}\mathrm{Int}\left(\frac{\tilde{x}'_j}{r_{\mathrm{I}}}\right)\right),\ T \in [j, j+1), \tag{4.82}$$

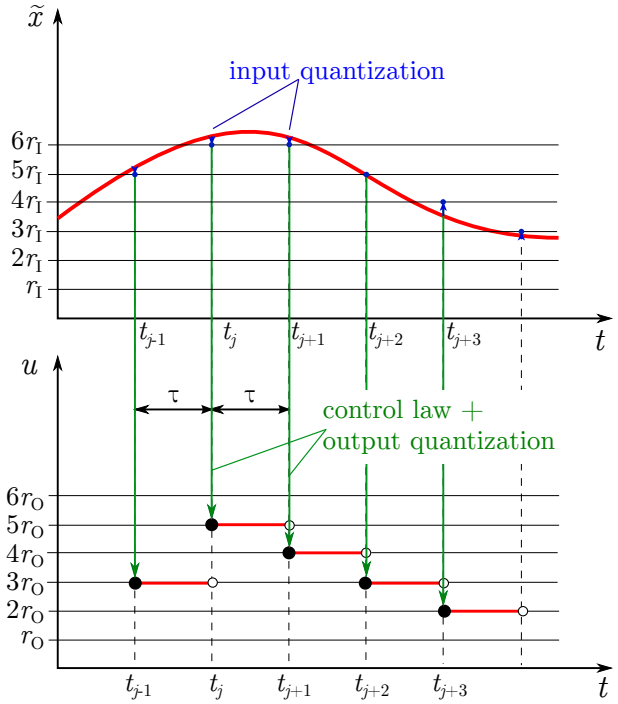

Figure 4.31: *Illustration of the quantization at the input (coordinate $\tilde{x}$) and output (control signal u) of the control system, and the zero-order-hold scheme.*

where the quantization is applied to both the input and the output.

In real applications, the velocity is usually calculated from measured displacement values, by a finite difference scheme. There are several possible choices, but all of these schemes use the earlier values of the displacement, too. To avoid the corresponding delay in the equation (that would result in the increase of the dimensionality of the problem), we assume that the velocity $\tilde{x}'$ is also measured, and its resolution is r_I/τ. Thus, according to the definition of the dimensionless time T, one can write

$$\frac{\mathrm{d}\tilde{x}}{\mathrm{d}t}\,\frac{\tau}{r_I} = \frac{\tilde{x}'}{r_I}. \tag{4.83}$$

This results in the same dimension in displacement and velocity with the same quantization resolution r_I at the input.

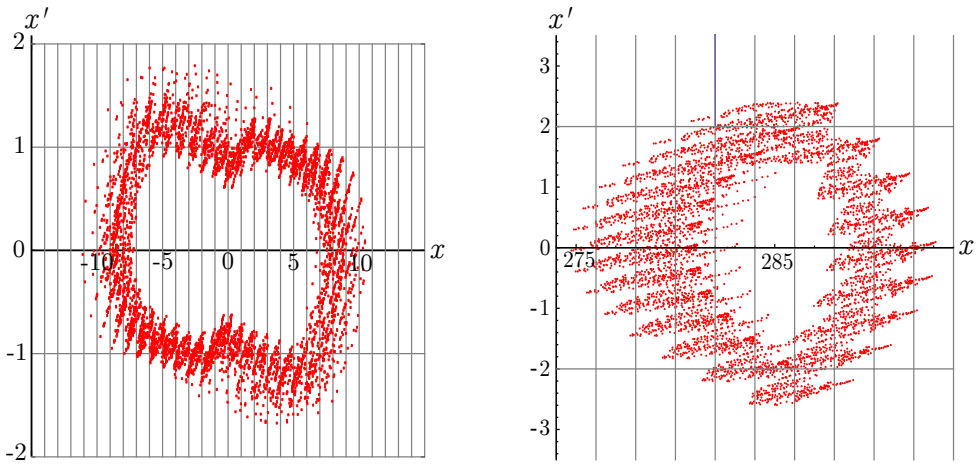

Figure 4.32: *Attractors obtained by inner quantization (left) at $P = D = 0.25$, $\alpha = 0.45$ and double quantization (right) at $P = 0.007$, $D = 0.02$, $\alpha = 0.074$ and $\rho_I = 2$*

In some cases, one of the quantizations is dominant over the other, and therefore the quantization with higher resolution can be neglected, and one of the *single quantization* models can be used (where either the input, or the output is quantized) **[38]**. In order to reduce the number of resolution parameters, we rescale the space coordinate with a properly chosen characteristic displacement.

Using the scaling $x = \tilde{x}/X_{\mathrm{O}}$, where $X_{\mathrm{O}} = r_{\mathrm{O}}\,\tau^2$, the equation of motion assumes the following form:

$$x''(T) + 2\beta x'(T) - \alpha^2 x(T) = -\mathrm{Int}\left(\frac{P\,r_{\mathrm{I}}}{r_{\mathrm{O}}}\mathrm{Int}\left(\frac{x_j\,r_{\mathrm{O}}\,\tau^2}{r_{\mathrm{I}}}\right) + \frac{D\,r_{\mathrm{I}}}{\tau\,r_{\mathrm{O}}}\mathrm{Int}\left(\frac{x'_j\,r_{\mathrm{O}}\,\tau^2}{r_{\mathrm{I}}}\right)\right).$$

Introducing $\rho_{\mathrm{I}} = r_{\mathrm{I}}/(r_{\mathrm{O}}\,\tau^2) = r_{\mathrm{I}}/X_{\mathrm{O}}$ one can write:

$$x''(T) + 2\beta x'(T) - \alpha^2 x(T) = -\mathrm{Int}\left(P\,\tau^2\,\rho_{\mathrm{I}}\,\mathrm{Int}\left(\frac{x_j}{\rho_{\mathrm{I}}}\right) + D\,\tau\,\rho_{\mathrm{I}}\,\mathrm{Int}\left(\frac{x'_j}{\rho_{\mathrm{I}}}\right)\right).$$

For the sake of simplicity, we introduce the parameters $\hat{P} = P\tau^2$ and $\hat{D} = D\tau$. By the abuse of notation, the hat symbols can be discarded, leading to

$$x''(T) + 2\beta x'(T) - \alpha^2 x(T) = -\mathrm{Int}\left(P\,\rho_{\mathrm{I}}\,\mathrm{Int}\left(\frac{x_j}{\rho_{\mathrm{I}}}\right) + D\,\rho_{\mathrm{I}}\,\mathrm{Int}\left(\frac{x'_j}{\rho_{\mathrm{I}}}\right)\right). \tag{4.84}$$

Note, that another possible scaling is $x = \tilde{x}/X_{\mathrm{I}}$, where $X_{\mathrm{I}} = r_{\mathrm{I}}$. In Eq. (4.84) a single *quantization ratio* (ρ_{I}) characterises the ratio of input and output quantization resolutions. For large ρ_{I}, the input quantization dominates, and the outer quantization can be practically neglected. Similarly, for small ρ_{I} values, the output quantization is more significant.

Solving the equation of motion between the subsequent sampling instants, one obtains the following micro-chaos map:

$$\mathbf{y}_{j+1} = \mathbf{A}\,\mathbf{y}_j + \mathbf{b}\,u_j, \quad \text{where} \quad u_j = \mathrm{Int}\left(\rho_{\mathrm{I}}\left(P\,\mathrm{Int}(x_i/\rho_{\mathrm{I}}) + D\,\mathrm{Int}(x'_i/\rho_{\mathrm{I}})\right)\right) \text{ if } X = X_{\mathrm{I}}. \tag{4.85}$$

Here u_j is the control effort between the dimensionless sampling instants $T = j$ and $T = j{+}1$.

It is clear, that the quantization causes the control effort u_j to be a piecewise constant function over the state space, which consists of domains, each corresponding to a specific u_j value. When the *output-quantization* is dominant, $u_j = \mathrm{Int}\left(P\,x_j + D\,x'_j\right)$. Thus, the aforementioned domains are parallel bands separated by parallel switching lines

$$x' = \frac{m - Px}{D}, \quad m \in \mathbb{Z}, \tag{4.86}$$

as we saw in Section 4.5. For the *input-quantization* case, however, these domains are rectangular areas since $u_j = P\,\mathrm{Int}(x_j) + D\,\mathrm{Int}(x'_j)$. Consequently, the quantization results in a grid of horizontal and vertical switching lines (see Fig. 4.33).

To illustrate the phase-space structure if both quantizations are present, the switching lines corresponding to relatively small values of ρ_{I} are shown in Fig. 4.34. If the input quantization is less significant compared to the output quantization, the switching lines become jagged, and the evolving stairs-like lines more or less follow the straight lines of the output-only quantization case.

However, as parameter ρ_{I} is increased, the input quantization will be more pronounced, and the size of the steps on the switching lines increase. At a certain value of ρ_{I}, two switching lines touch each other. This new bifurcation is referred to as *switching line collision* (SLC). The collision of neighbouring switching lines is the first order SLC, while the collision of SW_m and SW_{m+n} is referred to as nth order SLC.

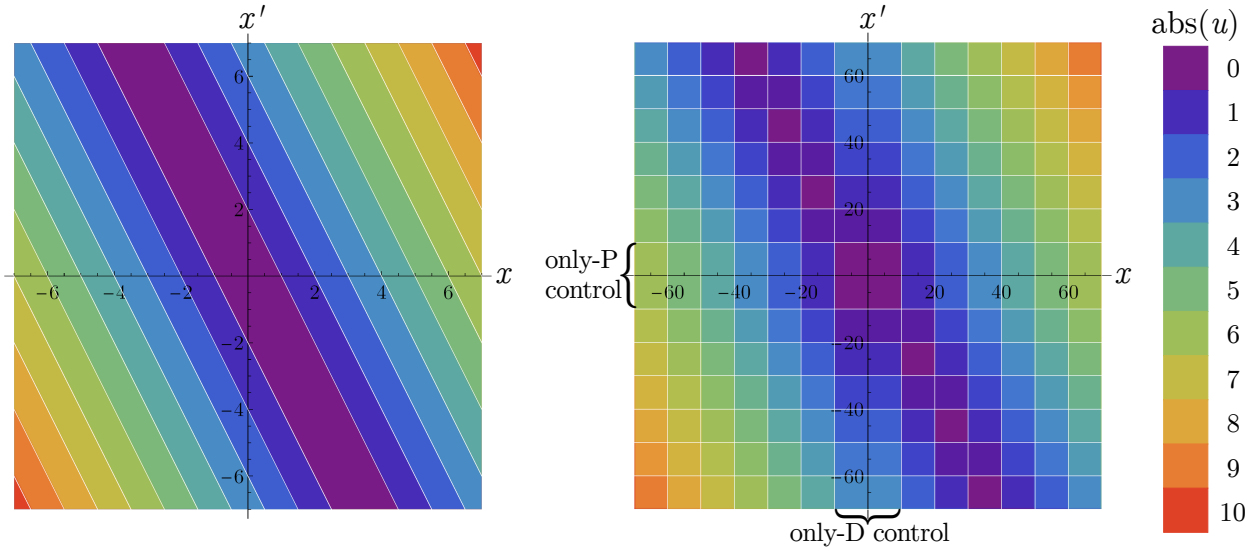

Figure 4.33: Left*: Switching lines and control effort bands in case of output quantization.* Right*: Switching line grid and control effort* tiles *in case of input quantization.*

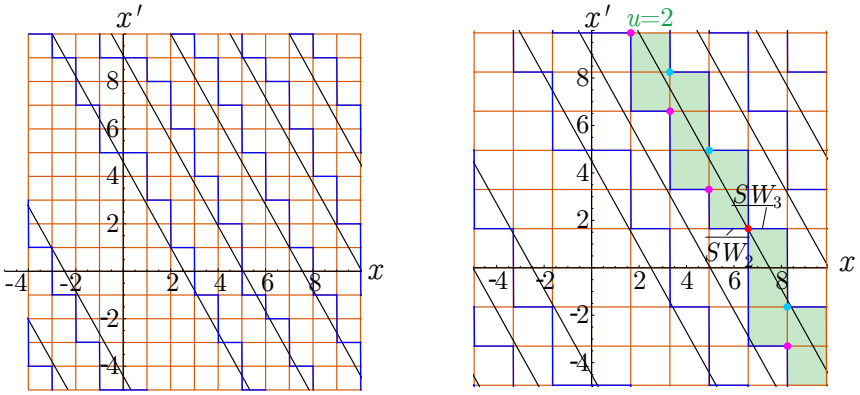

Figure 4.34: *Switching lines at $P = 2/5$, $D = 2/9$ and $\rho_{\mathrm{I}} = 1.0$ (left), $\rho_{\mathrm{I}} = 1.65$ (right). The latter value is slightly above $\rho_{\mathrm{I}}^{L,i} = 1/(P + D) \approx 1.61$. Black lines indicate the switching lines for the output quantization case, orange gridlines indicate the ρ_{I}-spaced grid corresponding to the input quantization. Red point highlights* switching line collision. *Green region indicates control effort band $u = 2$ which becomes disconnected due to SLC.*

It can be showed, that there is a *lowest quantization ratio* for a first order switching line collision to appear at a value $x = i\rho_{\mathrm{I}}$ in the state space:

$$\rho_{\mathrm{I}}^{L,i} = 1/(P + D), \tag{4.87}$$

When $\rho_{\mathrm{I}} \geq \rho_{\mathrm{I}}^{L,i}$, first order SLCs are present in the state space and by increasing ρ_{I}, they become more and more frequent (Fig. 4.35). Moreover, there is a *critical quantization ratio*:

$$\rho_{\mathrm{I}}^{1,i} = 1/P. \tag{4.88}$$

When $\rho_{\mathrm{I}} = \rho_{\mathrm{I}}^{1,i}$, every switching line collides with its neighbour at $x = i\,\rho_{\mathrm{I}}$, for all i. Note, that it does not imply that collision occurs for every $x' = k\,\rho_{\mathrm{I}}$, too (see Fig. 4.35 *left*).

Similarly, one can introduce the *highest quantization ratio* corresponding to the disappearance of first order switching line collisions:

$$\rho_{\mathrm{I}}^{H,i} = 1/(P - D) \quad \text{when} \quad 0 < D < P. \tag{4.89}$$

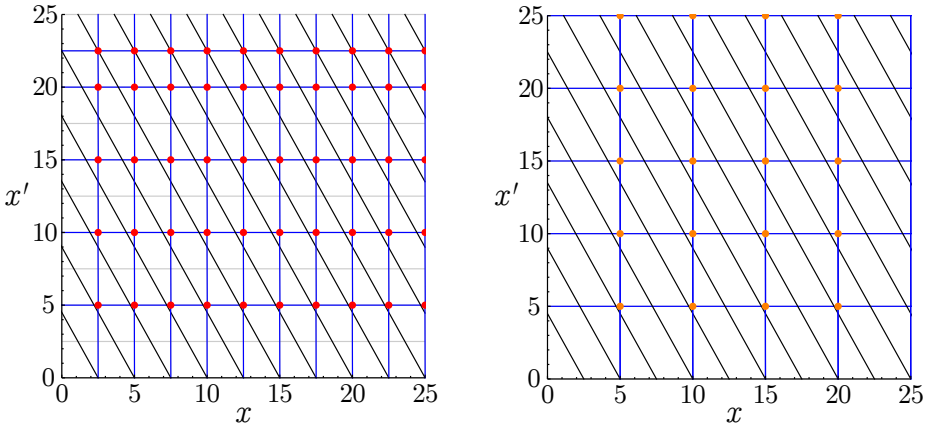

Figure 4.35: *Switching lines at $P = 2/5$, $D = 2/9$ and critical quantization ratios $\rho_{\mathrm{I}} = \rho_{\mathrm{I}}^{1,i} = 1/P$ (left), $\rho_{\mathrm{I}} = \rho_{\mathrm{I}}^{2,i} = 2/P$ (right). Trajectories going through intersection points may bypass certain control effort bands. Orange points: 2^{nd} order SLC's.*

When $\rho_{\mathrm{I}} > \rho_{\mathrm{I}}^{H,i}$, first order switching line collisions no longer present, because higher order collisions take their place.

Another *critical quantization ratio* can be derived if one wants a collision for every $x' = k\rho_{\mathrm{I}}$ (but not necessarily for every $x = i\,\rho_{\mathrm{I}}$):

$$\rho_{\mathrm{I}}^{1,k} = 1/D. \tag{4.90}$$

Combining Eqs. (4.88) and (4.90), one can express a *combined critical quantization ratio*:

$$\rho_{\mathrm{I}}^{1} = \max(\rho_{\mathrm{I}}^{1,i}, \rho_{\mathrm{I}}^{1,k}) = \max(1/P, 1/D). \tag{4.91}$$

If $\rho_{\mathrm{I}} \geq \rho_{\mathrm{I}}^{1}$, switching line collisions occur for all i and k. Expressing higher order switching line collisions in a similar fashion, one can arrive at the formulae of *nth order critical quantization ratios* for the collision of SW_m and SW_{m+n} at $\forall\, i \in \mathbb{Z}$ and $\forall\, k \in \mathbb{Z}$, respectively:

$$\rho_{\mathrm{I}}^{n,i} = n/P, \quad \rho_{\mathrm{I}}^{n,k} = n/D. \tag{4.92}$$

It is important to note, that due to the double deadzone of the mid-tread quantizer, switching line collisions of SW_{-1} and SW_{+1} are 2^{nd} order ones.

Another effect of twofold quantization – the so-called *deadzone crisis* – was also revealed in **[76]**. Deadzone crisis is an event, when a chaotic attractor turns to a transient chaotic repeller due to the change of the corresponding switching line's shape. The term deadzone crisis is originated from the observation, that this event is strongly related to the variation of input-deadzones in case of the 2D micro-chaos map. It was shown that this crisis event can strongly influence the maximal possible control error in the system, as it is illustrated in Fig. 4.36. At $\rho_{\mathrm{I}} \approx 1.3$, the outermost chaotic attractors, while at $\rho_{\mathrm{I}} \approx 2.4$, the innermost attractors disappear due to *deadzone crisis* (denoted by X). At $\rho_{\mathrm{I}} \approx 4.7$ the chaotic attractors merge (denoted by arrows) on both sides and lastly at $\rho_{\mathrm{I}} \approx 12$ they merge again resulting in a single recurring orbit with superimposed chaotic vibrations. The colour code shows the attractor sizes along the x direction. The results show that even the increase of a resolution parameter r_I or r_O can lead to smaller control error in certain cases.

4.7.3 Experimental detection of micro-chaos

Based on the generalizations discussed in the present section, a controlled inverted pendulum was built (see Fig. 4.37), utilizing an ST Nucleo L476 microcontroller unit (80 MHz processor

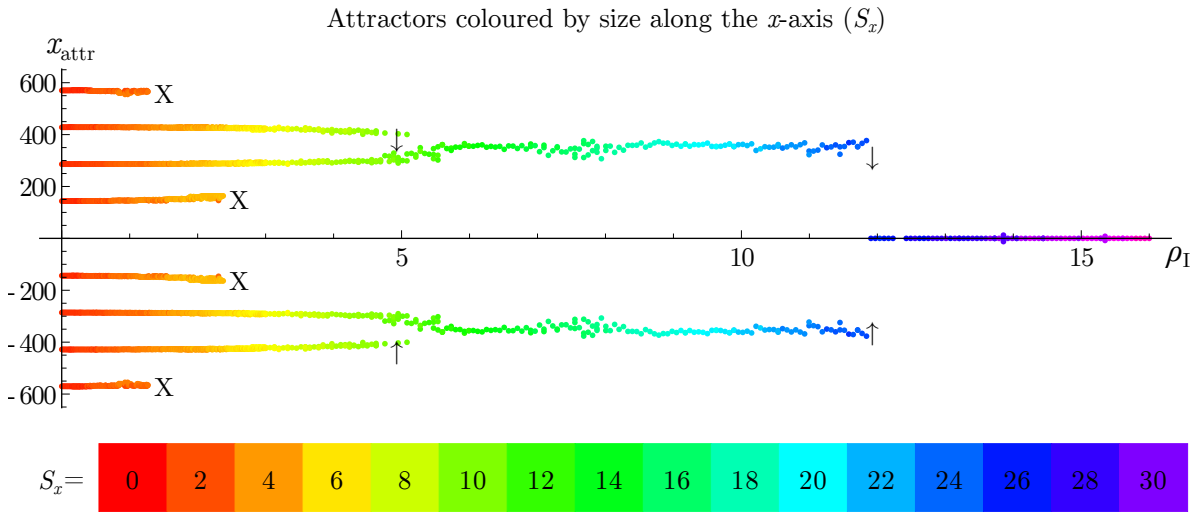

Figure 4.36: *Transition from output quantization to twofold quantization.*

frequency, 12-bit DAC), an ST VNH5019 motor driver (operating voltage: 5.5-24V, continuous 12A current), CUI Devices AMT102 rotary encoder (with 2048 pulse-per-revolution) and a lightweight aluminium tube directly attached to a brushed DC-motor.

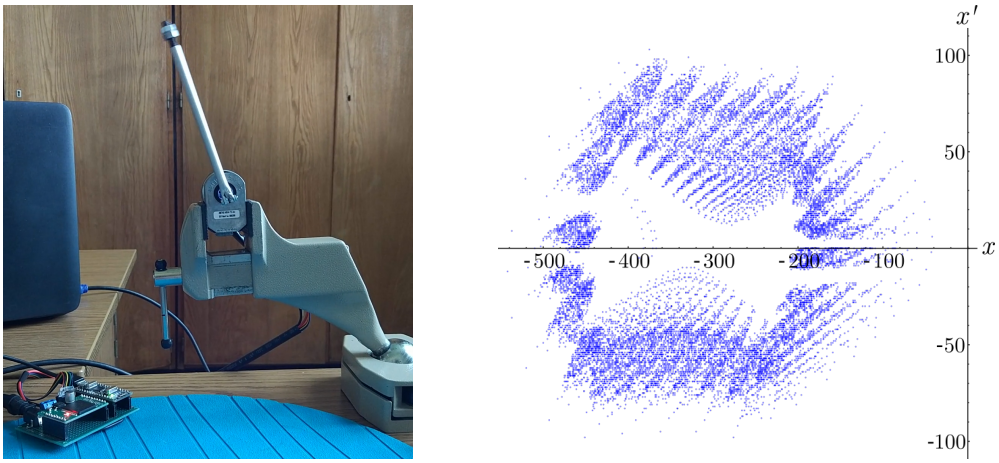

Figure 4.37: *Experimental device and the detected micro-chaotic behaviour*

The resolution of the encoder is $r_I = 2\pi/8096 = 7.76 \times 10^{-4}$ rad, while the control effort resolution is $r_O \approx 1.5 \times 10^{-4}$ Nm. In order to emphasize the digital effects, these resolutions were artificially lowered with a factor up to 200; $r_I^{\text{effective}} = N\, r_I$, $r_O^{\text{effective}} = M\, r_O$, $N, M \in \mathbb{Z}$. The control time step was $\tau = 20$ ms.

The angular velocity was determined by using the original, more accurate positions (r_I) with a first order numerical differentiation scheme and then artificially rounding the angular velocity to match the theoretical resolution of $r_I^{\text{effective}}/\tau$.

Fig. 4.37 shows a chaotic attractor surrounding a saddle point at $x = -310$ (in dimensionless position units), whose structure is familiar from numerical simulations (cf. Fig. 4.32).

Chapter 5

Principal Results

Principal result 1.

I analysed the asymmetric solutions of the harmonically forced oscillator with Coulomb friction damping and linear spring characteristic.

(a) I revised the assumption often exploited in the literature that the non-sticking trajectories of the frictional oscillator are symmetric, and found a family of non-sticking asymmetric solutions at the frequency ratios $1/(2n)$, $n = 1, 2, \ldots$, where the symmetry conditions fail.

(b) I derived that the aforementioned non-sticking asymmetric solutions exist if

$$S_0 \leq \frac{1}{4n^2 - 1},$$

where the rescaled static coefficient of friction S_0 is the ratio of the maximal static friction force and the forcing amplitude. I pointed out that almost all of the asymmetric solutions are marginally stable according to a third order normal form approximation. I proved that the special asymmetric solutions that just touch the boundary of the sticking region are stable with respect to perturbations towards the sticking zone. I demonstrated by numerical simulation that the zero-measure parameter domains of asymmetric solutions turn to finite parameter sets if the static coefficient of friction is greater than the kinetic one.

Related publications: [28, 29]. Related sections of the thesis: 2.2, 2.3, 2.4.

Principal result 2.

I examined the bifurcations and chaotic solutions of the oscillator described in Principal result 1, with different static and kinetic coefficients of friction.

(a) I formulated new switching conditions for the examination of the dry friction oscillator by the continuation method. I pointed out that symmetric periodic solutions turn to asymmetric ones via crossing-sliding or saddle-node bifurcations.

(b) I localised the parameter domains where the occurrence of chaotic solutions can be expected, estimated the value of the largest Lyapunov exponent in broad parameter domains and pointed out that

- irrespectively of the exact value of the static coefficient (provided it is larger than the static one), the frequency domain of asymmetric solutions stemming from $\Omega = 0.5$ – and the enclosed domain of possible chaotic solutions – expands if the kinetic coefficient of friction is decreased.

- The increase of the rescaled static coefficient of friction in the interval $S_0 \in [0.3, 0.8]$ implies that the domain of multi-periodic or chaotic solutions is extended towards larger excitation frequencies.

(c) (Joint work with Gábor Licskó.) We performed a brute-force bifurcation analysis to identify the parameter domains where the solutions are chaotic. We used two independent methods for the determination of the largest Lyapunov exponent in these domains. Based on these results, we found a narrow parameter regime where the solutions exhibit transient chaos and estimated the value of the largest finite-time Lyapunov exponent using a third method, approximating the dynamics by a piecewise linear 1D map.

My contribution was decisive in the selection and implementation of the calculation methods of the Lyapunov exponent, and also in the construction of the piecewise linear approximation function.

Related publications: [31, 110]. Related sections of the thesis: 2.5, 2.6.

Principal result 3.

I analysed Zoltán Pálmai's thermo-mechanical models of chip formation using the tools of nonlinear dynamics.

(a) I showed by the analysis of a four-dimensional model of chip formation that a period-doubling cascade leads to chaotic solutions at parameters corresponding to the cutting of austenitic steel. I also demonstrated that the period-doubling bifurcation points follow each other according to the Feigenbaum ratio. I localised the parameter domain of the dimensionless velocity of the chip where chaotic solutions exist and showed that the maximal Lyapunov exponent is positive at the parameters corresponding to the formation of aperiodic chips. I compiled a bifurcation diagram on the plane of two dimensionless technological parameters and identified several bistable domains where the dynamics is sensitive to perturbations. These domains should be avoided in practice.

(b) I examined the chip formation model of point (a) that takes the oscillation of a turned workpiece into account besides the thermo-mechanical effects. I could conclude that

- the originally periodic cutting process becomes quasiperiodic,
- the originally chaotic solution becomes transient chaotic leading to quasiperiodic vibrations, and
- the original equilibrium solution turns to small amplitude chaotic vibrations at the examined parameters, and
- the oscillations of the workpiece can lead to interrupted cutting in several elongated regions on the cutting speed-stiffness parameter plane.

(c) I determined the so-called Kaplan-Yorke dimension characterising the chaotic attractor of a time-delayed and piecewise smooth system that models the effects of the periodically forming and tearing built-up edge on chip formation during turning of soft steel. The results show that the solutions are chaotic and the dimension of the strange attractor of this infinite-dimensional system is finite.

Related publications: [32, 129, 131]. Related sections of the thesis: 3.2, 3.3, 3.4.

Principal result 4.

I determined dynamical characteristics of digitally controlled, full-state feedback systems, assuming that the open-loop system is linear with an unstable equilibrium, the sampling period is constant, zero order hold scheme is applied, and the elements of the measured state or the exerted control effort are quantized by constant resolutions.

(a) I showed that the dynamics of the considered systems can be described by piecewise affine maps, so-called micro-chaos maps. I provided general formulas for the determination of the regular fixed points and periodic orbits of the micro-chaos maps.

(b) I developed a specific method for the estimation of the mean lifetime of transient chaos in a one-dimensional (1D) micro-chaos map, that is based on the determination of the fractal dimension of the repeller.

(c) I showed that the consideration of processing delay (that is equal to the sampling period) turns the 1D micro-chaos map into a two-dimensional (2D) map and proved that the resulting map is chaotic in finite parameter domains.

(d) I proved that the 2D micro-chaos map describing the behaviour of a digitally PD-controlled linear oscillator with output quantization is chaotic in finite parameter domains. I showed that the structure of its phase-space is like phase portraits of several local baker's maps next to each other, and strange attractors or repellers are formed between each neighbouring pair of fixed points. I set up an algorithm for the determination of the attractor/repeller property of the strange sets, based on the consideration of boundary crisis bifurcations.

(e) (Joint work with Gergely Gyebrószki.) We developed a new Simple Cell Mapping (SCM) algorithm, the so-called Clustered Simple Cell Mapping, that is able to join separate SCM solutions and makes the adaptive extension of the analysed state space region possible, in any dimension. We showed that the joining procedure is linear in terms of the number of cells, and its main steps can be calculated in parallel.

My contribution was decisive during the selection of the method suitable for the investigation of systems with separated attractors – the cell mapping method –, the setting up of the requirements related to the operation of the algorithm, and the formulation of the definitions enabling the formal description of the procedure.

Related publications: [35, 38, 42, 43, 72]. Related sections of the thesis: 4.2,4.3, 4.4, 4.5,4.6.

Appendices

Appendix A

Stability Analysis of the Dry Friction Oscillator

A.1 FILIPPOV THEORY AND SALTATION MATRICES

One of the most contemporary stability calculation methods is based on Filippov theory and the application of so-called saltation matrices [12, 65, 109]. To apply this approach, we rewrite the equation of motion (2.3) into first order form:

$$\dot{\mathbf{X}} \equiv \begin{bmatrix} \dot{x} \\ \dot{v} \end{bmatrix} = \begin{cases} \mathbf{F}_+(x,v,t) & \text{if } v > 0, \\ \mathbf{F}_-(x,v,t) & \text{if } v < 0, \end{cases} \tag{A.1}$$

where

$$\mathbf{F}_\pm(x,v,t) = \begin{bmatrix} v \\ \cos(\Omega(t+t_0)) - x \mp S \end{bmatrix}. \tag{A.2}$$

The switching surface is defined by $h(x,v) \equiv v = 0$, thus, its normal vector on the $[x\ v]$ plane is $\mathbf{n} = [0\ 1]^T$. Let us consider a perturbation $\mathbf{Y}$ that is superposed on a known periodic solution $\mathbf{X}_P$. The evolution of the perturbation can be characterized by the variational equation

$$\dot{\mathbf{Y}} = \mathbf{J}(t, \mathbf{X}_P)\mathbf{Y}, \tag{A.3}$$

where the Jacobian matrix of the periodic solution is independent on the direction of the velocity:

$$\mathbf{J}(t, \mathbf{X}_P) = \begin{bmatrix} 0 & 1 \\ -1 & 0 \end{bmatrix}. \tag{A.4}$$

The fundamental set of solutions of the variational equation can be obtained by introducing linearly independent initial conditions: $\mathbf{Y}_1(0) = [1\ 0]^T$ and $\mathbf{Y}_2(0) = [0\ 1]^T$. The so-called fundamental solution matrix consists of the corresponding solutions in its columns:

$$\mathbf{\Phi}(t) = \begin{bmatrix} \cos(t) & \sin(t) \\ -\sin(t) & \cos(t) \end{bmatrix}. \tag{A.5}$$

This matrix is valid only between two crossings of the switching surface, because the fundamental solution matrix exhibits discontinuities when the sign of the velocity changes from

negative to positive ($- \to +$) or vice versa. These jumps can be described be the so-called saltation matrices [12]:

$$\mathbf{S}_{(-\to+)} = \mathbf{I} + \frac{(\mathbf{F}_+ - \mathbf{F}_-)\mathbf{n}^T}{\mathbf{n}^T\mathbf{F}_-}, \tag{A.6}$$

$$\mathbf{S}_{(+\to-)} = \mathbf{I} + \frac{(\mathbf{F}_- - \mathbf{F}_+)\mathbf{n}^T}{\mathbf{n}^T\mathbf{F}_+}, \tag{A.7}$$

where $\mathbf{I}$ is a unit matrix. The stability of the $2\pi/\Omega$-periodic symmetric solution derived in Section 2.2.1 can be characterized by the matrix

$$\mathbf{C} = \mathbf{S}_{(+\to-)}\mathbf{\Phi}(\pi/\Omega)\mathbf{S}_{(-\to+)}\mathbf{\Phi}(\pi/\Omega), \tag{A.8}$$

where the motion in both directions and the two crossings of the switching surface are taken into account. The periodic solution is stable if the Floquet multipliers – the eigenvalues $\lambda_{1,2}$ of $\mathbf{C}$ – are inside the unit circle on the complex plane. The results are illustrated in Fig. 2.7 at $S = 0.05$. Apparently, the symmetric solutions are only marginally stable at the frequencies $\Omega = 1/(2n)$, $n = 1, 2, \ldots$. Thus, the analysis of these special solutions requires a nonlinear stability calculation.

A.2 SHAW'S METHOD

Shaw [142] performed a more conventional stability analysis. His method provides the same Floquet multipliers as the Filippov theory, but this approach can be extended much easier with a nonlinear calculation. Shaw introduced the following Poincaré map P:

$$P\colon \begin{pmatrix} x_i \\ t_i \end{pmatrix} \to \begin{pmatrix} x_{i+1} \\ t_{i+1} \end{pmatrix}, \tag{A.9}$$

where x_i and t_i denote the coordinate and the time at the i^{th} stop. According to our notations, $t_1 = t_0 + \theta_1$ and $t_2 = t_0 + \theta_1 + \theta_2 = t_1 + \theta_2$. Consequently, $\theta_i = t_i - t_{i-1}$. The map P is not known explicitly, since the turning point times are roots of transcendental equations like (2.12). However, an approximating map can be constructed using implicit differentiation. We are interested in the propagation of errors as the initial coordinate and time are changed. Thus, we need the derivatives of t_1 and x_1 with respect to t_0 and x_0 [142].

For the calculation of $\partial t_1/\partial t_0$, we use the expressions $x^-(\theta_1) = x_1$ (see (2.5), (2.10) and (2.11)) and $\dot{x}^-(\theta_1) = 0$ (2.12). These equations can be expressed by the new variables t_i as follows:

$$x^-(\theta_1) = \left(x_0 - S + \frac{\cos(\Omega t_0)}{\Omega^2 - 1}\right)\cos(t_1 - t_0) - \frac{\Omega\sin(\Omega t_0)}{\Omega^2 - 1}\sin(t_1 - t_0) - \frac{\Omega\cos(\Omega t_1)}{\Omega^2 - 1} + S = x_1. \tag{A.10}$$

$$\dot{x}^-(\theta_1) = \left(S - x_0 - \frac{\cos(\Omega t_0)}{\Omega^2 - 1}\right)\sin(t_1 - t_0) - \frac{\Omega\sin(\Omega t_0)}{\Omega^2 - 1}\cos(t_1 - t_0) + \frac{\Omega\sin(\Omega t_1)}{\Omega^2 - 1} = 0. \tag{A.11}$$

Differentiation of (A.11) with respect to t_0 leads to an equation that can be used to determine $\partial t_1/\partial t_0$. The expression of $\partial t_1/\partial x_0$ can be obtained similarly, by differentiation of (A.11) with respect to x_0. The next step is the differentiation of (A.10) with respect to t_0. Taking into account that t_1 also depends on t_0, one obtains $\partial x_1/\partial t_0$ and $\partial x_1/\partial x_0$. The derivatives

of t_2 and x_2 with respect to t_1 and x_1 can be calculated similarly: only the indices must be increased by one in (A.10) and (A.11).

Let us denote the turning point times and coordinates of the known periodic solution by $\tilde{t}_i$ and $\tilde{x}_i$, while t_i and x_i will denote the corresponding quantities in case of a perturbed motion. This way, an error vector can be defined:

$$\begin{pmatrix} \xi_i \\ \eta_i \end{pmatrix} = \begin{pmatrix} x_i - \tilde{x}_i \\ t_i - \tilde{t}_i \end{pmatrix}. \tag{A.12}$$

The propagation of errors during a half cycle can be approximated as follows:

$$\begin{pmatrix} \xi_{i+1} \\ \eta_{i+1} \end{pmatrix} = \begin{pmatrix} x_{i+1} - \tilde{x}_{i+1} \\ t_{i+1} - \tilde{t}_{i+1} \end{pmatrix} = \begin{pmatrix} \frac{\partial x_{i+1}}{\partial x_i} & \frac{\partial x_{i+1}}{\partial t_i} \\ \frac{\partial t_{i+1}}{\partial x_i} & \frac{\partial t_{i+1}}{\partial t_i} \end{pmatrix} \begin{pmatrix} x_i - \tilde{x}_i \\ t_i - \tilde{t}_i \end{pmatrix} = R_{i+1} \begin{pmatrix} \xi_i \\ \eta_i \end{pmatrix}. \tag{A.13}$$

The derivatives are considered at the corresponding times $\tilde{t}_i$ and coordinates $\tilde{x}_i$ of a chosen solution. The stability of a periodic solution can be determined by constructing the error matrix $R = R_2 \cdot R_1$. The condition of stability is that the eigenvalues $\lambda_{1,2}$ of matrix R must be inside the unit circle.

A.3 EXTENSION OF SHAW'S METHOD

To determine the asymptotic behaviour of linearly marginally stable solutions at $\Omega = 1/(2n)$, a non-linear stability analysis was performed. For this purpose, we extended Shaw's calculations and approximated the elements of the error vector (A.12) by Taylor polynomials. Taking into account second and third order terms, we obtain

$$\begin{aligned} \xi_1 = x_1 - \tilde{x}_1 \approx \sum_{k=1}^{3} \sum_{i+j=k} \frac{1}{i!j!} \frac{\partial^{i+j} x_1}{\partial x_0^i \partial t_0^j} \xi_0^i \eta_0^j = \frac{\partial x_1}{\partial x_0} \xi_0 + \frac{\partial x_1}{\partial t_0} \eta_0 \\ + \frac{1}{2} \frac{\partial^2 x_1}{\partial x_0^2} \xi_0^2 + \frac{\partial^2 x_1}{\partial x_0 \partial t_0} \xi_0 \eta_0 + \frac{1}{2} \frac{\partial^2 x_1}{\partial t_0^2} \eta_0^2 \\ + \frac{1}{6} \frac{\partial^3 x_1}{\partial x_0^3} \xi_0^3 + \frac{1}{2} \frac{\partial^3 x_1}{\partial x_0^2 \partial t_0} \xi_0^2 \eta_0 + \frac{1}{2} \frac{\partial^3 x_1}{\partial x_0 \partial t_0^2} \xi_0 \eta_0^2 + \frac{1}{6} \frac{\partial^3 x_1}{\partial t_0^3} \eta_0^3 \end{aligned} \tag{A.14}$$

and

$$\eta_1 = t_1 - \tilde{t}_1 \approx \sum_{k=1}^{3} \sum_{i+j=k} \frac{1}{i!j!} \frac{\partial^{i+j} t_1}{\partial x_0^i \partial t_0^j} \xi_0^i \eta_0^j. \tag{A.15}$$

Similarly,

$$\xi_2 = x_2 - \tilde{x}_2 \approx \sum_{k=1}^{3} \sum_{i+j=k} \frac{1}{i!j!} \frac{\partial^{i+j} x_2}{\partial x_1^i \partial t_1^j} \xi_0^i \eta_0^j \tag{A.16}$$

and

$$\eta_2 = t_2 - \tilde{t}_2 \approx \sum_{k=1}^{3} \sum_{i+j=k} \frac{1}{i!j!} \frac{\partial^{i+j} t_2}{\partial x_1^i \partial t_1^j} \xi_0^i \eta_0^j. \tag{A.17}$$

Taking into account that $t_1 - t_0 = t_2 - t_1 = \pi/\Omega$ and $\Omega = 1/(2n)$, the derivatives can be obtained – see Equations (A.18)-(A.35)

$$\frac{\partial t_1}{\partial t_0} = \frac{(S - x_0 + 1)(1 - \Omega^2)}{(S - x_0)(1 - \Omega^2) + (1 + \Omega^2)}, \tag{A.18}$$

$$\frac{\partial^2 t_1}{\partial t_0^2} = \frac{\partial t_1}{\partial x_0} = \frac{\partial^2 t_1}{\partial x_0^2} = \frac{\partial^3 t_1}{\partial x_0^3} = \frac{\partial^3 t_1}{\partial x_0 \partial t_0^2} = 0, \tag{A.19}$$

$$\frac{\partial^3 t_1}{\partial t_0^3} = \frac{2(\Omega^6 - \Omega^4)((\Omega^2 - 1)^2(x_0 - S)^3 + (x_0 - S)(3\Omega^4 - 4\Omega^2 - 3) + 6\Omega^2 + 2)}{((S - x_0)(1 - \Omega^2) + (\Omega^2 + 1))^4}, \tag{A.20}$$

$$\frac{\partial^2 t_1}{\partial x_0 \partial t_0} = \frac{2\Omega^2(\Omega^2 - 1)}{((S - x_0)(1 - \Omega^2) + (\Omega^2 + 1))^2}, \tag{A.21}$$

$$\frac{\partial^3 t_1}{\partial x_0^2 \partial t_0} = \frac{-4\Omega^2(\Omega^2 - 1)^2}{((S - x_0)(1 - \Omega^2) + (\Omega^2 + 1))^3}, \tag{A.22}$$

$$\frac{\partial x_1}{\partial x_0} = 1, \tag{A.23}$$

$$\frac{\partial x_1}{\partial t_0} = \frac{\partial^3 x_1}{\partial t_0^3} = \frac{\partial^2 x_1}{\partial x_0^2} = \frac{\partial^2 x_1}{\partial x_0 \partial t_0} = \frac{\partial^3 x_1}{\partial x_0^3} = \frac{\partial^3 x_1}{\partial x_0^2 \partial t_0} = 0, \tag{A.24}$$

$$\frac{\partial^2 x_1}{\partial t_0^2} = \frac{2\Omega^2(x_0 - S - 1)}{(x_0 - S)(1 - \Omega^2) - (1 + \Omega^2)}, \tag{A.25}$$

$$\frac{\partial^3 x_1}{\partial x_0 \partial t_0^2} = \frac{-4\Omega^4}{((x_0 - S)(1 - \Omega^2) - (1 + \Omega^2))^2}, \tag{A.26}$$

$$\frac{\partial t_2}{\partial t_1} = \frac{(x_1 + S + 1)(1 - \Omega^2)}{(x_1 + S)(1 - \Omega^2) + (1 + \Omega^2)}, \tag{A.27}$$

$$\frac{\partial^2 t_2}{\partial t_1^2} = \frac{\partial t_2}{\partial x_1} = \frac{\partial^2 t_2}{\partial x_1^2} = \frac{\partial^3 t_2}{\partial x_1^3} = \frac{\partial^3 t_2}{\partial x_1 \partial t_1^2} = 0, \tag{A.28}$$

$$\frac{\partial^3 t_2}{\partial t_1^3} = \frac{-2(\Omega^6 - \Omega^4)((\Omega^2 - 1)^2(x_1 + S)^3 + (x_1 + S)(3\Omega^4 - 4\Omega^2 - 3) - 6\Omega^2 - 2)}{((S + x_1)(\Omega^2 - 1) - (\Omega^2 + 1))^4}, \tag{A.29}$$

$$\frac{\partial^2 t_2}{\partial x_1 \partial t_1} = \frac{2\Omega^2(\Omega^2 - 1)}{((S + x_1)(1 - \Omega^2) + (\Omega^2 + 1))^2}, \tag{A.30}$$

$$\frac{\partial^3 t_2}{\partial x_1^2 \partial t_1} = \frac{-4\Omega^2(\Omega^2 - 1)^2}{((S + x_0)(1 - \Omega^2) + (\Omega^2 + 1))^3}, \tag{A.31}$$

$$\frac{\partial x_2}{\partial x_1} = 1, \tag{A.32}$$

$$\frac{\partial x_2}{\partial t_1} = \frac{\partial^3 x_2}{\partial t_1^3} = \frac{\partial^2 x_2}{\partial x_1^2} = \frac{\partial^2 x_2}{\partial x_1 \partial t_1} = \frac{\partial^3 x_2}{\partial x_1^3} = \frac{\partial^3 x_2}{\partial x_1^2 \partial t_1} = 0, \tag{A.33}$$

$$\frac{\partial^2 x_2}{\partial t_1^2} = \frac{-2\Omega^2(x_1 + S + 1)}{(x_1 + S)(1 - \Omega^2) + (1 + \Omega^2)}, \tag{A.34}$$

$$\frac{\partial^3 x_2}{\partial x_1 \partial t_1^2} = \frac{-4\Omega^4}{((x_1 + S)(1 - \Omega^2) + (1 + \Omega^2))^2}. \tag{A.35}$$

Substituting these expressions into Equations (A.14)-(A.17), and substituting ξ_1 and η_1 into (A.16) and (A.17), one obtains a high-order polynomial. Neglecting fourth and higher order terms, ξ_2 and η_2 can be expressed in the following form:

$$\xi_2 = \lambda_1 \xi_0 + A\eta_0^2 + B\xi_0\eta_0^2, \tag{A.36}$$

$$\eta_2 = \lambda_2\eta_0 + C\xi_0\eta_0 + D\xi_0^2\eta_0 + E\eta_0^3, \tag{A.37}$$

where A, B, C, D, and E are lengthy algebraic expressions.

Thus, an iterative map can be defined by redefining the subscript as the serial number of the consequtive cycles of the periodic motion:

$$\xi_{i+1} = \lambda_1\xi_i + A\eta_i^2 + B\xi_i\eta_i^2, \tag{A.38}$$
$$\eta_{i+1} = \lambda_2\eta_i + C\xi_i\tau_i + D\xi_i^2\eta_i + E\eta_i^3. \tag{A.39}$$

To transform these equations into normal form [121], the resonant conditions must be examined:

$$\lambda_1^{q_1} \cdot \lambda_2^{q_2} = \lambda_1, \tag{A.40}$$
$$\lambda_1^{q_1} \cdot \lambda_2^{q_2} = \lambda_2, \tag{A.41}$$

where $2 \leq q_1 + q_2 \leq 3$. The integer numbers q_1 and q_2 are the exponents of the new, transformed variables y_i and τ_i in the normal form.

A.3.1 Symmetric solutions

In case of symmetric solutions, $\lambda_1 = 1$ and $0 < \lambda_2 < 1$. Thus, the possible solutions of (A.40) are

$$q_2 = 0 \quad \text{and} \quad q_1 = 2, 3. \tag{A.42}$$

$q_2 = 0$ means that the second variable (τ_i) can be eliminated from the first equation, while $q_1 = 2, 3$ implies that the square and the cube of the first variable (y_i) will appear in the transformed equation. (A.41) is fulfilled if

$$q_2 = 1 \quad \text{and} \quad q_1 = 1, 2, \tag{A.43}$$

that can be interpreted similarly. Consequently, the normal form of (A.38)-(A.39) is

$$y_{i+1} = y_i + \alpha y_i^2 + \beta y_i^3, \quad \text{and} \tag{A.44}$$
$$\tau_{i+1} = \lambda_2\tau_i + \gamma y_i\tau_i + \delta y_i^2\tau_i. \tag{A.45}$$

In the next step, the coefficients α, β, γ, and δ are to be determined. Assume that the variables ξ_i and η_i can be written in the following form:

$$\xi_i = y_i + a_{yy}y_i^2 + a_{y\tau}y_i\tau_i + a_{\tau\tau}\tau_i^2 + a_{yyy}y_i^3 + a_{y\tau\tau}y_i\tau_i^2 + a_{yy\tau}y_i^2\tau_i + a_{\tau\tau\tau}\tau_i^3 \tag{A.46}$$
$$\eta_i = \tau_i + b_{yy}y_i^2 + b_{y\tau}y_i\tau_i + b_{\tau\tau}\tau_i^2 + b_{yyy}y_i^3 + b_{y\tau\tau}y_i\tau_i^2 + b_{yy\tau}y_i^2\tau_i + b_{\tau\tau\tau}\tau_i^3. \tag{A.47}$$

Similar equations can be written for ξ_{i+1} and η_{i+1}, as well. Using (A.44) and (A.45), the left hand sides of (A.38) and (A.39) can also be expressed by y_i and τ_i.

Substituting (A.46) and (A.47) into the right hand sides of (A.38) and (A.39), ξ_{i+1} and η_{i+1} can be expressed by the new variables y_i and τ_i, again.

After neglecting fourth and higher order terms and taking into account that $C = 0$ in (A.39) in the symmetric case, (A.38) and (A.39) lead to the following equations for the unknown parameters of the transformation (A.46), (A.47):

$$\begin{aligned} -\alpha y_i^2 + a_{y\tau}(1-\lambda_2)y_i\tau_i + (A + a_{\tau\tau}(1-\lambda_2^2))\tau_i^2 - (\beta + 2a_{yy}\alpha)y_i^3 + \\ (a_{yy\tau}(1-\lambda_2) - a_{y\tau}(\gamma + \alpha\lambda_2) + 2Ab_{yy})y_i^2\tau_i + (a_{y\tau\tau}(1-\lambda^2) + \\ a_{y\tau\tau} + B + 2Ab_{y\tau})y_i\tau_i^2 + (a_{\tau\tau\tau}(1-\lambda_2^3) + 2Ab_{\tau\tau})\tau_i^3 = 0, \end{aligned} \tag{A.48}$$

$$b_{yy}(\lambda_2-1)y_i^2-\gamma y_i\tau_i+\lambda_2 b_{yy}(1-\lambda_2)\tau_i^2+(b_{yyy}(\lambda_2-1)-2b_{yy}\alpha)y_i^3+ (D-\delta-b_{y\tau}(\alpha\lambda_2+\gamma))y_i^2\tau_i+(b_{y\tau\tau}\lambda_2(1-\lambda_2)-2b_{\tau\tau}\lambda_2\gamma)y_i\tau_i^2+ (E+b_{\tau\tau\tau}\lambda_2(1-\lambda^2))\tau_i^3=0. \tag{A.49}$$

Since these equations must be valid for any pair of y_i and τ_i, every coefficient must be zero. Consequently, $\alpha=\beta=\gamma=0$, $\delta=D$, and

$$y_{i+1}=y_i, \tag{A.50}$$
$$\tau_{i+1}=\lambda_2\tau_i+Dy_i^2\tau_i. \tag{A.51}$$

The normal form (A.50) shows, that the periodic symmetric solutions are marginally stable in this third order approximation.

A.3.2 Asymmetric solutions

A similar calculation can be performed in case of the asymmetric solutions, too. $\lambda_1=1$ and $0<\lambda_2<1$ fulfils for almost every asymmetric solution. $C\neq 0$ in these cases, and the normal form reads:

$$y_{i+1}=y_i, \tag{A.52}$$
$$\tau_{i+1}=\lambda_2\tau_i+Cy_i\tau_i. \tag{A.53}$$

Thus, for $(4n^2+1)/(4n^2-1)-S<x_0<1+S$, we found a continuum of solutions that are marginally stable in this third order calculation. Higher order terms might have a stabilizing effect, but we expect that the whole family of these solutions is marginally stable to all orders due to the fact that these asymmetric periodic solutions are dense in a subsurface of the phase space.

Finally, consider the extremal asymmetric cases, $x_0=1+S$ and $x_0=(4n^2+1)/(4n^2-1)-S$. Since the eigenvalues are $\lambda_1=1$ and $\lambda_2=0$ in these cases, the resonance condition (A.40) fulfils if

$$q_2=0,\quad \text{and}\quad q_1=2,3, \tag{A.54}$$

and (A.41) is valid if

$$q_1=0,\quad \text{and}\quad q_2=2,3, \tag{A.55}$$
$$q_1=1,\quad \text{and}\quad q_2=1,2, \tag{A.56}$$
$$q_1=2,\quad \text{and}\quad q_2=1. \tag{A.57}$$

Thus, the normal form can be written as

$$y_{i+1}=y_i+\alpha y_i^2+\beta y_i^3, \tag{A.58}$$
$$\tau_{i+1}=\gamma y_i\tau_i+\delta y_i^2\tau_i+\varepsilon\tau_i^2+\kappa y_i\tau_i^2+\mu\tau_i^3. \tag{A.59}$$

The coefficients α, β, γ, δ, ε, κ, and μ can be determined similarly as in the case of Eqs. (A.44), (A.45). Taking into account that $A=0$ and $B=-1/2$ in case of $x_0=1+S$, we obtain

$$y_{i+1}=y_i, \tag{A.60}$$
$$\tau_{i+1}=Cy_i\tau_i+E\tau_i^3, \tag{A.61}$$

while in case of $x_0=(4n^2+1)/(4n^2-1)-S$, we arrive at

$$y_{i+1}=y_i, \tag{A.62}$$

$$\tau_{i+1} = Cy_i\tau_i + (E - AC)\tau_i^3. \tag{A.63}$$

Note, that in the extremal asymmetric cases the solution touches the stick-slip boundary. This result means that Eqs. (A.60)-(A.63) are valid only for perturbations that push the solution away from the boundary and towards non-sticking responses. In the opposite case, i.e., when the solution is pushed into the sticking region, another approach must be used, that is described in Section 2.3.3.

Since Eqs. (A.50)-(A.53) are valid for arbitrary small perturbations, this third order calculation leads us to the conjecture that families of equally marginally stable solutions exist at frequencies $\Omega = 1/(2n)$.

Appendix B

Pálmai's Chip Formation Models

B.1 DERIVATION OF THE 5D MODEL

The derivation of the equations (3.3)-(3.10) can be summarized as follows: the plastic shear stress τ_i $(i = 1, 2)$ occurring in the shear zone of size h_1 is in mechanical balance with the normal stress σ acting on length L (see Fig. 3.3), i.e., the inertial forces and the elastic deformation are neglected. Thus,

$$\sigma L = \tau_2 h_1 \equiv \frac{\tau_2 h}{\sin(\Phi)}. \tag{B.1}$$

The normal stress σ causes an elastic normal strain $\Delta u/h_1$ in the chip, parallel with the direction of the deformation layers. Thus, $\sigma = E\Delta u/h_1$, i.e, $\dot{\sigma} = E\sin(\Phi)\ \dot{u}/h$, that implies

$$\dot{\tau}_2 = \frac{EL\sin^2(\Phi)}{h^2}\dot{u}, \tag{B.2}$$

where E denotes the Young modulus and $\dot{u}$ is the deformation velocity parallel to the deformation layers. $\dot{u}$ is not equal to the corresponding component

$$v\cos(\Phi) \equiv \delta\dot{\varepsilon}_\Phi \tag{B.3}$$

of the cutting speed v, due to the plastic deformation of the material. The velocity of the plastic deformation is $\dot{\gamma}\delta$, thus, $\dot{u} = \delta\dot{\varepsilon}_\Phi - \delta\dot{\gamma}$. The consideration of two deformation layers implies

$$\dot{u} = \delta\dot{\varepsilon}_\Phi\left(1 - \frac{\dot{\gamma}_1}{\dot{\varepsilon}_\Phi} - \frac{\dot{\gamma}_2}{\dot{\varepsilon}_\Phi}\right). \tag{B.4}$$

Thus, substituting to (B.2),

$$\dot{\tau}_2 = \frac{ELv}{h^2}\sin^2(\Phi)\ \cos(\Phi)\ \left(1 - \frac{\dot{\gamma}_1}{\dot{\varepsilon}_\Phi} - \frac{\dot{\gamma}_2}{\dot{\varepsilon}_\Phi}\right). \tag{B.5}$$

To simplify the equations, a nondimensional time $\hat{t} = t/K$ and a nondimensional shear stress

$$\hat{\tau}_i = \frac{\tau_i}{\tau_\Phi} \tag{B.6}$$

were introduced, where τ_Φ is the mean shear stress [132] in the shear zone during the formation of continuous chips. According to the generally accepted approximation of the cutting

theory, τ_Φ can be considered as a material constant. The nondimensional time was chosen to be

$$K = \frac{\tau_\Phi h^2}{ELv\ \sin^2(\Phi)\ \cos(\Phi)}. \tag{B.7}$$

Using the new time scale and the notation

$$F_i \equiv \frac{\dot{\gamma}_i}{\dot{\varepsilon}_\Phi}, \tag{B.8}$$

the equation of mechanical balance on the boundary of layers 0 and 1 turns to the differential equation

$$\dot{\tau}_2 = 1 - (F_1 + F_2), \tag{B.9}$$

where the hat symbol showing the dimensionless nature of the variable τ is discarded and dot means differentiation with respect to the dimensionless time.

On the boundary of the two deformed layers, the plastic stress $\sigma_{\rm pl}$ in layer 2 must also be taken into account. Consequently, the mechanical equilibrium leads to

$$\tau_1 h_1 = \sigma L + \sigma_{\rm pl}\delta.$$

Pálmai assumed that $\sigma_{\rm pl} \approx \sqrt{3}\tau_{\rm pl}$ in the plastic state, where $\tau_{\rm pl} = \tau_2$. Thus, the differential equation of the nondimensional shear stress in layer 1 assumes the form

$$\dot{\tau}_1 = p\,(1 - (F_1 + F_2))\,, \tag{B.10}$$

where

$$p = 1 + \frac{\sqrt{3}\delta}{h}\sin(\Phi). \tag{B.11}$$

The determination of the parameter p is necessary for the application of the mathematical model. Unfortunately, the standard deviation of the data, found in the literature and measured in Pálmai's experiments about the thickness of the shear zone, is rather large. Most of the measurements published in the literature [94, 125] provide information about the state of the shear zone just after the interruption of the cutting process. The circumstances during the process were examined by Black [14] by electronmicroscope. Taking into account these results, one can choose $\delta = 12.5$ μm as a realistic approximation. Exploiting the definitions of ξ and ζ, one obtains the following expression:

$$\delta = \frac{\xi}{\zeta}\ \frac{4\lambda}{c\rho}\ \frac{1}{v\sin(\Phi)}. \tag{B.12}$$

In the considered case, $\delta = 1.278 \cdot 10^{-5}$ m, which well agrees with the measured value. Thus, $p = 1.03$, according to (3.5). The time scale K can be determined in two different ways, which makes the validation of the model possible. Measuring the mean width Δ_c of the lamellas of the periodic chip (Fig. 3.2), the real time period t_c can be determined as $t_c = \Delta_c/(v\sin(\Phi))$. In the mathematical model, $K = t_c/\hat{t}_c$, where $\hat{t}_c$ is the dimensionless time period. According to the measurements, $\Delta_c = 0.28$ mm, while using the mathematical model (3.4)-(3.9) in the case ζ= 3.4 (Fig. 3.2/c.), one obtains $\hat{t}_c = 0.95$. Thus, $K = 1.64 \cdot 10^{-4}$ s.

Parameter K can also be determined using the definition of parameter η, exploiting that $\tau_\Phi = 0.9$ GPa for the chip material of austenitic steel [174]. Taking into account that $T_w = 300$ K and $r = 0.95$, one obtains $K = 1.52 \cdot 10^{-4}$ s, which satisfactorily agrees with the previous value.

B.2 VARIATION OF THE CUTTING SPEED

To extend the 4D model to the case of varying cutting speed, one must take into account that the time scale K depends on the cutting speed v. Using this parameter for the expression of dimensionless equations is inappropriate if v can vary during the cutting process. Thus, a reference velocity v_0 is introduced to express the time scale:

$$K_0 = \frac{\tau_\Phi h^2}{EL \sin^2(\Phi)\ \cos(\Phi)} \frac{1}{v_0}, \tag{B.13}$$

with which the dimensionless time can be obtained as $\hat{t} = t/K_0$.

The actual cutting speed can be expressed as the multiple of the reference value: $v = v_0 f(t)$. Substituting $v = v_0 f$ into (B.5), one obtains

$$\frac{d\hat{\tau}_2}{d\hat{t}} = f\left(1 - (F_1 + F_2)\right). \tag{B.14}$$

Since the expressions of the system parameters η and ξ contain the velocity v, these parameters are also reformulated to depend on v_0, the reference speed. If the cutting speed differs from v_0, these parameters must be multiplied by f. Thus, the energy balance equations (3.28)-(3.29) turn to the forms

$$\begin{aligned} \dot{T}_0 &= \zeta(T_1 - 2T_0) - f\xi T_0, \\ \dot{T}_1 &= f\eta\ \tau_1 F_1(\tau_2, T_1) - \zeta(2T_1 - T_2 - T_0) - f\xi(T_1 - T_0), \\ \dot{T}_2 &= f\eta\ \tau_2 F_2(\tau_2, T_2) - (f\xi + \zeta)(T_2 - T_1). \end{aligned} \tag{B.15}$$

Thus, in the case of varying cutting speed, the mathematical model of chip formation – derived by Pálmai [129] – consists of the constitutive equations (3.31), together with the differential equations (B.14) and (B.15). The constants, the system parameters and the initial conditions remain unchanged.

B.3 OSCILLATION OF THE WORKPIECE OR THE TOOL

The machine-tool-workpiece system performs elastic vibrations as the cutting force varies. For the sake of simplicity, Pálmai neglected the elasticity of the machine and assumed that one end of the beam-shaped workpiece is fixed in the chuck of the turning machine. The velocity of the motion related to the oscillation of the workpiece and/or the tool is added to the cutting velocity.

Introduce the coordinate z that is measured parallel with the cutting speed, according to Fig. B.1. If the workpiece moves with velocity $\dot{z}$, the effective cutting speed will be $v_{\text{eff}} = (fv_0 - \dot{z})$. Clearly, if the tool oscillates, one obtains $v_{\text{eff}} = (fv_0 + \dot{z})$. Substituting $v = v_{\text{eff}}$ into (B.3) and (B.4) leads to

$$\dot{\varepsilon}_\Phi = \frac{fv_0 \cos(\Phi)}{\delta} \left(1 - \frac{\dot{z}}{fv_0}\right) \tag{B.16}$$

and

$$\dot{u} = fv_0 \cos(\Phi) \left(1 - \frac{\dot{z}}{fv_0}\right) \left(1 - \frac{\dot{\gamma}_1}{\dot{\varepsilon}_\Phi} - \frac{\dot{\gamma}_2}{\dot{\varepsilon}_\Phi}\right). \tag{B.17}$$

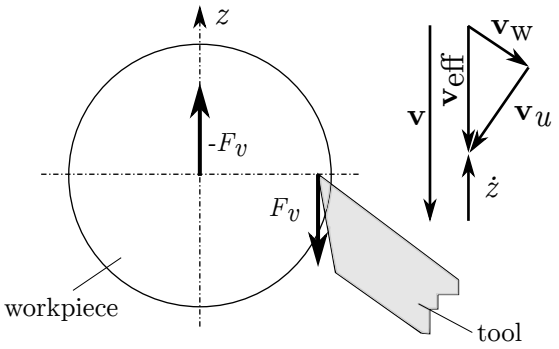

Figure B.1: *Relations among the velocity components in the elastic workpiece-tool system.*

Thus, $\dot{\tau}_2$ can be expressed as

$$\dot{\tau}_2 = \frac{EL}{h^2}\sin^2(\Phi) f v_0 \cos(\Phi)\left(1-\frac{\dot{z}}{f v_0}\right)\left(1-\frac{\dot{\gamma}_1}{\dot{\varepsilon}_\Phi}-\frac{\dot{\gamma}_2}{\dot{\varepsilon}_\Phi}\right). \tag{B.18}$$

Using the time scale K_0 and stress scale τ_Φ, one obtains (prime denotes differentiation w.r.t. dimensionless time):

$$\hat{\tau}_2' = f\left(1-\frac{z'}{K_0 f v_0}\right)(1-F_1-F_2). \tag{B.19}$$

To determine the motion law of the workpiece $z(\hat{t})$, the workpiece is modeled as a beam with one fixed end, and the principal cutting force is applied at the other end of the beam. The oscillation of this 1DoF system can be described by the differential equation

$$m_r\ddot{z} + kz = F_v, \tag{B.20}$$

where m_r denotes the equivalent mass of the workpiece (or the tool if the tool's elasticity is considered), reduced at the point of action of the force, and k (N/m) is the spring stiffness. The principal cutting force F_v can be approximated as

$$\begin{aligned} F_v &\approx c_F \cdot \tau, \quad \text{where} \\ c_F &\approx (\operatorname{cotan}(\Phi) + \operatorname{cotan}(\rho_\Phi)) \cdot q. \end{aligned} \tag{B.21}$$

Here τ denotes the shear stress in the shear zone in plastic state, while q denotes the area of the cross section of the cut layer. ρ_Φ is the angle of "internal friction", which can be defined in the shear zone, and can be expressed by the angle of friction $\bar{\rho}$ between the workpiece and the tool. Usually $\rho_\Phi = \pi/2 - (\Phi - \alpha + \bar{\rho})$, while in our case $\rho_\Phi = \pi/2 - \bar{\rho}$, i.e., $\operatorname{cotan}(\rho_\Phi) = \tan(\bar{\rho}) = \mu$, where μ denotes the usual Coulomb coefficient of friction. In the examples discussed in Section 3.3, the area of the cross section of the cut layer is $q = 0.73$ mm^2 and the corresponding angles are $\Phi = 30^o$ and $\rho_\Phi = 45^o$, thus, $c_F \approx 2$.

It is characteristic of turning processes that the point of action of the force usually approaches (or rarely, moves away from) the fixed end of the workpiece. Consequently, the spring stiffness k increases, and may assume a rather large value during the final part of the process. However, this variation is slow, and we suppose in our model that k=const. To rewrite the equations to dimensionless form, we introduce the notation

$$z = \tilde{L} \cdot \hat{z} \tag{B.22}$$

where the appropriate choice of $\tilde{L}$ is

$$\tilde{L} = \frac{2\tau_\Phi}{m_r} K_0^2. \tag{B.23}$$

Discarding the special symbols showing the dimensionless nature of the quantities, we obtain

$$\ddot{z} + A \cdot z = \tau, \tag{B.24}$$

where

$$A = \frac{kK_0^2}{m_r}. \tag{B.25}$$

According to what we have mentioned above, the final value of A may be several times larger than its initial value. The equivalent mass m_r of the beam is approximately $m_r \approx m/3$ for the workpiece fixed at one end.

The period of the free oscillations of the beam can be obtained as

$$T_{per} = \frac{2\pi}{\sqrt{A}} = 2\pi \frac{\sqrt{m_r \cdot k}}{K_0}, \tag{B.26}$$

while the natural angular frequency is

$$\omega = \frac{\sqrt{A}}{K_0}. \tag{B.27}$$

Pálmai estimated the order of magnitude of A based on a cutting experiment, performed at the Faculty of Technology of the Kecskemét College. The angular frequency was $\omega = 2\pi \cdot 1800$ rad/s, which corresponds to $T_{per} = 1/1800$ s $= 5.56 \cdot 10^{-4}$ s.

Consequently, $\sqrt{A} = 1800 \cdot 2\pi K_0 = 1.1304 \cdot 10^4 K_0$. For example, at $K_0 = 1.769 \cdot 10^{-4}$ s we obtain $A = 4$. The velocity of the workpiece, related to the oscillation is denoted by $\dot{z}$. According to Fig. B.1, this velocity must be subtracted from the circumferential velocity v – i.e., from the nominal cutting speed – to obtain the effective cutting speed v_{eff}. In the extremal case, when $\dot{z}$ is equal to the circumferential velocity, no chip is produced.

Using the length scale $z = \tilde{L}\hat{z}$, Equation (B.19) turns to

$$\hat{\tau}_2' = f\left(1 - \frac{\hat{z}'\tilde{L}}{K_0 f v_0}\right)(1 - F_1 - F_2). \tag{B.28}$$

Introducing the notation

$$V_0 = \frac{K_0 v_0}{\tilde{L}} = \frac{m_r v_0}{2\tau_\Phi K_0}, \tag{B.29}$$

the differential equation of the shear stress can be rewritten to

$$\hat{\tau}_2' = f\left(1 - \frac{\hat{z}'}{V_0 f}\right)(1 - F_1 - F_2). \tag{B.30}$$

The energy equations, describing the variation of the temperatures, are also modified: parameters ξ and η must be multiplied by $f\left(1 - \frac{\hat{z}'}{V_0 f}\right)$ that takes the variation of velocity into account.

The described transformations lead to the set of differential equations (3.12) - (3.16) if one discards the special symbols that denote the dimensionless nature of the variables.

B.4 PÁLMAI'S TIME-DELAYED MODEL OF CHIP FORMATION

B.4.1 Variation of the thickness of the cut layer

The most important phase of the formation of chips is the development of an active deformation zone between the workpiece and the chip (Fig. B.2), where the plastic shear deformation

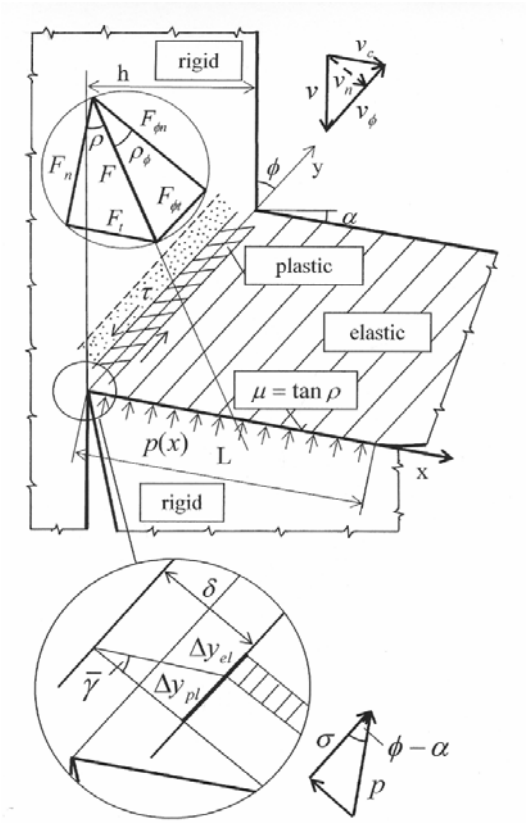

Figure B.2: *The model of chip formation (from [131]).*

is dominant. This process is responsible for 80% of the total energy consumption of the technology [141]. The remaining 20% is mostly devoted to the friction between the tool and the chip. In the previous models [127],**[129]** Pálmai neglected friction and assumed that the inclination angle ϕ of the shear zone and rake angle α of the tool were equal. In the new model, these simplifying assumptions are disregarded. It was assumed in the technological model [127], that the workpiece and the tool are rigid, the chip is elastic and the active shear zone of thickness δ is in plastic state. An inactive layer of thickness δ was also considered between the shear zone and the workpiece, which plays a role in thermal transfer processes only. It is expedient to rewrite the temperature, shear stress, deformation angle and time in dimensionless form: $\hat{T} = (T - T_w)/T_w$, $\hat{\tau} = \tau/\tau_\Phi$,$\hat{\gamma} = \gamma/\varepsilon_\Phi$, $\hat{t} = t/K$, where T_w denotes the temperature of the workpiece and K is the time-scale. The appropriate choice of K is given in Eq. (B.49). During the formation of the so-called continuous chips with uniform thickness, the temperature of the shear zone is T_Φ, the shear stress is τ_Φ, and the strain is

$$\varepsilon_\Phi = \frac{\cos(\alpha)}{\sin(\Phi)\cos(\Phi - \alpha)}, \tag{B.31}$$

while the strain rate [141] is,

$$\dot{\varepsilon}_\Phi = \frac{v}{\delta}\frac{\cos(\alpha)}{\cos(\Phi - \alpha)}. \tag{B.32}$$

As we have already shown **[129]**, the energy balance equation of the inactive layer assumes the following dimensionless form:

$$\frac{d\hat{T}_0(\hat{t})}{d\hat{t}} = \zeta(\hat{T}(\hat{t}) - 2\hat{T}_0(\hat{t})) - \frac{1}{\delta\hat{t}}\hat{T}_0(\hat{t}), \tag{B.33}$$

where $\hat{T}_0$ and $\hat{T}$ denote the temperature in the inactive and active layers, respectively.

During the motion of the material, heat flows from the inactive layer to the active layer. In the new model [130] it is taken into account that time is necessary to cover the distance δ, which corresponds to the thickness of the layer. Consequently, a delayed value of the temperature $\hat{T}_0(\hat{t}-\delta\hat{t})$ must be used in the calculations. Therefore,

$$\frac{d\hat{T}(t)}{d\hat{t}} = \eta\hat{\tau}(\hat{t})F(\hat{t}) - \zeta(\hat{T}(\hat{t}) - \hat{T}_0(\hat{t})) - \frac{1}{\delta\hat{t}}(\hat{T}(\hat{t}) - \hat{T}_0(\hat{t}-\delta\hat{t})). \tag{B.34}$$

where the following dimensionless system parameters were introduced:

$$\zeta = \frac{4K\lambda}{c\rho\delta^2} \quad \frac{1}{\delta\hat{t}} = \frac{Kv\sin(\Phi)}{\delta}, \quad \text{and} \quad \eta = \frac{rK\tau_\Phi v\cos(\Phi)}{c\rho\delta T_w\cos(\Phi-\alpha)}. \tag{B.35}$$

where c denotes the heat capacity, ρ is the density, λ is the thermal conductivity and r is the energy ratio ($r \approx 0.95$). $F(\hat{t})$ denotes the deformation speed expressed with the help of the constitutive equation, characteristic of the material of the workpiece [126]:

$$F(\hat{t}) \equiv \frac{\dot{\gamma}}{\dot{\varepsilon}_\Phi} = \frac{\hat{T}+1}{\hat{T}_\Phi+1}\exp\frac{\hat{\tau} - \frac{1+\varepsilon_\Phi^n\hat{\gamma}^n}{1+\varepsilon_\Phi^n} + a(\hat{T}-\hat{T}_\Phi)}{b(\hat{T}+1)}, \tag{B.36}$$

where a, b, and n are constant values, characteristic of the thermal softening, the sensitivity to velocity of deformation, and the strain-hardening, respectively. The deformation is described by the following equation [126]:

$$\frac{d\hat{\gamma}(\hat{t})}{d\hat{t}} = \left[F(\hat{t}) - F(\hat{t}-\delta\hat{t})\right]\frac{1}{\delta\hat{t}}. \tag{B.37}$$

It is also necessary to describe the mechanical equilibrium with another equation that takes the variation of the depth of cut into account as the built-up edge develops.

The so-called card model is used for setting up the equation of mechanical balance [133]. According to Fig. B.2, pressure $p(x,t)$ acts on the surface of the tool, which can be described by the empirical formula $p \approx p_0(1-x/L)^{\lambda'}$ along the surface of the tool [174], where $\lambda' = 2\div3$. As a consequence, normal stress $\sigma = p\cos(\Phi-\alpha)$ develops in the neighborhood of the shear zone. This normal stress is in equilibrium with the shear stress τ occurring in the shear zone during the plastic deformation:

$$\left[\cos(\Phi-\alpha) - \mu\sin(\Phi-\alpha)\right] w\int_0^L p(x)dx = \tau\frac{wh}{\sin(\Phi)}, \tag{B.38}$$

where μ denotes the friction coefficient, h is the depth of cut, while w is the chip width. After integration, Eq. B.38 can be rewritten as

$$\tau = \left[1 - \mu\tan(\Phi-\alpha)\right]\frac{L}{1+\lambda'}\sin(\Phi)\frac{\sigma}{h}. \tag{B.39}$$

According to [19], the projection of the cutting velocity to the shear plane

$$v_\Phi = v\frac{\cos(\alpha}{\cos(\Phi-\alpha)} \tag{B.40}$$

can be decomposed into two parts: $v_\Phi = \dot{y}_{pl} + \dot{y}_{el}$. As depicted in Fig. B.2, y_{pl} is the displacement in the shear zone, related to the plastic deformation, i.e., the $\bar{\gamma}$ plastic deformation

angle: $\Delta y_{pl} = \delta\bar{\gamma}$, while y_{el} denotes the elastic deformation in the chip parallel with the shear zone:

$$\Delta y_{el} = \frac{h\sigma}{E\sin(\Phi)}, \tag{B.41}$$

where E denotes Young's modulus. Using (B.32), we obtain

$$\dot{y}_{el} = v_\Phi - \delta\dot{\gamma} = v_\Phi\left[1 - \frac{\delta}{v_\Phi}\dot{\gamma}\right] = v_\Phi\left[1 - \frac{\dot{\gamma}}{\dot{\varepsilon}_\Phi}\right] = v_\Phi(1 - F(t)), \tag{B.42}$$

where $F(t) \equiv \dot{\gamma}/\dot{\varepsilon}_\Phi$, according to the constitutive equation (B.36). The differentiation of (B.41) leads to

$$\dot{y}_{el} = \frac{\dot{h}\sigma + h\dot{\sigma}}{E\sin(\Phi)} \tag{B.43}$$

which – together with (B.42) – makes the formulation of $\dot{\sigma}$ possible:

$$\dot{\sigma} = \frac{Ev_\Phi\sin(\Phi)[1 - F(t)]}{h} - \frac{\sigma\dot{h}}{h}. \tag{B.44}$$

As the BUE periodically develops and tears off, the thickness of the cut layer can be given in the form

$$h(t) = h_0[1 + f(t)]. \tag{B.45}$$

Using (B.39) and (B.44), we obtain

$$\frac{d\tau}{dt} = [1 - \mu\tan(\Phi - \alpha)]\frac{ELv\sin^2(\Phi)\cos(\alpha)}{(\lambda' + 1)h^2\cos(\Phi - \alpha)}[1 - F(t)] - 2\frac{\tau}{h}\frac{dh}{dt}. \tag{B.46}$$

It is expedient to rewrite the equation to dimensionless form:

$$\frac{d\hat{\tau}}{d\hat{t}} = [1 - \mu\tan(\Phi - \alpha)]\frac{ELv\sin^2(\Phi)\cos(\alpha)}{(\lambda' + 1)h_0^2\tau_\Phi\cos(\Phi - \alpha)}K\frac{1 - F(\hat{t})}{[1 + f(\hat{t})]^2} - 2\frac{\hat{\tau}}{h}\frac{dh}{d\hat{t}}. \tag{B.47}$$

By the appropriate choice of the time-scale K, the equation of mechanical balance turns to the following non-dimensional formula in the case of varying depth of cut $h(\hat{t})$:

$$\frac{d\hat{\tau}}{d\hat{t}} = \frac{1 - F(\hat{t})}{[1 + f(\hat{t})]^2} - 2\frac{\hat{\tau}}{h}\frac{dh}{d\hat{t}}, \tag{B.48}$$

where

$$K = \frac{(\lambda' + 1)h_0^2\tau_\Phi\cos(\Phi - \alpha)}{ELv\sin^2(\Phi)\cos(\alpha)}\frac{1}{1 - \mu\tan(\Phi - \alpha)}. \tag{B.49}$$

In summary, the new mathematical model of chip formation comprises the autonomous differential equations (B.33), (B.34), (B.37) and (B.48), along with the expression of the deformation speed (B.36). These equations should be applied as follows: only the shear stress changes in the initial interval $\hat{t} = 0 \ldots \delta\hat{t}$, according to (B.48), with initial condition $\hat{\tau}(0) = 0$.. This part of the solution corresponds to the formation of the deformation band. The other three variables remain zero in this period: $\hat{T}_0(\hat{t}) = 0$, $\hat{T}(\hat{t}) = 0$, $\hat{\gamma}(\hat{t}) = 0$. For times $\hat{t} > \delta\hat{t}$, the solution previously obtained for the shear stress provides the time history for the delayed differential equations.

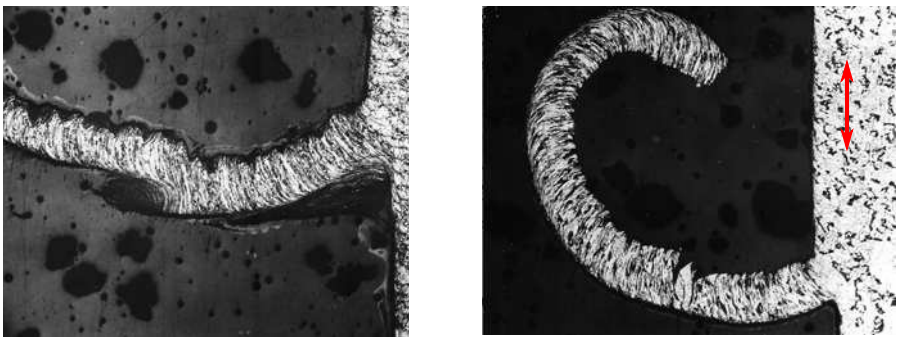

(a) (b)

Figure B.3: *Formation of built-up-edge and its influence on the cut chip. (⟷ 1 mm): (a) free-cutting steel and (b) free-cutting steel+Pb+Te.*

Quality	Charge #	C %	Mn %	Si %	P %	S %	Pb %	Te %	Al %
AS1	89694	0.08	0.91	0.05	0.098	0.208	-	-	0.02
AS1 Pb Te	89746	0.08	1.1	0.05	0.103	0.218	0.15	0.04	0.04

Table B.1: *Chemical composition of the experimental materials.*

B.4.2 Refinement of the model based on experimental results

To validate and refine the model, Pálmai used a material that can be cut both with and without the formation of BUE during the application of the same technology: the free-cutting steel. A Hungarian metallurgical company produced a new steel type by alloying free-cutting steel with Pb and Te. These components behave as lubricants during cutting, preventing the formation of BUE. The chemical composition of these two steel types is quite similar, as it is shown in Table B.1. These steel materials were turned in rolled state with high-speed steel tools. After the abrupt interruption of the process, the chips depicted in Fig. B.3 were obtained. Picture B.3/a shows the occurrence of BUE in the case of free-cutting steel, while continuous chips were produced without BUE as a consequence of the Pb and Te content, according to picture B.3/b.

The periodic formation and breaking off of the BUE can be observed well in Fig. B.3/a, where a previously torn off part of the BUE can be seen together with the actually forming BUE at the root of the chip. According to Fig. B.4 that shows a blow-up of Fig. B.3/a, the BUE formed at the tool tip tears off only partially, and a large portion of the material accumulates on the tool permanently, increasing its size. The periodic formation and tearing off of the BUE leads to the periodic variation of the depth of cut by Δh – see Fig. B.4. The depth of cut h gradually – approximately linearly – increases during the formation of the BUE. Then, the BUE tears off at a certain Δh value, and the thickness of the cut layer becomes h_0, again. Thus, the actual depth of cut $h(t)$ varies according to a saw-tooth profile. The frequency of the phenomenon can be determined by the examination of produced chips. Thus, Eq. (B.45) can be rewritten as

$$h(\hat{t}) = h_0[1 + H f_1(\hat{t})], \tag{B.50}$$

where $H = \Delta h/h_0$, and the saw-tooth profile is given by the function

$$f_1(\hat{t}) = \frac{\Omega}{2\pi}\left(\hat{t}\mathrm{mod}\frac{2\pi}{\Omega}\right) \equiv \frac{\Omega}{2\pi}\hat{t}_m. \tag{B.51}$$

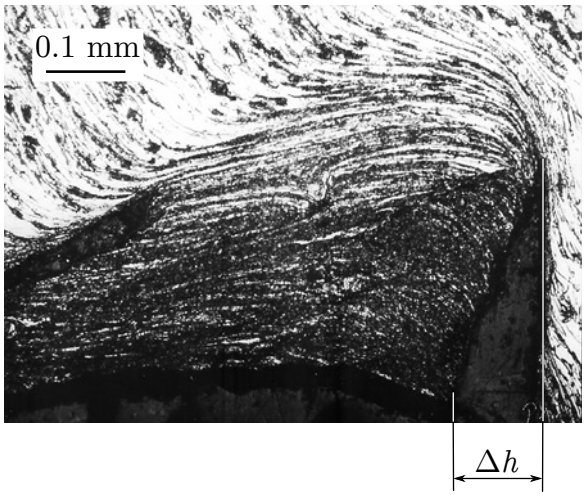

Figure B.4: *Variation Δh of the depth of cut.*

Here $\Omega = K\omega$, and ω is the angular frequency of the development of the BUE. Thus, the final form of Equation (B.48) is

$$\frac{d\hat{\tau}}{d\hat{t}} = \frac{1 - F(\hat{t})}{\left[1 + H\frac{\Omega}{2\pi}\hat{t}_m\right]^2} - 2\hat{\tau}\frac{H\frac{\Omega}{2\pi}}{1 + H\frac{\Omega}{2\pi}\hat{t}_m}. \tag{B.52}$$

Appendix C

Micro-chaos Map

C.1 STATE-SPACE MODEL OF FULL-STATE FEEDBACK

We consider systems described by first order linear differential equations, i.e.,

$$\begin{aligned}\dot{\mathbf{x}} =& \tilde{\mathbf{A}}\mathbf{x} + \tilde{\mathbf{B}}\mathbf{u},\\ \mathbf{u} =& \mathbf{K}\mathbf{x},\end{aligned} \tag{C.1}$$

where $\mathbf{x} \in \mathbb{R}^n$ denotes the state vector, $\tilde{\mathbf{A}} \in \mathbb{R}^{n\times n}$ and $\tilde{\mathbf{B}} \in \mathbb{R}^{n\times m}$ are the coefficient matrices, $\mathbf{u} \in \mathbb{R}^m$ is the vector of m control signals and $\mathbf{K} \in \mathbb{R}^{m\times n}$ is the matrix of feedback gains.

In the case of sampling with sampling period τ, zero-order-hold control scheme and neglected processing delay, the solution of the differential equations can be given in the form

$$\left.\begin{aligned}\mathbf{x}_{j+1} &= \mathbf{A}\mathbf{x}_j + \mathbf{B}\mathbf{u}_j\\ \mathbf{u}_j &= \mathbf{K}\mathbf{x}_j\end{aligned}\right\} \quad \Rightarrow \quad \mathbf{x}_{j+1} = (\mathbf{A} + \mathbf{B}\mathbf{K})\,\mathbf{x}_j \equiv \mathbf{S}\mathbf{x}_j. \tag{C.2}$$

where the coefficient matrices of the discrete system can be calculated as $\mathbf{A} = \exp(\tilde{\mathbf{A}}\tau)$ and $\mathbf{B} = \int_0^\tau \exp(\tilde{\mathbf{A}}z)dz\ \tilde{\mathbf{B}}$, where $\mathbf{A} \in \mathbb{R}^{n\times n}$ and $\mathbf{B} \in \mathbb{R}^{n\times m}$.

In real control systems, the derivatives (speed, angular velocity, etc.) are typically determined using a difference scheme. In the simplest case, when the feedback delay is neglected in a 1DoF system, the speed v at time instant $t = j\tau$ can be expressed by the actual and one step earlier value of the displacement x as

$$v_j = \frac{x_j - x_{j-1}}{\tau}. \tag{C.3}$$

As a consequence, the delayed values of the displacement appear in the governing equation of the system. If the control effort $\mathbf{u}$ depends on delayed values of the state, the state-space model can be given as

$$\begin{aligned}\mathbf{x}_{j+1} &= \mathbf{A}\mathbf{x}_j + \mathbf{B}\mathbf{u}_j,\\ \mathbf{u}_j &= \mathbf{K}_0\mathbf{x}_j + \mathbf{K}_1\mathbf{x}_{j-1} + \cdots + \mathbf{K}_d\mathbf{x}_{j-d}.\end{aligned} \tag{C.4}$$

To facilitate the stability analysis of the system, we complement the actual state vector $\mathbf{x}_j$ by its earlier values, resulting in a new state vector $\mathbf{y}_j = [\mathbf{x}_{j-d}^T\ \ldots\ \mathbf{x}_j^T]^T$, i.e., $\mathbf{y}_j \in \mathbb{R}^{(d+1)n}$ if the largest delay is $d\tau$. Using this extended state vector, the governing equation can be

rewritten as

$$\mathbf{y}_{j+1} \equiv \begin{bmatrix} \mathbf{x}_{j-(d-1)} \\ \vdots \\ \mathbf{x}_{j-1} \\ \mathbf{x}_j \\ \mathbf{x}_{j+1} \end{bmatrix} = \begin{bmatrix} \mathbf{0} & \mathbf{I} & \mathbf{0} & \dots & \mathbf{0} \\ \mathbf{0} & \mathbf{0} & \mathbf{I} & \dots & \mathbf{0} \\ \vdots & \vdots & \vdots & \ddots & \vdots \\ \mathbf{0} & \mathbf{0} & \mathbf{0} & \dots & \mathbf{I} \\ \mathbf{BK}_d & \mathbf{BK}_{d-1} & \dots & \mathbf{BK}_1 & \mathbf{A}+\mathbf{BK}_0 \end{bmatrix} \begin{bmatrix} \mathbf{x}_{j-d} \\ \vdots \\ \mathbf{x}_{j-2} \\ \mathbf{x}_{j-1} \\ \mathbf{x}_j \end{bmatrix} \equiv \mathbf{S}\mathbf{y}_j. \quad \text{(C.5)}$$

The size of each unit matrix is $\mathbf{I} \in \mathbb{R}^{n\times n}$. If there is no quantization, the general form of the map – with or without delay – is

$$\mathbf{y}_{j+1} = \mathbf{S}\mathbf{y}_j. \quad \text{(C.6)}$$

C.2 POSSIBLE TYPES OF QUANTIZATION

C.2.1 Quantization at the output

In this case, we assume that there is no round-off at the input, but the elements of the calculated control vector $\mathbf{u}_j = [u_{1j} \quad u_{2j} \quad \dots \quad u_{mj}]^T$ are sent out with different resolution values. The diagonal matrix

$$\mathbf{R}_O = \mathrm{diag}[r_{O1} \quad r_{O2} \quad \dots \quad r_{Ol}] \quad \text{(C.7)}$$

contains the values of the resolutions for the l control effort signals. Each signal must be an integer multiple of the corresponding resolution value. In this case,

$$\mathbf{x}_{j+1} = \mathbf{A}\mathbf{x}_j + \mathbf{B}\mathbf{R}_O\mathbf{Int}\left(\mathbf{R}_O^{-1}\mathbf{u}_j\right), \quad \text{(C.8)}$$

where

$$\mathbf{u}_j = \mathbf{K}_0\mathbf{x}_j + \mathbf{K}_1\mathbf{x}_{j-1} + \cdots + \mathbf{K}_d\mathbf{x}_{j-d}, \quad \text{(C.9)}$$

and the function $\mathbf{Int}\colon \mathbb{R}^l \to \mathbb{Z}^l$ calculates the integer parts of the elements of the output, rounding towards zero. Thus, the following map describes the evolution of the state instead of Equation (C.5):

$$\mathbf{y}_{j+1} \equiv \begin{bmatrix} \mathbf{x}_{j-(d-1)} \\ \vdots \\ \mathbf{x}_{j-1} \\ \mathbf{x}_j \\ \mathbf{x}_{j+1} \end{bmatrix} = \begin{bmatrix} \mathbf{0} & \mathbf{I} & \mathbf{0} & \dots & \mathbf{0} \\ \mathbf{0} & \mathbf{0} & \mathbf{I} & \dots & \mathbf{0} \\ \vdots & \vdots & \vdots & \ddots & \vdots \\ \mathbf{0} & \mathbf{0} & \mathbf{0} & \dots & \mathbf{I} \\ \mathbf{0} & \mathbf{0} & \dots & \mathbf{0} & \mathbf{A} \end{bmatrix} \begin{bmatrix} \mathbf{x}_{j-d} \\ \vdots \\ \mathbf{x}_{j-2} \\ \mathbf{x}_{j-1} \\ \mathbf{x}_j \end{bmatrix} + \begin{bmatrix} \mathbf{0} \\ \mathbf{0} \\ \vdots \\ \mathbf{0} \\ \mathbf{B}\mathbf{R}_O\mathbf{Int}\left(\mathbf{R}_O^{-1}\sum_{i=0}^{d}\mathbf{K}_i\mathbf{x}_{j-i}\right) \end{bmatrix}$$
$$\equiv \mathbf{A}^+\mathbf{y}_j + \mathbf{b}_j^+. \quad \text{(C.10)}$$

This expression can easily be reduced to

$$\mathbf{x}_{j+1} = \mathbf{A}\mathbf{x}_j + \mathbf{B}\mathbf{R}_O\mathbf{Int}\left(\mathbf{R}_O^{-1}\sum_{i=0}^{d}\mathbf{K}_i\mathbf{x}_{j-i}\right) \equiv \mathbf{A}\mathbf{x}_j + \mathbf{b}_j, \quad \text{(C.11)}$$

where $\mathbf{A}$ denotes the coefficient matrix of the uncontrolled system, with at least one eigenvalue outside the unit circle. If there is only one control signal, i.e., vector $\mathbf{u}_j$ is one-

dimensional with resolution r_O, integer numbers m_j describe the quantization at each sampling instant, leading to

$$\mathbf{y}_{j+1} = \mathbf{A}^{+}\mathbf{y}_j + \mathbf{b}^{+}m_j, \quad \text{and} \quad \mathbf{x}_{j+1} = \mathbf{A}\mathbf{x}_j + \mathbf{B}r_O\mathrm{Int}\left(r_O^{-1}\sum_{i=0}^{d}\mathbf{K}_i\mathbf{x}_{j-i}\right) \equiv \mathbf{A}\mathbf{x}_j + \mathbf{b}m_j. \tag{C.12}$$

C.2.2 Quantization at the input

If the measured inputs $\mathbf{x}_j$ are quantized instead of the output $\mathbf{u}_j$, the values of the resolution for the n state variables can be given by the n-dimensional diagonal matrix

$$\mathbf{R}_I = \mathrm{diag}[r_{I1} \quad r_{I2} \quad \dots \quad r_{In}]. \tag{C.13}$$

Only integer multiples of the resolutions r_{Ik}, $k = 1, \dots, n$ are used by the control system for the calculation of the exerted control effort. Using matrix $\mathbf{R}_I$, micro-chaos maps similar to (4.8) and (C.10) or to (4.13) can be formulated.

If one wants to emphasize the local unstable behaviour, the coefficient matrix of (C.10) can be used, and the map can be formulated similarly as (4.9):

$$\mathbf{x}_{j+1} = \mathbf{A}\mathbf{x}_j + \mathbf{B}\sum_{i=0}^{d}\mathbf{K}_i\mathbf{R}_I\mathbf{Int}\left(\mathbf{R}_I^{-1}\mathbf{x}_{j-i}\right) \equiv \mathbf{A}\mathbf{x}_j + \mathbf{b}_j, \tag{C.14}$$

where the element-wise integer-part function **Int** maps from $\mathbb{R}^n$ to $\mathbb{Z}^n$. The alternative form of the map that emphasizes the global attractive property of the origin assumes the form $\mathbf{y}_{j+1} = \mathbf{S}\mathbf{y}_j + \mathbf{c}_j$ that is similar to Eq. (4.13) with the same coefficient matrix $\mathbf{S}$, and the shift vector

$$\mathbf{c}_j = \begin{bmatrix} \mathbf{0} \\ \mathbf{0} \\ \vdots \\ \mathbf{0} \\ \mathbf{B}\sum_{i=0}^{d}\mathbf{K}_i\mathbf{R}_I\mathbf{F}_{j-i} \end{bmatrix}. \tag{C.15}$$

The fractional part vectors' elements are between -1 and 1, since

$$\mathbf{F}_{j-i} = \mathbf{R}_I^{-1}\mathbf{x}_{j-i} - \mathbf{Int}\left(\mathbf{R}_I^{-1}\mathbf{x}_{j-i}\right). \tag{C.16}$$

C.2.3 Twofold quantization at the input and output

It is straightforward to combine the input and output quantization cases to obtain the corresponding micro-chaos maps:

$$\mathbf{x}_{j+1} = \mathbf{A}\mathbf{x}_j + \mathbf{B}\mathbf{R}_O\mathbf{Int}\left(\mathbf{R}_O^{-1}\sum_{i=0}^{d}\mathbf{K}_i\mathbf{R}_I\mathbf{Int}\left(\mathbf{R}_I^{-1}\mathbf{x}_{j-i}\right)\right) \equiv \mathbf{A}\mathbf{x}_j + \mathbf{b}_j. \tag{C.17}$$

Using the other approach, i.e., substracting the fractional parts, the coefficient matrix $\mathbf{S}$ is the same as in (4.13), and the shift vector will be also similar:

$$\mathbf{c}_j = \begin{bmatrix} \mathbf{0} \\ \mathbf{0} \\ \vdots \\ \mathbf{0} \\ \mathbf{B}\mathbf{R}_O\mathbf{F}_j \end{bmatrix}. \tag{C.18}$$

Note, however, that the definition of vector $\mathbf{F}_j$ is different from (4.12):

$$\mathbf{F}_j = \mathbf{R}_O^{-1} \sum_{i=0}^{d} \left(\mathbf{K}_i \mathbf{R}_I \mathbf{Int} \left(\mathbf{R}_I^{-1} \mathbf{x}_{j-i} \right) \right) - \mathbf{Int} \left(\mathbf{R}_O^{-1} \sum_{i=0}^{d} \left(\mathbf{K}_i \mathbf{R}_I \mathbf{Int} \left(\mathbf{R}_I^{-1} \mathbf{x}_{j-i} \right) \right) \right). \quad \text{(C.19)}$$

Thus, we found that independently on the type of round-off, the discrete map describing the evolution of the system can be given as $\mathbf{y}_{j+1} = \mathbf{A}\mathbf{y}_j + \mathbf{b}_j$ or $\mathbf{y}_{j+1} = \mathbf{S}\mathbf{y}_j - \mathbf{c}_j$.

C.3 2D MICRO-CHAOS MAP WITH DELAY

C.3.1 Restrictions about the basic branches

(A) If $y_{\sup}^m > x_{m+1}^*$ and $m \geq 0$, the trajectory can jump from the mth basic branch to that part of the next ($m+1$st) basic branch that is on the other side of the fixed point $\mathbf{y}_{m+1}^*$. Consequently, the solution may reach the ($m+2$nd) basic branch, as well. This situation may occur if

$$b < n_{\sup,+}^m \equiv \frac{a^2(a-1)(m+1)}{ma^2+1}. \quad \text{(C.20)}$$

For example, $n_{\sup,+}^2 \approx 0.614 > b$ in the case $a = 1.5$, $b = 0.6$, shown in Figure 4.9. Thus, $\mathbf{p}_{\sup}^2$ is "over" the fixed point $\mathbf{y}_3^*$. Consequently, the solutions can reach band M_4 as they move away from $\mathbf{y}_3^*$, and finally, they reach the unstable line of $\mathbf{y}_4^*$. Since $n_{\sup,+}^3 \approx 0.58 < b$, the solutions cannot go further, to the unstable line of $\mathbf{y}_5^*$.

Similarly, if condition $y_{\inf}^m < x_{m-1}^*$ is fulfilled at $m > 0$, which means that

$$b > n_{\inf,+}^m \equiv \frac{a^2(a-1)m}{ma^2-1}, \quad \text{(C.21)}$$

the solutions can jump from the mth basic branch over the fixed point of the $(m-1)$st basic branch. Thus, the $(m-2)$nd branch can be reached by them. At $a = 1.5$ and $b = 0.6$ (Figure 4.9), $n_{\inf,+}^3 \approx 0.587 < b$, and $\mathbf{p}_{\inf}^3$ is under the fixed point $\mathbf{y}_2^*$. Consequently, the solutions can reach band M_1 as they move away from $\mathbf{y}_2^*$, and finally, they reach the basic branch of $\mathbf{y}_1^*$. Note that if $y_{\inf}^1 < x_0^*$, the positive solutions may jump to the negative domain. This situation occurs if $b > n_{\inf,+}^1 \equiv a^2/(a+1)$.

The corresponding formulae if negative coordinates are considered:

– if $y_{\inf}^m < x_{m-1}^*$ and $m \leq 0$,

$$b < n_{\inf,-}^m \equiv \frac{a^2(a-1)(m-1)}{ma^2-1}, \text{ while} \quad \text{(C.22)}$$

– $y_{\sup}^m > x_{m+1}^*$ and $m \leq 0$ implies

$$b > n_{\sup,-}^m \equiv \frac{a^2(a-1)m}{ma^2+1}. \quad \text{(C.23)}$$

(B) If $y_{\sup}^m > y_{m+2}^{m+1}$ and $y_{m+2}^{m+1} > m+2$, the rightmost accumulation point on the branch of U_{m+1} is not $\mathbf{f}(\mathbf{p}_{m+2}^{m+1}) = \mathbf{p}_{\sup}^{m+1}$, but $\mathbf{f}(\mathbf{p}_{\sup}^m)$. The condition of the occurrence of this situation is

$$b < g_{\sup,+}^m \equiv \frac{a^2(1+m) - a(m+2)}{am-1} \quad \text{if } m > 0, \quad \text{and} \quad \text{(C.24)}$$

$$b > g_{\sup}^0 \equiv 2a - a^2 \quad \text{if } m = 0. \quad \text{(C.25)}$$

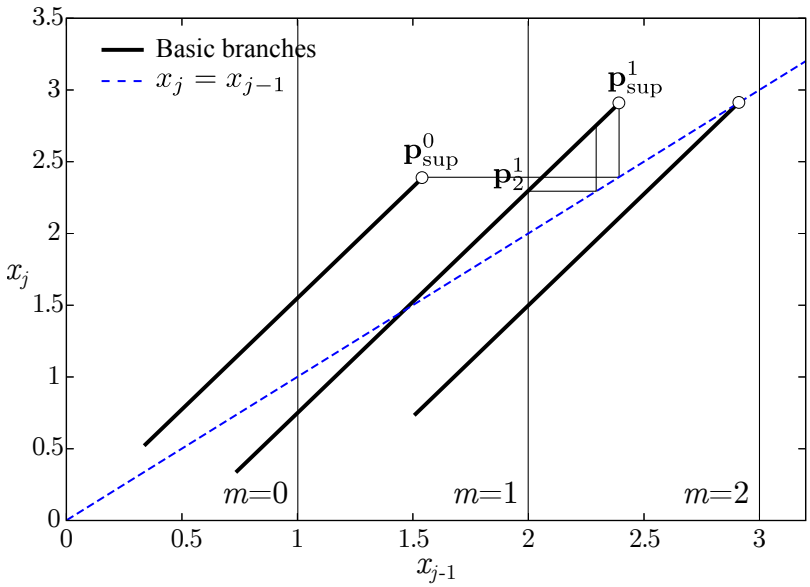

Figure C.1: *"Overstretching" of a basic branch at $a = 1.55$ and $b = 0.8$.*

For example, if $a = 1.55$ and $b = 0.8$ (see Figure C.1), $g^0_{\text{sup}} = 0.6975 < b$, thus, the rightmost accumulation point on the branch of U_1 is not $\mathbf{p}^1_{\text{sup}}$, the basic branch "stretches over" this point.

The same problem occurs if $y^m_{\text{inf}} < y^{m-1}_{m-1}$ and $m \geq 1$. In this case,

$$b > g^m_{\text{inf},+} \equiv \frac{a^2 m + a(1-m)}{am+1}, \tag{C.26}$$

and the lower endpoint of the $(m-1)$st branch is not $\mathbf{f}(\mathbf{p}^{m-1}_{m-1})$, but $\mathbf{f}(\mathbf{p}^m_{\text{inf}})$.

The corresponding formulae for negative solutions:

– $y^m_{\text{sup}} > y^{m+1}_{m+1}$ and $m \leq -1$:

$$b > g^m_{\text{sup},-} \equiv \frac{a^2 m + a(1-m)}{am}. \tag{C.27}$$

– $y^m_{\text{inf}} < y^{m-1}_{m-2}$ and $m < 0$:

$$b < g^m_{\text{inf},-} \equiv \frac{a^2(m-1) - a(m-2)}{am+1}. \tag{C.28}$$

(C) The basic branch on U_m $(m > 0)$ falls into smaller pieces (becomes dashed) if

$$\mathbf{f}(\mathbf{p}^{m-1}_{\text{sup}}) = \begin{bmatrix} (a^2 - ab - b)(m-1) + a^2 \\ a(a^2 - ab - b)(m-1) + a^3 - mb \end{bmatrix} \tag{C.29}$$

is such that its second coordinate is less than y^{m-1}_m. This is the case if

$$b > d^m \equiv \frac{am(a^2-1)}{(m-1)(a^2+a)+1}. \tag{C.30}$$

The basic branch on U_0 becomes dashed if $\mathbf{f}(\mathbf{p}^1_{\text{inf}})$ is above $\mathbf{p}^1_1$, which leads to the following condition:

$$b < d^0 \equiv \frac{a(a^2-1)}{a^2+a-1}. \tag{C.31}$$

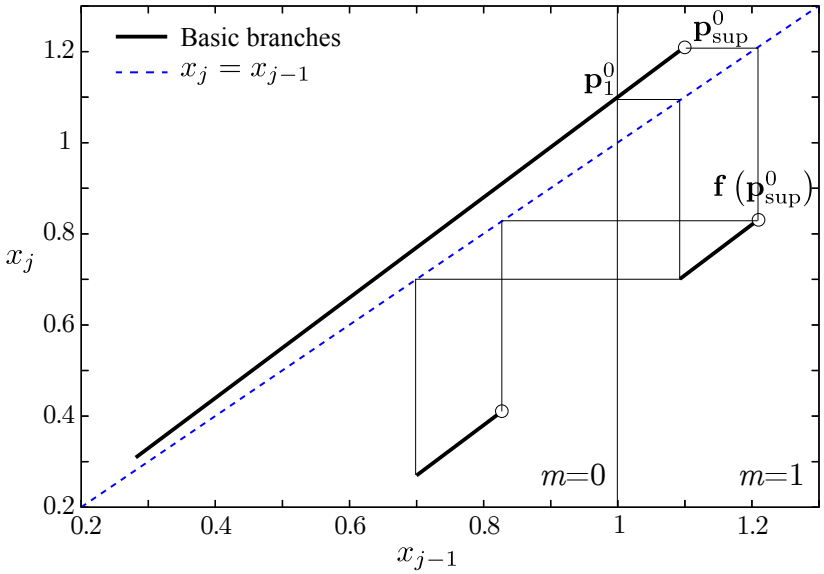

Figure C.2: *Dashed basic branch at $a = 1.1$ and $b = 0.5$.*

For example, see Figure C.2, where $d^1 = 0.231 < b = 0.5$, and $\mathbf{f}(\mathbf{p}^0_{\text{sup}})$ is below $\mathbf{p}^0_1$. As a consequence, a gap appears on the basic branch belonging to U_1.

(D) Note, that there are cases when more than two basic branches overlap. The condition of k-fold overlap of branches is $y^m_{m+1} > y^{m+k-1}_{m+k-1}$, which leads to

$$b > l^k \equiv \frac{a(k-2)}{k-1}. \tag{C.32}$$

If conditions (C.20)-(C.23) are not fulfilled, the basic branches of $\mathbf{y}^*_{m+1}$ or $\mathbf{y}^*_{m-1}$ become mangled, since the solution cannot jump to the other side of the corresponding fixed point.

Thus, the maximal and minimal numbers m, with which whole basic branches occur are

$$m_{\min} = \text{Int}\frac{b}{a^2(b+1-a)}, \tag{C.33}$$

$$m_{\max} = \text{Int}\frac{a^2(a-1)-b}{a^2(b+1-a)} + 1. \tag{C.34}$$

The rightmost accumulation point of the attractor can be obtained as $\mathbf{f}(\mathbf{p}^{m_{\max}}_{\text{sup}})$:

$$\begin{bmatrix} x_r \\ y_r \end{bmatrix} = \begin{bmatrix} a(a-b)-b)m_{\max} + a^2 \\ ax_r - b(m_{\max}+1) \end{bmatrix}. \tag{C.35}$$

The leftmost point of the attractor is $\mathbf{f}(\mathbf{p}^{m_{\min}}_{\text{inf}})$:

$$\begin{bmatrix} x_l \\ y_l \end{bmatrix} = \begin{bmatrix} a(a-b)-b)m_{\min} \\ ax_l - b(m_{\min}-1) \end{bmatrix}. \tag{C.36}$$

The introduced points are shown in Figure 4.9, together with the auxiliary lines L^0 : $x_j = \frac{a^2-ab-b}{a-b}x_{j-1}$ and L^+ : $x_j = \frac{a^2-ab-b}{a-b}x_{j-1} + \frac{ab}{a-b}$, passing through the endpoints of the basic branches.

For the sake of simplicity, we restrict ourselves to the cases when $(a, b) \in G$, the basic branches are not dashed, solutions cannot assume negative values, and the endpoints of

the basic branches are $\mathbf{p}^m_{\text{inf}}$ and $\mathbf{p}^m_{\text{sup}}$, respectively. Certain parameter domains, where these conditions are fulfilled, are shown in Figure 4.10.

The greatest domain, denoted by "01", corresponds to the parameter values where the basic branches lie on the unstable lines of the fixed points $\mathbf{y}^*_0$ and $\mathbf{y}^*_1$. The boundary curves of this domain are $n^0_{\text{sup},+} = a^2(a-1)$, $n^1_{\text{inf},+} \equiv g^1_{\text{inf},+} = a^2(a-1)/(a^2-1)$, $d^1 = a(a^2-1)$, and $d^0 = a(a^2-1)/(a^2+a-1)$.

Similarly, if the parameters are found in the domain "012", the attractor consists of three branches; the third branch is on the unstable line U_2. The boundary curves are $d^0 = a(a^2-1)/(a^2+a-1)$, $d^2 = 2a(a^2-1)/(a^2+a+1)$, $n^1_{\text{sup},+} = 2a^2(a-1)/(a^2+1)$, $g^0_{\text{sup}} = 2a - a^2$, and $g^2_{\text{inf},+} = (2a^2-a)/(2a+1)$.

C.3.2 Conditions of the construction of irreducible and primitive partitions

In order to find the parameter domain where irreducible and primitive partitions can be constructed, introduce the following notation: $\mathbf{f}_0(\mathbf{p}^1_1) = [a-b \quad a(a-b)]^T$ denotes the rightmost accumulation point of $\mathbf{f}_0(B^L)$ – this is the image of the point $\mathbf{p}^1_1$. Point $\mathbf{f}_0(\mathbf{p}^1_1)$ is in a pre-image of $B^U_{|9}$. $\mathbf{f}_0(B^L)$ fully covers at least two pre-images of $B^U_{|9}$ if $\mathbf{f}_0^{-3}(\mathbf{f}_0(\mathbf{p}^1_1))$ is still on the upper branch. This condition can be formulated as follows:

$$\frac{a-b}{a^2} \geq y_l \equiv a(a^2-ab-b), \quad \text{thus} \tag{C.37}$$

$$b \geq c^u_m \equiv \frac{a(a^4-1)}{a^4+a^3-1}. \tag{C.38}$$

For example, at $a = 1.3$, $b \geq c^u_m = 0.5953$.

$\mathbf{f}_1(\mathbf{p}^0_1) = [a \quad a^2-b]^T$ denotes the leftmost accumulation point of $\mathbf{f}_1(B^U)$ – this is the image of the point $\mathbf{p}^0_1$. Point $\mathbf{f}_1(\mathbf{p}^1_1)$ is in a pre-image of $B^U_{|9}$. $\mathbf{f}_1(B^U)$ fully covers one pre-image of $B^L_{|4}$ if $\mathbf{f}_1^{-2}(\mathbf{f}_1(\mathbf{p}^0_1))$ is still on the lower branch. This condition means that

$$\frac{a+b}{a} \leq y_r \equiv a^3 - b, \quad \text{thus} \tag{C.39}$$

$$b \leq c^l_s \equiv \frac{a^4-a}{a+1}. \tag{C.40}$$

For example, at $a = 1.3$, $b \leq c^l_s = 0.6766$. If $b \geq c^u_m$, the image $\mathbf{f}_0(B^L)$ covers at least two regions on the upper branch. Moreover, if $b \leq c^l_s$, the image $\mathbf{f}_1(B^U)$ covers at least one region on the lower branch. Thus, the partition is irreducible and primitive.

The conditions, implying that the image of the basic region B^L covers at least one region on the upper branch and the image of the basic region B^U covers more than one region on the lower branch, can be obtained in a similar way:

$$b \geq c^u_s \equiv \frac{a^4-a}{a^3+a^2-1}. \tag{C.41}$$

$$b \leq c^l_m \equiv \frac{a(a^4-1)}{1+a+a^2}. \tag{C.42}$$

The parameter domains, where conditions (C.38) and (C.40) or (C.41) and (C.42) are fulfilled, are shown in Figure C.3.

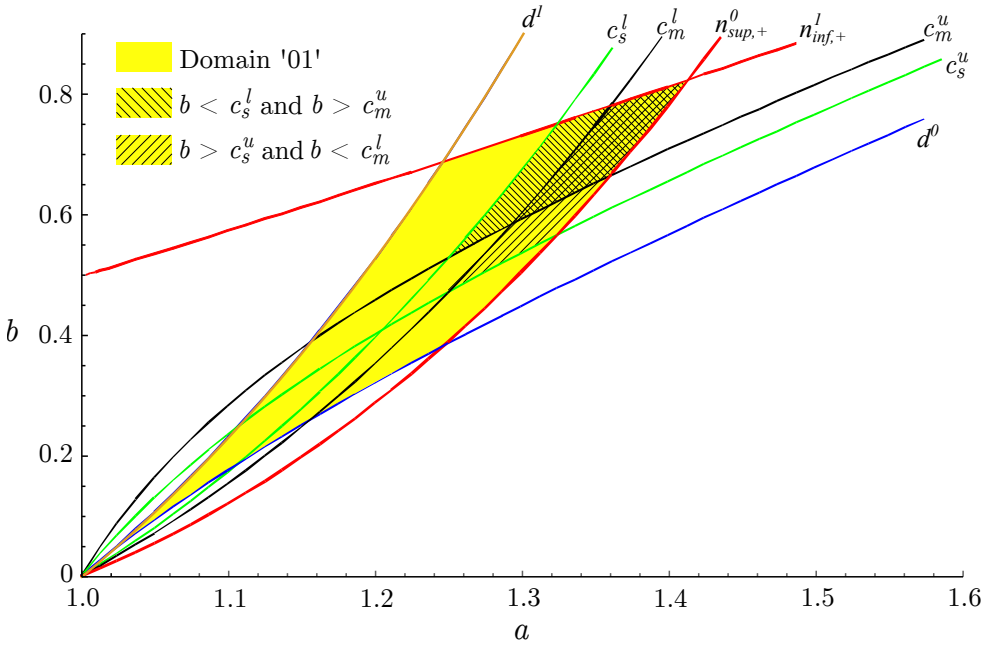

Figure C.3: *Parameter domains, where primitive partitions can be constructed.*

C.4 2D MAP WITHOUT DELAY

C.4.1 Domain of stability

The origin $\mathbf{x} = \mathbf{0}$ is asymptotically stable with respect to the map (4.61) if the roots of the characteristic equation

$$\mu^2 + \frac{(sD - 2\gamma c)\alpha^2 - P(\gamma(e-c) - \beta s)}{e\gamma\alpha^2}\mu + \frac{\gamma\alpha^2 - Des\alpha^2 - P(e\beta s - e\gamma c + \gamma)}{e^2\gamma\alpha^2} = 0$$

reside inside the unit circle on the complex plane.

To check this condition using the Routh-Hurwicz criterions, we applied a Möbius transformation, i.e., introduced a new variable η as $\mu = (\eta+1)/(\eta-1)$. After substitution, we obtained another characteristic equation ($\mathrm{Re}(\eta) < 0 \Longleftrightarrow |\mu| < 1$) in the form

$$b_2\eta^2 + b_1\eta + b_0 = 0, \tag{C.43}$$

where

$$\begin{aligned} b_2 &= (P-\alpha^2)\gamma(2ce - 1 - e^2), \\ b_1 &= -\alpha^2(-2sDe + 2\gamma(1-e^2)) - 2P(ec\gamma - es\beta - \gamma), \\ b_0 &= \alpha^2(\gamma(e^2+1+2ce) - 2sDe) - P(2es\beta + \gamma(1-e^2)). \end{aligned} \tag{C.44}$$

The origin is stable if these coefficients are greater than zero. At $b_2 = 0$ one of the characteristic multipliers becomes 1 (saddle node bifurcation in the nonlinear system). At $b_0 = 0$ one of them becomes -1 (period doubling), while at $b_1 = 0$ the characteristic roots become complex with unit modulus (Neimark-Sacker bifurcation).

The differential gain along the curves $b_0 = 0$ and $b_1 = 0$ can be expressed as

$$\begin{aligned} D_{b_0} &= \frac{\alpha^2(1+2ce+e^2)\gamma + P((-1+e^2)\gamma - 2\beta es)}{2\alpha^2 es}, \\ D_{b_1} &= \frac{\alpha^2(\gamma - e^2\gamma) + P((-1+ce)\gamma - \beta es)}{\alpha^2 es}. \end{aligned} \tag{C.45}$$

These two lines cross each other at the rightmost corner of the stability domain, at

$$P_{\max} = \frac{\alpha^2\,(1 - 2ce - 3e^2)}{1 - 2ce + e^2}, \tag{C.46}$$

$$D(P_{\max}) = \frac{(-3e + 2c^2e + e^3 + c\,(-1 + e^2))\,\gamma}{(2ce - e^2 - 1)\,s} + \frac{(1 - 2ce - 3e^2)\,\beta}{(2ce - e^2 - 1)}. \tag{C.47}$$

Note, that since $\exp(\beta) > 0$ and $\gamma > 0$, $2ce - 1 - e^2 > 0$ is fulfilled. It means that the condition $b_2 > 0$ corresponds to $P > \alpha^2$, independently of the damping. Thus, the minimal admissible proportional gain is $P_{\min} = \alpha^2$.

If the stable domain disappears during the continuous variation of parameters, the three border lines must have a common intersection point. This situation would arise only at $\beta \to -\infty$. According to the formulae, the domain of stability would disappear at $\alpha = 0$, too. However, solution (4.60) and the stability calculation are not valid if $\alpha = 0$. For the treatment of this case, see **[38]** and **[40]**. Thus, if parameter α is strictly positive and β is finite, the equilibrium can be asymptotically stabilized at every positive value of the sampling time τ – with properly chosen gains P and D. It is worth noting here that the equation of motion of a real inverted pendulum is nonlinear. Thus, if one wants to keep the pendulum in the vicinity of the upright position in order to apply the linearized equations, parameter α – and consequently, the sampling period τ – must be rather small.

C.4.2 Conditions of boundary crisis bifurcations

The crossing of $f_l(P^{LUSW})$ and $f_l(P^{RUSW})$ with W_R^S will be denoted by $Out+$ and $Out-$, while the crossing of $f_r(P^{RUSW})$ and $f_r(P^{LUSW})$ with W_L^S will be denoted by $In+$ and $In-$, respectively. These four families of crisis bifurcation curves at various values of index m form straight lines on the PD parameter plane, as illustrated in Figure 4.19. The corresponding formulae can be derived in a straightforward way.

Out_+:

$$D = -\frac{\beta e + \gamma(e + 2(c + s)(m - 1))}{\alpha^2 e}P + \frac{2\gamma m(c + s)}{e}. \tag{C.48}$$

In_+:

$$D = -\frac{(\beta + \gamma)e - 2\exp(\gamma)\gamma}{\alpha^2 e}P - \frac{2\gamma m \exp(\gamma)}{e}. \tag{C.49}$$

Out_-:

$$\begin{aligned} D = {} & \frac{\gamma((c - e)(\beta + \gamma) - 2c\gamma m) + (\alpha^2 + \beta(\beta + \gamma) - 2\gamma^2 m)s}{(\beta - \gamma)(\alpha^2 s + (\beta + \gamma)(c\gamma - e\gamma + \beta s))}P \\ & + \frac{2m\alpha^2(c + s)\gamma^2}{(\beta - \gamma)(\alpha^2 s + (\beta + \gamma)(c\gamma - e\gamma + \beta s))}. \end{aligned} \tag{C.50}$$

In_-:

$$\begin{aligned} D = {} & \frac{\gamma^2(s + c)(2m - 1) - \gamma^2 e + \beta\gamma(c - e + s)}{(\beta - \gamma)(\alpha^2 s + (\beta + \gamma)(c\gamma - e\gamma + \beta s))}P \\ & - \frac{2m\alpha^2(c + s)\gamma^2}{(\beta - \gamma)(\alpha^2 s + (\beta + \gamma)(c\gamma - e\gamma + \beta s))}. \end{aligned} \tag{C.51}$$

C.4.3 Eigenvalues of matrix S

If the eigenvalues of **S** are real, the number of sign changes in the characteristic equation (C.43) is equal to the number of positive eigenvalues, according to Descartes's sign rule. The coefficient of μ changes sign if the gain D assumes the value

$$D_1 = \frac{2c\gamma\alpha^2 + (e\gamma - c\gamma - \beta s)P}{\alpha^2 s}, \tag{C.52}$$

while the constant term changes sign at

$$D_0 = \frac{\gamma\alpha^2 + (ce\gamma - \gamma - \beta es)P}{\alpha^2 es}. \tag{C.53}$$

The eigenvalues $\mu_{1,2}$ are complex if the differential gain is between these two values:

$$D_c^{\pm} = \frac{\gamma\,(P - 2\,\alpha^2)\,(e - c) - P\beta\,s}{\alpha^2 s} \pm 2\,\frac{\gamma\,\sqrt{(\alpha^2 - P)\,(-2\,ec + 1 + e^2)}}{\alpha\,s}. \tag{C.54}$$

We are interested in cases when the eigenvalues are inside the unit circle. It means that – since $D_c^+|_{P=\alpha^2} = D_c^-|_{P=\alpha^2}$ is fulfilled – D_c^- does not intersect the domain of stability. It can be shown after some algebra that

$$\begin{array}{cll} \mu_{1,2} \in \mathbb{C} & \text{if} & D_{b_1} < D < D_c^+, \\ \mu_{1,2} > 0 & \text{if} & D_c^+ < D < D_0, \\ \mu_1 > 0 \text{ and } \mu_2 < 0 & \text{if} & D_0 < D < D_{b_0}, \\ \mu_{1,2} < 0 & \text{if} & D_c^+ < D < D_0, \\ \mu_1\mu_2 < 0 \text{ and } D < D_1 & \Rightarrow & \mu_1 > |\mu_2|. \end{array} \tag{C.55}$$

The domains of various pairs of eigenvalues in the domain of stability are shown in Figure C.4. Topologically, the arrangement of these domains is invariant to the changes in the parameters: curve D_c^+ is tangent to D_{b_0} and D_{b_2} at the rightmost and lower left apexes of the triangular domain, respectively. D_0 is tangent to D_c^+, and D_1 passes through this tangent point and the upper left corner of the domain.

It is worth to mention that both eigenvalues are zero at the intersection point of D_0 and D_1 – this point corresponds to the quickest convergence towards the equilibrium position, if there is no quantization. The proportional gain assumes the value

$$P_{\text{quick}} = \frac{\alpha^2(1 - 2ce)}{1 - 2ce + e^2} \tag{C.56}$$

at this special point.

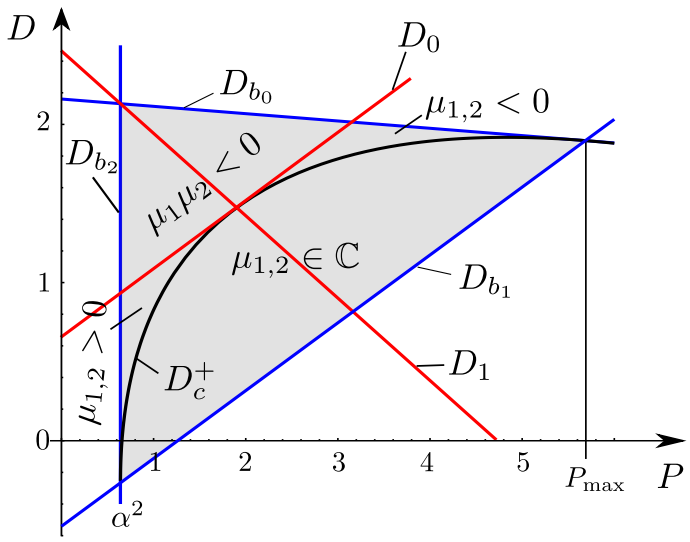

Figure C.4: *The domain of asymptotic stability ($|\mu_{1,2}| < 1$) of the desired state* $\mathbf{x} = \mathbf{0}$ *without considering processing delay and quantization at* $\alpha = 0.8$ *and* $\beta = 0.3$. *The subdomains of various pairs of eigenvalues are also shown.*

C.4.4 The algorithm of joining in the C-SCM method

This subsection describes the algorithm of joining adjacent SCM solutions. The algorithm is divided into preprocessing and two stages of classifying cell sequences which previously led to the sink cell.

For the sake of simplicity, object oriented notation is used, with simple classes for describing the cell and SCM solution including the cell state space. See Algorithms C.1 and C.2 for these classes. In the pseudo codes the . (dot) operator is used to access data or function members of these objects. For instance `scm.cells[i].index` accesses the *index* of the i-th cell of the `scm` object. Furthermore, ▷ indicates clarifying comments.

Algorithm C.1 Class for cell

```
class CELL
    index ⊂ ℕ
    image ⊂ ℕ
    domain
    group ⊂ ℕ
    step ⊂ ℕ
    type ⊂ { UNKNOWN, TRANSIENT, PERIODIC }
    state ⊂ { UNTOUCHED, UNDER_PROCESSING, PROCESSED }
end class
```

Algorithm C.2 Class for simple cell mapping

```
class SCM
    cell array of CELL objects
    cellCount ⊂ ℕ ▷ the number of cells in the cell state space
    periodicGroupCount ⊂ ℕ ▷ the number of periodic groups in the SCM solution
    index(...)
    domain(...)
end class
```

During preprocessing the cells corresponding to the domain of attraction of the sink cell for both SCM solutions are identified. This can be done by selecting cells with group number 0, which belong to the 1-P group of the sink cell. Checking the step number is not necessary, since all cells with 0 group number must be transient cells. For the pseudo code of preprocessing see Algorithms C.3 and C.4.

Algorithm C.3 Identification of sink cell's domain of attraction

Input: *scm* object representing an SCM solution
Output: array of indices of sink cell's domain of attraction GetSinkDomainOfAttraction*scm*

1: $sinkDoA \leftarrow \emptyset$ $i \leftarrow 1, scm.cellCount$ $scm.cell[i].group = 0$
2: $sinkDoA \leftarrow sinkDoA \cup i$
3: $scm.cell[i].state \leftarrow$ UNTOUCHED ▷ invalidate previously processed cell
4: $sinkDoA$

Algorithm C.4 Preprocessing of two SCM solutions

Input: objects representing SCM solutions
Output: array of indices for both sink's domain of attraction Preprocess$scm1, scm2$

1: $sinkDoA1 \leftarrow$ GetSinkDomainOfAttraction$(scm1)$
2: $sinkDoA2 \leftarrow$ GetSinkDomainOfAttraction$(scm2)$
3: $\{sinkDoA1, sinkDoA1\}$

Once the domain of attraction of the sink cell is identified for each SCM solution, the first stage of joining examines *transient cell sequences* and updates cells in Case 1 of Section 4.6.2, see Algorithm C.5.

Algorithm C.5 Stage 1 of the joining procedure

Input: Examined SCM solution and its DoA of sink, other SCM solution
Output: Updated SCM solution object *scm*, cell trees which require further processing
Stage1$scm, sinkDoA, otherScm$
1: $cellTrees \leftarrow \emptyset$ $i \leftarrow 0, sinkDoA.size$
2: $seq \leftarrow \emptyset$
3: $z \leftarrow sinkDoA[i]$ $scm.cell[z].state =$ UNTOUCHED
4: ▷ Create new cell sequence
5: $seq \leftarrow seq \cup z$
6: $left \leftarrow$ false $left =$ false
7: $imz \leftarrow scm.cell[z].image$ $imz \neq 0$
8: $cmimz \leftarrow scm.cell[imz].cmid$ $cmimz = cmid$ $scm.cell[imz].state =$ UNDER_PROCESSING
9: ▷ This sequence touches another sequence under processing
10: $left \leftarrow$ true
11: $ct \leftarrow scm.cell[imz].cellTreeIndex$
12: Tag cells in seq as UNDER_PROCESSING, assign ct as $cellTreeIndex$
13: ▷ The current sequence is prepended to cell sequence/tree with index ct
14: $cellTrees[ct] \leftarrow seq \cup cellTrees[ct]$ $scm.cell[imz].state =$ PROCESSED
15: ▷ This sequence touches an already processed cell (Case 1.b)
16: $left \leftarrow$ true
17: $g \leftarrow scm.cell[imz].group$
18: $cm \leftarrow scm.cell[imz].cmid$
19: Tag cells in seq as PROCESSED and assign new group number g and cmid cm
20: ▷ Append cell to sequence and continue
21: $seq \leftarrow seq \cup imz$
22: $z \leftarrow imz$
23: ▷ This sequence touches another sequence transiting to the other SCM (Case 1)
24: $left \leftarrow$ true
25: $g \leftarrow scm.cell[imz].group$
26: $cm \leftarrow scm.cell[imz].cmid$
27: Tag cells in seq as PROCESSED and assign new group number g and cmid cm
28: ▷ This sequence leaves the cell state space ($imz = 0$)
29: $left \leftarrow$ true
30: ▷ Get image using the other SCM's cell state space
31: $imz \leftarrow otherScm.index(step(scm.cell[z].center))$ $imz \neq 0$
32: ▷ This sequence enters other SCM solutions cell state space
33: $g \leftarrow otherScm.cell[imz].group$ $g \neq 0$
34: ▷ This sequence touches a periodic group with $g > 0$ (Case 1.b)
35: $cm \leftarrow otherScm.cell[imz].cmid$

The **for** loop in line 1 starts a new cell sequence by taking the next UNTOUCHED cell from the domain of attraction of the sink cell. The **while** loop in line 6 builds the cell sequence and updates all cells accordingly. If the condition in line 7 is true, then the cell sequence is still within the original cell state space. In this case the *cmid* is checked in line 8. If the currently examined cell has the same *cmid*, the current cell sequence either touches another cell sequence (line 9) and prepended to that cell sequence (thus forming a cell tree), or touches an already processed cell (line 15) in which case the cell sequence can be updated accordingly, or touches an UNTOUCHED cell (line 20) which results in continuing the current

36: Tag cells in *seq* as PROCESSED and assign new group number g and cmid cm
37: ▷ This sequence touches a transient cell of the other SCM's sink,
38: ▷ save this sequence for further analysis (Case 2)
39: Tag cells in *seq* as UNDER_PROCESSING and assign new group g and cmid cm
40: $cellTrees \leftarrow cellTrees \cup seq$
41: ▷ This sequence leads to the reduced sink (Case 1.a)
42: Tag cells in *seq* as PROCESSED
43: ▷ skip cell
44: $cellTrees$

sequence by examining that cell's image.

If the condition in line 8 (*cmid* check) yields false, the cell sequence touches another cell sequence transiting to the other SCM's state space, therefore the current sequence can be updated accordingly. In cases, when $imz = 0$ is fulfilled (line 27), the cell sequence leaves the cell state space. Line 31 checks whether the current cell sequence enters the cell state space of the other SCM. In this case the sequence either touches a cell with $g \neq 0$ (line 33) when the current sequence is updated, or touches a cell with $g = 0$ (line 36) when the current cell sequence (*seq*) is stored in the array of cell trees ($cellTrees$) for further analysis. Lastly, if both cell state spaces have 0 (sink) index for the cell (see line 40), the current sequence leads to the reduced sink.

In the second stage, for Case 2 in Section 4.6.2 a *cell tree mapping* is carried out (Algorithm C.6). The **for** loop in line 1 starts examining an UNTOUCHED cell tree and the **while** loop in line 6 builds a sequence of cell trees (see variable: *treeSequence*). While examining the image tree ($ctImage$) of the current cell tree ($cellTrees[i]$), the following cases can occur:

- The image of the current cell tree is a cell which was updated in Stage 1 of the procedure (line 6). All cells in the sequence of trees can be updated.

- The image tree of the current cell tree is PROCESSED (line 11), the sequence of trees touches a known destination, and all cells in the sequence of trees can be updated.

- The image tree of the current cell tree is UNDER_PROCESSING (line 15), and a new periodic group and transient cells are found. All cells within the sequence of trees are examined and tagged as *periodic* (cycle in the sequence of trees) or *transient* (branches). See Figure 4.24.

- The image tree of the current cell tree is UNTOUCHED (line 20), the image tree is appended to the sequence of trees, and the examination of the tree sequence is continued.

In the end of Stage 2, all cell trees are processed and new periodic groups (if any) with their domain of attraction (transient cells) are found. The complete procedure of joining is summarized in Algorithm C.7. The two SCM solutions joined this way form a cluster of cell mapping solutions, which can be extended further similarly.

Algorithm C.6 Stage 2 of the joining procedure

Input: Cell Sequences Tree arrays and SCM objects
Output: Updated SCM solutions Stage2$cellTrees1, cellTrees2, scm1, scm2$
1: $cellTrees \leftarrow cellTrees1 \cup cellTrees2$ $i \leftarrow 0, cellTrees.size$ $cellTrees[i].state =$ UNTOUCHED
2: ▷ Start examining sequence of cell trees
3: $cellTrees[i].state \leftarrow$ UNDER_PROCESSING
4: $treeSequence \leftarrow \emptyset \cup i$
5: $processing \leftarrow True$
6: $ctImage \leftarrow cellTrees[i].imageTree$ processing $ctImage = null$
7: ▷ There is no sequence image, image cell must be already PROCESSED in Stage 1
8: $imageCell \leftarrow cellTrees[i].cell[0].image$
9: Update all cells in each cell tree of the current $treeSequence$
10: Tag all cell tree in $treeSequence$ as PROCESSED
11: ▷ Cell tree mapping $cellTrees[ctImage].state ==$ PROCESSED
12: ▷ The sequence of trees leads to a known destination
13: Update all cells in each cell tree of the current $treeSequence$
14: Tag all cell tree in $treeSequence$ as PROCESSED
15: $processing \leftarrow False$ $cellState[ctImage].state =$ UNDER_PROCESSING
16: ▷ New periodic group and transient cells are found
17: $g \leftarrow nextGroupNumber()$
18: Update all cells in each cell tree of the current $treeSequence$
19: Tag all cell tree in $treeSequence$ as PROCESSED
20: $processing \leftarrow False$
21: ▷ $cellTrees[ctImage].state ==$ UNTOUCHED
22: ▷ Tag this cell tree as UNDER_PROCESSING,
23: ▷ append to $treeSequence$ and continue
24: $treeSequence \leftarrow treeSequence \cup ctImage$
25: $cellTrees[ctImage].state \leftarrow$ UNDER_PROCESSING
26: ▷ Get next image sequence
27: $ctImage = cellTrees[ctImage].imageSeq$ $cellTrees[i].state =$ PROCESSED
28: ▷ Skip already processed cell tree
29: $\{scm1, scm2\}$

Algorithm C.7 Procedure of joining two SCM solutions

Input: SCM objects representing SCM solutions
Output: updated SCM objects Join$scm1, scm2$
1: $\{sinkDoA1, sinkDoA2\} \leftarrow$ PREPROCESS$(scm1, scm2)$ ▷ See Algorithm C.4
2: $cellTrees1 \leftarrow$ STAGE1$(scm1, sinkDoA1, scm2)$ ▷ See Algorithm C.5
3: $cellTrees2 \leftarrow$ STAGE1$(scm2, sinkDoA2, scm1)$
4: $\{scm1, scm2\} \leftarrow$ STAGE2$(cellTrees1, cellTrees2, scm1, scm2)$ ▷ See Algorithm C.6
5: $\{scm1, scm2\}$

C.4.5 Complexity of Simple Cell Mapping

The number of times of execution and cost for some lines are denoted at line endings in Algorithm C.8. The **for** loop is executed $n + 1$ times, let t_z be the number of times the **while** loop is executed for that value of z. Let s_z be the length of the sequence accumulated

Algorithm C.8 Simple Cell Mapping

Input: Cell State space
Output: SCM solution — Number of execution, cost

1: $g \leftarrow 0$ $z \leftarrow 0, n$ — $n+1, 1$ $state[z] =$ UNTOUCHED
2: $processing \leftarrow True$
3: $sequence \leftarrow \emptyset \cup z$
4: $im \leftarrow z$ $processing$ — $\sum_{z=0}^{n-1} t_z, 1$ $state[im] =$ PROCESSED
5: Tag cells in sequence as processed and transient — $\sum_{z=0}^{n-1} 1, s_z$
6: $processing \leftarrow False$ $state[im] =$ UNDER_PROCESSING
7: ▷ New periodic group and possibily some transients found — $\sum_{z=0}^{n-1} 1, s_z$
8: Examine sequence, starting with im and tag cells as periodic, assign group g and step 0
9: Tag remaining cells as transient, assign $group \leftarrow g$ and calculate $step$ numbers
10: $g \leftarrow g + 1$
11: $processing \leftarrow False$
12: ▷ $state[im] =$ UNTOUCHED, continue along the $image$ track — $\sum_{z=0}^{n-1} t_z, 1$
13: $state[im] \leftarrow$ UNDER_PROCESSING
14: $sequence \leftarrow sequence \cup im$
15: $im \leftarrow image[im]$
16: ▷ Skip this cell

starting with cell z. By examining the algorithm, one can see, that $s_z = t_z$, since no branches of the **if-else** structure append new cell to the sequence or terminates the **while** loop at the same time. New cells are only appended to the sequence in line 14, while the processing of a sequence is either terminated at line 6 (reaching an already determined destination) or at line 11 (finding a new PG and transient cells). Therefore the cost of the algorithm is

$$C_{\mathrm{SCM}} = n\,c_1 + \sum_{z=0}^{n-1}(2\,s_z + t_z\,c_2) = (2 + c_1)\,n + \sum_{z=0}^{n-1} t_z\,c_2 = O(n),$$

where the sum of the length of sequences $\sum_{z=0}^{n-1} s_z = n$, c_1 is the total cost of constant-cost operations in the **for** loop outside the **while** loop, and c_2 is the total cost of constant-cost operations within the **while** loop.

Bibliography

[1] Albrecht, P.: Self-induced Vibrations in Metal Cutting. *Trans. Amer. Soc. Mech. Engrs., Series B., J. of Eng. For Ind.* 84, 405 (1962).

[2] Allgower E.L., Georg, K.: *Numerical continuation methods: an introduction.* Springer-Verlag Berlin, Heidelberg, (1990).

[3] Ang, K.H., Chong, G., Lim, Y.: PID control system analysis, design, and technology. *IEEE Transactions on Control Systems Technology*, 13(4), 559-576 (2005).

[4] Appel, U.: Bounds on Second-Order Digital Filter Limit Cycles, *IEEE Transactions on Circuits and Systems*, 22(7), 630-632 (1975)

[5] Armarego, E.J.A., Brown, R.H.: *The Machining of Metals.*, Prentice-Hall, Inc., Englewood Cliffe, New Jersey, (1969).

[6] Awrejcewicz, J.: Chaos in Simple Mechanical Systems with Friction. *Journal of Sound and Vibration*, 109(1), 178-180 (1986).

[7] Awrejcewicz, J., Lamarque, C.-H.: *Bifurcation and Chaos in Nonsmooth Mechanical Systems.* World Scientific, Singapore, (2003).

[8] Balcerzak, M., Dabrowski, A., Blazejczyk–Okolewska, B., Stefanski, A.: Determining Lyapunov exponents of non-smooth systems: Perturbation vectors approach. *Mechanical Systems and Signal Processing*, 141, 106734 (2020).

[9] Bánhelyi, B., Csendes, T., Garay, B.M.: Optimization and the Miranda approach in detecting horseshoe-type chaos by computer. *Int. J. Bifurcation and Chaos*, 17, 735-748 (2007).

[10] Barnsley, M.F.: *Fractals Everywhere.* 2nd edition, Morgan Kaufmann, (2000).

[11] Berger, E.J.: Friction Modeling for Dynamic System Simulation. *ASME Appled Mechanics Reviews*, **55** (6), 535-577 (2002).

[12] Bernardo, M., Budd, C., Champneys, A.R., Kowalczyk, P.: *Piecewise-smooth Dynamical Systems – Theory and Applications.* Applied Mathematical Sciences 163, Springer-Verlag London, (2008).

[13] Bertram, J.E.: The effect of quantization in sampled-feedback systems. *Transactions of the American Institute of Electrical Engineers, Part II: Applications and Industry* 77(4), 177-182 (1958)

[14] Black, J.T.: Shear Front-Lamella Structure in Large Strain Plastic Deformation Processes. *ASME Journal of Engineering for Industry*, pp. 307-316 (1972).

[15] Blazejczyk-Okolewska, B., Kapitaniak, T.: Dynamics of Impact Oscillator with Dry Friction. *Chaos, Solitons and Fractals*, 7, 1455-1459 (1996).

[16] Budai, C., Kovács, L.L., Kövecses, J., Stépán, G.: Effect of dry friction on vibrations of sampled-data mechatronic systems, *Nonlinear Dynamics*, 88, 349-361 (2017)

[17] Budai, C., Kovács, L.L., Kövecses, J.: Combined effect of sampling and coulomb friction on haptic systems dynamics, *Journal of Computational and Nonlinear Dynamics*, 13(6), 061005 (2018)

[18] Budai, C., Kovács, L.L., Kövecses, J., Stépán, G.: Combined effects of sampling and dry friction on position control, *Nonlinear Dynamics*, 98(4), 3001-3007 (2019)

[19] Burns, T.J., Davies, M.A.: Nonlinear Dynamics Model Chip Segmentation in Machining. *Physical Review Letters*, 379, 447-450 (1997).

[20] Burns, T.J., Davies, M.A.: On repeated adiabatic shear band formation during high-speed machinig. *Int. Journ. of Plasticity*, 18, 487-506 (2002).

[21] Cabrera, J.L., Milton, J.G.: Stick balancing: On-off intermittency and survival times. *Nonlinear Studies*, 11(3), 305-317 (2004).

[22] Champneys, A.R., Várkonyi, P.L.: The Painlevé paradox in contact mechanics. *IMA Journal of Applied Mathematics*, 81, 538-588 (2016).

[23] Chen, Q., Ott, E., Hurd, L.P.: Calculating topological entropies of chaotic dynamical systems. *Physics Letters A*, 156(1-2) 48-52 (1991).

[24] Chen, G. Dong, X.: *From Chaos to Order: Methodologies, Perspectives and Applications.* Singapore, World Scientific, (1998).

[25] Cheng, G., Zu, J.W.: A Numerical Study of a Dry Friction Oscillator with Parametric and External Excitations. *Journal of Sound and Vibration*, 287, 329-342 (2005).

[26] Conti, P.: Sulla Resistenza di Attrito. *Accrd. Lincei.*, 11(16), (1875).

[27] Csernák, G.: Lifetime Estimation of Chaotic Transients in Applied Mechanical Problems. PhD dissertation, Supervisor: Gábor Stépán, Department of Applied Mechanics, Budapest University of Technology and Economics, (2003).

[28] Csernák, G., Stépán, G.: On the Periodic Response of a Harmonically Excited Dry-friction Oscillator. *Journal of Sound and Vibration*, 295, 649-658, DOI: 10.1016/j.jsv.2006.01.030, (2006).

[29] Csernák, G., Stépán, G., Shaw, S.W.: Sub-harmonic Resonant Solutions of a Harmonically Excited Dry Friction Oscillator. *Nonlinear Dynamics*, 50, Article number: 93, https://doi.org/10.1007/s11071-006-9145-6, (2007).

[30] Csernák, G., *Lifetime Estimation of Chaotic Transients in Applied Mechanical Problems*, Ph.D. dissertation, Budapest University of Technology and Economics, Budapest, (2003).

[31] Csernák, G., Licskó, G.: Asymmetric and chaotic responses of a dry friction oscillator with different static and kinetic coefficients of friction, *Meccanica*, 56, 2401-2414 (2021).

[32] Csernák, G., Pálmai, Z.: Exploration of the chaotic phenomena induced by fast plastic deformation of metals. *Int J of Advanced Manufacturing Technology*, 40, 270-276 (2009).

[33] Csernák, G., Stépán, G.: Fractal Dimension as Measure of Control Time. *Periodica Polytechnica Ser. Mech. Eng.*, 48(1), 17-25 (2004).

[34] Csernák, G., Stépán, G.: Life Expectancy of Transient Microchaotic Behaviour. *J. Nonlinear Sci.* 15(2), 63-91 (2005).

[35] Csernák, G., Stépán, G.: Quick Estimation of Escape Rate with the Help of Fractal Dimension. *Communications in Nonlinear Science and Numerical Simulation*, 11(5), 595-605 (2005).

[36] Csernák, G., Stépán, G.: Life expectancy calculation of transient chaos in the 2D micro-chaos map. *Periodica Polytechnica*, 51(2), 59-62 (2007).

[37] Csernák, G., Stépán, G.: Micro-chaotic Behaviour in PD-controlled Systems. *Proceedings of CHAOS'09 Second IFAC meeting related to analysis and control of chaotic systems*, June 22nd-24th, London, UK, (2009).

[38] Csernák, G., Stépán, G.: Digital Control as Source of Chaotic Behavior. *International Journal of Bifurcation and Chaos*, 20(5), 1365-1378 (2010).

[39] Csernák, G., Stépán, G.: Sampling and Round-off, as Sources of Chaos in PD-controlled Systems. *Proceedings of the 19th Mediterranean Conference on Control and Automation*, Corfu, June 20-23, (2011).

[40] Csernák, G., Stépán, G.: Disconnected Chaotic Attractors in Digitally Controlled Linear Systems. *Recent Researches in Automatic Control, Systems Science and Communications*, Proceedings of the 8th WSEAS International Conference on Dynamical Systems and Control, Published by WSEAS Press, ISBN: 978-1-61804-103-6, 97-102 (2012).

[41] Csernák, G., Stépán, G.: The state-space model of micro-chaos, *Proc. the 2013 International Conference on Systems, Control, Signal Processing and Informatics*. Rhodes, p. 420-425 (2013).

[42] Csernák, G., Gyebrószki, G., Stépán, G.: Multi-baker Map as a Model of Digital PD Control. *Int. J. Bifurcat. Chaos*, 26(2) (2016).

[43] Csernák, G.: Quantization-induced control error in a digitally controlled system. *Nonlinear Dyn.*, 85, 2749-2763 (2016).

[44] Cvitanović, P., Artuso, R., Maineri, R., Tanner, G., Vattay, G.: *Classical and Quantum Chaos*, `www.nbi.dk/ChaosBook`, Niels Bohr Institute, Copenhagen, (2001).

[45] Dahl, P.R.: Measurement of Solid Friction Parameters of Ball Bearings, in *Proceedings of 6th Annual Symposium on Incremental Motion, Control Systems and Devices*, University of Illinois (1977).

[46] Dankowicz, H.: On the Modeling of Dynamic Friction Phenomena. *Zeitschrift für Angewandte Mathematik und Mechanik*, 79(6), 399-409 (1999).

[47] Dankowicz, H., Nordmark, A.B.: On the Origin and Bifurcations of Stick-Slip Oscillations. *Physica D*, 136, 280-302 (2000).

[48] Dankowicz, H., Schilder, F.: *Recipes for Continuation.* SIAM, Series: Computational Science & Engineering, (2013).

[49] Deimling, K.: *Multivalued Differential Equations.* de Gruyter Series in Nonlinear Analysis and Applications, 1, Berlin, New York (1992).

[50] Delchamps, F.D.: Stabilizing a linear system with quantized state feedback. *IEEE Trans. Autom. Contr.*, 35, 916-924 (1990).

[51] Den Hartog, J.P.: Forced Vibrations with Combined Coulomb and Viscous Damping. *Transactions of the American Society of Mechanical Engineers*, 53, 107-115 (1930).

[52] Devaney, R.L.: *An Introduction to Chaotic Dynamical Systems.* CRC Press; 2nd edition, (2003).

[53] Doedel, E.J., Fairgrieve, T.F.: Sandstede, B., Champneys, A.R., Kuznetsov, Y.A., Wang, X., AUTO-07P: Continuation and bifurcation software for ordinary differential equations, (2007).

[54] Doi, S.: Chatter of Lathe Tool. *J. Soc. Mech. Engrs. Japan*, 3, 94 (1937).

[55] Domokos, G., Szász, D.: Ulam's Scheme Revisited: Digital Modeling of Chaotic Attractors Via Micro-Perturbations. *Discret. Contin. Dyn. S.*, Series A. 9(4), 859-876 (2003).

[56] D'Sousa, A.F., Dweib, A.H.: Self-excited Vibrations Induced by Dry Friction. Part 2: Stability and Limit-cycle Analysis. *Journal of Sound and Vibration*, **137** (2), 177-190 (1990).

[57] Eckmann, J.P., Ruelle, D.: Ergodic Theory of Chaos and Strange Attractors. *Reviews of Modern Physics*, 57(3), Part I, 617-656 (1985).

[58] Enikov, E., Stépán, G.: Microchaotic Motion of Digitally Controlled Machines. *Journal of Vibration and Control*, 4, 427-443 (1998).

[59] Ernst, H., Martellotti, M.: The Formation of the built-up edge. *ASME Mech. Engng.*, 57, 478-498 (1938).

[60] Farmer, J.D., Ott, E., Yorke, J.A.: The dimension of chaotic attractors. *Physica*, 7D, 153-180 (1983).

[61] Feeny, B., Guran, A., Hinrichs, N., Popp, K.: A Historical Review on Dry Friction and Stick-Slip Phenomena. *ASME Applied Mechanics Reviews*, 51, 321-341 (1998).

[62] Feeny, B., Moon, F.C.: Chaos in a Forced Dry-friction Oscillator: Experiments and Numerical Modelling. *Journal of Sound and Vibration*, 170, 303-323 (1994).

[63] Feigenbaum, M.J.: Quantitative Universality for a Class of Nonlinear Transformations. *J. Stat. Phys.*, 19, 25-52 (1978).

[64] Field, M., Merchant, M.E.: Mechanics of Formation of Discontinuous Chip in Metal Cutting. *Trans. Amer. Soc. Mech. Engrs.*, 71, 421 (1949).

[65] Filippov, A.F.: Differential Equations with Discontinuous Right-hand Side. *American Mathematical Society Translations*, Series 2, 42, 199-231 (1964).

[66] Finnie, I.: Rewiew of the Metal-Cutting. Analyses of the Past Hundred Years. *Mechanical Engineering*, 715-721 (1956).

[67] Galton, G.: The action of brakes. On the effect of brakes upon railway trains. *Engineering*, 25, 469-472 (1878).

[68] Gao, C., Kuhlmann-Wilsdorf, D., Makel, D.: The Dynamic Analysis of Stick-Slip. *Wear*, 173, 1-12 (1994).

[69] Garay, B.M., Csikja, R., Tóth, J.: Some chaotic properties of the beta-hysteresis transformation. *Proc. of the 2008 International Symposium on Nonlinear Theory and its Applications*, Budapest, Hungary, 191-194 (2008).

[70] Gidea, M., Zgliczinski, P.: Covering relations for multidimensional dynamical systems. *J. Differ. Eq.* 202, 32-58 (2004).

[71] Gosline, A.H.C., Hayward, V., Michalska, H.: Ineluctability of Oscillations in Systems with Digital Implementation of Derivative Feedback. *Automatica*, 47(11), 2444-2450 (2011).

[72] Gyebrószki, G., Csernák, G.: Clustered Simple Cell Mapping: An extension to the Simple Cell Mapping method. *Communications in Nonlinear Science and Numerical Simulation*, 42, 607-622 (2017).

[73] Gyebrószki, G., Csernák, G.: Inherent control error in a multi-pd controlled double inverted pendulum. *Proceedings of the 9th European Nonlinear Dynamics Conference*, ENOC, Budapest University of Technology and Economics, Hungary, pages 1–5. (2017).

[74] Gyebrószki, G., Bachrathy, D., Csernák, G., Stepan, G.: Stability of turning processes for periodic chip formation. *Adv. Manuf.*, 6, 345–353 (2018).

[75] Gyebrószki, G.: Micro-chaos in digitally controlled mechanical systems. PhD dissertation, Supervisor: Gábor Csernák, Department of Applied Mechanics, Budapest University of Technology and Economics, (2019).

[76] Gyebrószki, G., Csernák, G.: Twofold quantization in digital control: deadzone crisis and switching line collision. *Nonlinear Dyn* 98, 1365–1378 (2019).

[77] Gyebrószki, G., Csernák, G.: The Hybrid Micro-chaos Map: Digitally Controlled Inverted Pendulum with Dry Friction. *Periodica Polytechnica Mechanical Engineering*, 63(2), 148–155 (2019).

[78] Haller, G., Stépán, G.: Micro-Chaos in Digital Control. *J. Nonlinear Sci.*, 6, 415-448 (1996).

[79] Haussner, A.: Das Hobeln von Metallen (Planing of Metals). *Mitteilungen des Technische Gewerbe Museums in Wien*, No. 2. 117 (1982).

[80] Hegger, R., Kantz, H., Schreiber, T.: Practical Implementation of Nonlinear Time Series Methods: The TISEAN Package. *Chaos*, 9(2), 413-435 (1999).

[81] Hendricks, E., Jannerup, O., Sørensen, P.H.: *Linear Systems Control – Deterministic and Stochastic Methods.* Springer, (2008).

[82] Hong, H.-K., and Liu, C.-S.: Coulomb Friction Oscillator: Modelling and Responses to Harmonic Loads and Base Excitations. *Journal of Sound and Vibration*, 229(5), 1171-1192 (2000).

[83] Hong, H.-K., and Liu, C.-S.: Non-Sticking Oscillation Formulae for Coulomb Friction Under Harmonic Loading. *Journal of Sound and Vibration*, 244(5), 883-898 (2001).

[84] Hsu, C.S.: A theory of index for point mapping dynamical systems. *J. Applied Mechanics*, 47, 85-190 (1980).

[85] Hsu, C.S.: *Cell-to-Cell Mapping. A Method of Global Analysis for Nonlinear Systems*, Applied Mathematical Sciences, Vol. 64., Springer-Verlag, New York, (1987).

[86] Ibrahim, R.A.: Friction-Induced Vibration, Chatter, Squeal, and Chaos, Part I: Mechanics of Contact and Friction. *ASME Applied Mechanics Reviews*, 47(7), 209-226 (1994).

[87] Ibrahim, R.A.: Friction-Induced Vibration, Chatter, Squeal, and Chaos, Part II: Dynamics and Modeling. *ASME Applied Mechanics Reviews*, 47(7) 227-253 (1994).

[88] Insperger, T., Milton, J., Stépán, G.: Semidiscretization for Time-Delayed Neural Balance Control. *SIAM J. Appl. Dyn. Syst.*, 14(3), 1258–1277 (2015).

[89] Jarvis, R.P., Mills, B.: Vibrations Induced by Dry Friction. *Proceedings of the Institution of Mechanical Engineers*, 178(32), 847-866 (1963/1964).

[90] Kalmár-Nagy, T., Moon, F.C.: Mode-coupled Regenerative Machine Tool Vibrations. in: *Nonlinear Dynamics of Production Systems*. Edited by G. Randons and R. Neugebauer, Wiley-VCH Verlag GmbH & Co. KGaA, Weiheim, pp. 129-151 (2004).

[91] Kantz, H., Schreiber, T.: *Nonlinear time series analysis*, Cambridge nonlinear science series, Cambridge University Press, (1997).

[92] Kato, S., Yamaguchi, K., Matsubayashi, T.: Stick-Slip Motion of Machine Tool Slideway. *ASME Journal of Engineering for Industry*, 96(2), 557-566 (1974).

[93] Karnopp, D.: Computer Simulation of Stick-Slip Friction in Mechanical Dynamics Systems. *ASME Journal of Dynamical Systems Measurement and Control*, 107(1), 100-103 (1985).

[94] Kececioglu, D.: Shear-Strain in Metal Cutting and Its Effects on Shear-Flow Stress. *Transactions of the ASME*, pp. 158-168 (1958).

[95] Kelly, R., Santibanez, V., Loria, A.: *Control of Robot Manipulators in Joint Space.* Springer, London, (2005).

[96] Kinkaid, N.M., O'Reilly, O.M., Papadopoulos, P.: Automotive Disc Brake Squeal. *Journal of Sound and Vibration*, 267(1), 105-166 (2003).

[97] Klages, R.: Deterministic diffusion in one-dimensional chaotic dynamical systems. PhD thesis. TU Berlin, (1996).

[98] Komanduri, R., Schroeder, T., Hazra, J., von Turkovich, B.F.: On the catastrophic shear instability in high-speed machinig of an AISI 4340 steel. *J. Engng Industry* 104, 121-131 (1982).

[99] Komanduri, R.: Machining and grinding: historical review of the classical papers. *Appl. Mech. Rev.* 46, 80-132 (1993).

[100] Korondi, P.: *Csúszómód-szabályozás a teljesítményelektronikában és mechatronikában* (Sliding mode control in power electronics and mechatronics, in Hungarian), Akadémiai Kiadó, e-book, ISBN: 978 963 454 100 4, DOI: 10.1556/9789634541004, https://mersz.hu/kiadvany/246, (2017).

[101] Kowalczyk, P., Piiroinen, P.T.: Two-parameter sliding bifurcations of periodic solutions in a dry-friction oscillator. *Physica D: Nonlinear Phenomena*, 237, 1053-1073 (2008).

[102] Kowalczyk, P. and di Bernardo, M.: Two-parameter degenerate sliding bifurcations in Filippov systems. *Physica D: Nonlinear Phenomena*, 204(3-4), 204-229 (2005).

[103] Kunze, M.: *Non-Smooth Dynamical Systems.* Lecture Notes in Mathematics, No. 1744, Springer-Verlag Berlin Heidelberg, ISBN 3-540-67993-6, (2000).

[104] Kuo, B.C.: *Digital Control Systems*, (SRL Publishing, Champaign, IL, USA), ISBN-13: 978-0195120646, (1977).

[105] Kuznetsov, Y.A., Rinaldi, S., Gragnani, A.: One-parameter Bifurcations in Planar Filippov Systems. *International Journal of Bifurcation and Chaos*, 13(8), 2157–2188 (2003).

[106] Lakshmikantham, V., Leela, S., Martynyuk, A.A.: *Practical Stability of Nonlinear Systems.* World Scientific, Singapore (1990).

[107] Landberg, P.: Vibrations Caused of by Chip Formation, *Microtechnic*, 10, 219 (1956).

[108] Landry, M., Campell, S.A., Morris, K., Aguilar, C.O.: Dynamics of an inverted pendulum with delayed feedback control. *SIAM Journal on Applied Dynamical Systems*, 4(2), 333-351 (2005).

[109] Leine, R.I., Nijmeijer, H.: *Dynamics and Bifurcations of Non-Smooth Mechanical Systems*, Springer-Verlag, Berlin, Heidelberg ISBN 978-3-642-06029-8, (2004).

[110] Licsko, G., Csernak, G.: On the chaotic behaviour of a simple dry-friction oscillator. *Math. Comput. Simul.*, 95, 55–62 (2013).

[111] van Luttervelt, C.A.: The split shearzone - mechanism of chip segmentation. *Annals of the CIRP*, 25: 33-38 (1977).

[112] Marino, L., Cicirello, A.: Experimental investigation of a single-degree-of-freedom system with Coulomb friction. *Nonlinear Dynamics*, 99(3), 1781-1799 (2020).

[113] Marino, L., Cicirello, A.: Coulomb friction effect on the forced vibration of damped mass–spring systems, *Journal of Sound and Vibration*, 535, 117085 (2022).

[114] Milton, J.G., Bélair, J.: Chaos, Noise and Extinction in Models of Population Growth. *Theor. Popul. Biol.*, 37(2) (1990).

[115] Milton, J., Insperger, T., Cook, W., Harris, D., Stepan, G.: Microchaos in human postural balance: Sensory dead zones and sampled time-delayed feedback. *Physical Review E*, 98(2), 022223 (2018).

[116] Mischaikov, K., Mrozek, M.: Chaos in the Lorenz equations: a computer-assisted proof. *Bull. Amer. Math. Soc.*, 32, 66-72 (1995).

[117] Müller, P.C.: Calculation of Lyapunov Exponents for Dynamic Systems with Discontinuities. *Chaos, Solitons & Fractals*, 5(9), 1671-1681 (1995).

[118] Narayanan, S., Jayaraman, K.: Chaotic Vibration in a Non-Linear Oscillator with Coulomb Damping. *Journal of Sound and Vibration*, 146(1), 17-31 (1991).

[119] Natsiavas, S.: Stability of Piecewise Linear Oscillators with Viscous and Dry Friction Damping. *Journal of Sound and Vibration*, 217, 507-522 (1998).

[120] Natsiavas, S., Verros, G.: Dynamics of Oscillators with Strongly Nonlinear Asymmetric Damping. *Nonlinear Dynamics*, 20, 221-246 (1999).

[121] Nayfeh, A.H.: *The Method of Normal Forms*, WILEY-VCH Verlag GmbH & Co. KGaA, ISBN 978-3-527-41097-2, (2011).

[122] Nusse, H.E., Yorke, J.A.: Basins of attraction. *Science*, 271, 1376–1380 (1996).

[123] Oden, J.T., Martins, J.A.C.: Models and Computational Methods for Dynamic Friction Phenomena. *Computer Methods in Applied Mechanics and Engineering*, 52, 527-634 (1985).

[124] Oseledec, V.I.: A Multiplicative Ergodic Theorem. Lyapunov Characteristic Numbers for Dynamical Systems. *Trudy Mosk. Mat. Obsc.* (Moscow Math Soc.), 19, 197, (1968).

[125] Oxley, P.L.B.: *Eine teoretische Näherungesmethode zur Bewertung der maschinellen. Bearbeitbarkeit.* 2. Teil. Fertigung No. 2. pp. 49-58. (1974).

[126] Pálmai, Z.: Aperiodic Deformation Occuring as a Result of Thermoplastic Instability of Metals. *Materials Science Forum*, 473-474, 369-374 (2005).

[127] Pálmai, Z.: Chaotic Phenomena Induced by the Fast Plastic Deformation of Metals During Cutting. *ASME J. Appl. Mech.*, 73, 241-245 (2006).

[128] Pálmai, Z.: Aperiodic deformation occuring as a result of thermoplastic instability of metals. *Materials Science Forum*, 537-538, 541-548 (2007).

[129] Pálmai, Z., Csernák, G.: Chip formation as an oscillator during the turning process. *Journal of Sound and Vibration*, 326, 809-820 (2009).

[130] Pálmai, Z.: A method for the approximate determination of the specific material properties of metals under the extreme conditions of fast deformation. *Materials Science Forum* 659, 79-84 (2010).

[131] Pálmai, Z., Csernák, G.: Effects of built-up edge-induced oscillations on chip formation during turning. *Journal of Sound and Vibration*, 332(8), 2057-2069 (2013).

[132] Piispanen, V.: Lastunmoudostumisen Teoriaa (Theory of chip formation), in Finnish. *Teknillinen Aika Kauslehti*, 27, 315 (1937).

[133] Piispanen V.: Plastic Deformation of Metals: Theory of Simulated Sliding. *Wear*, 38, 43-72 (1976).

[134] Popp, K., Stelter, P.: Stick-Slip Vibrations and Chaos. *Philosophical Transactions of the Royal Society of London A*, 332, 89-105 (1990).

[135] Potapov, A., Ali, M.K.: Chaotic Neural Control. *Physical Review E*, 63(4), 046215, (2001).

[136] Pratt T.K., Williams, R.: Non-Linear Analysis of Stick/Slip Motion. *Journal of Sound and Vibration*, 74(4), 531-542 (1981).

[137] Rabinowicz, E.: *Friction and wear of materials*, John Wiley and Sons, (1995).

[138] Rapatz, F.: Das Oberflächenaussehen bei der Spanabhebenden Bearbeitung Insbesondere beim Drehen. (The Surface Quality in Case of Chip-removing Processes, Especially in Case of Turning), *Archiv für das Eisenhüttenwesen*, 3, 717 (1929-1930).

[139] Robinson, C.: *Dynamical systems. Stability, symbolic dynamics, and chaos.* Studies in Advanced Mathematics. CRC Press, Boca Raton, FL, (1995).

[140] Rosenhain, W., Sturney, A.C.: Flow and Rupture of Metals During Cutting. *Proceedings of The Institution of Mechanical Engineers*, Part 1, 141 (1925).

[141] Shaw, M.C.: *Metal Cutting Principles.* Clarendon Press, Oxford, (1984).

[142] Shaw, S.W.: On the Dynamic Response of a System with Dry Friction. *Journal of Sound and Vibration*, 108(2), 305-325 (1986).

[143] Shteinberg, J.S.: *Ustranenie vibratsi, vozn ikayushchikh pri rezanii metallov na tokarnom.* (Elimination of Vibrations Excited During Turning), USSR, Mashgiz, (1947).

[144] Parker, S.R., Yakowitz, S.: A general method for calculating quantization error bounds due to roundoff in multivariable digital filters, *IEEE Transactions on Circuits and Systems*, 22(6), 570-572 (1975)

[145] Sieber, J., Krauskopf, B.: Complex Balancing Motions of an Inverted Pendulum Subject to Delayed Feedback Control. *Physica D.* 197(3-4), 332-345 (2004).

[146] Slaughter, J.B.: Quantization errors in digital control systems, *IEEE Transactions on Automatic Control*, 9(1), 70-74 (1964)

[147] Stefanski, A., Kapitaniak, T.: Using chaos synchronization to estimate the largest Lyapunov exponent of nonsmooth systems. *Discrete Dynamics in Nature and Society*, 4(3) 207-215 (2000).

[148] Stefanski, A, Dabrowski, A., Kapitaniak, T.: Evaluation of the largest Lyapunov exponent in dynamical systems with time delay. *Chaos, Solitons and Fractals*, 23, 1651-1659 (2005).

[149] Stépán, G.: Modelling nonlinear regenerative effects in metal cutting. *Phil. Trans. R. Soc. Lond. A*, 359, 739-757 (2001).

[150] Stepan, G., Milton, J., Insperger, T.: Quantization improves stabilization of dynamical systems with delayed feedback. *Chaos*, 27, 114306 (2017).

[151] Szalai, R., Stépán, G., Hogan, S.J.: Global dynamics of low immersion high-speed milling. *Chaos: an interdisciplinary journal of nonlinear science*, 14(4), 1069-1077 (2004).

[152] Takens, F.: *Detecting Strange Attractors in Turbulence.* Lecture notes in Math. Vol. 898, Spinger, New York, (1981).

[153] Tél, T.: Escape Rate from Strange Sets as an Eigenvalue. *Physical Review A*, 36(3), (1987).

[154] Tél, T.: Fractals, Multifractals, and Thermodynamics. An Introductory Review. *Z. Naturforsch.*, 43a, 1154-1174 (1988).

[155] Tél, T.: Transient Chaos., Published in: *Directions in Chaos*, Vol. 3. Edited by Hao Bai-lin; World Scientific Publishing Company, Singapore, 149-211, (1990).

[156] Tél, T. Gruiz, M.: *Chaotic Dynamics.* Cambridge University Press, (2006).

[157] Tlusty, J., Spacek, L.: Self-excited vibrations on machine tools. Prague: Nakl CSAV. (In Czech.) (1954).

[158] Tlusty, J.: Analysis of the state of research in cutting dynamics. *Ann. CIRP*, 27, 583-589 (1978).

[159] Tobias, S.A.: *Machine Tool Vibration.* Glasgow, Blackie and Son Ltd. (1965).

[160] Trefethen, L. N., Embree, M.: *Spectra And Pseudospectra: The Behavior of Nonnormal Matrices And Operators.* Princeton University Press,. (2005).

[161] Tucker, W.: The Lorenz attractor exists. *C. R. Acad. Sci. Paris. Sér. Math.*, 328, 1197-1202 (1999).

[162] Ushio T., Hsu, C.: Chaotic rounding error in digital control systems, *IEEE Transactions on Circuits and Systems*, 34(2) 133-139 (1987)

[163] Utkin, V.I: *Variable Structure Control Optimization.* Springer-Verlag, (1992).

[164] Várkonyi, P.L.: Dynamics of mechanical systems with two sliding contacts: new facets of Painlevé's paradox. *Arch Appl Mech*, 87, 785–799 (2017). https://doi.org/10.1007/s00419-016-1165-1

[165] Widrow, B.: A study of rough amplitude quantization by means of Nyquist sampling theory. *Transactions*, Professional Group on Circuit Theory, Institute of Radio Engineers, New York, CT-3, 266-276 (1956)

[166] Widrow, B., Kollár, I.: *Quantization Noise: Roundoff Error in Digital Computation, Signal Processing, Control, and Communications.* Cambridge University Press, Cambridge, UK, (2008).

[167] Wiggins, S.: *Introduction to Applied Nonlinear Dynamical Systems and Chaos.* Texts in Applied Mathematics 2, Springer, New York, (1990).

[168] Xie, J.Q., Bayoumi, A.E., Zbib, H.M.: Analytical and Experimental Study of Shear Localization in Chip Formation in Ortogonal Machining. *Journal of Materials Engineering and Performance*, 4(1), 32-39 (1995).

[169] Xiong, F.-R., Qin, Z.-C., Xue, Y., Schtze, O., Ding, Q., Sun, J.-Q.: Multi-objective optimal design of feedback controls for dynamical systems with hybrid simple cell mapping algorithm. *Commun Nonlinear Sci Numer Simul*, 19(5), 1465–73 (2014).

[170] Yi, A.Y., Hezlep, M., Pol. T.: A computer controlled optical pin polishing machine. *Journal of Materials Processing Technology*, 146(2), 156-162 (2004).

[171] Zgliczinski, P.: Fixed point index for iterations of maps, topological horseshoe and chaos. *Topol. Methods. Nonlin. Anal.*, 8, 169-177 (1996).

[172] Zgliczinski, P.: Computer assisted proof of chaos in the Rössler equations and in the Hénon map. *Nonlinearity*, 10, 243-252 (1997).

[173] Zou. H., Xu, J.: Improved generalized cell mapping for global analysis of dynamical systems. *Sci China Ser E*, 52(3), 787–800 (2009).

[174] Zorev, N.N., Granovskij, G.I., Loladze, T.N.: *Razvitie nauki o rezanii metallov.* Mashinostroenie, Moskva, (1967).